Environmental Dependence of Star Formation in Nearby Barred Spiral Galaxies

Hsi-An Pan

Doctor of Science

Department of Astronomical Science
School of Physical Sciences
The Graduate University For Advanced Studies

March 2014

Abstract

The purpose of this thesis is to understand how the physical properties of giant molecular clouds (GMCs) and their ability of star formation vary with galactic environments. We focus on the influence of surface density of gas (Σ_{H_2}) and dynamics of bar structure.

In the first part of this thesis, relation of molecular gas and SFR is investigated in terms of Kennicutt-Schmidt law (K–S law). ^{12}CO (1–0) and optically thin ^{13}CO (1–0) are independently used to derive Σ_{H_2} of IC 342. ^{12}CO-to-H_2 conversion factor is calibrated with metallicity and CO intensity for entire galaxy. Σ_{H_2} is also derived with the standard derivation of ^{13}CO-base column density. Slopes of K–S law are found to be ~ 1.4 at the low-Σ_{H_2} regions ($\leqslant 100$ $M_\odot$ pc^{-2}), while it becomes $\sim$2.0 in the high-Σ_{H_2} regions ($\geqslant 100$ $M_\odot$ pc^{-2}). The variable slopes attributed to the different star forming mechanisms. In the spiral arm (low-Σ_{H_2} regions), star formation is induced by the gravitational instability. At the central region of the galaxy where Σ_{H_2} is high, K–S law suggests that the star formation is triggered by cloud-cloud collisions or a self-regulated star formation. Our results of IC 342 are confirmed with similar analysis in 15 galaxies. Hence, the non-universal K–S law is common in galaxies. Besides, how molecular gas been collected into a region is a key factor in controlling the degree of star formation activity. This issue is addressed further in terms of galactic dynamics in the next project.

The aim of the second project is to explore the role of galactic bar in regulating GMC properties and star formation. High resolution (100 pc) ^{13}CO (1–0) map in the bar and central region of NGC 6946 is created by single dish and interferometer observations. An asymmetric bar is seen in the map, that is, the northern bar shows a typical gas distribution of a bar, whereas the morphology of the southern bar is unclear. The strong bar (northern bar) is warmer and denser than the weak (southern) bar. Star formation efficiency (SFE) has been enhanced in the strong bar. Moreover, based on the analysis of the position-velocity diagrams, the strong bar is ongoing larger velocity jumps (shocks) across the bar. We compare the resolved GMCs properties of the strong, weak bar, and the galactic disk of NGC 6946. We found that GMCs properties are similar in the weak bar and galactic disk. However, for the GMCs with equivalent masses, GMCs in the strong bar are more compact and denser than other areas. Consequently, they have shorter free-fall time and higher SFE. We compile GMC data from literature, and compare the GMCs properties of NGC 6946 with that of other nearby galaxies. The compact GMCs are found in the high-SFE environments, such as the Antennae galaxies, Galactic center, and the inner disk of spiral galaxies. The formation of those compact GMCs may be an outcome of their high external pressure environments.

Acknowledgements

I would like to thank my supervisor Prof. Nario Kuno for his direction. He was always positive, patient, and encouraging. He also gave me large degree of freedom in research topics and quick response when I got stuck on a problem for too long. I thank Prof. Daisuke Iono for the comments of not only the science but also my research career. I thank Dr. Jin Koda for the help on the CARMA and the combined data, and provided me a great chance to visit the Stony Brook University for one and half months. In addition to the science (always harsh but critical comments), I learn an important lesson from my senior Dr. Akihiko Hirota. That is, people who is smarter than me even work much harder than me. I will keep in my mind all the time. I acknowledge the useful comments on the observation proposals and the thesis from Profs. Ken'ichi Tatematsu, Kohji Tomisaka, Naomasa Nakai, Masanori Iye, Kazuo Sorai , Dr. Hiroyuki Kaneko and Ms. Michiko Umei.

This work cannot be done without the telescope team of Nobeyama Radio Observatory leaded by Prof. Shuro Takano. Thanks for their hard working on maintaining the performance of the 45-m telescope. In addition, I would like to thank all staffs in Nobeyama Radio Observatory for helping my life in the observatory, especially Ms. Ide, Hidemi. I would like to thank the graduate education support office at Mitaka for helping my stay and study in Japan as well.

Outside the work, I would like thank my best friend Satoki for his understanding of my plans and my choices all the time and lived through it with me. Finally, I thank my family for their unconditionally support and the tolerance of my absence from almost all family reunions in the past several years and near future. Words cannot express my gratitude to them.

Financial support of this research was provided by the Associate Support System of the National Astronomical Observatory of Japan. The stay in the Stony Brook University was supported by the Short-Stay Study Abroad Program 2013 of the Graduate University for Advanced Studies (SOKENDAI).

Contents

List of Figures

List of Tables

Chapter 1

Introduction

Star formation is taking place in molecular gas which is assembled into molecular clouds. Hence, the thesis starts from the basic properties of molecular clouds. This chapter is organized as follows. An overview of the physical properties of molecular clouds and the star formation in molecular clouds are introduced in §1.1, following by the observations of molecular clouds in the Milky Way and external galaxies in §1.2. The issues that we would like to address and the structure of the main content are shown in §1.3.

1.1 Brief Overview of Giant Molecular Clouds

1.1.1 Formation of Molecular Clouds

Interstellar medium (ISM) is composed of atomic and molecular gas. Formation of molecular gas (H_2) from atomic gas (H) depends on the ability of the interstellar clouds to shield from the photodissociative (ultraviolet, UV) radiation (Elmegreen, 1993). The conversion of H to H_2 can take place within a galaxy where mass accretion is ongoing or surface density of gas is increasing. Density wave can also accelerate the conversion to H_2 by increasing pressure (Elmegreen, 1993). However, H_2 can be converted back to H quickly as a result of the increase in the radiation by surrounding stars.

Giant molecular clouds (GMCs) are composed of molecular gas. They are often found with a definite boundary. The boundary shows the rapid transition from molecular gas to atomic gas. There are two preferred formation mechanisms of GMCs (McKee & Ostriker, 2007). "Top-down" scenario suggests that GMCs are formed via galactic-scale instability, such as Parker instability and Jeans instability (Blitz & Shu, 1980, Elmegreen & Elmegreen, 1983, Kim et al., 2002, Koyama & Inutsuka, 2000, Mouschovias et al., 1974, Parker, 1966). On the contrary, "bottom-up" mechanism proposes that the formation

of GMC is a result of random collisional agglomeration of small clouds and that mass and size of the clouds are growing until a self-gravitating cloud (giant molecular cloud) is reached (e.g., Field & Saslaw, 1965, Scoville & Hersh, 1979, Tomisaka, 1984). The problem of bottom-up mechanism is that it takes too long time ($> 5 \times 10^8$ yr) to grow a cloud to a typical GMC mass via the collisions of small clouds with a density (~ 1 cm^{-3}) of diffuse ISM at the Solar neighborhood (Kwan, 1979, McKee & Ostriker, 2007). The required collision time is about ten to hundred times larger than the observed lifetime of molecular clouds; even so, the "bottom-up" mechanism could be more efficient at the regions where the volume density of small clouds are high in the first place, such as galactic centers, mergers and interacting galaxies (e.g., Komugi et al., 2006).

1.1.2 Structure of Molecular Clouds

Structure of GMCs is inhomogeneous, that is, they consist of a diffuse, low density envelope and a/multiple discrete, dense core(s). The cores have density as high as 10^{4-6} cm^{-3} (Bergin & Tafalla, 2007, Nozawa et al., 1991). Dense cores are the exact cradles where star formation likely to occur.

Table 1.1 shows the current knowledge of GMC structure and the tracers of each component, including clumps and cores. Observationally, the Galactic clumps typically have mass[1] about 20% of the virial mass[2] for those GMCs with $M_{vir} > 10^5$ $M_\odot$ (Heyer et al., 2009). On the other hand, the dense cores account for only 1 – 10% of total mass of a GMC (Kato et al., 1999, Lada & Lada, 1991). The fraction of dense cores varies with evolutionary stages of GMCs. Specifically, young clouds have small fraction of dense core, whereas, more evolved clouds may have larger fraction of dense gas (Kato et al., 1999, Lada & Lada, 1991).

Figure 1.1 shows the two-dimensional morphology of some cloud cores observed in NH_3, CS, and $C^{18}O$ by Myers et al. (1991). Since the critical density of CS is larger than that of $C^{18}O$ by about 200 times (Myers et al., 1991), the size of CS emitter is smaller and surrounded by $C^{18}O$ in most of cores. NH_3 is sensitive to not only high density but also cold temperature, therefore, NH_3 emitters are found in the innermost regions enclosed by CS and $C^{18}O$ in the majority of the cores, and they are often associated with stars (crosses in Figure 1.1). The mean FWHM of all cores in Myers et al. (1991) are 0.15 pc (NH_3), 0.27 pc (CS) and 0.36 pc ($C^{18}O$).

[1] estimated by virial mass based on ^{13}CO (1–0)
[2] determined by ^{12}CO (1–0)

TABLE 1.1: Structure of GMC.

	Size [pc]	Mass [$M_\odot$]	Volume Density [cm^{-3}]	Tracers
GMC	5 - 70	10^4 – 10^6	50 – 100	^{12}CO[a]
Clump	1 - 15	10^2 – 10^5	10^2 – 10^3	^{13}CO, $C^{18}O$[b]
Core	0.05 - 1	10^1 – 10^3	$\geqslant 10^4$	^{13}CO, $C^{18}O$, CS, NH_3[c]

[a] Oka et al. (1998), Solomon et al. (1987)
[b] McQuinn et al. (2002), Roman-Duval et al. (2010), Wong et al. (2008), Yonekura et al. (2005)
[c] Bergin & Tafalla (2007), Lada et al. (1991), Launhardt et al. (1996), Myers et al. (1991), Teyssier et al. (2002), Tieftrunk et al. (1998)

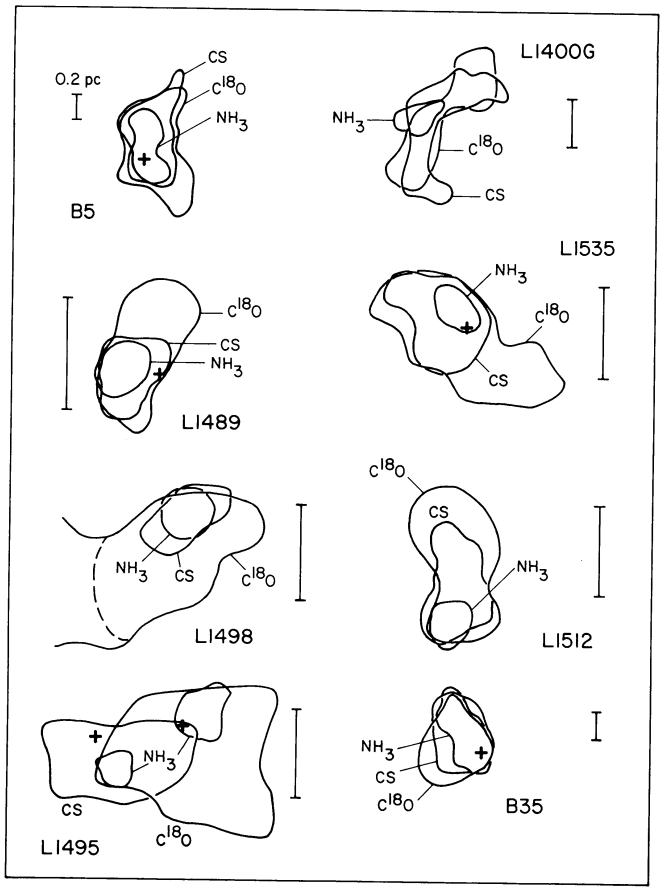

FIGURE 1.1: Observational results of the sub-structure of molecular cores in the transitions of NH_3 (cold cores), CS (cores), and $C^{18}O$ (cores). Contours indicate the half-maximum intensity of each transition. The physical scale of 0.2 pc is indicated with a vertical line in each panel. For all cores, north is up and east is left. The associated star of a core is indicated with a cross. The figure is taken from Myers et al. (1991).

There are more core maps in the original paper, we only show part of them here.

1.1.3 Lifetime of Molecular Clouds

Lifetime of GMCs is an important matter but still under-debated. Since GMCs have been dispersed around the OB stars with age > 10 Myr, lifetime of the GMCs are reckoned to be ≤ 20 Myr (Leisawitz et al., 1989). With similar method, current observations obtain a lifetime of $20 - 30$ Myr for the clouds with typical mass of 10^6 $M_\odot$ in our Galaxy (Murray, 2011). The lifetimes of GMCs measured in external galaxy are consistent with the value observed in our Galaxy (e.g., Kawamura et al., 2009). Such a consistency can be one of hints that nearby galaxies do share the same cloud properties with our Galaxy (e.g., Bolatto et al., 2008). However, some authors suggest a much shorter lifetime of 2-3 Myr or much longer of 100 Myr. In addition, simulations of GMC evolution in a normal two-arm galactic disk conclude a wide range of $4 - 25$ Myr for GMCs with mass $> 10^5$ $M_\odot$ (Dobbs et al., 2013). Thus the lifetime of GMCs is still very uncertain, ranging from about a free-fall time [3] to twenty free-fall time.

1.1.4 Star Formation Efficiency in Giant Molecular Clouds

Milky Way contains about 10^9 $M_\odot$ of GMCs with mean volume density of $50 - 100$ cm^{-3}. If all GMCs are bound and collapse in a free-fall time, a star formation rate (SFR) of 250 $M_\odot$ yr^{-1} is expected. However, the value is about two order of magnitude larger than the observed SFR. The Galactic SFR estimated by population synthesis is about $0.7 - 1.5$ $M_\odot$ yr^{-1}, consistent with the observed number of young stellar objects at the Galactic plane (Robitaille & Whitney, 2010). The contradictory of the amount of gas and SFR implies that GMCs are supported by some processes based on the theoretical studies, such as magnetic fields (Shu et al., 1987, 2007), and turbulence (Krumholz & McKee, 2005).

In terms of observations, some of mass in GMCs may be blown out by the protostellar outflows. Alves et al. (2007) compare the dense core mass function of Pipe Nebula and the stellar mass function of Trapezium cluster. The profiles of two mass functions are surprisingly similar but the dense core mass function is shifted to high-mass end by about four times (Figure 1.2). They suggest that the offset is caused by the parent cloud cores of protostars disrupted by the protostellar outflows. Eventually, only about 30% of mass remains to set the final mass functions of stars, but this amount of mass loss is not enough to explain the low SFR of the Milky Way alone.

Finally, GMCs may not be bound in the first place. If unbound objects dominate the populations of GMC (Dobbs et al., 2011b), star formation rate is consequently lower than that estimated from the total mass of GMCs.

[3] Free-fall time is about a few Myr.

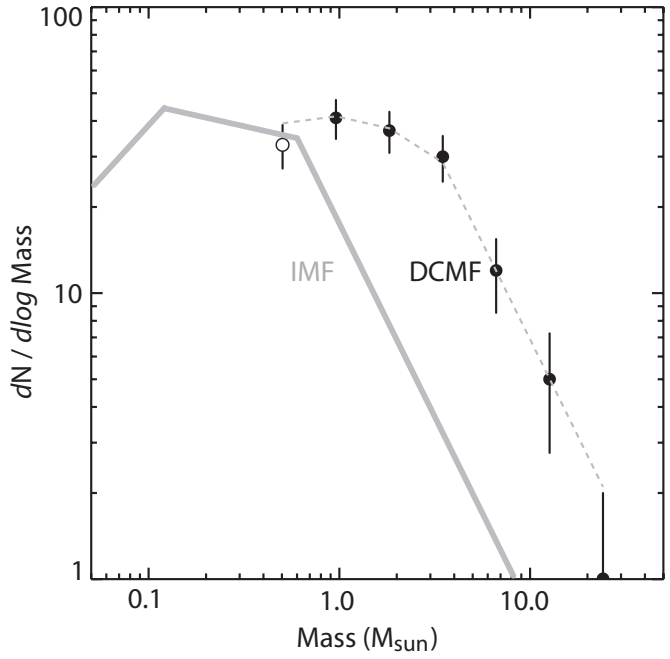

FIGURE 1.2: Dense core mass function of Pipe Nebula in circles and stellar mass function of Trapezium cluster in grey line. The dashed line represents stellar mass function binned to the same resolution of dense core mass function and then shifted toward high-mass end by a factor of four. The figure is taken from Alves et al. (2007).

1.2 Observations of Molecular Clouds

The most abundant ingredient of molecular clouds is molecular hydrogen (H_2). H_2 is a homonuclear linear molecule without permanent dipole moment. Hence, H_2 are challenging to observe. Moreover, the lowest pure rotational lines of H_2 is at 28.2 μm, equivalent to a temperature of $\sim$ 150 K. This is about ten times higher than the temperature of molecular clouds which are prone to star formation ($\sim$ 10 K). Therefore, it is difficult to observe H_2 of molecular clouds directly. Other observable species are required to trace molecular gas.

1.2.1 Observations of Molecular Clouds with ^{12}CO

^{12}CO is the most abundant molecule after H_2. The abundance of ^{12}CO relative to H_2, i.e., $\frac{[^{12}\mathrm{CO}]}{[\mathrm{H_2}]}$, ranges from $\sim 10^{-4}$ in our Galactic GMCs to 10^{-6} – 10^{-8} in the diffuse gas which is translucent against the dissociating radiation (Sonnentrucker et al., 2007). The rotational transition $J = 1 - 0$ ($\nu \approx 115.27120$ GHz or $\lambda \approx 2.6$ mm) of ^{12}CO has been widely used as a probe of H_2. The excitation of CO relies on the collisions with H_2 (Schinke et al., 1985). The minimum gas temperature required to excite a molecule at transition $J \rightarrow J - 1$ is

$$T_{\mathrm{min}} \approx \frac{\nu h(J+1)}{2k}, \tag{1.1}$$

where h and k are Planck and Boltzmann constant, respectively. For ^{12}CO (1 – 0), $T_{\rm min}$ is about 5.5 K. Thus, it is an ideal species to trace the molecular clouds because the temperature of Galactic GMCs is about 10 K.

1.2.2 Molecular Clouds in the Milky Way

There are many surveys of GMCs in our Galaxy through ^{12}CO (e.g., Burton et al., 2013, Dame et al., 1986, 2001, Heyer et al., 1998, Jackson et al., 2006, Sanders et al., 1986, Scoville & Solomon, 1975). The results suggest that the total mass of molecular gas in the Milky Way is $\sim 2 \times 10^9$ M$_\odot$ (Ferrière, 2001, Solomon et al., 1987). Most of gas is arranged in cloud structures. Majority of molecular clouds are located at the Galactic center and the molecular ring inside the solar neighborhood at 3 – 7 kpc (see the thick line in Figure 1.3). Size and mass of GMCs in Milky Way are 5 – 70 pc and 10^4 – 10^6 M$_\odot$, respectively (Solomon et al., 1987), corresponding to a volume density of $\sim 50 - 100$ cm^{-3}. Some small clouds with mass $< 10^3$ M$_\odot$ are found at the high galactic latitude and the outer disk of the Milky Way (Heyer et al., 2001, Magnani et al., 1985). Heyer et al. (2001) suggest that the small molecular clouds are not self-gravitational bound due to the absence of sufficient external pressure.

Observed linewidth or velocity dispersion of the Galactic plane GMCs is $\sim 1 - 10$ km s^{-1}. The values are significantly larger than the thermal linewidth of a 10 K cloud (< 1 km s^{-1})[4], implying the presence of turbulence, and the turbulence should dominate the internal velocity dispersion of GMCs. By analyzing the size (L), velocity dispersion (σ), mass (M) and volume density (n) of GMCs, previous works have concluded three scaling laws for Galactic GMCs, that is, (1) $\sigma \propto L^{0.38}$, GMCs are supported by turbulence, (2) $2GM/\sigma^2 L \simeq 1$, GMCs are approximately in virial equilibrium, and (3) $n \propto L^{-1.1}$ (Larson, 1981, Solomon et al., 1987). The third law suggests that GMCs have comparable surface density of gas, which is about 170 M$_\odot$ pc^{-2} (Solomon et al., 1987).

1.2.3 Molecular Clouds in External Galaxies

Our Milky Way has a relatively low SFR, 0.7 – 1.5 M$_\odot$ yr^{-1} (Robitaille & Whitney, 2010). Its disk-average SFR and gas mass are located at the lower end compared with other normal spiral and irregular galaxies (Figure 11(a) in Kennicutt & Evans (2012)). Hence, whether GMCs in external galaxies hold the same properties as the Galactic GMCs is a long-standing question.

[4] $\Delta v_{\rm th} = 0.188\sqrt{\frac{T}{10{\rm K}}}$ [km s^{-1}] (McKee, 1999).

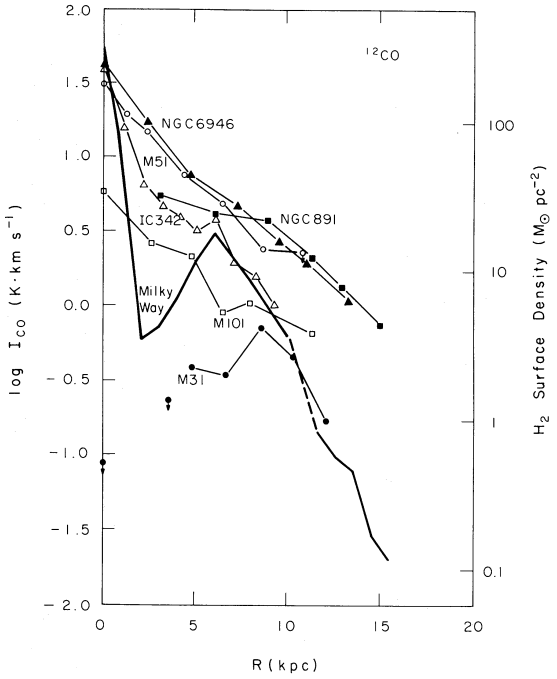

FIGURE 1.3: Radial distribution of Galactic CO intensity observed with FCRAO 14-m telescope and NRAO 11-m telescope. This figure is taken from Sanders et al. (1984).

Observations of GMCs in external galaxies are limited by the performance of telescopes, i.e., resolution and sensitivity. Table 1.2 lists the physical scale of 1″ of nearby galaxies at various distance from 1 Mpc to 40 Mpc. As seen in the table, to fully resolve a GMC in a galaxy at 6 Mpc with ^{12}CO (1 – 0), an angular size of 1″ is needed. To achieve such a fine resolution, an antenna with 600 m in diameter is required. For the closest galaxy cluster, Virgo cluster, which contains more than thousand nearby galaxies, subarsec is required to resolve a GMC. For galaxies at far beyond 20 Mpc, the physical scale of 1″ is even larger than the largest GMC in our Galaxy ($\sim$ 70 pc). Turning to sensitivity, if external GMCs do share similar physical properties as Galactic GMCs, there is no doubt that the time required to detect external GMCs will rapidly increase when the distance of the object increase. With these instrumental limitations, single dish observation of external GMCs with a quality comparable to Galactic survey is feasible only in very nearby objects. GMCs in the galaxies beyond the Local Group greatly rely on interferometers. However, one should keep in mind that observations with different types of telescopes may produce artificial variation of GMC properties (Sheth et al., 2008a).

Currently, some comparative works have been carried out to explore the difference between the Galactic GMCs and the external GMCs. Due to the limited samples, telescopes, and the method of clouds identifications, different conclusions were claimed. Specifically,

TABLE 1.2: Examples of physical scale of 1″ in various distances. The distances are taken from NED.

Galaxy	Distance [Mpc]	Physical Scale of 1″ [pc]
M 33	0.9	4
IC 342[a]	3.3	16
NGC 6946[a]	5.5	27
Virgo cluster galaxies	∼14	68
NGC 7552	21.7	105
NGC 5430[b]	42.3	205

[a] Main targets (observations) in this thesis
[b] New observations in this thesis, but not the main target

1. With interferometric observations of CAMRA[5], Donovan Meyer et al. (2013) conclude that the sizes and velocity dispersions of GMCs in the center and the inner disks of nearby galaxies (NGC 2403, NGC 3031, NGC 4736, NGC 4826, and NGC 6946) are consistent with Galactic GMCs. The ^{12}CO-to-H_2 conversion factor measured by CO luminosities and virial masses are consistent with the Galactic standard value (2×10^{20} cm^{-2} (K km s^{-1})$^{-1}$) within a factor of two.

2. Hughes et al. (2013) define GMCs in M51, M33, and the LMC through the observations of PdBI[6]. They found different GMC properties between M51 and other low-mass galaxies. For a given size of GMC, GMCs in M51 have higher peak CO brightness and velocity dispersion. The results can be explained by the ambient interstellar pressure altering the states of GMCs. In addition, a caution arises from this work is that the appearance of Larson's size–linewidth relation is sensitive to the method of cloud identification (Figure 1.4). They can produce either no relation or a strong correlation with different procedures (Details are shown in the caption of Figure 1.4).

3. Sheth et al. (2008a) compare GMCs properties in M31 (BIMA[7]), M33 (OVRO[8]) and Milky Way (CfA[9] 1.2 m telescope). To fairly compare single dish to interferometric data, they project Galactic GMCs to the distance of M31 and simulate the corresponding results of BIMA. They suggest that there is no significant difference among the GMCs in these three galaxies in terms of linewidths, sizes, and flux.

4. Bolatto et al. (2008) measure GMC properties in 11 dwarf galaxies with BIMA, OVRO, PdBI, and SEST[10], then compare the data with Galactic GMCs (Sanders et al., 1986), M31 (BIMA from Rosolowsky, 2007), and M33 (BIMA from Rosolowsky

[5]The Combined Array for Research in Millimeter-wave Astronomy
[6]The Plateau de Bure Interferometer
[7]The Berkeley Illinois Maryland Association
[8]Owens Valley Radio Observatory
[9]Harvard-Smithsonian Center for Astrophysics
[10]Swedish-ESO 15m Submillimeter Telescope

et al., 2003). They found that, for a given luminosity of CO and velocity dispersion, GMCs in dwarf galaxies are slightly larger than GMCs in the Milky Way, M31 and M33 (Figure 1.5). Other than that, the Galactic Larson's relations are still held for those low metallicity galaxies.

5. Rosolowsky & Blitz (2005) observed NGC 4826 with BIMA in ^{12}CO, ^{13}CO and HCN (1–0) and define GMCs using the ^{13}CO map. They found some GMCs are as large as $> 10^7$ $M_\odot$, substantially larger than the mass of Galactic GMCs. The high-mass GMCs are significantly smaller and denser than that predicts by the extrapolation of Local Group GMCs. As a result, the surface density of GMCs in NGC 4826 is larger than that of Local Group GMCs by 2.5 times. Moreover, the mass-linewidth relation of GMCs in NGC 4826 are more like those in the Galactic center and the Antennae galaxy.

6. Blitz & Rosolowsky (2004a) compile GMC data of Local Group Galaxies, including Milky Way (Dame et al., 1986, Heyer et al., 2001, Solomon et al., 1987), LMC (NANTEN[11] Mizuno et al., 2001) and M33 (BIMA from Engargiola et al., 2003). The Larson's scaling relations are held for the GMCs in Local Group galaxies, suggesting the clouds are self-gravitating and the gas surface density of GMCs are identical (~ 100 $M_\odot$ pc^{-2}). However, the mass spectrum of GMCs varies among galaxies (Figure 1.6).

1.2.4 GMC Properties and Star Forming Activities

Even though most of studies suggest similar properties of GMCs in nearby galaxies and the Milky way, their ability of star formation may not be the same. As an example, even though the properties of GMCs in nearby gas-rich spiral galaxies are similar with each other (Donovan Meyer et al., 2013), some nearby galaxies contain starburst centers, while Milky Way shows an underproduction of stars (Kauffmann et al., 2013, Kruijssen et al., 2013), suggesting that the cloud properties, ability of clouds to form stars and/or the threshold density of star formation vary with environments (e.g., Gardan et al., 2007, Gratier et al., 2012, Hirota et al., 2011, Kruijssen et al., 2013, Wong et al., 2011). Similar results are found in the Galactic disk GMCs. Williams et al. (1994) analyzed hundred clumps in Rosette and Maddalena molecular clouds. The clump properties of temperature, mass, velocity dispersion are very similar in the two clouds, but Rosette is ongoing star formation, Maddalena is not.

[11] the NANTEN telescope from

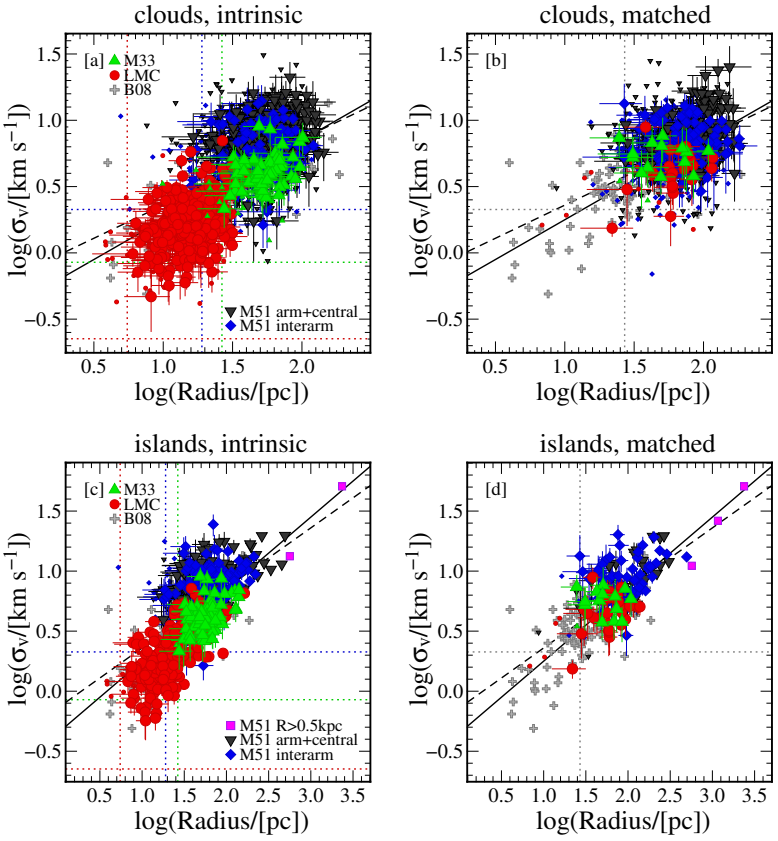

FIGURE 1.4: Larson's relation of velocity dispersion versus radius of external GMCs in M51, M33, the LMC. Descriptions of symbols and colors are shown in panel (a) and (c). Four panels are made with different resolution and method of cloud identifications. They are indicated at the top of each panel. *Islands* represents the contiguous clouds identified with algorithm of CPROPS. *Clouds* is a decomposition of *islands*. *Intrinsic* denotes that the data cubes fed to CPROPS have original observed resolution in three axises. In order to reduce the impact from sensitivity and physical resolution, cubes of different galaxies are matched to a resolution of ∼50 pc and 5 km s^{-1}. Results with matched resolution are marked with *matched*. In all panels, the black dashed and solid line indicate the Larson's law suggested by the Galactic GMCs of Solomon et al. (1987) and the extragalactic GMCs from Bolatto et al. (2008). The horizontal and vertical dotted lines denote the spatial and spectral resolution of each observation. The B08 represents Bigiel et al. (2008). This figure is taken from Hughes et al. (2013).

Hirota et al. (2011) define GMCs in a spiral arm of IC 342 with observations of NMA[12]. They classify GMCs into two groups based on whether they are associated with star forming regions. GMCs properties of IC 342 are shown in Figure 1.7. Non-star forming GMCs have smaller radius of 40 pc, while the radius of star forming GMCs cross a wide range from 40 pc to 70 pc. Smaller linewidth is found for GMCs with star formation. Similarity is suggested by Muraoka et al. (2009) to the observations of M83 disk. However, at the galactic centers where star formation is expected to be high, large linewidths are found (Donovan Meyer et al., 2012, Oka et al., 1998). Moreover, star forming GMCs are more massive than non-star forming GMCs in IC 342.

[12]Nobeyama Millimeter Array

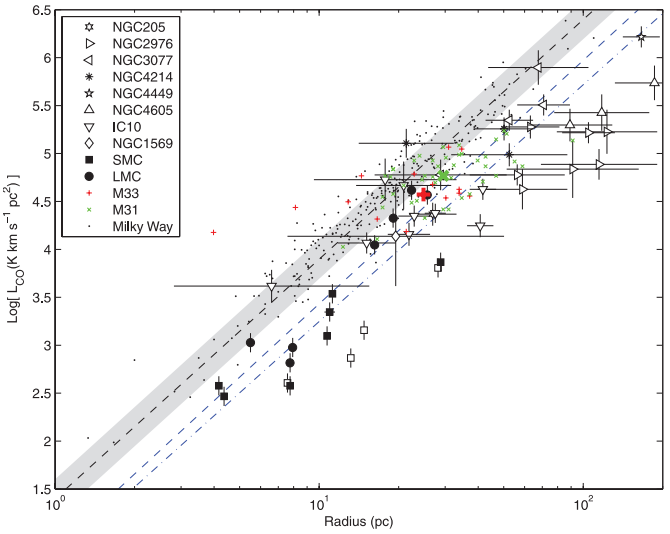

FIGURE 1.5: CO luminosity versus velocity dispersion of 10 dwarf galaxies (black symbols), spiral galaxies (red and green symbols), and Milky Way (black dots). The black dashed line and the gray area represent the fit of Milky Way data and 1 σ dispersion of the fit, respectively. The blue dashed line indicates the fit of external GMCs. The blue dot-dashed line denotes the fit of dwarf galaxies only. This figure is taken from Bolatto et al. (2008).

Turning to other galaxies, in the LMC and M33, higher CO brightness is observed for star forming GMCs than non-star forming GMCs (Gratier et al., 2012, Hughes et al., 2010). With simulations, Dobbs et al. (2013) consider the age of stellar population in GMCs at different galactic environment. GMCs at spiral arms are associated with young stars with age < 10 Myr. At inter-arms regions, stars are about two times older. These results can be explained by the GMCs/stars going away from spiral arms. More precisely, at spiral arms, spiral shocks activate star formation, thus contain more young stars. After that, evolved stars and GMCs leave the arm and travel to inter-arms regions, hence older stars are found in this area.

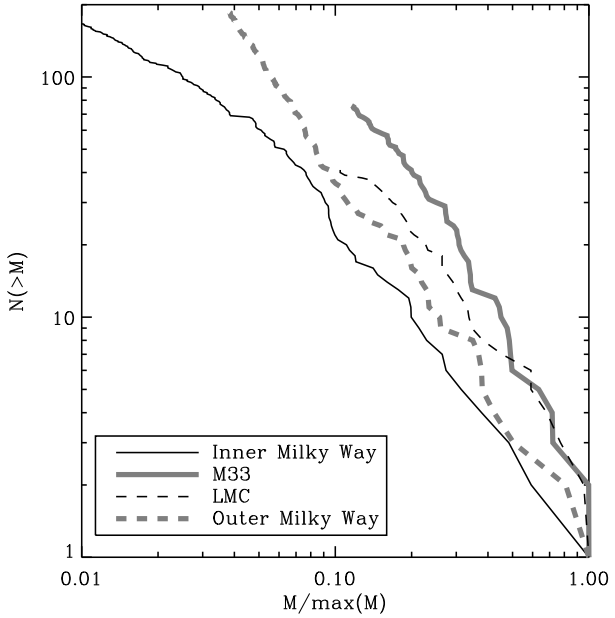

FIGURE 1.6: The mass spectrum for Milky Way, SMC and M33. The mass spectra can be described with a power law: $\mathrm{d}N/\mathrm{d}M \propto M^{-\alpha}$, where α is 2.3 for M 33, and 1.9 for the Milky Way. This figure is taken from Blitz & Rosolowsky (2004a).

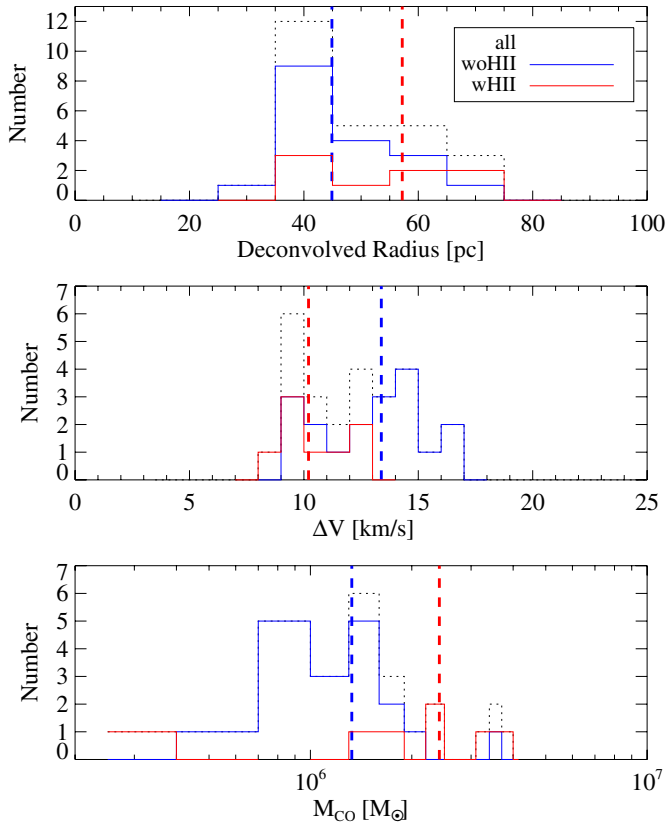

FIGURE 1.7: GMC properties in a spiral arm of IC 342, top – effective radius, middle – velocity dispersion, and bottom – luminosity mass. Red and blue histograms indicate the GMCs with and without star formation, respectively. Vertical lines denote the median value of each population. This figure is taken from Hirota et al. (2011).

1.3 The Issues to Address and Structure of the Thesis

The purpose of this thesis is to understand how star formation rate/efficiency respond to the environment. We focus on the influence of the difference of surface density of gas and dynamics of bar structure as the difference of the environments in this thesis.

In the first place, we consider whether star formation simply depends on the molecular gas mass or whether star formation efficiency is constant in a galaxy. We study the relation of molecular gas and star formation in IC 342 in terms of spatially resolved Kennicutt-Schmidt Law in Chapter 2. In this study, Kennicutt-Schmidt Law is examined under sub-kiloparsec resolution. With this resolution, uncertainties arise from the evolution of GMCs and star forming regions, such as the drift of star forming regions from their parent clouds (Onodera et al., 2010), have been averaged and thus negligible. Even so, the sub-kiloparsec resolution still faithfully resolves the variation of gas surface density at different galactic structures, such as galactic center and spiral arms.

If star formation rate is independent to environment, i.e., simply relies on the amount of gas, one would expect a linear correlation between the amount of gas and star formation rate, implying that gas is converted to stars with a constant rate all the time. However, if not, which factor determine the star formation rate and the star formation efficiency in a region?

If there are other factors which determine star formation activity, galactic dynamics must be the most probable candidate. Especially, bar is expected to have strong influence on the gas properties as shown in the previous studies (cf. §3.1.2). In the second part of this thesis, we investigate whether galactic bar can alter the physical properties of GMCs and star formation efficiency in the nearby barred spiral galaxy NGC 6946. The results of NGC 6946 are shown in Chapter 3, following by a comparison of GMC properties in our target and nearby galaxies.

Finally, main results of this thesis are summarized in Chapter 4. Future plan of following work is described in Chapter 5.

Chapter 2

Dependence of Star Formation on the Amount of Gas

2.1 Introduction

Molecular gas is one of the most fundamental constituents in galaxies. They are ubiquitous with various forms as mentioned in §1.2.3, representing the dynamics of the local ISM and the host galaxy itself. When molecular gas becomes dense enough, star formation can start by consuming the molecular gas. Stars are the main energy sources in ISM. In the later stage of stars, they recycle their material back to ISM. The *contaminated* ISM can affect the properties, such as metallicity, of GMCs in the next generation. Thus the relation between molecular gas and star formation are rather complicated because it depends on the evolutionary cycle of the ISM.

In this Chapter I investigate how star formation rate/efficiency vary with surface density of gas in terms of Kennicutt-Schmidt law. The outline of this chapter is as follows: In §2.1.1 I introduce Kennicutt-Schmidt (K–S) law and the derivation of column density with current methods. Review of ^{13}CO observations in the Milky Way and nearby galaxies are presented in §2.2. Motivation and methodology of this work are shown in §2.3. Target galaxy IC 342 is introduced in §2.4. The radio and infrared archival data we used in this work are presented in §2.5. The study of the radial distribution of the gas and SFR is shown in §2.6. The methods of deriving Σ_{H_2} from ^{12}CO (1–0) and ^{13}CO (1–0) are demonstrated in §2.7 and §2.8, respectively. The uncertainties of the methods are discussed in §2.9. Section 2.10 presents the derived K–S law with both ^{12}CO (1–0) and ^{13}CO (1–0). In §2.11, we examine the K-S law in other nearby galaxies using the published data of ^{12}CO and metallicity to confirm the results from IC 342. The probable

mechanisms of star formation in IC 342 are considered in §2.12. Main results of this chapter are outlined in §2.13.

2.1.1 Star Formation Law

The most straightforward study of the correlation between the star formation and the amount of molecular gas is Kennicutt-Schmidt (K–S) law. Schmidt (1959) and Kennicutt (1998) propose an empirical star formation law between the surface density of star formation rate ($\Sigma_{\rm SFR}$) and the total gas ($\Sigma_{\rm Gas}$).

The K–S law is written as the form of

$$\Sigma_{\rm SFR}({\rm M_\odot yr^{-1}kpc^{-2}}) \propto \Sigma^N_{\rm Gas}({\rm M_\odot pc^{-2}}). \tag{2.1}$$

As stars are formed from molecular gas, $\Sigma_{\rm Gas}$ in the K–S law is often replaced with $\Sigma_{\rm H_2}$.

With ^{12}CO observations and the Galactic Standard CO-to-H$_2$ conversion factor ($X_{\rm CO}$ = 2.3 $\times$ 10^{20} cm^{-2} (K km s^{-1})$^{-1}$; Strong et al. (1988)), numerous works show that N is in the range of 1.0 – 2.0. The slope of the K–S law may give us a clue to understand the mechanism of star formation. For example, if star formation only depends on the mass of Giant Molecular Clouds (GMCs), a constant SFR per unit mass of molecular gas is expected, leading to a linear relation between $\Sigma_{\rm SFR}$ and $\Sigma_{\rm H_2}$, namely, $N \approx 1.0$ (Bigiel et al., 2008, Dobbs & Pringle, 2009). If molecular gas is converted to stars with a timescale of free-fall time, and the scale height of gas is about constant everywhere in galaxies, a slope of 1.5[1] is expected (Elmegreen, 1994, 2002, Li et al., 2006). If cloud-cloud collisions trigger star formation, star formation timescale is set by the collision rate of the virially bound objects, resulting to a slope of $\sim$2.0[2] (Tan, 2000, Tasker & Tan, 2009).

2.1.2 Column Density Determined from ^{12}CO

Column density of H$_2$ ($N_{\rm H_2}$) is required to calculate $\Sigma_{\rm H_2}$. ^{12}CO is commonly used as a tracer of $N_{\rm H_2}$ because ^{12}CO directly arises from the molecular gas and the emission is strong. Since individual molecular clouds are not resolved in most external galaxies, CO-to-H$_2$ conversion factor ($X_{\rm CO}$, in unit of cm^{-2}(K km s^{-1})$^{-1}$) is required to derive the mass and $\Sigma_{\rm H_2}$ of molecular clouds. With an observed intensity of CO ($I_{\rm CO}$ in unit

[1] We will show why it is 1.5 in §2.12.1.
[2] We will show why it is 2.0 in §2.12.2.

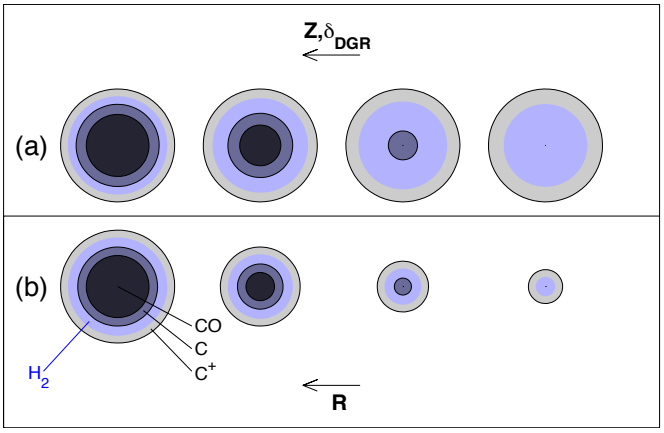

FIGURE 2.1: This figure is taken from Bolatto et al. (2013). The effect of metallicity (a) and size of GMCs (b) on the the fraction of CO in a cloud and $X_{\rm CO}$.

of K km s^{-1}), one can simply scale $I_{\rm CO}$ to $N_{\rm H_2}$ by a factor of $X_{\rm CO}$:

$$N_{\rm H_2} = X_{\rm CO} \times I_{\rm CO}\ [{\rm cm}^{-2}]. \tag{2.2}$$

The most common way is adopting the Galactic standard $X_{\rm CO}$ (e.g., Bigiel et al., 2008, Leroy et al., 2008), which is 2.3 $\times$ 10^{20} cm^{-2} (K km s^{-1})$^{-1}$. However, it becomes more and more obvious from recent works that the Galactic standard $X_{\rm CO}$ is no more valid in some particular environments.

The first environment is low-metallicity regime where low C and O abundances are seen. $X_{\rm CO}$ is found to be higher than the Galactic number (Arimoto et al., 1996, Dickman et al., 1986, Narayanan et al., 2012, Wilson, 1995) in low-metallicity galaxies. At low-metallicity environments, the amount of dust is not sufficient to protect CO from photodissociation of UV photons (low dust-to-gas ratios; see panel (a) of Figure 2.1), thus the amount of CO is small and the CO emission is too weak to be detected. At the same time, H_2 has better ability of self-shielding, thus can survive from the photodissociation. As a result, a higher $X_{\rm CO}$ is needed to estimate the total amount of H_2 from CO observations. Figure 2.2 shows a plot of $X_{\rm CO}$ as a function of metallicity in nearby galaxies from Arimoto et al. (1996). They compiled published $X_{\rm CO}$ of nearby galaxies, which are derived with either virial mass of clouds or visual extinction mapping. The dwarfs galaxies SMC, LMC and IC 10 have high $X_{\rm CO}$, which is about 3 – 10 times larger than the Milky Way, while their metallicity is lower than the Milky Way. The same situation is seen in the HI-dominant spiral galaxy M33. On the contrary, in the molecular rich and higher SFR ($\sim$ 3.4 M$_\odot$ yr^{-1}) galaxy M51, the conversion factor is lower than the Galactic $X_{\rm CO}$, along with a larger metallicity. The correlation of $X_{\rm CO}$ and metallicity (Z) of the galaxies in Arimoto et al. (1996) can be described with a power-law relation of $X_{\rm CO} \propto Z^{-0.5}$.

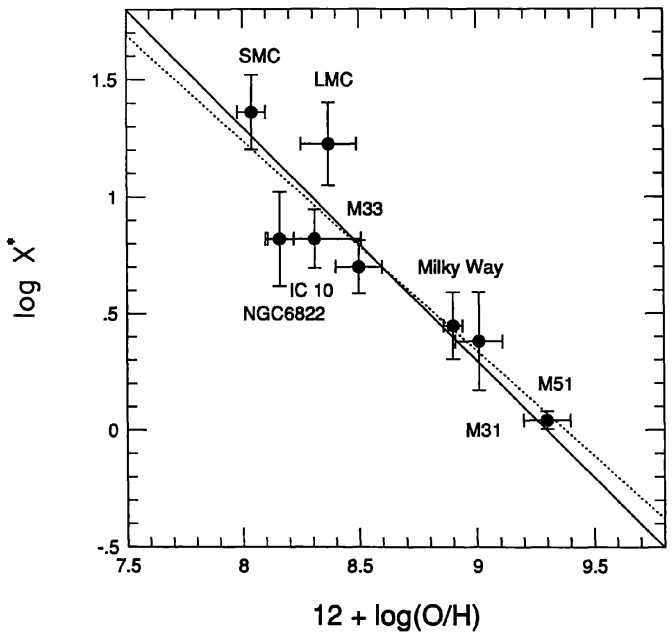

FIGURE 2.2: This figure is taken from Arimoto et al. (1996). The conversion factor X^* is in the unit of 10^{20} cm^{-2} (K km s^{-1})$^{-1}$. The dotted line is a least-square fit of the data. The solid line indicates the linear relation between X^* and metallicity.

The second special environment is high-$N_{\rm H_2}$ (or high $I_{\rm CO}$) regime. The mass of molecular gas in some galaxy mergers and high redshift galaxies derived by the Galactic standard $X_{\rm CO}$ exceeds their dynamical mass, suggesting that the true $X_{\rm CO}$ should be lower than the Galactic value (Downes & Solomon, 1998, Downes et al., 1993, Narayanan, 2013, Narayanan et al., 2012, Solomon et al., 1997, Wilson et al., 1997). A possible reason is that the process of galaxy merging is highly turbulent and that ^{12}CO emission becomes moderately thick (Iono et al., 2007), specifically, the nature of ^{12}CO has been changed. Another possible reason is that size of GMCs in mergers are larger than normal GMCs, presumably to the effective collisions and agglutinations of clouds. The large size can protect the interior CO from photoionizataion more effectively than small GMCs. Therefore, GMCs in mergers have a larger fraction of CO and a smaller $X_{\rm CO}$ is required (see panel (b) of Figure 2.1).

Some works suggest that the two effects, metaiilcity and $I_{\rm CO}$, determine $X_{\rm CO}$ together (Nakai & Kuno, 1995, Narayanan et al., 2012). $I_{\rm CO}$ and metailcity are function of galactic radii (e.g., Moustakas et al., 2010, Pilyugin et al., 2004). As a result, $X_{\rm CO}$ does change within a single galaxy. For example, $X_{\rm CO}$ is 0.75 $\times$ 10^{20} cm^{-2} (K km s^{-1})$^{-1}$ within the inner 1.′2 of M51. It is $\sim$3 times lower than the Galactic Standard $X_{\rm CO}$, while the value rises to (1 – 4) $\times$ 10^{20} cm^{-2} (K km s^{-1})$^{-1}$ at $>$ 2.′0 (Nakai & Kuno, 1995).

2.1.2.1 Uncertainty of Column Density Determined from ^{12}CO

The nature of ^{12}CO limits its ability to determine Σ_{H_2}. First drawback arises from the unsure X_{CO}. The derived value of Σ_{H_2} depends on the calibration of metallicity and I_{CO}.

Secondly, since ^{12}CO is optically thick ($\tau \gg 1$), it traces the emission from the envelope of GMCs rather than dense clumps/cores where stars are formed. Likewise, due to its high opacity, the intensity of ^{12}CO does not indicate the amount of gas when GMCs start to pile up along the line of sight.

Thirdly, ^{12}CO can be excited at low density area. Critical density of a molecular line is defined as

$$n_{crit} = \frac{A_{ul}}{C_{ul}} \ [cm^{-3}], \tag{2.3}$$

where A_{ul} and C_{ul} are Einstein coefficient of spontanous emission in s^{-1} and collision rate for a transition in $cm^3\ s^{-1}$, respectively. For transition of $J = 1 \rightarrow 0$, ^{12}CO has a n_{crit} of $(7.2 \times 10^{-8})/(3.3 \times 10^{-11}) \approx 2000\ cm^{-3}$. This calculation is based on optically thin assumption. However, since ^{12}CO is optically thick, the probability of a photon to escape the cloud (β) should be considered:

$$\beta = \frac{1 - \exp(-\tau)}{\tau}. \tag{2.4}$$

Then the effective n_{crit} (n^*) becomes

$$n^* = \frac{\beta A_{ul}}{C_{ul}} \ [cm^{-3}]. \tag{2.5}$$

For optically thin domain, $\tau \rightarrow 0$, thus $\beta \rightarrow 1$ (Equation 2.3). For optically thick lines, $\tau \gg 1$, so $\beta \ll 1$. Due to the large τ of ^{12}CO, n^* of ^{12}CO can be as low as $\sim 10^2\ cm^{-3}$. Hence, ^{12}CO is an ideal probe of molecular clouds, but the clouds are not necessary to be associated with star forming regions.

2.1.3 Column Density Determined from Extinction

Two principal methods have been used to determine the column density in molecular clouds through extinction mapping, reddening of stars (color-excess) and stellar counting.

N_{H_2} can be estimated with optical and infrared measurements of star lights. The idea is to measure the amount of lights extincted by dust in the molecular cloud at the line of sight (Alves et al., 2001, Lada et al., 1994, Lombardi et al., 2006). This method is only

applicable in the nearby clouds, because the intrinsic properties of background stars are required to calculate their reddening (Bolatto et al., 2013).

Stellar counting points that N_{H_2} can be estimated by comparing the stellar density of an interested area with the background stellar density (Dickman, 1978, Dobashi, 2011, Schnee et al., 2005, Stepnik et al., 2003). A drawback of the classical stellar counting method is that the size of the concerned area brings uncertainties to the calculations, for example, if the size of the cell is too small that there is no star in the cell, the method would suggest it as a highly extinguished regions. The method has been improved by fixing the number of stars in a cell by Cambrésy (1999), but the intrinsic uncertainties still exist in the region with bright stars or the region is highly obscured.

2.1.4 Column Density Determined from Dust Emission

Dust emission can be measured directly from far infrared to mm–wavelengths (Langer et al., 1989, Schlegel et al., 1998). Calibration to convert the observed properties to the amount of dust and gas relies on the assumption of physical condition of dust, such as dust temperature, dust-to-gas ratio, and dust emissivity. Since physical conditions of gas can vary along the line of sight, large uncertainty may involve.

2.2 Review of ^{13}CO Observations

Perhaps the most efficient way to derive X_{CO}, N_{H_2} and mass of molecular gas/clouds is through an optically thin emission (Aalto et al., 2010, Bolatto et al., 2013). The optically thin emission could be dust, chemical species or CO isotopic lines. Firstly, accurate results from dust are limited in the Galactic clouds because of the requirement of background and foreground information. Secondly, observations of chemical species are impractical in the disk of external galaxies due to their weak intensity. It turns out optically thin CO isotopic lines, such as ^{13}CO, become the most reliable and practical probe of gas. Even though ^{13}CO is generally 5 – 20 times weaker than ^{12}CO across galactic disks (Tan et al., 2011), observations of ^{13}CO become feasible in nearby objects since the sensitivity of telescopes have been improved recently.

^{13}CO is an ideal transition to study molecular gas by several reasons. First of all, ^{13}CO is an optically thin transition, even in extreme starburst regions (Matsushita et al., 1998, Pan et al., 2013). Secondly, intensity of ^{13}CO is relatively strong compared to other CO isotopic lines, although the ^{12}CO to ^{13}CO ratio is still as high as 5 – 20 in nearby galaxies (Aalto et al., 1995, Paglione et al., 2001, Tan et al., 2011). Thirdly, the effective critical

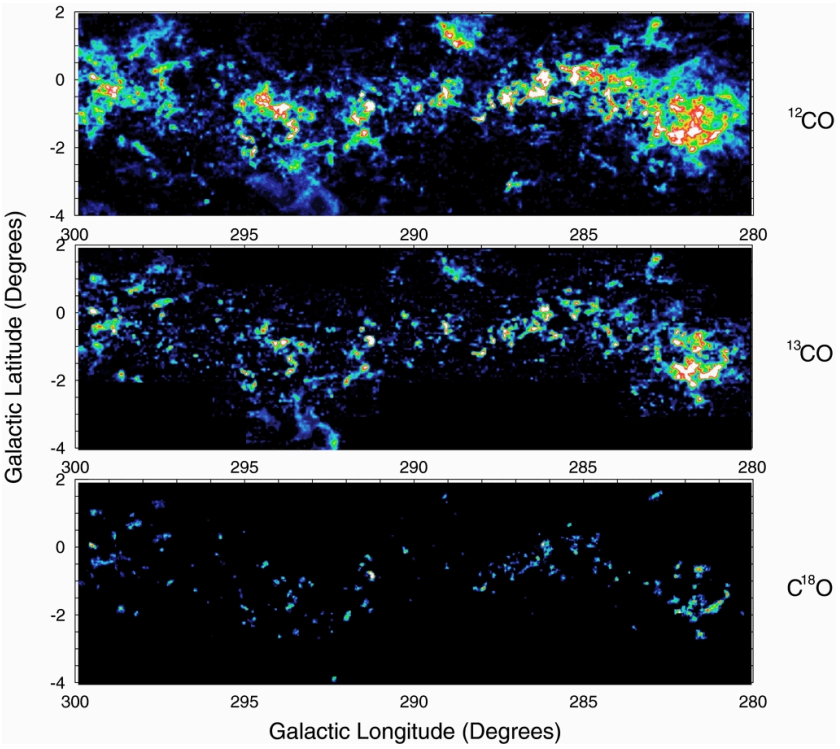

FIGURE 2.3: Integrated intensity maps of Galactic plane in ^{12}CO (top), ^{13}CO (middle), and C^{18}O (bottom) observed by NANTEN. All lines are at the transition of 1 – 0. This figure is taken from Barnes et al. (2011).

density of ^{13}CO is about 10 times higher than that of ^{12}CO owing to its low opacity, tracing slightly denser gas. By comparing ^{13}CO, CS (2–1) clumps and IRAS sources, McQuinn et al. (2002) suggest that ^{13}CO is as useful as CS for identifying (potential-) star forming clumps/cores. The virial mass of the Galactic clumps/cores traced by ^{13}CO account for about 20% of the virial mass derived from ^{12}CO (Heyer et al., 2009). As a result, ^{13}CO can highlight more compact structures than ^{12}CO. Figure 2.3 shows three integrated intensity maps of the Galactic plane in ^{12}CO (top), ^{13}CO (middle), and C^{18}O (bottom), tracing the gas progressively denser, thus size of gas emitters are getting compact. Fourthly, variation of ^{13}CO abundance is small at the regions with volume density < 5000 cm^{-3}, and temperature of > 15 K (Bachiller & Cernicharo, 1986, Caselli et al., 1999, Heyer & Ladd, 1995)[3].

2.2.1 ^{13}CO Observations in the Milky Way

The first ^{13}CO (1–0) observation in our Galaxy was carried out by Solomon et al. (1979). They observed Galactic GMCs across the Galactic plane from ∼3 kpc to 9 kpc. The radial distribution of ^{13}CO intensity appears to follow the variation of ^{12}CO emission

[3]The fourth advantage of ^{13}CO may not occur in this thesis because the interested galactic areas in this project and also Chapter 3 contain relatively strong star forming activities. Density at these areas could be more than 10^4 cm^{-3}.

(See Figure 1.3 for the radial distribution of ^{12}CO). The most important conclusion of Solomon et al. (1979) is that they constrain the *standard* ^{12}CO to ^{13}CO line ratio (R_{10}) for Galactic GMCs. R_{10} is about 5.5 $\pm$ 0.63, with variation less than 40% between 4 kpc to 8 kpc.

2.2.2 ^{13}CO Observations in External Galaxies

The first ^{13}CO observations in nearby galaxies are carried out by Encrenaz et al. (1979) with the 7-m telescope of Bell Telephone Laboratories, corresponding to a beamsize of 1.7′. Eight galaxies were observed in this work. Encrenaz et al. (1979) suggest a global R_{10} of ∼12 for nearby galaxies, which is about two times larger than the values derived in Milky Way by Solomon et al. (1979). Young & Sanders (1986) observe ^{13}CO in the disks of six late-type spiral galaxies with 14-m telescope of the FCRAO (beamsize is about 45″) later on. R_{10} varies between 6 to 20 within individual galaxies.

The earliest works have suggested that ^{13}CO is significantly weaker than ^{12}CO in nearby galaxies, therefore, in the later studies, most of ^{13}CO observations are made toward the central regions of galaxies (e.g., Chou et al., 2007, Harrison et al., 1999, Helfer & Blitz, 1995, Israel, 2009, Israel & Baas, 2001, Kikumoto et al., 1998, Martín et al., 2010, Matsushita et al., 2010, 1998, Meier & Turner, 2004, Meier et al., 2000, 2008, Neininger et al., 1998, Paglione et al., 2004, Pan et al., 2013, Papadopoulos & Seaquist, 1999, Petitpas & Wilson, 2003, Reynaud & Downes, 1999, Sakamoto et al., 2007, 2011, 2006, Schulz et al., 2001). Some of them were made in the sub-regions of the disks of nearby galaxies (Hirota et al., 2010, 2011, Muraoka et al., 2012, Rebolledo et al., 2012, Tosaki et al., 2002, Turner & Hurt, 1992, Wilson & Walker, 1994, Wilson et al., 1997), or galaxy mergers (e.g., Aalto et al., 2010, 1997, Glenn & Hunter, 2001, Papadopoulos et al., 2012, Taniguchi & Ohyama, 1998, Wilkins et al., 2008, Zhu et al., 2003).

Single pointing observations of ^{13}CO along the major axis of galaxies have been performed by several authors (Paglione et al., 2001, Sakamoto et al., 1997, Tan et al., 2011, Young & Sanders, 1986). The most popular discussion in these studies is what cause the variation of R_{10} across the galactic disks? R_{10} as a function of radius with largest sample and best resolution are displayed in Figure 2.4 (Paglione et al., 2001). There is no significant difference of radial distribution of ^{13}CO among galaxies. In general, intensity of ^{13}CO decreases with increasing radius. R_{10}, however, can be either a increasing (e.g., M51 and NGC 5055) or a decreasing (e.g., NGC 4631 and NGC 6946) function of galactic radii or nearly identical across the disk (e.g., NGC 1068 and NGC 3556). Moreover, R_{10} changes from ∼5 to ∼25, suggesting that those molecular clouds in external galaxies may not be identical with the Galactic clouds.

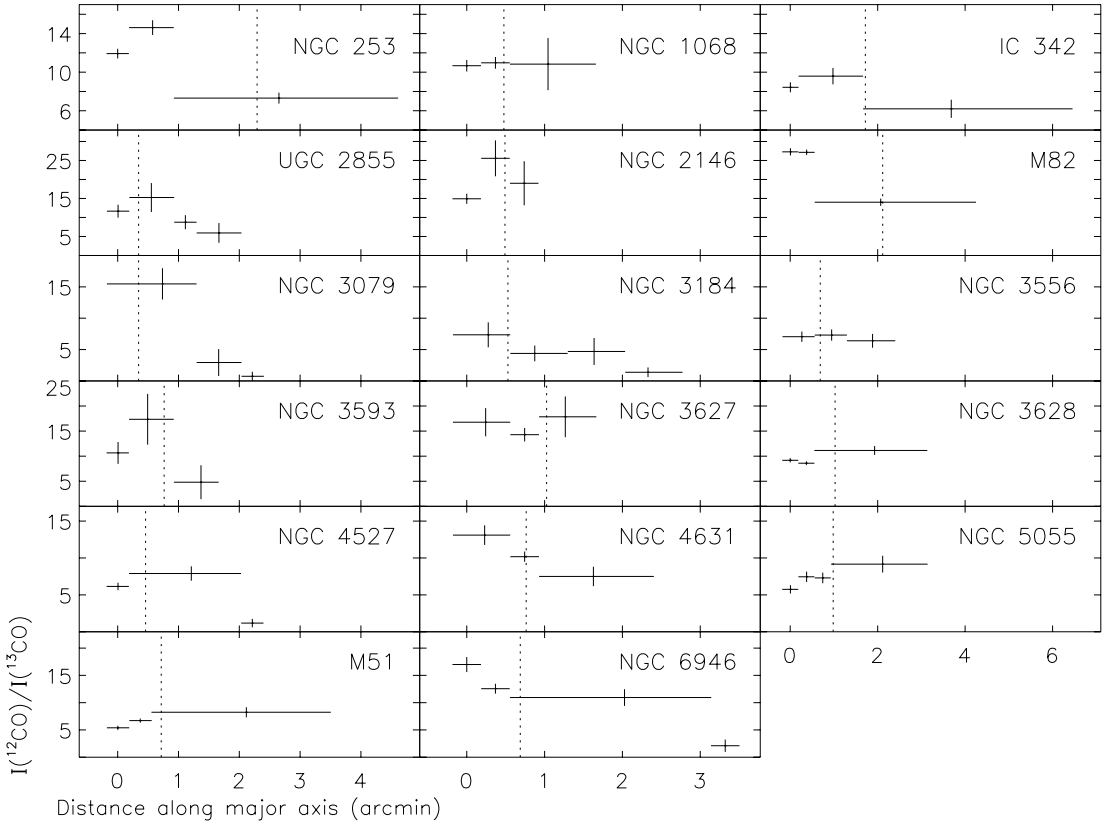

FIGURE 2.4: R_{10} of various galaxies taken from Paglione et al. (2001). The data are binned at the nucleus and the disks to generate the uniform uncertainties.

There are only few galaxies which have been mapped with ^{13}CO in large scale (Aalto et al., 2010, Hirota et al., 2010, Hüttemeister et al., 2000, Watanabe et al., 2011). Although the targets are relatively nearby, the physical resolutions are still much larger than the size of GMCs in most of studies.

Hüttemeister et al. (2000) observed a barred galaxy NGC 7479 with OVRO in ^{13}CO and ^{12}CO (1–0). An angular resolution of $\sim 6''$ corresponds to a physical scale of $\sim$900 pc. The ^{13}CO map of NGC 7479 shows an offset from the ^{12}CO maximum, coinciding with the prominent dust lane in the southern bar. Such offset, however, is not seen in the ^{12}CO map, suggesting that these two lines do trace different components. The configuration of ^{13}CO and ^{12}CO leads to a scenario that ^{13}CO traces high column (and probably also volume) density gas. These gas are compressed in the region where the velocity gradient of the bar is large. Some ^{12}CO emission traces the same gas population as ^{13}CO, but most of them come from a diffuse gas. R_{10} ranges from 5 to $\geqslant 30$ at the bar of NGC 7479. The high R_{10} is a result of the presence of gas with moderate optical depth.

Watanabe et al. (2011) observed barred galaxy NGC 3627 with NRO[4] 45-m telescope in

[4]Nobeyama Radio Observatory

^{13}CO (1–0). The angular resolution of ∼16″ corresponds to a physical scale of ∼800 pc. The morphology of ^{13}CO and ^{12}CO[5] resemble each other. ^{13}CO emission peaks at the galactic center and the bar ends, while a few small peaks are found at the spiral arms, which have intensities <50% of the center and the bar ends. In general, R_{10} decreases along the galactocentric radii with a rate of -1.4 ± 0.4 kpc^{-1}, but R_{10} is as high as 20 within the bar region, comparable to the center of its host galaxy. The low R_{10}, ∼10, are found at the bar ends. Such change of R_{10} over the disk of barred galaxy is consistent with that of NGC 7479 (Hüttemeister et al., 2000). By using the Hα and 24μm images as SFR indicators, Watanabe et al. (2011) conclude that SFE is highest at the bar ends, nearly two times larger than the galactic center. On the other hand, SFE inside the bar region is considerably depressed, about ∼3 times lower than the bar ends.

Aalto et al. (2010) observe Medusa merger (NGC 4194) in ^{13}CO (1–0) by using OVRO. They obtain a beamsize of ∼ 4.5″, equivalent to ∼ 860 pc. They found ^{13}CO (1–0) traces post-shock regions in the starburst area, where the gas are more bound. On the other hand, ^{12}CO (1–0)[6] traces diffuse gas in Medusa merger. R_{10} is found to be 16 – > 40. The wide range of R_{10} attributes to the change of gas temperature and density.

Hirota et al. (2010) observed barred spiral galaxy IC 342 with NRO 45-m telescope in ^{13}CO (1–0). The angular resolution of ∼20″ corresponds to a physical scale of ∼320 pc. The ^{13}CO observations of IC 342 cover the galactic center, galactic bar and most of the primary spiral arm. The most striking discrepancy between the ^{13}CO and ^{12}CO[7] maps is seen in the spiral arm. At a specific area of the arm, only one GMA, a product of gas compressed by the density wave potential, is found. However, the GMA is associated with three ^{13}CO peaks. Such kind of inconsistency is also found at the northern bar end of IC 342. These again confirm that ^{12}CO and ^{13}CO trace different gas components in galaxies. R_{10} is about 7 – 10 in IC 342.

Hirota et al. (2011) then further observe portion a spiral arm of IC 342 with NMA[8]. The physical resolution of this work is only 60 pc. So far this is the best resolution of ^{13}CO in nearby galaxy, although their observing area is relatively small. They identify GMC with algorithm of CLUMPFIND and classify the GMCs with their star forming activity. They found that star forming GMCs have low R_{10} (∼ 6) while R_{10} is as high as 16 in non-star forming GMCs. They explain the results with the presence of diffuse gas associated with non-star forming GMCs, namely, larger $I_{^{12}\mathrm{CO}}$.

[5] ^{12}CO is taken from Kuno et al. (2007), made by NRO
[6] ^{12}CO is taken from Aalto & Hüttemeister (2000), made by OVRO
[7] ^{12}CO is taken from Kuno et al. (2007), made by NRO
[8] Nobeyama Millimeter Array

2.3 Motivation and Methodology

From the previous Chapter and sections, we have got some facts as follows:

- Kennicutt-Schmidt law ($\Sigma_{\rm SFR}$ versus $\Sigma_{\rm H_2}$) can be a hint of star formation mechanism.
- GMC properties and their ability to form stars may change with environments. If so the Kennicutt-Schmidt law would change as well.
- Ideally Kennicutt-Schmidt law can be derived once the column density of molecular gas is determined. The methods of extinction and dust emission seem to be impractical in the study of nearby galaxies. Hence, the derivation of the column density and the mass of molecular clouds relies on the integrated intensity map of molecular line emission.
- Kennicutt-Schmidt law can be derived by using ^{12}CO as the tracer of $\Sigma_{\rm H_2}$.
  - CO-to-H_2 conversion factor ($X_{\rm CO}$) is needed to derive ^{12}CO-base $\Sigma_{\rm H_2}$.
  - $X_{\rm CO}$ is a function of CO intensity and metalicity.
  - the problem of ^{12}CO is its high opacity, and the high opacity also leads to a low effective critical density ($\sim 10^2$ cm^{-3}).
- Kennicutt-Schmidt law can be derived by using ^{13}CO as the tracer of $\Sigma_{\rm H_2}$.
  - ^{13}CO is optically thin.
  - Because of the low opacity, ^{13}CO is a tracer of denser regions in GMCs ($\sim 10^3$ cm^{-3}).

The information inspires us to revisit Kennicutt-Schmidt law by using the latest calibration of $X_{\rm CO}$ and an optically thin transition for the first time. We study how $\Sigma_{\rm SFR}$ change with $\Sigma_{\rm H_2}$ and the reason of different star forming ability in different regions of a galaxy.

The best physical resolution to study K–S law is sub-kiloparsec scale. This resolution spatially resolves galactic structures, i.e., spiral arms, galactic bar and center, but remains $\Sigma_{\rm H_2}$ and $\Sigma_{\rm SFR}$ as beam-average parameters. Specifically, the difference among galactic structures are distinguishable, but the uncertainties in the evolution of individual GMCs and star forming regions (e.g., Onodera et al., 2010) are negligible. We chose IC 342 as our target by several reasons:

1. Since the galaxy is close, even single dish can reach a sub-kpc resolution of 320 pc.

2. Both ^{13}CO and ^{12}CO data are available from archive. The images are large enough to cover galactic disk and center.

3. There are archival images tracing SFR.

4. A bar-driven starburst region is observed in the central region of IC 342, the high density region splits the physical environment from the galactic disk, providing a chance to study the environmental dependence of K–S law in diverse physical conditions of molecular gas.

With these data, we study Kennicutt-Schmidt law with ^{12}CO and ^{13}CO, separately. Then discuss the reasons which lead to the change of Kennicutt-Schmidt law in different galactic areas. We also perform similar analysis for other galaxies to compare with the results of IC 342.

2.4 The Target: IC 342

IC 342 (Figure 2.5) is located in IC 342/Maffei Group. It is the closest galaxy group to our Local Group. More than a dozen of galaxies are residing in this galaxy group. The main galaxies in IC 342/Maffei Group are IC 342, Maffei 1 and Maffei 2. Both IC 342 and Maffei 2 are classified as SAB(rs)bc, while Maffei 1 is an elliptical galaxy. Tidal tails extending between IC 342 and irregular galaxy UGCA 86 are seen in some HI observations (e.g., Johnson, 2013, Stil et al., 2004). The parameters of IC 342 are listed in Table 2.1 . IC 342 is located at 3.2 Mpc, where $1''$ corresponds to 16 pc. Since the galaxy is very close, the physical resolution of single dish observation in CO (1–0) lines can be down to sub-kpc scale even only with a 12-m dish (e.g., Crosthwaite et al., 2001).

Table 2.1: Parameters of IC 342.

Morphology	SAB(rs)cd
R.A.	$03^{h}46^{m}48\overset{s}{.}6$
Dec.	$68°5'47''$
Distance	3.2 Mpc*
Physical Scale of $1''$	16 pc
Systemic Velocity	32 km s^{-1}**
Inclination	31°**
P,A	37°**

* Saha et al. (2002)
** Crosthwaite et al. (2000)

The CO map made with a single dish has shown a clear molecular bar with length of about 4.5 kpc (Crosthwaite et al., 2001). A primary spiral arm emerging from the

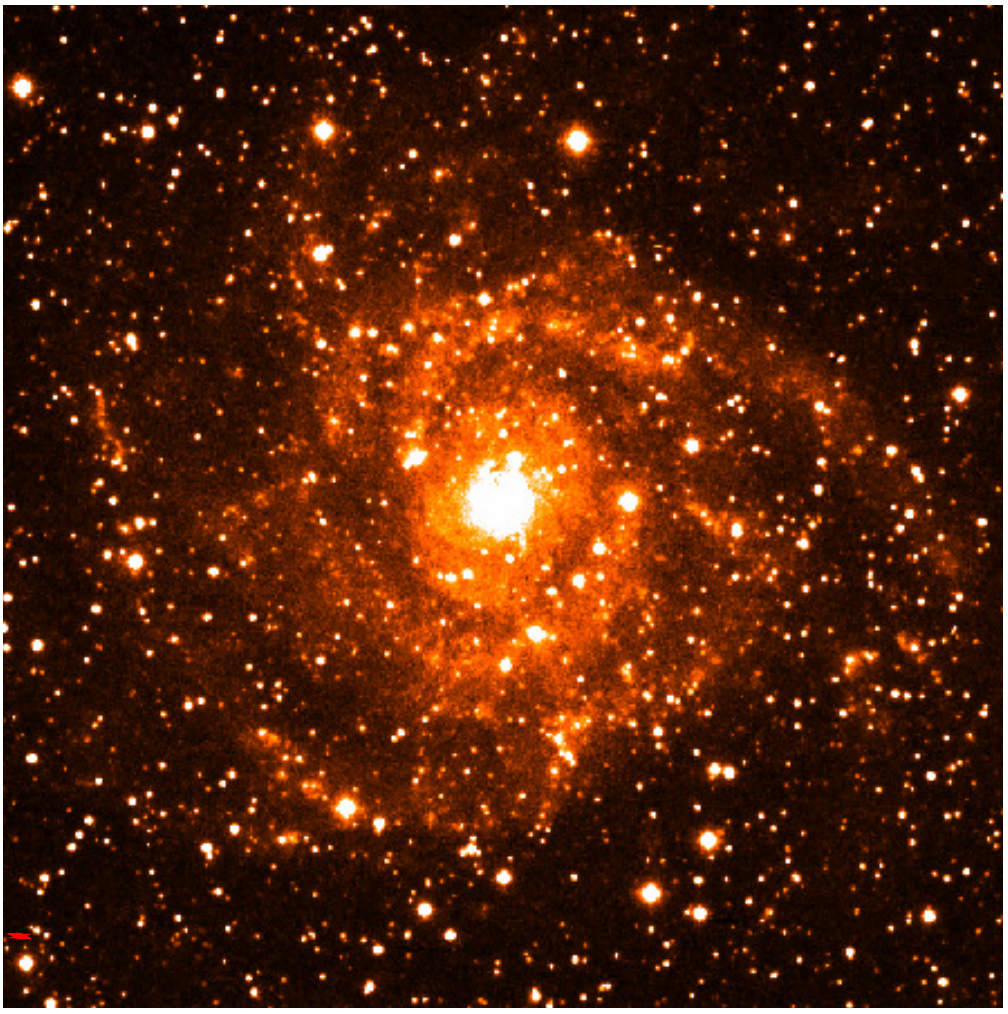

FIGURE 2.5: The optical image of IC 342 (103aE, 6450Å) taken from NED.

southern bar end is seen in the CO map as well. IC 342 is undergoing bar-driven gas inflow (Schinnerer et al., 2003) which triggers the starburst at the center. In the central $1'$, molecular gas appears to be a spiral structure (Figure 2.6). The spirals corresponds to the x_1 orbit of galactic bar (parallel to the bar). The two spirals wrap around at the central $15''$, creating a ring-like structure. Inside the ring is a star cluster with age $6 - 60$ Myr (Boker et al., 1997). The volume density of the gas in the central region (central $1'$) must be considerably high since HCN[9] clearly traces at the spirals and the ring (Figure 2.7). For this reason, the central region is able to split the physical environment from the galactic disk, providing a chance to study the K–S law in diverse physical conditions of molecular gas.

[9]Critical density of HCN (1–0) is about $(2.4 \times 10^{-5})/(2 \times 10^{-11}) \approx 10^6$ cm^{-3}. Considering the high optical depth of HCN (1–0) (optically thick) (Matsushita et al., 1998), the effective critical density of HCN (1–0) is on the order 10^5 cm^{-3}.

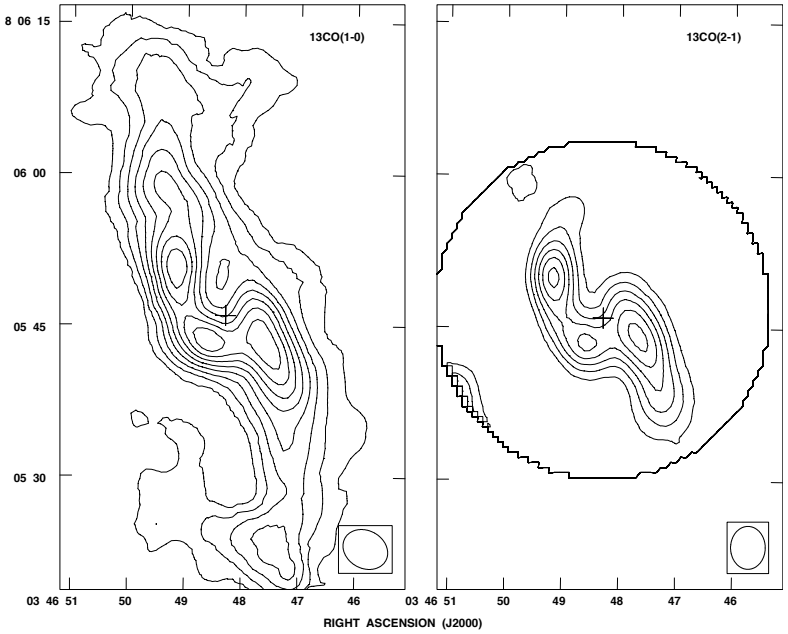

FIGURE 2.6: The ^{13}CO maps of IC 342 taken from Meier et al. (2000).

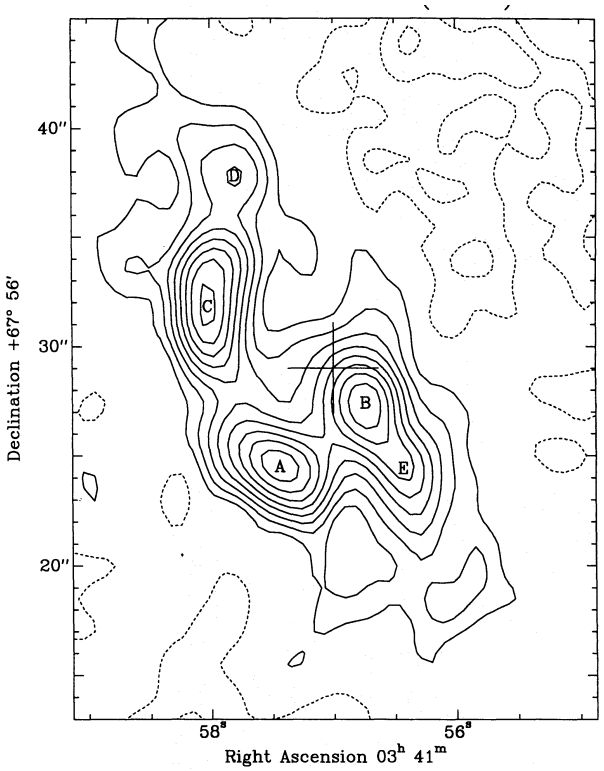

FIGURE 2.7: HCN map of IC 342 at the central 1′. taken from Downes et al. (1992).

2.5 Data

2.5.1 NRO CO Maps

The ^{12}CO ($J = 1 \rightarrow 0$) (hereafter ^{12}CO) image of IC 342 (Figure 2.8) was taken from the Nobeyama CO Atlas of Nearby Spiral Galaxies (Kuno et al., 2007). The observations were made by the Nobeyama 45-m telescope. The angular resolution of the map is 20″ at 115 GHz, corresponding to a physical resolution of ∼320 pc. The map extends up to a galactocentric radius of about 6.5 kpc (406″). The rms noise is about 1.5 K km s^{-1} or ~ 5 M$_\odot$ pc^{-2} with the Galactic standard CO-to-H$_2$ conversion factor ($X_{\rm CO} = 2.3 \times 10^{20}$ cm^{-2} (K km s^{-1})$^{-1}$) (Strong et al., 1988).

The ^{13}CO ($J = 1 \rightarrow 0$) (hereafter ^{13}CO) image (yellow contours in Figure 2.9) was also taken with the Nobeyama 45-m telescope by Hirota et al. (2010). The map covers the galactic center, the bar, and the spiral arm emerging from the southern barend with a total area of ∼320″ ×320 ″ (5.1 kpc × 5.1 kpc), which is about a fourth of the ^{12}CO map. The angular resolution is also 20″ (320 pc) at 110.2 GHz and the rms noise is 0.4 K km s^{-1}.

2.5.2 VLA HI Map

The atomic hydrogen (HI) image of IC 342 is taken from Crosthwaite et al. (2000). The observations were carried out by VLA using C and D configurations. The resulting angular resolution is 38″ × 37″ (610 pc × 590 pc) at the wavelength of 21 cm. The HI image has a radius of 1300″ (∼21 kpc), which is far beyond the molecular disk of IC 342 by about three times.

2.5.3 Spitzer 24 μm Map

IC 342 is not included in either the Spitzer Local Volume Legacy Survey (LVL) or The Spitzer Infrared Nearby Galaxies Survey (SINGS) but in several individual programs, presumably due to its too low latitude (b=10.°58). We use the 24μm data as SFR tracer from Spitzer Heritage Archive (SHA). The data was obtained by Multiband Imaging Photometer (MIPS) (Rieke et al., 2004). The angular resolution of 24 μm map is ∼5.″7 (∼ 91 pc).

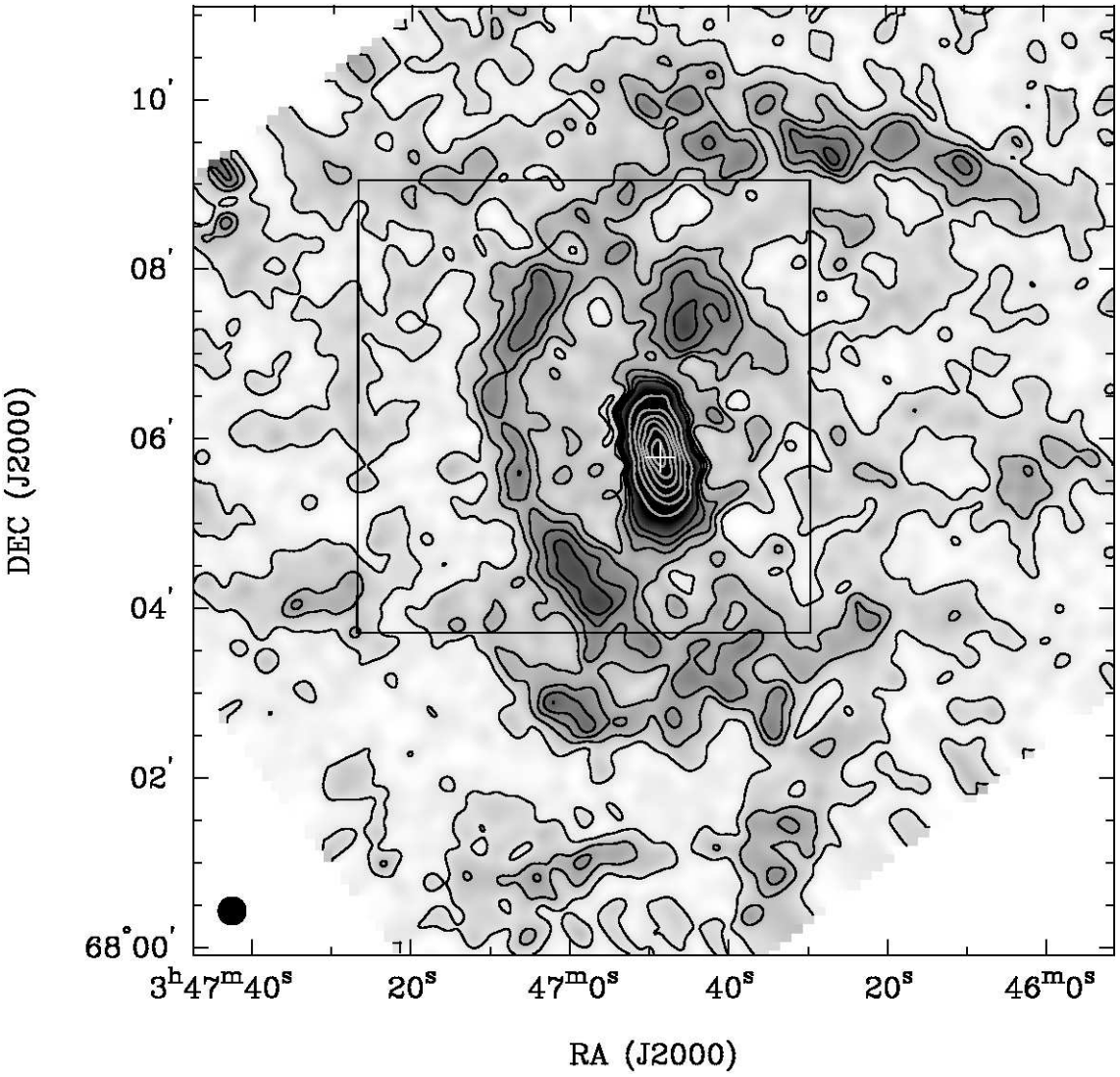

FIGURE 2.8: ^{12}CO map of IC 342 taken from Kuno et al. (2007). Contours represent 4.5 (3 σ),10, 15, 20, 25, 50, 80, 110, 140, 170, and 200 K km s^{-1}. The white cross marks the galactic center. The beam size of 20″ is shown at the bottom left of the figure. The area of ^{13}CO (1-0) observation made by Hirota et al. (2010) is indicated with the box.

2.5.4 Hershel Mid- Far-Infrared Maps

The Hershel telescope provides infrared data ranges from 70 to 500μm. The data are useful to derive the dust/gas temperature from the spectral energy distribution (SED), which is required in our analysis. IC 342 is one of the samples in the project of Key Insights on Nearby Galaxies: a Far-Infrared Survey with Herschel (KINGFISH) (Kennicutt et al., 2011). The data are available in the project website. Herschel PACS and SPIRE instruments provide the wavelength 70, 100, 160 μm (PACS) and 250, 350, 500 μm (SPIRE). The original unit of the images, pixel size and the resolution are listed in Table 2.2. The process of data reduction are described in the KINGFISH Data Products Delivery Users Guide.

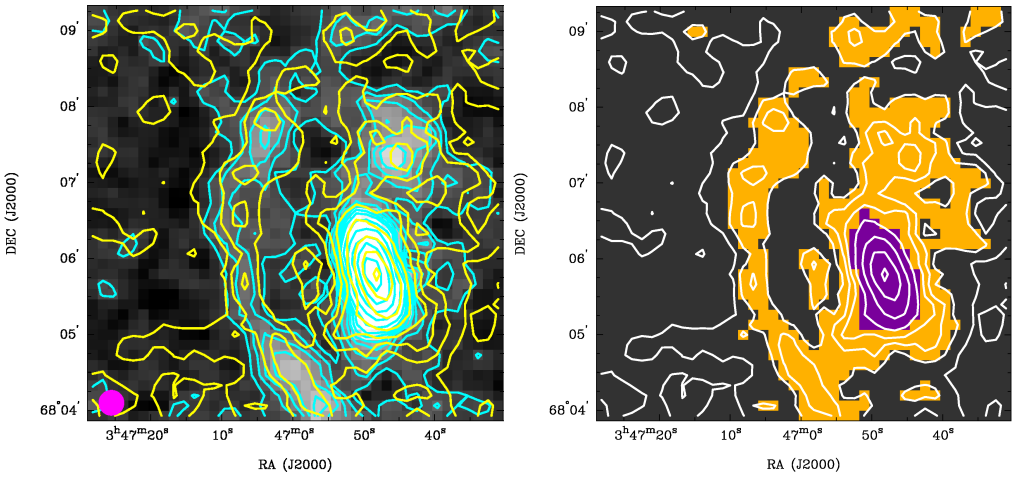

FIGURE 2.9: Velocity-integrated intensity maps of CO and the defined galactic features. Left: The integrated maps of two CO lines. Cyan and yellow contours denote the ^{12}CO and ^{13}CO velocity-integrated intensity maps, respectively. The ^{12}CO is the one shown in Figure 2.8. The beam size is overlaid in the bottom left. The grey scale is also ^{12}CO map. The contours of ^{12}CO map are 10 (6.5 σ), 15, 20, 25, 30, 35, 40, 50, 70, 100, 140, and 190 K km s^{-1}. The contour levels of ^{13}CO map are 1 (2.5 σ), 2, 3, 4, 6, 10, 16, and 22 K km s^{-1}. Right: The defined galactic features. The white contours is the ^{13}CO in left panel with same steps. The purple area corresponds to the pixels categorized as galactic center, while the oranges area tags the pixels belonging to the defined spiral arm.

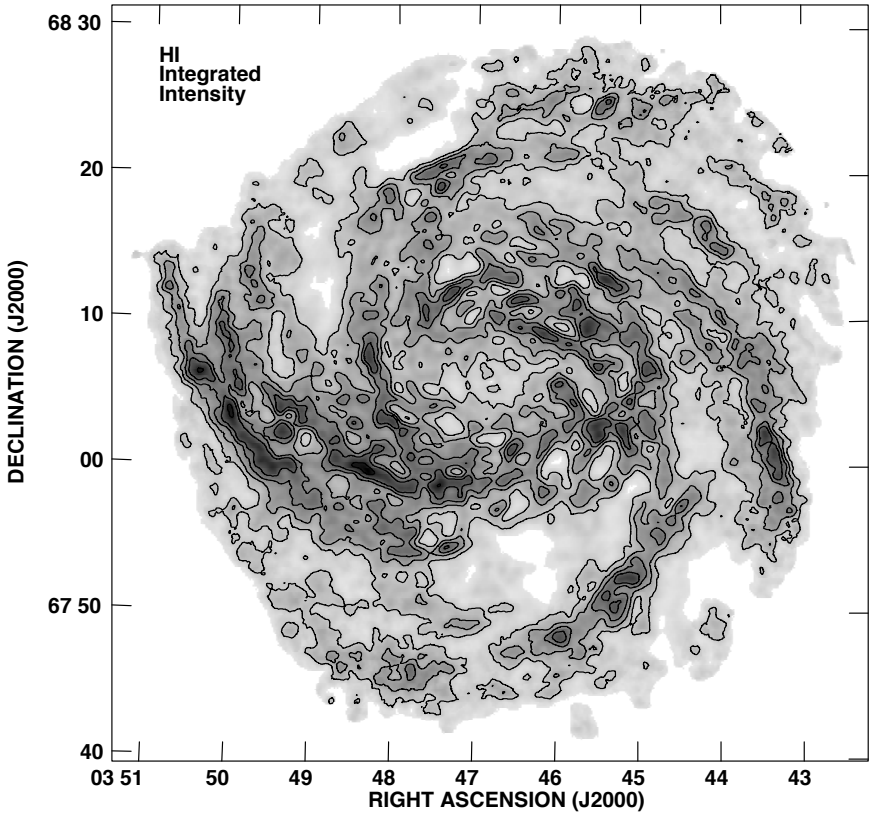

FIGURE 2.10: HI map taken from Crosthwaite et al. (2000). Gray scale ranges from 0 – 3 Jy beam^{-1} km s^{-1}. Contours are with steps of 0.4 × 1, 2, 3, and 4 Jy beam^{-1} km s^{-1}. The largest structure that VLA can resolve under this configuration is 15′.

TABLE 2.2: Information on the original infrared data from archives.

Wavelength (μm)	24[a]	70[b]	100[b]	160[b]	250[c]	350[c]	500[c]
FWHM(arcsec)	5.7	5.2	7.7	12	18	25	37
Pixel size (arcsec)	2.5	1.4	1.7	2.85	6	10	14
Image Unit	MJy/sr	Jy/pixel	Jy/pixel	Jy/pixel	MJy/sr	MJy/sr	MJy/sr

[a] Spitzer
[b] Herschel PACS
[c] Herschel SPIRE

2.6 Radial Distribution of Gas and Star Formation

2.6.1 Radial Distribution of Gas

The neutral gas in a galaxy consists of molecular and atomic gas. The former one is required for star formation, but some nearby spiral galaxies harbour larger amount of atomic gas relative to the molecular gas, such as M33. Accordingly, we consider the content of the gas in IC 342 as the first step. The task `ellint` in `MIRIAD` (Sault et al., 1995) is used to find the radial intensity distribution of all the gas and SFR tracers in this section.

Since ^{12}CO was mapped in entire galaxy, we use the image of ^{12}CO to measure the radial distribution of Σ_{H_2}. The inclination and the position angle of the galaxy are 31° and 37°, respectively (Crosthwaite et al., 2000). The step size between each azimuthal average data point is 10″, starting from 0″ to 400″ (6.4 kpc) or $R/R_{25} \approx 0.30$, where $R_{25} = 22.3'$ or 21.4 kpc (Pilyugin et al., 2004). X_{CO} of 2.3×10^{20} cm^{-2} (K km s^{-1})$^{-1}$ (Strong et al., 1988) is adopted to derive Σ_{H_2}.

The radial profile of Σ_{H_2} is shown as crosses in Figure 2.11. Σ_{H_2} peaks at the galactic center ($\sim$750 M$_\odot$ pc^{-2}) and then gradually decreases to $\sim R/R_{25} = 0.05$. A small bump at radius of $R/R_{25} \approx 0.1$ ($\sim$2 kpc) is contributed by the brightest spiral arm. Beyond the spiral arm, Σ_{H_2} decreases to $\sim$20 M$_\odot$ pc^{-2} at $R/R_{25} = 0.3$.

For barred galaxies, there are two characteristics in their radial profile of gas: the enhanced amount of gas at the central region and the shallower gas distribution in the bar region (Kuno et al., 2007, Nakai, 1992, Regan et al., 2006). For barred galaxies, the intensity of CO exceeds the inward extrapolation of the radial distribution of the disk. On the other hand, at the barred region, the radial distribution is shallower (e.g., NGC 3627, NGC 3351, and NGC 4321 in Regan et al. (2006) and NGC 2903 in Nakai (1992)). For IC 342, the excess of CO intensity at central region is cleanly seen, and the shallower distribution of gas occurs at about 1.1 kpc (Figure 2.11). In contrast, for non-barred galaxies, the radial profile of gas show a smooth exponential increase toward

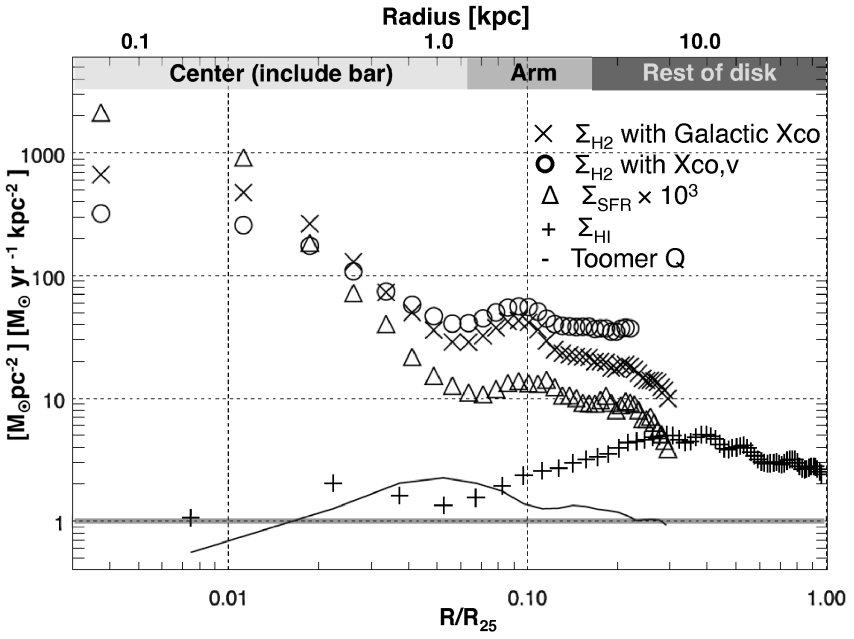

FIGURE 2.11: Radial distribution of Σ_{H_2} (crosses and circles), Σ_{HI} (pluses) and Σ_{SFR} (triangles). The radial step Σ_{H_2} and Σ_{SFR} is 10″. The radial profile of Σ_{HI} is sampled every 20″. The solid black line represents the Toomre Q parameter (§). The grey solid line marks the intensity of 1 to compare with Q.

the center, but then drop at the center of some galaxies (e.g., NGC 0628 and NGC 7331 in Regan et al. (2006)).

The column density of atomic hydrogen (HI) is calculated by

$$N(\mathrm{HI})(\mathrm{cm}^{-2}) = 1.823 \times 10^{18} \int T_\mathrm{b} \mathrm{d}v, \tag{2.6}$$

where T_b is brightness temperature (Wilson et al., 2009). The step size between each azimuthal average of HI data is 20″ (320 pc), starting from 0″ to 1300″ ($\mathrm{R/R_{25}} \approx 0.97$). The radial profile of Σ_{HI} is shown in Figure 2.11 with plus symbol. As seen in most of spiral galaxies, the distribution of HI emission extends well beyond the molecular/optical disk (Pan et al., 2013). Σ_{HI} hits the lowest point at the galactic center. The *hole* of HI emission around the central region of galaxies is attributed to the strong radiation of UV photons which ionize the atomic hydrogen, and the ionized hydrogen is forced to form molecules with other elements. Beyond the galactic center, the radial Σ_{HI} profile shows an upward trend till $\mathrm{R/R_{25}} = 0.3$. Then Σ_{HI} gently declines to $\mathrm{R/R_{25}} \approx 1$. Even though there are some variations in Σ_{HI}, Σ_{HI} varies within a narrow range of 1 – 5 $\mathrm{M_\odot\ pc^{-2}}$, occupying <35% of total gas. Hence, IC 342 is a H_2 dominant spiral galaxy, with potential for significant star formation.

2.6.2 Radial Distribution of Star Formation

The mid-infrared 24 μm emission traces the dust grains heated by the UV photons radiated by young stars and therefore serves as a tracer of obscured SFR with a timescale no longer than 10 Myr (Calzetti et al., 2005). On the other hand, Hα traces the ionized gas surrounding the massive stars, and thereby reckoned as the tracer of unobscured SFR (Calzetti et al., 2005). Hence, 24 μm and Hα is often used to obtain the total SFR in a given region (e.g., Calzetti et al. (2007), Kennicutt et al. (2007)).

Since, however, IC 342 is located behind the galactic plane (b=10.°5), Hα emission is severely suffered from dust extinction and, moreover, there is no available digital Hα image to access. For these reasons we use an infrared image as the SFR indicator. The monochromatic infrared SFR is calculated as

$$\mathrm{SFR}(\mathrm{M}_\odot\ \mathrm{yr}^{-1}) = 1.31 \times 10^{-38}[L_{24\mu\mathrm{m}}(\mathrm{ergs\ s}^{-1})]^{0.885} \tag{2.7}$$

(Calzetti, 2012, Calzetti et al., 2007) based on a two-component IMF, in which the slope is -1.3 between 0.1 $\mathrm{M}_\odot$ to 0.5 $\mathrm{M}_\odot$ and -2.3 in the range of 0.5 $\mathrm{M}_\odot$ – 120 $\mathrm{M}_\odot$. Equation (2.7) is calibrated for local SFR with spatial scale of $\sim$ 500 pc and is valid in the range of $1 \times 10^{40} \lesssim [L_{24\mu\mathrm{m}}] \lesssim 3 \times 10^{44}$. IC 342 is in the range. The uncertainty of the power and the coefficient are 0.02 and 15% , respectively.

We have smoothed the 24 μm image from the resolution of $\sim$6″ to 20″ to match with the CO image, using task `convol` of `MIRAD`. The 24μm image is also re-gridded to match with the CO image for further analysis with task `regrid`. For this reason the step size and the radial range of Σ_{SFR} (triangles) is the same as $\Sigma_{\mathrm{H_2}}$ (crosses). The radial distribution of Σ_{SFR} resembles that of $\Sigma_{\mathrm{H_2}}$ in IC 342. Σ_{SFR} also shows an excess at the central region as in the profile of $\Sigma_{\mathrm{H_2}}$. In non-barred galaxies, the intensity of SFR tracers also drop at the center as in $\Sigma_{\mathrm{H_2}}$ (Regan et al., 2006).

The characteristic features of the radial distribution of $\Sigma_{\mathrm{H_2}}$, Σ_{HI}, and Σ_{SFR} are summarized as follows: a) The radial distribution of $\Sigma_{\mathrm{H_2}}$ and Σ_{HI} reveal that IC 342 is a molecular-dominant galaxy; b) The molecular gas is concentrated in the center and the bright spiral arm at the radius of $\sim$2 kpc; c) The radial distribution of Σ_{SFR} resembles that of $\Sigma_{\mathrm{H_2}}$.

2.7 Surface Density of $\mathrm{H_2}$ Derived from ^{12}CO

In this section, we consider the spatial distribution of molecular gas by using the standard Galactic CO-to-$\mathrm{H_2}$ conversion factor (X_{CO}) and the conversion factor ($X_{\mathrm{CO,v}}$) which

depends on the metallicity and line intensity (Narayanan et al., 2012).

2.7.1 Surface Density of H_2 Derived with X_{CO}

First of all, the standard Galactic X_{CO} of 2.3×10^{20} cm^{-2} (K km s^{-1})$^{-1}$ is applied to the entire ^{12}CO map.

The peak value of Σ_{H_2} is 756 $M_\odot$ pc^{-2} at the galactic center. Such high Σ_{H_2} is commonly seen in the circumnuclear starburst (e.g., $\Sigma_{H_2} \approx 10^{2-3}$ $M_\odot$ pc^{-2} in Kennicutt (1998)). The 3σ detection limit of ^{12}CO corresponds to $\Sigma_{H_2} \approx 15$ $M_\odot$ pc^{-2}. The mean Σ_{H_2} of IC 342 is 36 $M_\odot$ pc^{-2}, principally contributed by the galactic disk.

2.7.2 Surface Density of H_2 Derived with $X_{CO,v}$

Both observations (e.g., Arimoto et al. (1996)) and simulations (e.g., Narayanan et al. (2012)) suggest that metallicity is a key parameter to affect X_{CO}. In metal-poor regions, X_{CO} tends to be higher than the Galactic Standard X_{CO} due to the photodissociation of CO. Furthermore, Narayanan et al. (2012) suggest that X_{CO} depends on the CO intensity as well. Such dependence of X_{CO} on CO intensity is also seen within single galaxy (Nakai & Kuno, 1995).

Therefore, we adopt the simulation X_{CO}–Z'–W_{CO} relation derived by Narayanan et al. (2012). First, they preform hydrodynamical simulation of galaxy evolution, including isolated disk galaxy and merger over a range of redshift. This simulation sets up the kinematic and mass of ISM and the stellar populations. The fraction of H_2 and carbon, the amount of these molecules locked in GMCs, metallicity of GMCs, heating and cooling of gas and the radiation transfer of dust are required as well to establish the physical and chemical states of ISM. The *continuous* X_{CO} is a function of CO intensity and metallicity:

$$X_{CO,v} = \frac{6.75 \times 10^{20} \times \langle W_{CO} \rangle^{-0.32}}{Z'^{0.65}}, \tag{2.8}$$

where the $\langle W_{CO} \rangle$ is ^{12}CO line intensity measured in K km s^{-1} and Z' is the metallicity divided by the solar metallicity (Z). The conversion between Z' and the common used form of metallicity $12 + \log[O/H]$ is

$$\log Z' = 12 + \log[O/H] - 8.76, \tag{2.9}$$

where the solar metallicity in log scale is assumed to be 8.76 (Krumholz et al., 2008). Equation (2.8) is available from sub-kpc scale to unresolved galaxies (Narayanan et al., 2012).

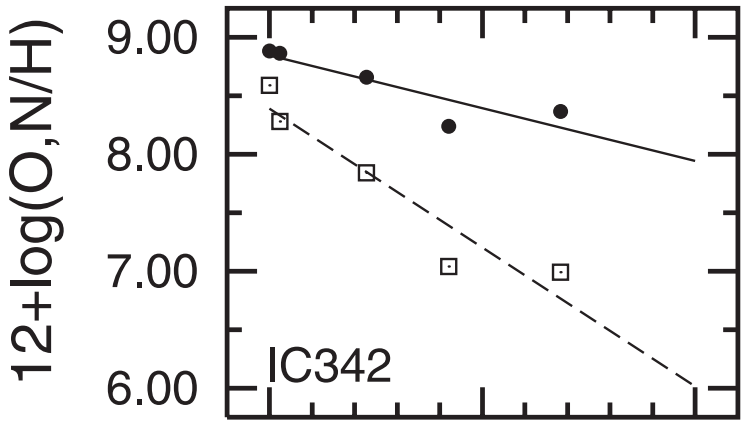

FIGURE 2.12: Oxygen (filled circles) and nitrogen (open squares) abundances of IC 342. The five data points of each gradient represent five HII regions in different radii. This figure is taken from Pilyugin et al. (2004).

For IC 342, as most of galaxies, the gradient of metallicity is measured from HII regions in various radii of the galaxy. Pilyugin et al. (2004) derived the oxygen abundance for the HII regions observed by McCall et al. (1985). The derivation of oxygen abundance requires observed intensity of [OII]]λ3727 + λ3729, [OIII]]λ4959 + λ5007, [OIII]]λ4363, and Hβ. Then Pilyugin et al. (2004) fitted the gradient with the form:

$$12 + \log[\mathrm{O/H}] = 12 + \log[\mathrm{O/H}]_0 + C_{\mathrm{O/H}} \times (R/R_{25}), \tag{2.10}$$

where $12 + \log[\mathrm{O/H}]_0$ is the extrapolated central oxygen abundance, $C_{\mathrm{O/H}}$ is the slope of the oxygen abundance gradient respect to the fractional radius R/R_{25}. The HII regions in IC 342 indicate a clear negative gradient of the abundance with increasing radius (Figure 2.12). $12 + \log[\mathrm{O/H}]_0$ is 8.85 and $C_{\mathrm{O/H}}$ is –0.9 . The uncertainty of the derived log[O/H] is 0.12. Metallicity of individual pixel is calculated and substituted into Equation (2.8) and Equation (2.9) to gain the $X_{\mathrm{CO,v}}$ at each position.

$X_{\mathrm{CO,v}}$ has range (1 – 6) $\times$ 10^{20} cm^{-2} (K km s^{-1})$^{-1}$. Figure 2.13 displays a correlation of $\Sigma_{\mathrm{H_2}}(X_{\mathrm{CO}})$ versus the ratio of $\Sigma_{\mathrm{H_2}}(X_{\mathrm{CO,v}})/\Sigma_{\mathrm{H_2}}$ (X_{CO}) and the $X_{\mathrm{CO,v}}$. The figure indicates $X_{\mathrm{CO,v}} < X_{\mathrm{CO}}$ when $\Sigma_{\mathrm{H_2}}(X_{\mathrm{CO}}) > 100$ M$_\odot$ pc^{-2}, and vice versa. In addition, $\Sigma_{\mathrm{H_2}}(X_{\mathrm{CO}}) \approx \Sigma_{\mathrm{H_2}}(X_{\mathrm{CO,v}})$ occurs at $\sim$100 M$_\odot$ pc^{-2}.

The $X_{\mathrm{CO,v}}$ map is shown in Figure 2.14. In the galactic center, the $X_{\mathrm{CO,v}}$ is as low as 10^{20} cm^{-2} (K km s^{-2})$^{-1}$, consistent with the value measured by the high resolution C^{18}O, 1.3 mm dust continuum, and the virial theorem in IC 342 (Meier & Turner, 2001). Thus the utilization of the Galactic standard X_{CO} leads to the overestimation of $\Sigma_{\mathrm{H_2}}$ at the central region. The peak $\Sigma_{\mathrm{H_2}}$ becomes 344 M$_\odot$ pc^{-2} by using $X_{\mathrm{CO,v}}$, which is about 2 times lower than the mass obtained from the Galactic X_{CO}. The compact regions in

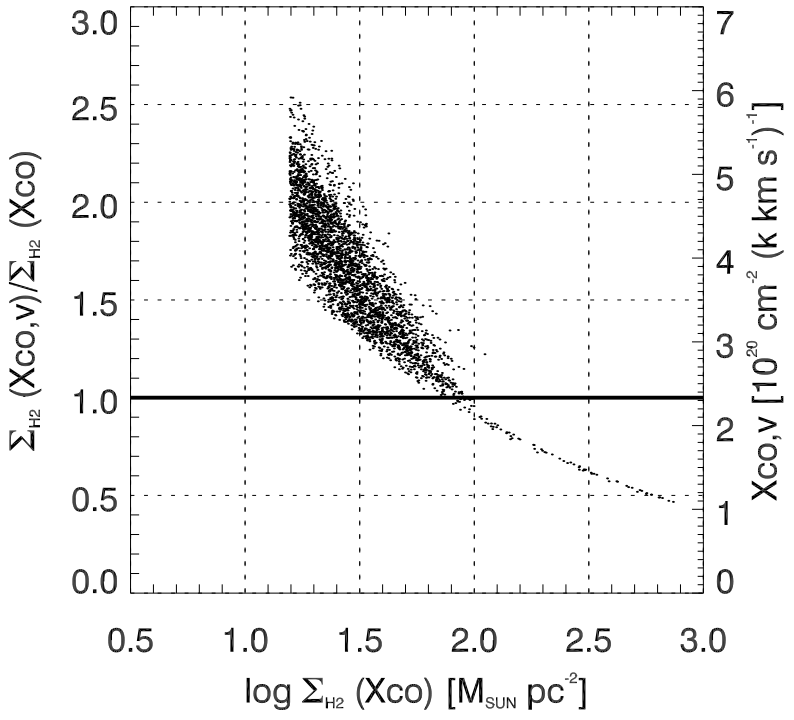

FIGURE 2.13: $\Sigma_{\rm H_2}(X_{\rm CO})$ versus the ratio of $\Sigma_{\rm H_2}(X_{\rm CO,v})/\Sigma_{\rm H_2}$ $(X_{\rm CO})$ and $X_{\rm CO,v}$. The horizontal line marks the $\Sigma_{\rm H_2}(X_{\rm CO,v})/\Sigma_{\rm H_2} = 1$. The vertical line indicates the $\Sigma_{\rm H_2}(X_{\rm CO}) = 100$ M$_\odot$ pc^{-2}. It also corresponds to $\Sigma_{\rm H_2}(X_{\rm CO,v}) \approx 100$ M$_\odot$ pc^{-2} because the ratio of these two values is about unity, i.e., the point where the two lines cross each other.

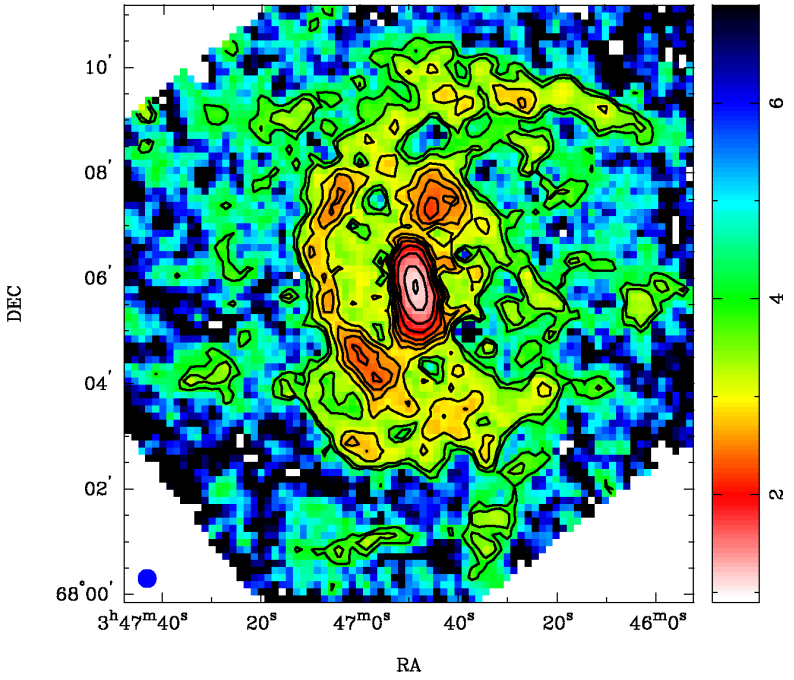

FIGURE 2.14: The $X_{\rm CO,v}$ map of IC 342. The right color bar of $X_{\rm CO,v}$ is in the unit of 10^{20} cm^{-2} (K km s^{-1})$^{-1}$. The beam size of 20″ is indicated in the lower left.

the spiral arms has $X_{\rm CO,v}$ close to the Galactic $X_{\rm CO}$. The remaining diffuse parts have $X_{\rm CO,v} > 3 \times 10^{20}$ cm^{-2} (K km s^{-2})$^{-1}$. Eventually, the detection limit (3 σ detection) $\Sigma_{\rm H_2}$ based on the $X_{\rm CO,v}$ is about 26 M$_\odot$ pc^{-2} and the mean $\Sigma_{\rm H_2}$ is approximately 51 M$_\odot$ pc^{-2}.

The radial distribution of $\Sigma_{\rm H_2}$ based on $X_{\rm CO,v}$ is plotted as circles in Figure 2.11. $\Sigma_{\rm HI}$ is still negligible not only at the central region but also the disk.

2.8 Surface Density of H_2 Derived from ^{13}CO

The velocity-integrated intensity map of ^{13}CO acquired from Hirota et al. (2010) is shown in the left panel of Figure 2.9 with yellow contours. ^{13}CO to ^{12}CO ratio is 0.05 – 0.2 (Hirota et al., 2010). Owing to the low intensity of ^{13}CO, only the pixels with significant detection are considered. The central $\sim 1'$ corresponding to the galactic nucleus seen in the high resolution map (Meier & Turner, 2005) is defined as *galactic center*. This region has detection at least 15 σ. The central region is colored with purple in the right panel of Figure 2.9. Apart from the galactic center, the pixels with ≥ 5 σ detection are taken as well. The criterion chiefly captures the primary spiral arm and the bar end. We refer this region as *spiral arm*. This region is colored with orange in Figure 2.9.

Provided that ^{13}CO is in local thermal equilibrium (LTE) and optically thin, the column density of H_2 is computed by

$$\begin{aligned} N(\mathrm{H_2})_{^{13}\mathrm{CO}} &= 2.41 \times 10^{14} \times \frac{\tau\left(^{13}\mathrm{CO}\right)}{1 - \mathrm{e}^{-\tau(^{13}\mathrm{CO})}} \\ &\times \frac{[\mathrm{H_2}]}{[^{13}\mathrm{CO}]} \times \frac{I_{^{13}\mathrm{CO}}}{1 - e^{-5.29/T_{\rm ex}}}, \end{aligned} \tag{2.11}$$

where τ is the optical depth of ^{13}CO, $\frac{[\mathrm{H_2}]}{[^{13}\mathrm{CO}]}$ is the inverse of ^{13}CO abundance, $I_{^{13}\mathrm{CO}}$ is intensity of ^{13}CO in K km s^{-1}, and $T_{\rm ex}$ is the excitation temperature in Kelvin (Wilson et al., 2009). As seen in the Equation (2.11), the prior knowledge of optical depth, ^{13}CO abundance, and gas (excitation) temperature are required.

The optical depth is estimated by

$$\tau\left(^{13}\mathrm{CO}\right) \approx I_{^{13}\mathrm{CO}} / I_{^{12}\mathrm{CO}}, \tag{2.12}$$

in which ^{12}CO is assumed to be optically thick and ^{13}CO is optically thin (Paglione et al., 2001).

The isotopic abundance ratio $[^{12}\mathrm{C}]/[^{13}\mathrm{C}]$ is ≈ 30 – 50 measured for the galactic center of IC 342 (Henkel et al., 1998, Henkel & Mauersberger, 1993). Given that $[^{12}\mathrm{C}]/[^{13}\mathrm{C}]$

= $[^{12}CO]/[^{13}CO]$ (e.g., Espada et al. (2010)) and the $[^{12}CO]/[H_2]$ is about (5 – 8) × 10^{-5}, we adopt a constant $[^{13}CO]/[H_2]$ as 1.5×10^{-6} in all interested regions. The value is consistent with the mean ^{13}CO abundance seen in the Galactic star forming clouds (Pineda et al., 2008, 2010).

The gas temperature is also required to obtain the column density of H_2. The assumption that *the gas temperature (T_g) is equal to the dust temperature (T_d)* is made. Then, the dust/gas temperature can be yielded by the infrared SED.

The SED is constructed with the 24μm observations by Spitzer (§2.5.3) and the 70 – 500μm observation of Herschel (§2.5.4). All images are converted to the unit of Jy , then convolved to the lowest resolution among the images, i.e. the FWHM = 37″ of Herschel 500 μm map. The method of convolution kernels between Spitzer and Herschel images is described in Aniano et al. (2011). We use the kernels and the IDL procedure `conv_image` (Gordon et al., 2008) to convolve the images. Then a two component Plank distribution

$$D = C_w \left[\lambda^{-2} B_\nu (T_w)\right] + C_c \left[\lambda^{-\beta_c} B_\nu (T_c)\right] \tag{2.13}$$

is assumed as the shape of SED, where B_ν is Planck function, T_w and T_c are temperature for the warm and cold component, respectively, C_w and C_c are the scaling constant of each component (Galametz et al., 2012). Moreover, the Planck functions are modified by the dust emissivity index β. For the warm component, the warm dust emissivity index (β_w) is fixed at 2 as suggested by Li & Draine (2001). On the other hand, the cold dust emissivity index (β_c) is one of free parameters to fit. The β_c is in the range of 1 – 3, so the program is forced to find the best value of β_c in this range. To sum up, there are five free parameters to fit: C_w, C_c, T_w, T_c, and β_c. Finally, the IDL function `MPCURVEFIT` (Markwardt, 2009) is used to carry out a Levenberg–Marquardt least–squares fit of the data. For the reason that the images have final resolution significantly lower than our CO maps, SEDs for the global (center + arm), galactic center and arm are obtained with the total flux in each defined region in Figure 2.9, instead of a pixel-by-pixel fitting. The SEDs are displayed in Figure 2.15. The derived β_c is in the typical range of 2.0 – 2.4. The galactic center has higher temperature in both warm and cold components (warm: 64.7 ± 1.6 K, cold: 25.1 ± 0.4 K) than those of the spiral arm (warm: 56.3 ± 1.1 K, cold: 19.0 ± 0.5 K). The global SED represents the average of the center and disk with T_w = 62.1 ± 1.3 K and T_c = 23.7 ± 0.8 K. Galametz et al. (2012) derive $19\,K < T_c < 25\,K$ and $55\,K < T_c < 63\,K$ in 11 nearby galaxies with similar method and data set. The temperatures of IC 342 is compatible with other galaxies.

The cold dust component is associated with the dust, molecular and atomic hydrogen clouds mostly heated by the interstellar radiation field (ISRF). On the other hand, the warm dust component is heated up by the OB stars in HII regions (Bernard et al.,

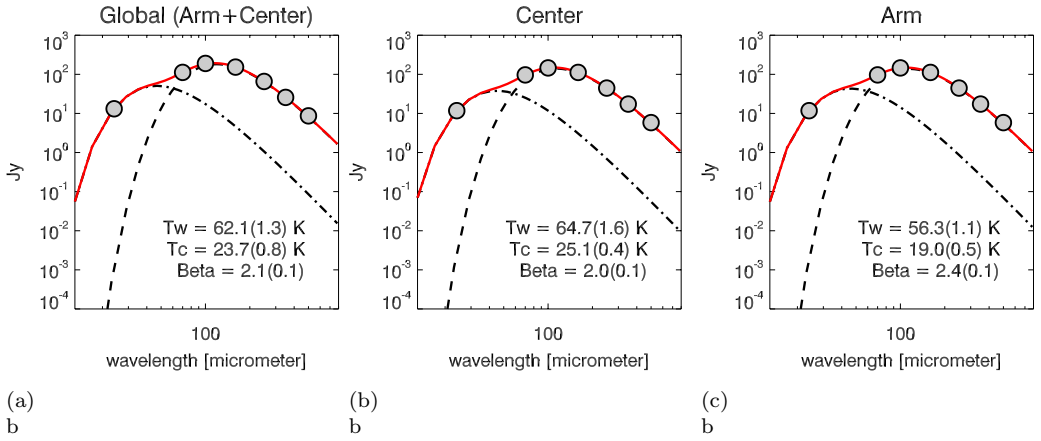

FIGURE 2.15: Infrared SEDs in log–log scale. The global (center + arm) SED is shown in the Left, the central and arm SEDs are displayed in the Middle and Right, respectively. The black circles are the observed data points. The dash-dotted and dashed curves are the derived Planck distribution of the warm and cold components, respectively. The red curve is the sum of two components. The derived $T_{\rm w}$, $T_{\rm c}$, and $\beta_{\rm c}$ are presented in each panel.

2010, Cox, 1989, Popescu et al., 2002). Accordingly, $T_{\rm c}$ (∼25 K for the center and ∼19 K for the arm) is substituted into Equation (2.11) to derive $\Sigma_{\rm H_2}$ based on ^{13}CO. The resulting $\Sigma_{\rm H_2}$ lie within 23 – 485 $M_\odot$ pc^{-2}. The mean $\Sigma_{\rm H_2}$ is 90 $M_\odot$ pc^{-2}. The mean $\Sigma_{\rm H_2}$ obtained by ^{13}CO is significantly larger than those from ^{12}CO (§2.7) because the observations and the selection of available pixels is biased to the CO bright region due to the weak intensity of ^{13}CO.

$\Sigma_{\rm H_2}$ obtained from the ^{12}CO($X_{\rm CO,v}$) and ^{13}CO are compared in Figure 2.16. Only the corresponding pixels in ^{12}CO map with significant ^{13}CO detection (Figure 2.9 right panel) are selected to compare. The central and arm region are displayed with purple and orange crosses, respectively. $\Sigma_{\rm H_2}$ derived from both lines are consistent at which $\Sigma_{\rm H_2}$ ⩾100 M$_\odot$ pc^{-2}. Such high $\Sigma_{\rm H_2}$ is dominated by the central region of the galaxy.

However, $\Sigma_{\rm H_2}$ acquired from ^{13}CO is smaller than that from ^{12}CO at $\Sigma_{\rm H_2} \lesssim 100$ M$_\odot$ pc^{-2}. It can be seen from Figure 2.16 that the low $\Sigma_{\rm H_2}$ is governed by the spiral arm. The deviation of $\Sigma_{\rm H_2}$ between two lines can be attributed to the overestimation of the ^{13}CO abundance by adopting the central value to anywhere outside the center. The uncertainty of ^{13}CO abundance will be discussed in the next section (§2.9.2). Nevertheless, we should note that in the spiral arm, ^{12}CO and ^{13}CO peaks do not coincide with each other (see Figure 2.9). Therefore, it is not necessary to expect a consistent result from these lines. Since the dynamic range of the data with $\Sigma_{\rm H_2} \lesssim 100$ M$_\odot$ pc^{-2} is small, the data at this regime does not significantly affect the result of the slope of K–S law (It will be shown later on in §2.10.2.2).

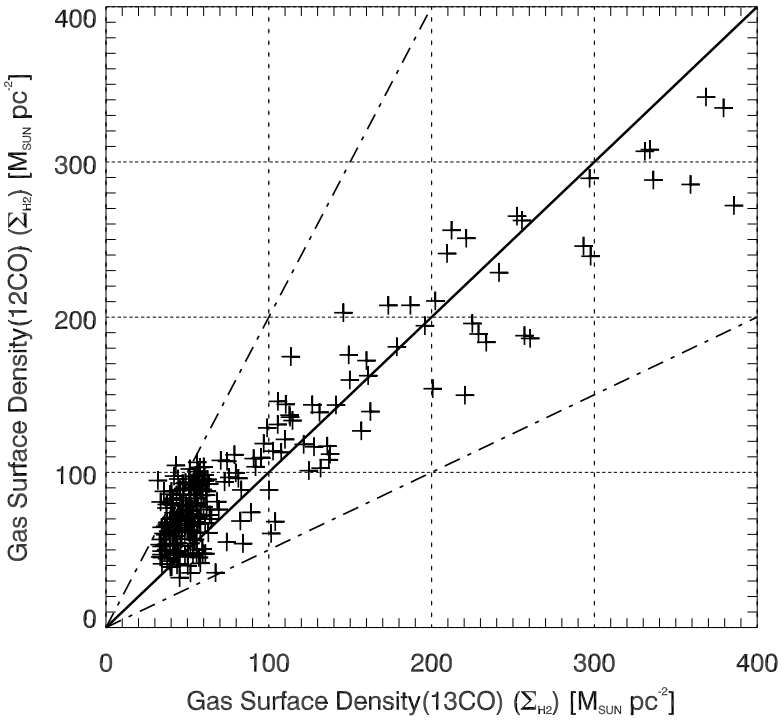

FIGURE 2.16: Σ_{H_2} derived from ^{12}CO with $X_{CO,v}$ versus Σ_{H_2} derived from ^{13}CO. The black solid line indicates the slope of unity. The upper and lower dashed lines are the slope of 2.0 and 0.5, respectively. The two green lines identify 100 $M_\odot$ pc^{-2} in both axes.

2.9 Uncertainties of Σ_{H_2}

2.9.1 Uncertainty of Radial Oxygen Abundance

To obtain Σ_{H_2} map based on ^{12}CO, the gradient of oxygen abundance is required. The emission lines of HII regions spanning a large fraction of the galactic disk is needed to construct the metallicity gradient of a galaxy. The relevant studies have demonstrated that the metallicity (12+[O/H]) is a function of galactocentric radius in spiral galaxies, although the slopes can vary between positive and negative (Werk et al., 2011). For IC 342, only 5 HII regions are observed to infer the metallicity gradient (McCall et al., 1985). It seems that the gradient is affected by the number of HII regions observed. Moustakas et al. (2010), however, derive the gradient of metallicity with 8 HII regions for NGC 6946, classified as SAB(rs)cd as IC 342, and the result is consistent with Cedrés et al. (2012), who observed >200 HII regions in the galaxy. The comparison evidences that the variation of oxygen abundance is in global scale and the local fluctuation is not significant. The uncertainty of $X_{CO,v}$ comes from the measurement of oxygen abundance is ∼30%.

2.9.2 Uncertainty of ^{13}CO abundance

The isotopic ratio [^{12}C]/[^{13}C] increases with radius in our Galaxy (Milam et al., 2005). However, due to the lack of abundance ratio along the galactocentric radius of IC 342, a constant ^{13}CO abundance measured at the center is adopted for whole interested region in this work.

^{13}C is produced during the CNO cycles of stars. In active star forming region, e.g., galactic center, ^{13}C is produced faster, which influences the interstellar isotope abundances. There are two subsequent mechanisms changing the ^{13}CO abundance once it is formed: fractionation reaction and photodissociation. The fractionation reaction $^{13}C^{+} + ^{12}$ CO $\rightarrow ^{13}$ CO $+ ^{12}$ C^{+} enriches ^{13}CO but requires relatively low temperature ($<$ 35K) (Watson et al., 1976) and UV photons to provide the ionized carbons, preferentially happening near the UV-exposed edges of GMCs. However, UV photons cause the photodissociation of both ^{12}CO and ^{13}CO as well ($CO + h\nu \rightarrow C + O$). Since self-shielding is more effective for H_2 than CO lines, the photodissociation can reduce the ^{12}CO and ^{13}CO abundances relative to H_2. In addition, since ^{12}CO has more effective self-shielding and larger abundance, the photodissociation destroys ^{13}CO faster than ^{12}CO. Combining both phenomena, the abundance of ^{13}CO depends on the relative rate of the fractionation and photodissociation.The combined effect can be small and compensate with each other (Keene et al., 1998), or leads to the underestimation of Σ_{H_2} by 30%–50% (Goldsmith et al., 2008, Wolfire et al., 2010). Provide that the [^{12}C]/[^{13}C] (or [^{12}CO]/[^{13}CO] as we have assumed) has a slope of gradient same as our Galaxy (Milam et al., 2005), the isotopic ratio then increases from $\sim$40 at the galactic center to $\sim$50 at the spiral arm at 2 kpc. This deviation of isotopic ratio is smaller than the uncertainties suggested by the above chemical processes. We have insufficient information to quantify the actual error. A maximum error of 50 % contributed from the uncertainty of ^{13}CO abundance is quoted to this work, but such large uncertainty is unlikely true if the abundance gradient is similar to that of Milky Way.

Finally, the ^{12}CO abundance can also range widely depending on the physical condition of the gas. The [^{12}CO]/[H_2] is about 10^{-4} derived from millimeter and radio observations of CO and in Galactic GMCs, but it can be as low as 10^{-8--6} in diffuse gas or the translucent gas around dissociating photons (Sonnentrucker et al., 2007).

2.9.3 Uncertainty of Gas/Dust Temperatures

The interaction and energetics of gas and dust are complex. In terms of simulations, Yao et al. (2006) made a starburst models to correlate the observed FIR/submm/mm

properties of gas and the star formation history of starburst galaxy. The model predicts that T_g is close to T_d in high column density regions. Goldsmith (2001) use LVGs model to calculate the radiative transfer of the cooling and heating of gas and dust.The result shows that in the high density region with $n \geq 10^{4.5}$ cm^{-3} the gas and dust grains become well-coupled and $T_g \approx T_d$. Recent works have also suggested a similar threshold of 10^4 cm^{-3}(Martel et al., 2012, Narayanan et al., 2011) for well coupling T_g and T_d. The critical density of ^{13}CO is $\sim 10^3$ cm^{-3}, tracing the gas with density $> 10^3$ cm^{-3}. ^{13}CO is useful to locate the dense cores embedded in GMCs (McQuinn et al., 2002), which have typical density of $\sim 10^{4-7}$ cm^{-3} (e.g., Bergin et al. (1996), Pirogov et al. (2003)), and therefore it is not surprised to see ^{13}CO coexists with 24 μm emission in both spiral arm and the center of IC 342 (Hirota et al., 2010).

The infered dust/gas temperature from SED fitting is $\sim 20 - 25$ K in the infrared bright galaxy IC 342. Although the temperature is consistent with the temperature of the cloud complexes in other infrared bright galaxy (Rebolledo et al., 2012), the Galactic GMCs have typical temperature ~ 10 K, which is $\sim$2 times lower than that of these infrared bright galaxies. Nonetheless, it is unclear whether the external galaxies, espeially the infrared bright galaxies, hold the similar gas properties as in our Milky Way (e.g., Henkel et al. (1998)).

2.10 K–S Law in IC 342

Since ^{12}CO is detected throughout the entire galaxy (Figure 2.8), the map is first used to conduct the K–S plot by using the Σ_{H_2} based on X_{CO} and $X_{CO,v}$.The fitting of the K–S plot is dominated by the area with $\Sigma_{H_2} \ll 100$ M$_\odot$ pc^{-2} due to the bulk of data points in this range. We therefore refer to the results as *the K–S law at the low* Σ_{H_2} *region*. On the contrary, considering the fact that ^{13}CO was only observed toward the CO bright regions, the K–S plots made with ^{13}CO and the corresponding ^{12}CO pixels are referred to as *the K–S law at the high* Σ_{H_2} *region*.

Since the fitting procedures can alter N (the power of Σ_{H_2}) of K–S law (Cedrés et al. (2012) and references therein), the routines we employed are described below. The `IDL` routine `MPFIT` (Markwardt, 2009) is used to implement all the fitting of K-S plots in this work. Similar as the `MPCURVEFIT` in §2.8, `MPFIT` allows a user-defined function, then performs Levenberg-Marquardt least-squares minimization for the dataset. We fitted the data with a single power law, i.e., $y = Nx + A$, where $y = \log_{10}(\Sigma_{SFR})$, $x = \log_{10}(\Sigma_{H_2})$, N is the slope of K–S plot and A is a constant. Since both Σ_{H_2} and Σ_{SFR} contain measured uncertainties, a model function `LINFITEX` from the `MPFIT` library is utilized.

`LINFITEX` is developed to handle a linear fitting to the data with uncertainties at both directions, following the methodology of *Numerical Recipes*.

2.10.1 K–S Law at the Low Σ_{H_2} Regions

2.10.1.1 K–S Plot with X_{CO}

The K–S law is examined with Σ_{H_2} derived with the Galactic standard X_{CO} in §2.7.1 and the SFR from Equation (2.7) (The 24 μm image has been re-gridded to the same spacing and the resolution as the ^{12}CO map in §2.6.2). The K–S plot is shown in the left panel of Figure 2.17. Gray, red, orange, yellow, and green indicate the contours of 1, 10, 40, 65, and 100 data points per 0.1 dex-wide cell of both Σ_{H_2} and Σ_{SFR} respectively. Fifty percent of the data points are inside the yellow area with $\Sigma_{H_2} \approx 15$ (sensitivity limit) – 40 $M_\odot$ pc^{-2}. Thus the result is controlled by the low Σ_{H_2} region. The slope of the K–S plot (N) is 1.11 $\pm$ 0.02.

Bigiel et al. (2008) made the K–S plots for seven nearby spiral galaxies by the same method but with ^{12}CO (2–1), assuming a constant ratio of ^{12}CO (2–1)/(1–0). Σ_{H_2} in their samples mostly lie in the range of 3–50 $M_\odot$ pc^{-2}. The lower end of Σ_{H_2} in Bigiel et al. (2008) is smaller than ours due to the better sensitivity. The samples in Bigiel et al. (2008) have physical resolution of 750 pc, about two times larger than ours. Previous works show that the physical resolution can affect N of K–S law owing to the evolution of GMCs. In small scale ($\sim$ 60 pc – 100 pc), the discrete star forming systems have different evolutionary stages. For example, youngest GMCs have no star formation but large amounts of molecular gas (large Σ_{H_2}, low Σ_{SFR}), while old GMCs have opposite situation (small Σ_{H_2}, large Σ_{SFR}). These populations then scatter the K–S relation (Onodera et al., 2010). Our resolution of 320 pc and the 750 pc of Bigiel et al. (2008) are considerably larger than the physical size of GMCs; therefore the above mentioned situation does not exist. Instead, K–S law represents a time-averaged relation, averaging many elements with various evolutionary stages and thus the scaling relation of Σ_{H_2} and Σ_{SFR} can be kept (Feldmann et al., 2011, Schinnerer et al., 2010).

N of 1.11 $\pm$ 0.02 in IC 342 is comparable to the average slope of 1.0 $\pm$ 0.2 among the galaxies in Bigiel et al. (2008). N of unity implies that the gas depletion time (τ_{dep}) and SFE are independent of Σ_{H_2}. τ_{dep} of IC 342 is about 2 $\times$ 10^9 yr, or SFE $\sim$ 5 $\times$ 10^{-10} yr^{-1} (Figure 2.17 left panel).

In conclusion, based on the comparison with the larger sample in Bigiel et al. (2008), we suggest that the relation of gas and star formation properties in IC 342 are not considerably different from other galaxies. However, we should note that in addition

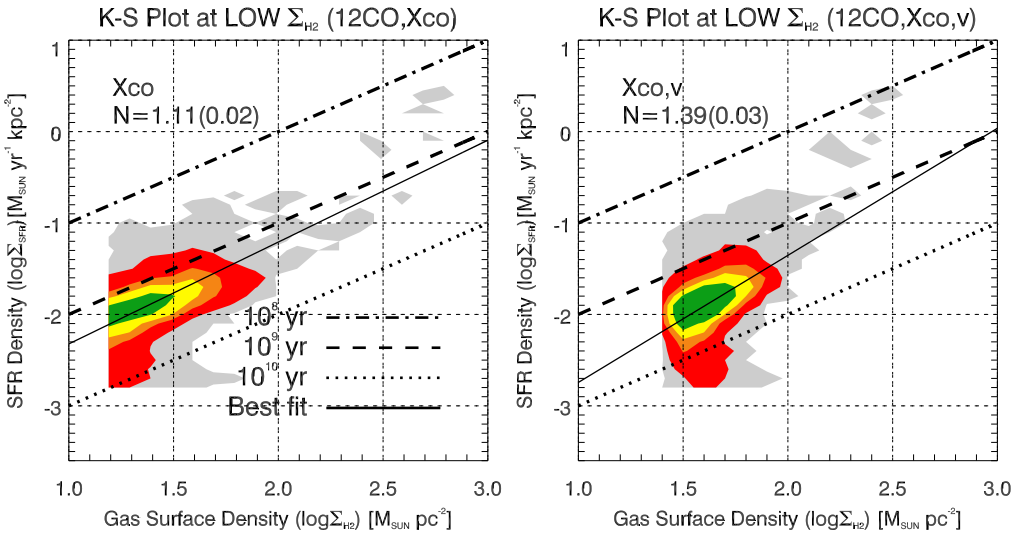

FIGURE 2.17: K–S plot at low Σ_{H_2} regions derived from ^{12}CO. Left: K–S plot with X_{CO}. Grey, red, yellow, and green correspond to the contours of 1, 10, 40, 65, and 100 data points per 0.1 dex-wide cell of both Σ_{H_2} and Σ_{SFR} axises, respectively. 50% of data points locate inside the yellow region. The best fit has slope of 1.11 ± 0.02 shown as solid black line. The three parallel lines denote the SFE of 10^{-8}, 10^{-9}, and 10^{-10} yr^{-1}, corresponding to gas depletion time of 10^8, 10^9, and 10^{10} yr. The green vertical line marks the Σ_{H_2} = 100 $M_\odot$ pc^{-2}. Right: K–S plot with $X_{CO,v}$. The color of contours and the lines are same as in left panel. 50% of data points locate inside the green region. The slope of best fit is 1.39 ± 0.03.

TABLE 2.3: The slopes of K–S law derived in §2.10 and 2.11

	^{12}CO (X_{CO})	^{12}CO ($X_{CO,v}$)	^{13}CO
IC 342			
low Σ_{H_2} (all data)	1.11 ± 0.02	1.39 ± 0.03	...
high Σ_{H_2} (all data)	1.33 ± 0.02	1.94 ± 0.11	1.78 ± 0.07
high Σ_{H_2} (> 100 $M_\odot$ pc^{-2})	1.96 ± 0.16	2.65 ± 0.22	2.27 ± 0.21
Spiral Galaxies (exclude IC 342)			
low Σ_{H_2} (disk)	0.96 ± 0.06	1.35 ± 0.07	...
high Σ_{H_2} (starburst)	1.88 ± 0.14	2.32 ± 0.13	...

to the influence from the intrinsic properties of GMCs (Feldmann et al., 2011, Onodera et al., 2010), Cedrés et al. (2012) suggest that the configuration of GMCs and stars can affect N of star formation law when observations are made with ∼kpc resolution. Under this physical resolution, the distribution of molecular gas is spatially resolved but individual GMCs are not. As a result, the observed N is a convolution of intrinsic star formation mode, cloud mass spectrum in the sampled area, volume filling factor, and the region size (physical resolution) (Cedrés et al., 2012). These parameters may change among individual galaxies. In general, N would decrease when the physical resolution increases, although we did not see the significant change among IC 342 and the samples of Bigiel et al. (2008).

2.10.1.2 K–S Plot with $X_{\rm CO,v}$

We made the K–S plot in same way as in §2.10.1.1 but using $X_{\rm CO,v}$ instead. The result is displayed in the right panel of Figure 2.17. The color scale is same as in §2.10.1.1. Fifty percent of the data points are located inside the green region ranging from 25 – 60 $M_\odot$ pc^{-2}. The figure shows that the relation between $\Sigma_{\rm H_2}$ and $\Sigma_{\rm SFR}$ is steepened. The derived N is 1.39 $\pm$0.03. Because of the superlinear relation, $\tau_{\rm dep}$ and SFE are no longer constant. Specifically, $\tau_{\rm dep}$ declines with increasing $\Sigma_{\rm H_2}$, namely, SFE rises when $\Sigma_{\rm H_2}$ increases.

Since the fitting is dominated by the bulk of the data points at low $\Sigma_{\rm H_2}$ (about 25 – 60 $M_\odot$ pc^{-2}). The high surface density regions with $\Sigma_{\rm H_2} > 100$ $M_\odot$ pc^{-2} are located beyond the best fit, suggesting a steeper trend.

2.10.2 K–S Law at High $\Sigma_{\rm H_2}$ Regions

In this section we study the K–S law in the area with high $\Sigma_{\rm H_2}$. ^{13}CO selects the region with high $\Sigma_{\rm H_2}$ because 1) ^{13}CO is a weak line, and thus ^{13}CO is biased to high $\Sigma_{\rm H_2}$ regions, and 2) owing to its higher critical density, ^{13}CO is one of transitions available for locating the dense cores in GMCs. These dense cores have higher column density ($\Sigma_{\rm H_2}$) and volume density prepared for the future star formation.

In Figure 2.9 right panel, the pixels with ^{13}CO detection greater than 5σ are masked with color. These pixels are used to derive K–S plot based on ^{13}CO.

2.10.2.1 K–S plot Based on ^{13}CO

With the surface density derived in §2.8, K–S plot in terms of ^{13}CO is displayed in Figure 2.18. In this domain, $\Sigma_{\rm H_2}$ ranges from about 30 $M_\odot$ pc^{-2} – 400 $M_\odot$ pc^{-2}. $\tau_{\rm dep}$ (or SFE) changes by more than one order magnitude over this range, from $\sim 1.5 \times 10^9$ yr at $\Sigma_{\rm H_2} \approx 30$ $M_\odot$ pc^{-2} to 10^8 yr at $\Sigma_{\rm H_2} \approx 400$ $M_\odot$ pc^{-2}. N of the K–S plot is derived as 1.78 $\pm$ 0.07.

The best fit of low $\Sigma_{\rm H_2}$ region based on ^{12}CO ($X_{\rm CO,v}$) is over-plotted in Figure 2.18. It can be seen that $\Sigma_{\rm SFR}$ of high $\Sigma_{\rm H_2}$ regions lie beyond the best fit of low $\Sigma_{\rm H_2}$ regions, implying a higher SFR at a given $\Sigma_{\rm H_2}$.

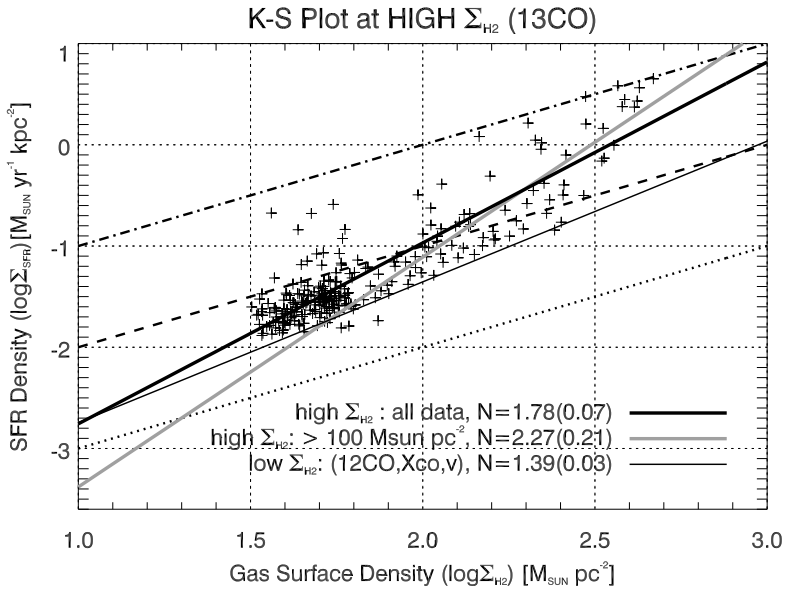

FIGURE 2.18: K–S plot at high Σ_{H_2} region derived from ^{13}CO. The purple crosses denote the galactic center and the orange crosses are for spiral arm. The purple line is the slope of K–S plot of galactic center. The red line is the result of all (arm + center) data points. The parallel black lines denote the SFE of 10^{-8}, 10^{-9}, and 10^{-10} yr^{-1} or the gas depletion time of 10^8, 10^9, and 10^{10} yr, respectively. The green vertical line highlights the $\Sigma_{H_2} = 100$ M$_\odot$ pc^{-2}. The grey shadow indicates the K–S law at low Σ_{H_2} region derived from ^{12}CO based on $X_{CO,v}$ (right panel of 2.17

2.10.2.2 K–S Law at the High Σ_{H_2} Based on ^{12}CO

The corresponding pixels in the ^{12}CO map with significant ^{13}CO emission are used to conduct the K–S plot at high Σ_{H_2} region for the comparison.

First, the K–S plot is made with the Galactic Standard X_{CO}. The result is displayed in the left panel of Figure 2.19. Σ_{H_2} lie between 20 to 800 M$_\odot$ pc^{-2}. N is 1.33 ± 0.02 with all data, slightly larger than the slope at low Σ_{H_2} (^{12}CO, X_{CO}). The K–S plot with $X_{CO,v}$ is shown in the right panel of Figure 2.19. The derived N is approaching 2 (1.94 ± 0.11) with all data points. N derived in this section are larger than those in the environment of low Σ_{H_2}, regardless whether X_{CO} or $X_{CO,v}$ is used. The variation of the power law index of K–S law in this Section is summarized in Table 2.3.

2.10.3 The Environmental Variation of K–S Law

There are two conclusions acquired from the above K-S plots. First of all, the adoption of $X_{CO,v}$ steepens the K–S plots in both low and high Σ_{H_2} regimes. This is reasonable to expect from the difference of X_{CO} and $X_{CO,v}$ (Figure 2.13). Secondly, there is a trend that N would increase with increasing Σ_{H_2}. The steeper slope at higher Σ_{H_2} area is confirmed by the independent measurement of ^{13}CO.

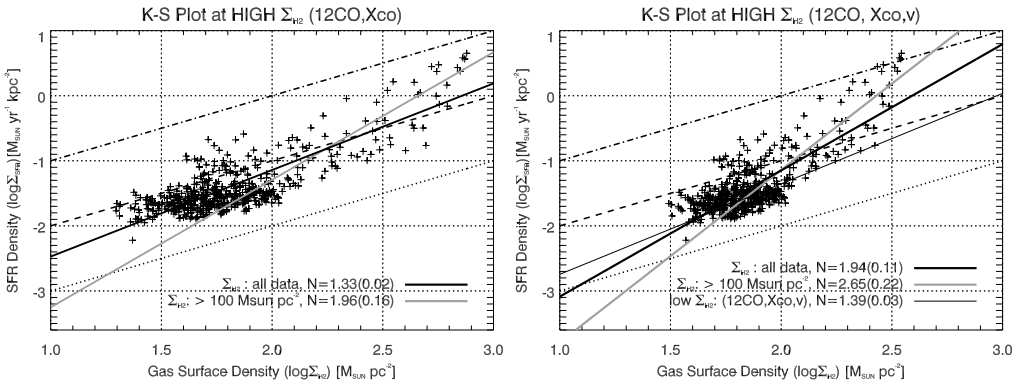

(a) (b)
b b

FIGURE 2.19: K–S plot derived at high Σ_{H_2} regions from ^{12}CO. The color and the lines represent the same meaning as in Figure 2.18. Left: K–S plot based on X_{CO}. For comparison, the result of K–S plot derived at the low Σ_{H_2} region with X_{CO} is overlaid with grey shadow (left panel of Figure 2.17). Right: K–S plot at high Σ_{H_2} based on $X_{CO,v}$. The grey shadow denotes the K–S law at the low Σ_{H_2} region based on $X_{CO,v}$ (right panel of Figure 2.17

A quantitative analysis of the dependence of N on the Σ_{H_2} considered is displayed in Figure 2.20. Figure 2.20 displays the derived N with a different lower threshold of the used data. Only the data greater than the defined threshold of Σ_{H_2} are used. In other words, the dynamic range of fitting is narrowed down from *all data* to $\Sigma_{H_2} > 130\ M_\odot\ pc^{-2}$, with intervals of $>$ 60, 100, and 130 $M_\odot$ pc^{-2}. The analysis was performed on three datasets, ^{12}CO (X_{CO}), ^{12}CO ($X_{CO,v}$), and ^{13}CO. Even though N with higher thresholds suffer from large uncertainties because of the scatter of measurements and limited data points, there is a clear trend that the slopes rise with an increasing threshold. In the low-Σ_{H_2} region (squares), N is generally less than two. In the environment of $\Sigma_{H_2} >$ 100 $M_\odot$ pc^{-2}, N increases to around two to three. Such a phenomenon is observed in both transitions.

Various studies have concluded that the SFR is well correlated with the amount of dense gas. The most straightforward evidence is the linear correlation between L_{IR} and L'_{HCN}. The correlation is seen from Galactic dense cores to extragalactic unresolved sources (Gao & Solomon, 2004a, Wu et al., 2005). Simulations of turbulent molecular clouds show that the SFR is controlled by the density probability distribution function (PDF) (e.g., Kravtsov (2003), Wada & Norman (2007)). The galactic turbulent can be driven by gravitational instability, shocks or interaction of galaxies. Kravtsov (2003) simulates the PDF of different gas surfaces density across $\sim$ 20 – 2000 $M_\odot$ pc^{-2}. The result shows that the fraction of dense gas (i.e., sufficiently dense for star formation) increases with gas surfaces density (see Figure 3 of Kravtsov (2003)). Such trend shown by the simulations has already been observed in the molecular clouds of our Milky Way (e.g.,

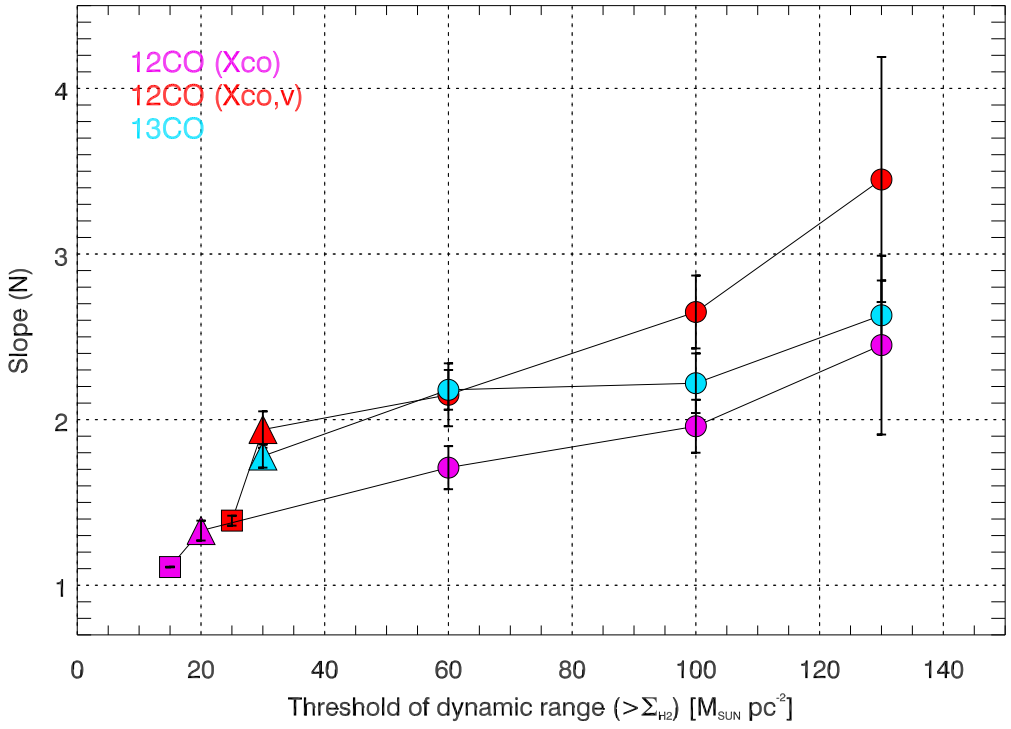

FIGURE 2.20: Dynamical range of fitting versus the K–S slopes (N). The data points with color of magenta, red, and cyan represent the Σ_{H_2} from ^{12}CO (X_{CO}), ^{12}CO ($X_{CO,v}$), and ^{13}CO, respectively. The results used all available data in the dataset of low and high Σ_{H_2} are presented in squares and triangles, respectively. The x-axis for these *all data* points correspond to the detection limits. The circles denote the results with various thresholds.

Kainulainen et al. (2009)). Hence, the larger N in the higher Σ_{H_2} regime indicated by low density tracers (e.g., CO) may be a reflection of the increasing dense gas fraction.

2.11 Comparisons with Other Galaxies

The results of IC 342 show that the K–S law may not be identical within a galaxy, namely, the slope steepens up toward the high Σ_{H_2} region, reflecting a shorter gas depletion time (or higher SFE) and perhaps a different star formation mechanism. We examine whether the results of IC 342 are particular to this galaxy or a general situation by using published data of some nearby galaxies.

There are two selection criteria for sample galaxies. At first, the galaxy has to be studied in terms of the metallicity based on the framework of the P-method (Pilyugin, 2000, 2001a,b, Pilyugin & Thuan, 2005). The candidates reaching this criterion are shown in Pilyugin et al. (2004) and Moustakas et al. (2010). Pilyugin et al. (2004) and Moustakas et al. (2010) derive the metallicity gradient with HII regions for their sample galaxies. Moustakas et al. (2010) also derive the metallicity of the nuclear and circumnuclear

regions for some of their samples. Secondly, the galaxy has to be studied in Σ_{H_2} and Σ_{SFR}. The Σ_{H_2} and Σ_{SFR} data are compiled from literature and divided into two groups. The first group includes ten galaxies with published radial Σ_{HI}, Σ_{H_2}, and Σ_{SFR} from Leroy et al. (2008).The physical resolution of the observations is ∼800 pc. Σ_{H_2} and Σ_{SFR} with $>3\sigma$ detection are used. Furthermore, to fairly compare with IC 342, only the radii with $\Sigma_{H_2}>\Sigma_{HI}$ are used, i.e., the H_2 dominated regions. With the above two criteria, some data points at the outskirts of the galaxies are eliminated. The galaxies (NGC 628, NGC 3184, NGC 3198, NGC 3351, NGC 3521, NGC 4736, NGC 5055, NGC 5194, NGC 6946, and NGC 7331) in the first group will be used as the samples of *galactic disks* with lower Σ_{H_2}. The second group comprises nine *starburst galaxies* from Kennicutt (1998), representing the high Σ_{H_2} domain. Most of starburst samples have CO observations with sub-kpc resolution towards their circumnuclear disks. At such active star forming regions, it is reasonable to assume $\Sigma_{H_2} \gg \Sigma_{HI}$ as seen in the center of IC 342. The metallicity of the starburst samples are from either the 'circumnuclear' metallicity in Moustakas et al. (2010), or the extrapolation of the gradient toward the center from Pilyugin et al. (2004). The second group contains NGC 253, NGC 1097, NGC 2093, NGC 3034, NGC 3351, NGC 4736, NGC 5194, NGC 5236, and NGC 6946.

The K–S laws are examined based on the Galactic Standard X_{CO} and $X_{CO,v}$ calculated from the ^{12}CO intensity and the metallicity. The results are shown in Figure 2.21. N for *disk*, low Σ_{H_2} samples with X_{CO} (green circles) is 0.96 ± 0.06 and 1.35 ± 0.07 for the same samples but using $X_{CO,v}$ (red circles). Both values are consistent with the slopes of IC 342 at low Σ_{H_2} regime (1.11 ± 0.02 and 1.39 ± 0.03, respectively).

For the circumnuclear starbursts, Σ_{H_2} are greater than 100 $M_\odot$ pc^{-2}, no matter X_{CO} or $X_{CO,v}$ is used. N are 1.88 ± 0.14 and 2.32 ± 0.13 by using the X_{CO} and $X_{CO,v}$, respectively. Both numbers are in good agreement with the N derived from IC 342 with threshold of 100 $M_\odot$ pc^{-2}, i.e., N = 1.96 ± 0.16 and 2.65 ± 0.22 for Σ_{H_2} (^{12}CO, X_{CO}) and Σ_{H_2} (^{12}CO, $X_{CO,v}$), respectively. (The slopes in this Section are summarized in Table 2.3 as well). Thus, we then have a certain level of confidence that the results of IC 342 is not particular but universal for nearby spiral galaxies. The similar trend was found in M51 by Nakai et al. (1991).

2.12 Star Formation Mechanisms

The slope of K–S plot depends on the mechanisms of star formation as mentioned above. We discuss two possible mechanisms of star formation in IC 342, the gravitational instability and cloud-cloud collisions, as well as the theoretical aspects of changing the power law index of K–S law due to GMCs properties.

	R25(′)	Gradient (dex/R25)	$12+[O/H]_0$	ref.
NGC 628	5.24	-0.27±0.05	8.43±0.02	1, 3
NGC 3184	3.71	-0.46±0.06	8.65±0.02	1, 3
NGC 3198	4.26	-0.50±0.14	8.49±0.04	1, 3
NGC 3351	3.71	-0.28±0.04	8.69±0.01	1, 3
NGC 3521	5.48	-0.16±0.33	8.44±0.05	1, 3
NGC 4736	5.61	-0.33±0.18	8.40±0.01	1, 3
NGC 5055	6.30	-0.63±0.29	8.59±0.07	1, 3
NGC 5194	5.61	-0.31±0.06	8.64±0.01	1, 3
NGC 6946	5.74	-0.17±0.15	8.45±0.06	1, 3
NGC 7331	5.24	-0.24±0.35	8.41±0.06	1, 3
Circumnuclear Starburst				
		$12+[O/H]_0$		ref.
NGC 253		8.71±0.10		2, 4
NGC 1097		8.57±0.07		2, 3
NGC 2903		8.94±0.09		2, 4
NGC 3034		8.46±0.05		2, 3
NGC 3351		8.67±0.04		2, 3
NGC 4736		8.60±0.05		2, 4
NGC 5194		8.92±0.06		2, 4
NGC 5236		8.79±0.07		2, 4
NGC 6946		8.70±0.06		2, 4

TABLE 2.4: The metallicity of nearby galaxies. The first reference of each galaxy is the source of the Σ_{H_2} and Σ_{SFR}. References refer to 1. Leroy et al. (2008) or 2. Kennicutt (1998). The Σ_{H_2} is correct to the conversion factor of 2.3×10^{20} cm^{-2} (K km s^{-2})$^{-1}$. The second reference is for the metallicity, 3. Moustakas et al. (2010), or 4. Pilyugin et al. (2004).

.

2.12.1 Gravitational Instability

For star formation by gravitational instability, it is assumed that a constant fraction of molecular gas will be converted to stars per free fall time. Since

$$t_{\rm ff} = \sqrt{3\pi/32G\rho_{\rm gas}} \text{ and} \tag{2.14}$$

$$\rho_{\rm SFR} \propto \rho_{\rm gas}/t_{\rm ff}, \tag{2.15}$$

where $\rho_{\rm gas}$ and $\rho_{\rm SFR}$ are gas mass and SFR per unit volume, $\rho_{\rm SFR}$ is proportional to $\rho_{\rm gas}^{1.5}$, or

$$\Sigma_{\rm SFR} \propto \Sigma_{\rm gas}^{1.5}, \tag{2.16}$$

assuming that the scale height of gas disk is constant in galaxies. This naturally explains the well-known "disk-averaged" K–S law with a power law index of 1.4 in Kennicutt (1998). Our results of K–S plot of 1.39 ± 0.03 at the low Σ_{H_2} region (§2.10.1) with $X_{\rm CO,v}$

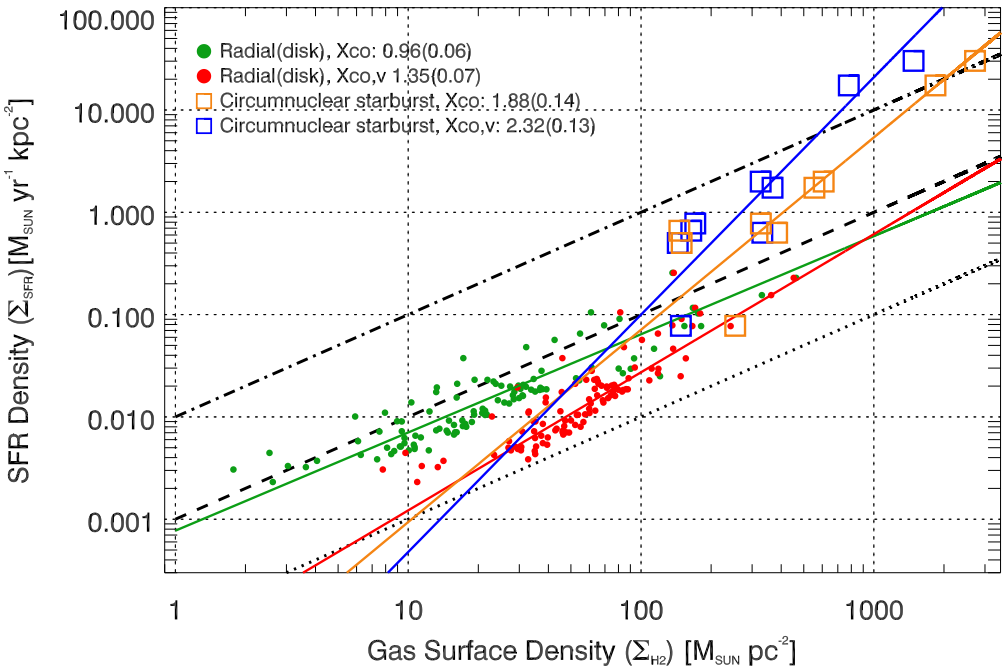

FIGURE 2.21: K–S plot of nearby galaxies (exclude IC 342). The solid lines indicate the fitting results of the data points with same color. Green circles: data from galactic disks with Σ_{H_2} from X_{CO} (Leroy et al., 2008), Red circles: data from galactic disks with Σ_{H_2} from $X_{CO,v}$, Orange squares: data from starburst (SB) centers (Kennicutt, 1998) with Σ_{H_2} from X_{CO}, and Blue squares: data from starburst (SB) centers with Σ_{H_2} from $X_{CO,v}$. The $X_{CO} = 2.3 \times 10^{20}$ cm^{-2} (K km s^{-1})$^{-1}$ is used for the Σ_{H_2} based on Galactic X_{CO}. The resulting slopes of K–S Law are shown in the legend.

is consistent with the slope expected by the theory and simulations of the collapse of molecular cloud through the gravitational instability (Elmegreen, 1994, 2002, Li et al., 2006).

We then investigate the relation between the gravitational instability of gas and star formation in IC 342 via Toomre Q parameter (Toomre, 1964) and 24μm image. Toomre (1964) suggests that the gas can collapse when the Σ_{gas} exceeds the critical density (Σ_{crit}), leading to the Toomre-Q parameter less than unity since

$$Q = \frac{\Sigma_{crit}}{\Sigma_{gas}}, \tag{2.17}$$

where Σ_{gas} is Σ_{H_2+HI}. Σ_{crit} is determined by the epicyclic frequency κ and velocity dispersion σ as

$$\Sigma_{crit} = \frac{\kappa\sigma}{\pi G}. \tag{2.18}$$

The HI map of IC342 was observed by Crosthwaite et al. (2000) with VLA (see §2.5.2). The rotation curve is derived with the Brandt model in Crosthwaite et al. (2000) with the HI data. The maximum velocity ~170 km s^{-1} is located at the radius of ~5 kpc. κ at a radius of r is calculated by $\kappa^2(r) = 2(\frac{v^2}{r^2} + \frac{v}{r}\frac{dv}{dr})$. The map of HI velocity dispersion

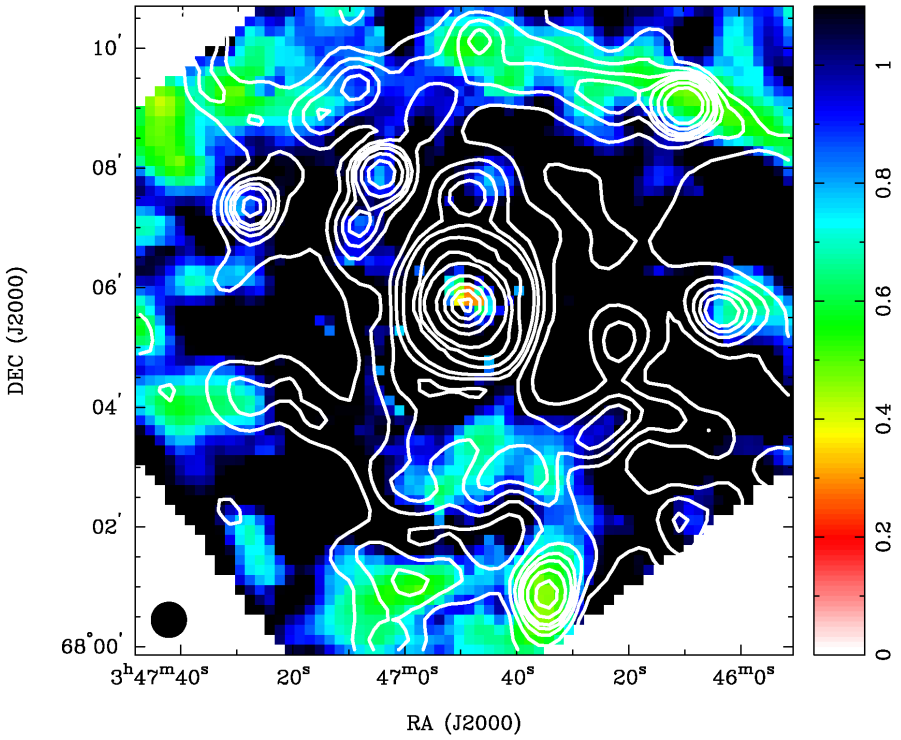

FIGURE 2.22: The map of Tommre Q in color scale overlaid with 24μm image in contours. The wedge indicates the corresponding value of Q parameter to the color. The angular resolution in this map is 38″ to adjust with the HI map made with VLA. The synthesized beam is plotted in the lower left of the figure.

(Crosthwaite et al., 2000) is used to estimate σ in Equation (2.18). σ has range around 7 – 25 km s^{-1}. To fairly derive the total gas mass at each pixel, the ^{12}CO ($X_{\rm CO,v}$) and 24μm images are convolved to the same resolution with HI image (38″ × 37″).

Firstly, the radial distribution of Q parameter is displayed as black solid line in Figure 2.6. The radial profile shows that only the galactic center has Q < 1. Outside the galactic center, the average Q parameter varies around 1 – 2. Since the gas distribution of IC 342 is not symmetric at each position angle of the galaxy, the radial distribution may smooth the real distribution of Q parameter. For this reason, we then conduct the spatial distribution of Q. Figure 2.22 shows the spatial distribution of Toomre Q parameter in color scale overlaid on the 24μm image in contours. The region prone to collapse are shown in color. The innermost region of the galaxy, bar end and several knots in spiral arms have Q = 0.5-0.8. The region where Q < 1 is in agreement with the peaks of 24μm, indicating that the stars in the disk is likely formed through the gravitational instability there. Indeed, Yang et al. (2007) suggest that >60% of massive young stellar objects are inhabiting in the regions where the gas is unstable.

2.12.2 Star Formation via Cloud-Cloud Collisions

It is known that star formation can occur in the regions with efficient cloud-cloud collisions (Koda & Sofue, 2006, Tan, 2000). The collision time scale is

$$t_{\rm coll} \propto 1/nv\sigma \propto 1/\Sigma_{\rm gas}, \tag{2.19}$$

where n is the number density of clouds, v is the relative velocity of the clouds, and σ is the average cloud cross section. $\Sigma_{\rm SFR}$ per collision time is then proportional to $\Sigma^2_{\rm gas}$. This is consistent with the slope of 2.37 ± 0.26 and 2.13 ± 0.15 acquired with both ^{12}CO (with $X_{\rm CO,v}$) and ^{13}CO in the central region, respectively.

Ho et al. (1982) suggest that there are $\sim$ 100 molecular cores in the central region of IC 342 and the cores are colliding with each other. The origin of the collisions can be attributed to the bar-induced orbital crowding. The shocks produced after the cloud-cloud collisions has been found by shock tracer molecule, e.g., CH_3OH and HNCO (Meier & Turner, 2005). These observations highlight the promoted collisional regions: along the leading side of the bar and the intersections of the bar and the circumnuclear ring (These two regions are located in the defined *center* in Figure 2.9, with size about 1′; Meier & Turner (2005)). Indeed, both regions are associated with Hα, IR/radio star forming regions (Becklin et al., 1980, Hirota et al., 2010, Turner & Ho, 1983). Hence, star formation induced by the cloud-cloud collisions may result to the slope of $\sim$2 as seen in the central region of IC 342.

Even though star formation by cloud-cloud collisions is suggested by previous observations with various lines, the possibility of gravitational instability cannot be ruled out because the Tommre Q parameter is well below unity in the central region of the galaxy (Figure 2.22).The two mechanisms may work together (Rand & Kulkarni, 1990). That is, the gravitationally bound molecular clouds ($\sim 10^7$ M$_\odot$) are formed through the gravitational instability; at the same time, cloud-cloud collisions are taking place between the clouds to form giant molecular cloud associations (GMAs). This scenario is able to explain the high SFE of the spiral arm in M51 (Rand & Kulkarni, 1990). If the above scenario take places in the high-$\Sigma_{\rm H_2}$ region of IC 342, $N = 2 - 3$ in this region represents a mix of the mechanisms.

2.12.3 Star Formation Self-regulation

Self-regulation of star formation is proposed by Ostriker et al. (2010), Ostriker & Shetty (2011), Sherman (2012). The principle idea of the theory is that stellar populations contribute to the dynamical equilibrium of ISM. To satisfy the dynamical equilibrium,

the total pressure at the midplane should equalize the weight of the overlying ISM, that is,

$$P_{\rm tot} = W. \tag{2.20}$$

The total pressure $P_{\rm tot}$ consists of thermal ($P_{\rm th}$) and turbulent ($P_{\rm ter}$) pressures at the regime of 100 – 10000 $M_\odot$ pc^{-2}. Each pressure is proportional to star formation rate in some way. As gas is heated by stars, the thermal pressure would be proportional to the amount of UV photons which controlled by the SFR.

$$P_{\rm th} \propto J_{\rm UV} \propto \Sigma_{\rm SFR} \tag{2.21}$$

The turbulent pressure is also proportional to $\Sigma_{\rm SFR}$ given that the supernova explosion is the main mechanism driving the turbulence in the ISM, thus

$$P_{\rm ter} \propto \Sigma_{\rm SFR}. \tag{2.22}$$

Hence,

$$P_{\rm tot} = P_{\rm th} + P_{\rm ter} \propto \Sigma_{\rm SFR}. \tag{2.23}$$

Based on these ideas, in the then suggest a star formation with a index of 2.0. The result is consist with the observed slope of K–S law at the high-$\Sigma_{\rm H_2}$ regions. They also predict that the self-regulation star formation is effective when $\Sigma_{\rm H_2}$ is greater than 100 $M_\odot$ pc^{-2}, consistent with the critical surface density we found in IC 342 as well as the critical surface density predicted by Komugi et al. (2006).

2.12.4 Critical $\Sigma_{\rm H_2}$ of Different Star Formation Mechanisms

The idea of a transition of different star formation mechanisms is proposed by Komugi et al. (2006). If star formation is dominated by the gravitational instability, the path that a cloud move during its formation of stars, i.e., $t_{\rm ff}v$,where $t_{\rm ff}$ is free-fall time and v is inter-cloud velocity dispersion, should be smaller than the path that they will meet another cloud (mean free path of the cloud, $\lambda_{\rm mfp}$). On the other hand. if $\lambda_{\rm mfp} < t_{\rm ff}v$, then the star formation is dominated by cloud-cloud collisions.

With assumption of inter-cloud velocity and $\Sigma_{\rm H_2}$ of clouds, Komugi et al. (2006) conclude that the critical $\Sigma_{\rm H_2}$ of the two mechanisms occur at about 100 $M_\odot$ pc^{-2}. The value is close to the point where the K–S law start to be steepened in this work.

2.12.5 GMCs Properties and the Star Formation Law

In addition to the difference in the effective star formation mechanism, the K–S law may be altered because of the change in the intrinsic properties of GMCs.

Krumholz et al. (2009) have performed theoretical calculations of a two-component star formation law regardless of the galactic-scale process. The transition of Σ_{H_2} is approximately 85 $M_\odot$ pc^{-2}. In the regions where the Σ_{H_2} is greater than ∼85 $M_\odot$ pc^{-2}, the galactic ISM pressure is sufficiently large to be comparable with the internal pressure of GMCs, and thus the density of GMCs is forced to increase with growing Σ_{H_2} to balance the pressures. At the same time, the free-fall time of the GMCs is reduced (Krumholz et al., 2009), resulting in faster star formation. On the other hand, at low-Σ_{H_2} regions, GMCs are independent of the environment so Σ_{SFR} is determined only by the GMCs themselves, implying a flattened K–S relation.

2.13 Summary of Chapter 2

We studied the Kennicutt-Schmidt (K–S) law in the nearby barred spiral galaxy IC 342 with published ^{12}CO (1–0), ^{13}CO (1–0), and infrared data. The main results are summarized as follows:

- After correcting for the oxygen abundance and ^{12}CO intensity, the ^{12}CO-to-H_2 conversion factor ($X_{CO,v}$) was found to be 2–3 times lower than the Galactic standard X_{CO} in the center of IC 342 and ∼2 times higher than the X_{CO} in the galactic disk (§2.7).
- The power law index of the K–S plot is approximately 1.4 in the low-Σ_{H_2} (^{12}CO,$X_{CO,v}$) regions (often 25 – 60 $M_\odot$ pc^{-2}), and increases to approximately 2 – 3 at high-Σ_{H_2} (^{12}CO,$X_{CO,v}$) regions (around > 100 $M_\odot$ pc^{-2}) (§2.10.1.2, §2.10.2.2). The larger slope in the environment of high surface density is confirmed with independent measurement of ^{13}CO (§2.10.2.1).
- By setting different lower limits of the dynamic range for fitting, we confirmed that the slope of the K–S law is gradually steepened with increasing Σ_{H_2}, presumably as a result of the increase in the dense gas fraction (§2.10.3).
- Using the published data of Σ_{H_2}, Σ_{SFR} (measured at the sub-kpc scale), and the metallicity of nearby galactic disks and starburst centers, we confirm that the environmental variation in the K–S law in IC 342 may be a general case for spiral galaxies (§2.11).

- The varied slopes from ∼1.4 in the low-Σ_{H_2} domain to $\sim 2-3$ in the central region may indicate the change in the main mechanism of star formation among the sub-regions in IC 342, that is, the star formation is triggered by gravitational instability in the disk; at the galactic center, the combination of gravitational instability and cloud-cloud collisions is favored (§2.12.1 and §2.12.2). The slope of 2.0 observed at the regions of $\geqslant 100$ $M_\odot$ pc^{-2} can be explained by a self-regulated star formation as well (§2.12.3).

- The derived variable K–S law in a single galaxy also matches the theoretical prediction that the GMC properties change at the Σ_{H_2} of approximately 85 $M_\odot$ pc^{-2} and star formation efficiency increases with Σ_{H_2} (§2.12.5).

Chapter 3

The Impact of Galactic Bar on Star Formation

3.1 Introduction

Secular evolution (Kormendy, 1979) is a process that rearranges properties of galaxies, such as angular momentum and mass. While the (fast) evolution can be driven by external environment, galaxy merger for example, secular evolution can be activated by (slow) internal dynamics of galaxies as well, such as disk instabilities. The former is more common in the early Universe, and the slow secular evolution plays an essential role in the local Universe. In this Chapter, I study whether/how secular evolution of galaxy alter star forming activity in a galaxy. The secular evolution refers to galactic bars in this study because galactic bars are the most important structure driving internal evolution of disk galaxies in the nearby Universe (Athanassoula, 2013, Cheung et al., 2013, Coelho & Gadotti, 2011, Gadotti, 2011). They have implication to the presence of spiral arms, rings and pseudobulges.

This chapter is organized as follows. An overview of bar structure and star formation properties in bars are introduced in §3.1. Motivation and methodology of this project are shown in §3.2. §3.3 summarizes the information of the main target NGC 6946. Observations and the combining procedures of single dish and interferometer data are shown in §3.4, following by the results in §3.5. Physical properties inferred by line ratios, LVG calculations, infrared color map and the mass of gas are shown in §3.6. Star forming activity of the interested regions are presented in §3.7, including an azimuthal Kennicutt-Schmidt law. §3.8 illustrates the velocity jumps across the bars in terms of position-velocity diagrams. We make comparisons of resolved GMCs properties among the galactic structures of NGC 6946 in §3.9. Finally, comparisons of GMC properties

of NGC 6946 and other galaxies are discussed in §3.10. Main results of this chapter is highlighted in §3.11.

3.1.1 Bar Structure and Its Roles in Galaxy Evolution

The non-axisymmetric bar produces the flow of gas, that is, gas between the Co-rotation radius (CR) of bar and Inner Lindblad resonance (ILR) is pulled inward. In this area there are two regions where gas tends to pile up: galactic bar and circumnuclear region. Figure 3.1 shows the orbits of gas inside CR. Gas flows are indicated with single headed arrows. Gas travels on elliptical orbits, so-called x_1 orbits. The P.A. of x_1 orbits gradually changes with radii (Figure 3.1). Imaging that the system is rotating clockwise, such a configuration produces orbit crowding at the downstream of the bar, in which gas are pilling up, creating a high-$\Sigma_{\rm gas}$ region (Figure 3.2). Since material are piling up at orbit crowding regions, they are visible as *dust lanes* or *offset ridges* in optical (star light), near-infrared (dust) and radio images (molecular gas) (Figure 3.3(a) and 3.3(b), respectively).

Inside the dust lanes, gas experiences shocks and thus loses angular momentum, falling towards the galactic center. When the gas reaches the ILR (around at the circumnuclear ring; CNR), some of the gas fall to the CNR (or x_2 orbits). This is the second region where gas can quickly accumulate. At the same time, some of the gas are sprayed back out to large radii, encounter another shock at the opposite dust lane, then continue their travel on x_1 orbits. Figure 3.2 shows a simulation of $\Sigma_{\rm gas}$ in a barred galaxy from Regan et al. (1999). Darker area represents higher $\Sigma_{\rm gas}$. As shown in the figure, accumulation of the gas is advanced at the bar and CNR. Figure 3.3(b) shows an example of observed gas distribution of barred galaxy NGC 5430[1]. It is clearly seen that there is a gas concentration at the galactic center (the white cross). Two elongated structures corresponding to dust lane appear beyond the central concentration.

The above theory of gas orbits suggests that galactic bar is playing a role to re-distribute materials on galactic scale. It is not easy to observe the gas orbits, the infalling gas, and the gas infall rate. Even so, theory is supported indirectly by some observational results, such as the shallower abundance gradient and CO distribution within bars (e.g., Kuno et al., 2007, Martin & Roy, 1994). Figure 3.4 shows a plot of abundance gradient as a function of bar strength of $E_{\rm B} = 10(1 - b/a)$, where a and b are major and minor axis of bar (Martin & Roy, 1994). As can be seen, shallow gradients are found in strong bars with large $E_{\rm B}$.

[1]Observations were made with CARMA on July 2013 by Pan et al.

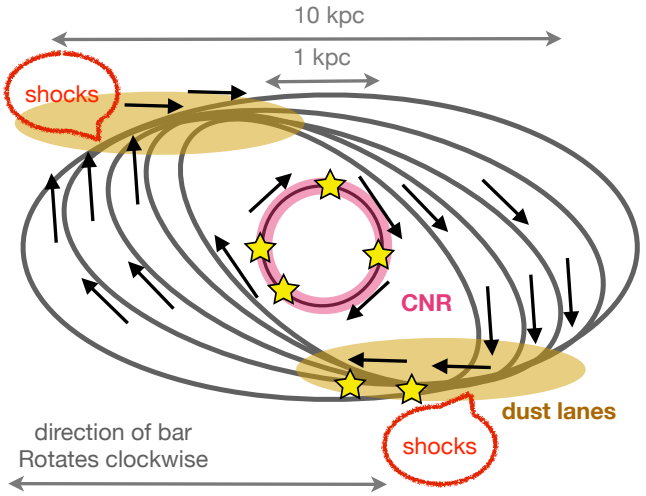

FIGURE 3.1: Theoretical gas orbits in barred galaxy. Colored areas denote the sites where molecular gas are pilling up, yellow for dust lanes and pink for CNR. Direction of gas flows are indicated with single headed arrows. The galaxy is rotating clockwise.

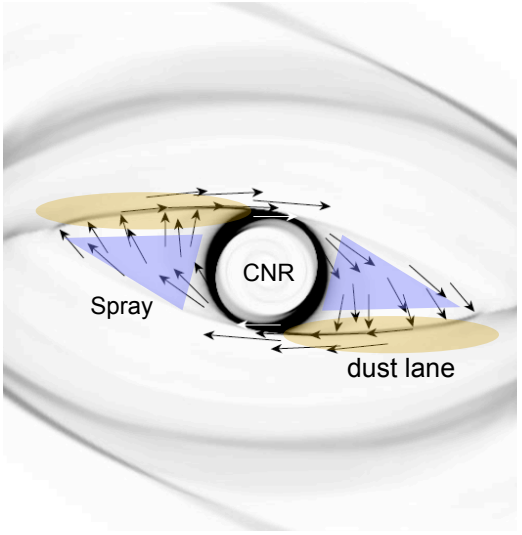

FIGURE 3.2: The gas surface density from hydrodynamic simulation, taken from Regan et al. (1999). The orientation of bar is same as in Figure 3.1. High gas surface density is shown with color black. Direction of gas flows are indicated with single headed arrows. Dust lanes are colored yellow, and the spray regions are colored purple.

Some studies claim that bars are long-live structures and can survive at least 5 Gyr (Berentzen et al., 2007). This idea is supported by recent observations. Analysis with HST data shows that the bar fraction is roughly constant, sustaining as present value out to $z \approx 0.3$ (recent 4 Gyr). During $z = 0.4 - 0.8$ (3 Gyr – 7 Gyr), the fraction of barred galaxies decreases to $\sim 20\%$. Such variation, however, seems to be caused by increase in the fraction of the low mass, blue spiral galaxies; the fraction of bar in massive and luminous spiral galaxies is compatible with the present value out to $z \sim 0.8$ (about recent 7 Gyr) (Sheth et al., 2008b).

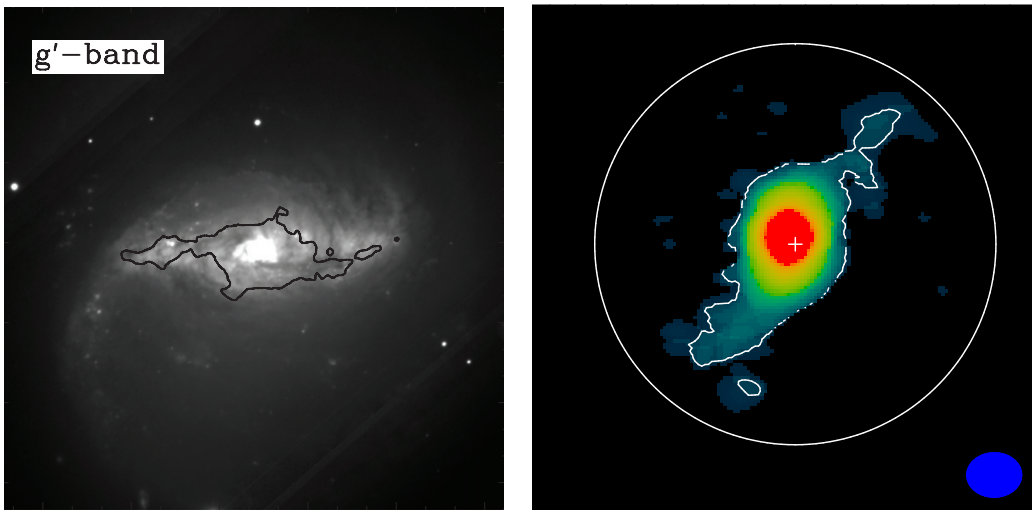

(a) Barred galaxy in optical (b) Barred galaxy in molecular gas

FIGURE 3.3: (a) Optical image (greyscale) of barred galaxy NGC 7552 is taken from Gemini South. The black contour represents dust emission at 5.8μm from Spitzer with 5.5 MJy sr^{-1}. This figure is taken from (Pan et al., 2013). (b) Molecular gas of NGC 5430 (Pan et al. in preparation). The primary beam of CARMA with size of 1′ is indicated with a white circle. The beamsize of ∼8″ (1.6 kpc) is overlaid at bottom right.

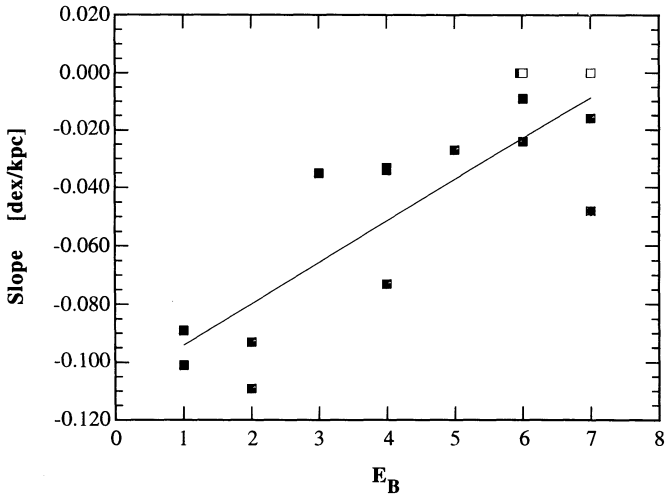

FIGURE 3.4: Slope of abundance gradient versus axis ratio of bar as $E_{\rm B} = 10(1-b/a)$, where a and b are major and minor axis of bar. $E_{\rm B}$ is inversely proportional to the bar strength. This figure is taken from Martin & Roy (1994).

On the contrary, some people suggest that bars are periodic products in galaxies. Bars are dissolved within 1 – 2 Gyrs due to the growth of the central mass concentration (Bournaud et al., 2005). Transfer of angular momentum from the infalling gas to the bar is another possible mechanism to weaken the bar (Bournaud & Combes, 2002). In this scenario, when the bar is getting weaker, gas starts to populate at the disk and forms stars. Then the self-gravity of the disk increases again, providing a suitable condition for a new bar formation (Bournaud & Combes, 2002).

3.1.2 Properties of Gas and Star Formation in Bars

The previous section has introduced two regions in barred galaxies where gas tends to pile up, dust lanes (bars) and CNRs. However, these two regions show different star forming properties.

Observationally, gas mass of CNR is as high as $> 10^9$ $M_\odot$ in some galaxies. In other words, all gas in the Milky Way are stuffed into the inner 1 kpc of barred galaxy. Since $\Sigma_{\rm gas}$ becomes dramatically high, as a result, SFR is also high in CNR. Indeed, the mean radial profile of Hα shows a central peak in barred galaxies, while a downward trend is seen in that of unbarred galaxies (Figure 3.6). So far, in disk galaxies, CNR is the only region where super star clusters are found (Maoz et al., 2001). Moreover, SFR of CNR is high enough to dominate the global SFR of the host galaxy (e.g., Pan et al., 2013).

However, star formation in bars is complicated and has not yet been well understood. The puzzling part is that the loci of orbit crowding (dust lanes) are the loci of strong shocks as well (Athanassoula, 1992). Due to the shocks, gravitationally bound structures (e.g., GMCs, dense gas cores) are prevented to form, as a result, star formation is prevented in bars (e.g., Kohno et al., 1999, Reynaud & Downes, 1998, Tubbs, 1982, Zurita et al., 2004). Indeed, star formation is absent in some bars, such as NGC 1300 and NGC 1530. Figure 3.5 shows the profiles of surface brightness of Hα (dotted lines) and residual velocity (solid lines) parallel (left column) and perpendicular (right column) to the bar of NGC 1530 (Zurita et al., 2004). The residual velocity (non–circular velocity) corresponds to a rotation-curve-subtracted observed velocity field. It can be seen from the figure that there is a clear anticorrelation between the two variables. Specifically, high surface brightness (high SFR) is associated with smaller residual velocity, suggesting that high velocity inhibits star formation.

James et al. (2009) observe Hα emission in $\sim$ 300 nearby galaxies with Jacobus Kapteyn Telescope. They found that, however, the mean radial profile of Hα emission shows a bump at bar region, whereas it smoothly decreases in unbarred galaxies (Figure 3.6). Moreover, the bump appears from strong to weak bar. Martin & Friedli (1997) analyze

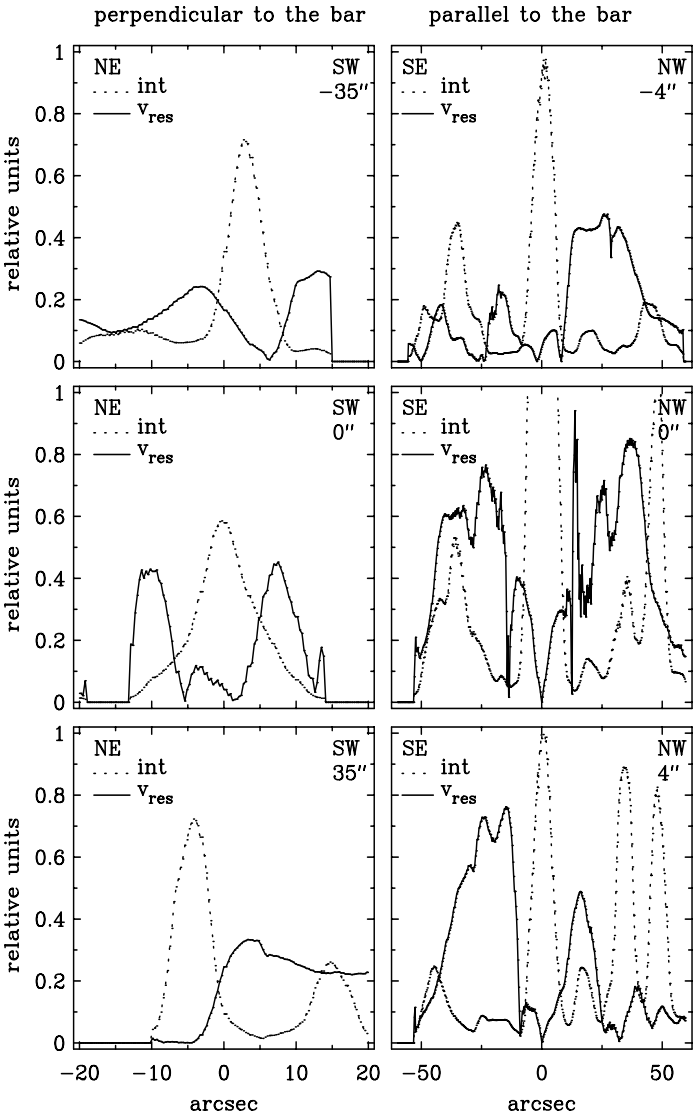

FIGURE 3.5: Normalized surface brightness of Hα (dotted lines) and residual velocity (solid lines) parallel (left column) and perpendicular (right column) to the bar of NGC 1530. The residual velocity represents non–circular velocity. The x-axis shows the distance relative to the center along the slit which is either parallel or perpendicular to the bar. The distance between the slit itself and the galactic center is indicated in the top right of each plot. This figure is taken from Zurita et al. (2004).

the HII regions of eleven late-type barred galaxies. They found that the SFR in the bar has a wide range of 0.03 – 1.44 $M_\odot$ yr^{-1}. Such a phenomena suggests that bars have considerable impact on star formation, and GMCs must survive under certain conditions in bars. Koda & Sofue (2006) estimate the escape velocity from a cloud and compare the value with observed velocity jump (shock) across the bar of NGC 4303, they conclude that the shock is not large enough to destroy GMCs.

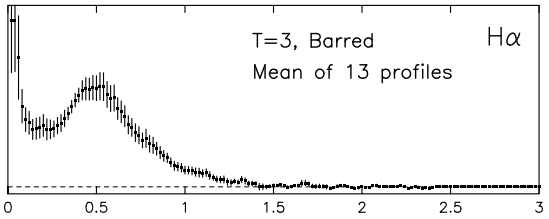

(a) Barred galaxy in optical

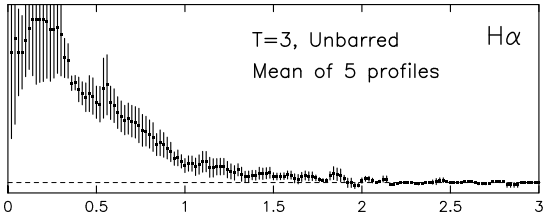

(b) Barred galaxy in molecular gas

FIGURE 3.6: Mean radial profile of Hα (star forming regions) of galaxies with morphology of T = 3 (Sb). Panel (a) is mean of 13 barred galaxies (SBb). Panel (b) is mean of 5 unbarred galaxies (Sb). The figure is taken from James et al. (2009).

3.2 Motivation and Methodology

Distribution of star forming regions are diverse in bars. Some bars are lacking of star forming regions. Some galaxies have star forming regions only at the bar ends, while some galaxies show a string of HII regions and HCN emission along entire bars (Leon et al., 2008, Martin & Friedli, 1997). Martin & Friedli (1999) study HII regions in 10 barred galaxies with standard optical diagnostic diagrams. The results suggest that the properties (e.g., electron density, extinction) of the HII regions within the bars and the disks are similar. In other words, the HII regions in bar is just as normal as in the rest of disk. Therefore, bars provide an excellent laboratory to study the impact of secular evolution on the promotion and inhibition of star forming activity. The relation of the gas and star formation in bars would help to understand how nearby galaxies evolve, and the physical conditions that favor star formation in galactic disks.

3.3 The Target: NGC 6946

NGC 6946 is a barred spiral galaxy (Figure 3.7). The basic parameters of the galaxy is listed in Table 3.1. NGC 6946 is located at 5.5 Mpc, where 1″ corresponds to 27 pc. The galaxy is rather face-on, with an inclination only 33°. The infrared luminosity derived using four IRAS bands is $10^{10.22}$ $L_{\odot}$ (Sanders et al., 2003).

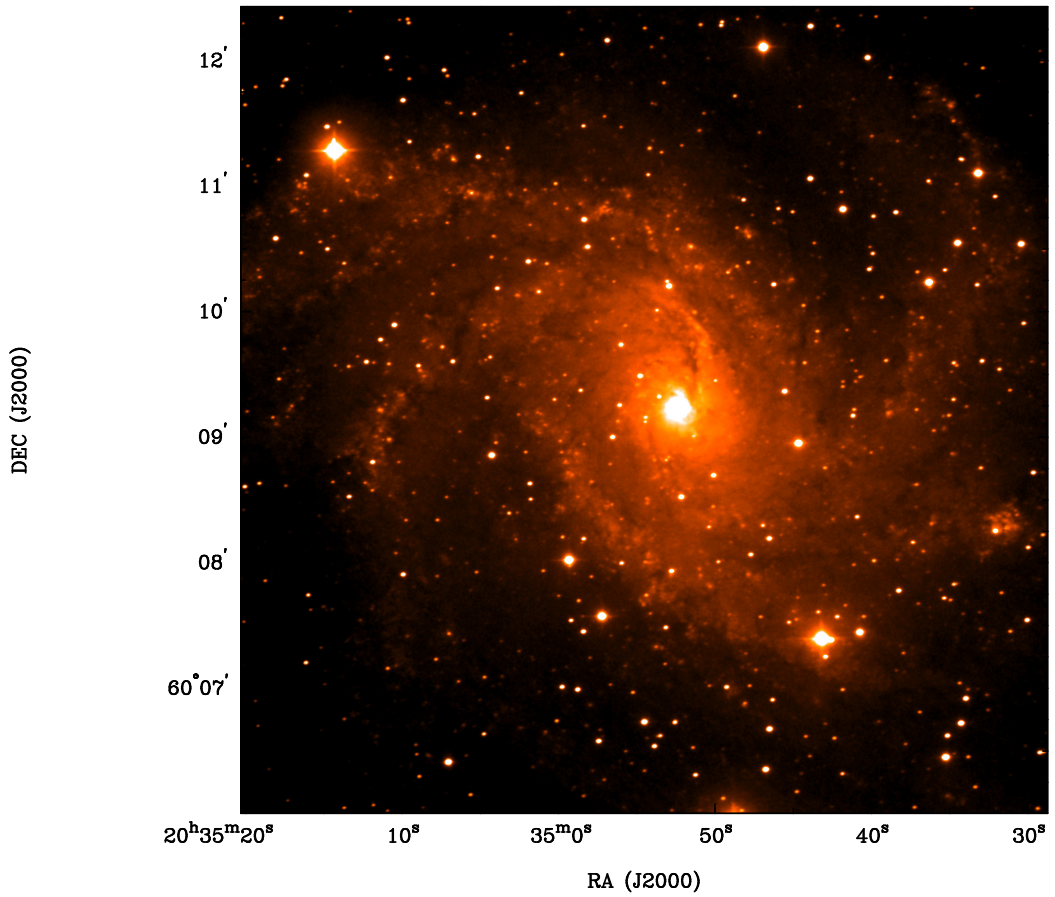

FIGURE 3.7: Optical image of NGC 6946 in i-band from Knapen et al. (2004).

HI observations clearly detect two dwarf galaxies, UGC 11583 and L149 at ∼33 – 37 kpc away from NGC 6946 (Boomsma et al., 2008, Pisano & Wilcots, 2000). A plume-like structure has been observed in HI at the north-western edge of NGC 6946 (see Figure 3.8) by Boomsma et al. (2008). However, since the intensity of the plume-like structure is weak that the structure is only seen in the low resolution (high sensitivity) map. The plume is on the same side of the companions. The velocity of the plume is also in the same range as the two companion galaxies. Hence, the plume-like structure may be the result of recent interaction between NGC 6946 and the companions.

NGC 6946 is undergoing nuclear starburst. Starburst model suggests that the nuclear statburst is combination of two events that occurred 7 Myr and 20 Myr ago (Engelbracht et al., 1996). Moreover, stars formed in the nuclear region of NGC 6946 tend to be high mass stars (Engelbracht et al., 1996).

Because of its close distance and bright emission, NGC 6946 is included in many galaxy surveys, including VLA THINGS (atomic hydrogen at 21 cm), Spitzer SINGS (near to mid-infrared and optical), Herschel KINGFISH (far-infrared) and GALEX NGS (NUV and FUV). The images trace the distributions of atomic gas, dust, and star formation.

TABLE 3.1: Parameters of NGC 6946

Morphology[a]	SAB(rs)cd
R.A. (J2000)[a]	20:34:52.3
Dec. (J2000)[a]	60:9:14
Distance [b]	5.5 Mpc
Inclination[c]	33°
P.A.[c]	243°

[a] NED
[b] Rebolledo et al. (2012)
[c] Walter et al. (2008)

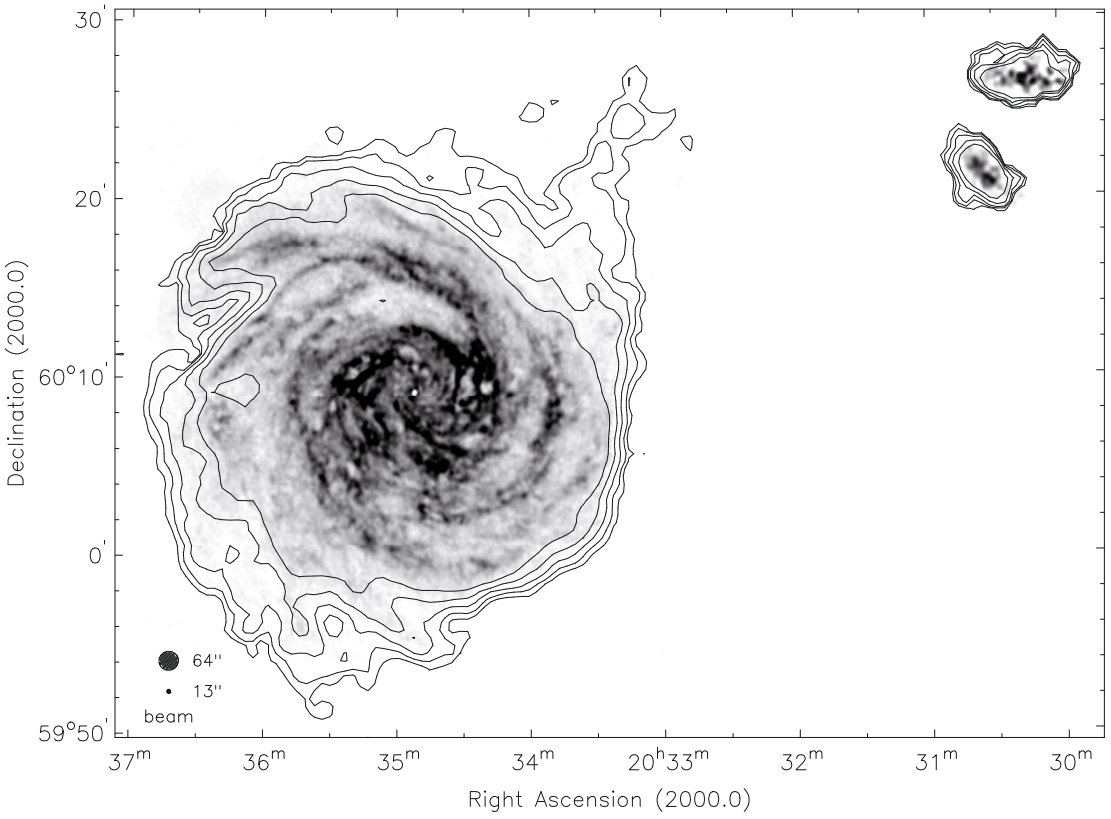

FIGURE 3.8: HI integrated intensity map of NGC 6946 and its two companions. The upper companion is UGC 11583 and the lower one is L149. The high resolution maps (13″) of three galaxies are shown in greyscale. The low resolution images (64″) are shown in contours. The plume-like structure is observed at the north-western edge of NGC 6946. The intensity of the plume is weak, so it is only visible in the low resolution, high sensitivity map. The beam sizes are indicated in the lower left corner. This figure is taken from Boomsma et al. (2008)

TABLE 3.2: Summary of radio data in this work

Type of telescopes	Transitions	Telescope (Year)	Observing mode	References
Single dish	^{13}CO (1–0)	NRO45 (2013)	mapping	This work
Interferometer	^{13}CO (1–0)	CARMA (2009)	mapping	This work
Single dish	^{12}CO (1–0)	NRO45 (2008–2010)	mapping	Donovan Meyer et al. (2012)
Interferometer	^{12}CO (1–0)	CARMA (2009)	mapping	Donovan Meyer et al. (2012)
Single dish	HCN (1–0)	NRO45 (2013)	single point	This work

All data in the surveys have been released to archives and therefore be available to be compared with the molecular gas that we aim to obtain.

^{12}CO observations of NGC 6946 have been done with many authors. Donovan Meyer et al. (2012) made the best angular resolution and largest map of NGC 6946 with CARMA and Nobeyama 45-m telescope (NRO45). Since ^{12}CO to ^{13}CO intensity ratio is a useful tool to infer the physical conditions of molecular gas, we challenge large scale ^{13}CO (1–0) observations in NGC 6946. In addition, to obtain the total amount of dense gas, we made single dish HCN (1–0) observations toward several interested regions with single-point mode. Table 3.2 shows a summary of the data of molecule in this work, including telescopes, transitions, observing years and modes.

3.4 Observations and Data Reduction

3.4.1 CO Observations and Data Reduction with Single Dish

The single dish observations of ^{13}CO (1–0) were made with Nobeyama 45-m telescope, using the dual-polarization receiver, TZ (Asayama & Nakajima, 2013, Nakajima et al., 2013) coupled with the spectrometer SAM45. Observations were made during January – February 2013. The beam size of a 45-m dish is 20″ at 110.2 GHz. We observed with a spectral resolution of 488.24 kHz (1.3 km s^{-1} at 110 GHz), and effective bandwidth of 1600 MHz ($\sim$ 4356 km s^{-1}). The On-the-Fly method was used to map the galaxy, scanning along R.A. (x scans) and Dec. (y scans) directions. Typical $T_{\rm sys}$ is 160 – 180 K. The mapping area is 160″ $\times$ 160″ with P.A. = 0° (Figure 3.9). The center of the map is the galactic center of NGC 6946. Each scan has 20 seconds. An OFF point 8′ away from the map was observed every two scans for sky subtraction. It took about 1.5 minutes for one ON-OFF cycle (ON-ON-OFF). Each scan is separated by 5″. Each map took about 31 minutes to complete, containing 33 x- or y- scans. Before the observation of each map, we made pointing observations. SiO maser T-Cep was used as pointing source. Pointing observations were performed at 43 GHz with receiver S40. Galactic object S140X was observed for intensity calibration once per day. The total observing

time is about 60 hours, including the observations of the pointing source and intensity calibrator.

The data reduction was done with package `NOSTAR`, which was developed for OTF data of NRO 45-m telescope based on `AIPS`. We subtracted the baseline with a 1-order polynomial fit, then checked each scan of each maps, flagged the bad integration. Then we combined the scan maps with a grid size $6''$, creating an x-cube and a y-cube in FITS format. Finally, PLAIT method was performed on the cubes in `NOSTAR` to reduce the scanning effect and generate the final cube which is a combination of the x-cube and y-cube. We made two final cubes with different velocity increment. Both of them have pixel increment $6''$ in x and y direction, 2.65 and 10 km s^{-1} in velocity axis. Channel width of 2.65 km s^{-1} corresponds to two-channel wide of NRO's spectrometer and the instrumental velocity width of CARMA. This cube will be used for combing single dish and interferometric data. The rms noise of cubes are 12.1 mK and 6.6 mK in $T_{\rm A}^*$ for the velocity resolution of 2.65 and 10 km s^{-1}, respectively. Main beam efficiency of 40% is adopted for the conversion between $T_{\rm A}^*$ and $T_{\rm mb}$, i.e., $T_{\rm mb} = T_{\rm A}^*/0.4$.

3.4.2 Integrated Intensity Map of Single Dish CO Observation

Integrated intensity map of ^{13}CO was made with `MIRAD` task, `moment`. The *clip* parameter which defines the range of excluded intensity is -infinity – 1.5σ of channel map, that is, -999 – 18 mK. ^{13}CO integrated intensity map of single dish is shown in Figure 3.10. Actual structure of the galaxy is resolved with single dish. The integrated intensity map is dominated by a central blob with a size of about $30'' \times 70''$ along R.A and Dec. direction, respectively. In addition to the central blob, there is an elongated structure emerging from the north of the central concentration. The length of the elongated emission is about 800 pc. From the end of the elongated structure, molecular gas extends eastward.

Since single dish observations are used to compensate the missing flux of interferometric observations, and used as a standard flux to check the combing result, it is important that the intensity of ^{13}CO is reliable. The galactic center of NGC6946 was observed in ^{13}CO(1-0) with NRO 45-m telescope by Matsushita et al. (2010). The intensity of ^{13}CO in Matsushita et al. (2010) is 21.9 $\pm$ 1.4 K km s^{-1}, while the intensity at the center is 21.7 $\pm$ 0.7 K km s^{-1} in this work. In this work, the noise integrated intensity map ($\sigma_{\rm I}$) is calculated with

$$\sigma_{\rm I} = \sigma_{\rm ch} \sqrt{N_{\rm ch}}\, \Delta v, \tag{3.1}$$

where $\sigma_{\rm ch}$ is the noise of channel map, $N_{\rm ch}$ is the number of channel containing significant emission, and Δv is the channel width. The results of this work and Matsushita et al.

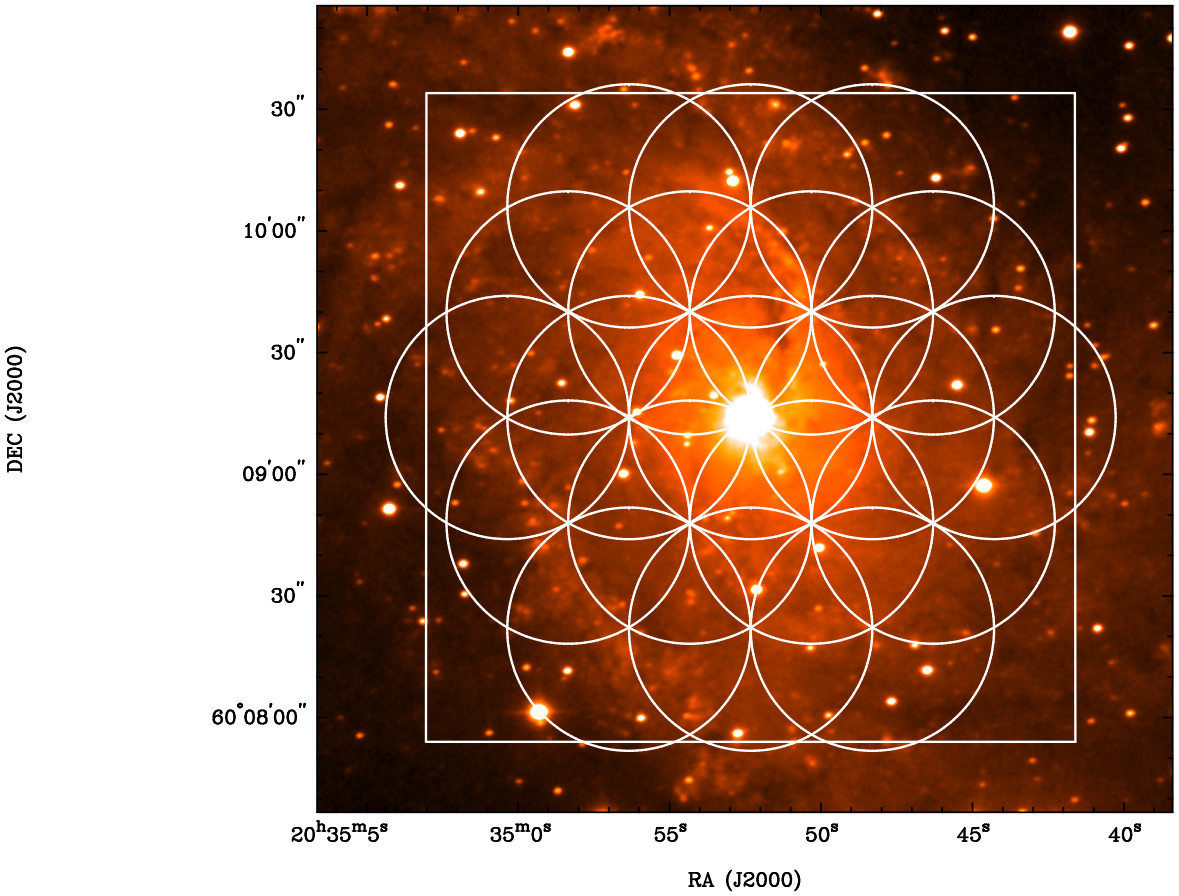

FIGURE 3.9: Observing area overlaid on the optical image of NGC 6946 in i-band. The white box indicates the observing area of Nobeyama 45-m telescope. The center of the box corresponds to the galactic center. Size of the box is $160'' \times 160''$. The 19 circles indicate the mosaic pattern of CARMA observations. The circles have diameter of $1'$, corresponding to the primary beam of CARMA. The central pointing is centered at the galactic center.

(2010) are in excellent agreement. During the data reduction, we did not subtract any specific region but performed the same reduction procedures to entire map all the time. Therefore, the intensity of our ^{13}CO (1–0) should be reliable not only in the galactic center but also the entire map.

3.4.3 HCN Observations and Data Reduction with Single Dish

We made HCN observations with NRO 45-m telescope coupled with the receiver TZ and spectrometer SAM45. We observed three positions at $20^{\rm h}34^{\rm m}52\overset{\rm s}{.}9$ $60°8'55''$ (the southern ridge; cf. §3.5.2), $20^{\rm h}34^{\rm m}51\overset{\rm s}{.}3$ $60°9'38''$ (the northern ridge), and the galactic center (see Figure 3.11; within the beamsize of $19''$, the HCN observation of southern ridge cover half of the south arm and the southern blob). $I_{\rm HCN}$ is generally low outside the centers of nearby galaxies. In addition, the purpose of the HCN observations is to measure the amount of dense gas, their actual distribution is not so important at this

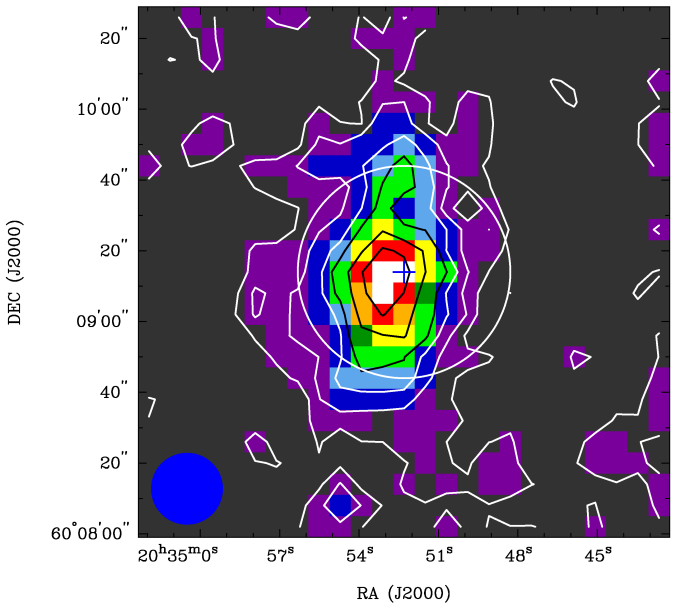

FIGURE 3.10: Integrated intensity map of ^{13}CO observed with NRO45 in both color scale and contours. The contours are 13%, 20%, 30%, 40%, 60%, 80% of the peak brightness. The blue cross marks the galactic center. The grey circle indicates the 1′ primary beam of CARMA.

moment. For these reasons, we did not perform mapping but single-point observations. Observations were done in January 2013. We observed with a spectral resolution of 488.24 kHz (1.6 km s^{-1} at 88.6 GHz), and effective bandwidth of 1600 MHz ($\sim$ 5416 km s^{-1}). SiO maser T-cep was used for pointing observations. Pointing observation was made every 45 minutes. An OFF point 8′ away from the target was observed every 15 seconds for the sky subtraction. $T_{\rm sys}$ is about 140 K during the observations. A standard flux calibrator S140 was observed once per day. Total on-source integrated time is about one hour at each position. Data reduction was carried out with `NewStar`. `NewStar` is a reduction software developed specifically for spectral line data of the NRO 45-m telescope based on AIPS (Astronomical Image Processing System).

The spectra of the HCN emission at the northern ridge, southern ridge and the center are presented as black solid curved in Figure 3.12(a), 3.12(b), and 3.12(c), respectively. Only the galactic center of NGC 6946 has been observed in HCN (1–0) with NRO 45-m telescope in the past by Matsushita et al. (2010). Our result ($I_{\rm HCN}$ = 18.9 $\pm$ 1.4 K) is consistent with that in Matsushita et al. (2010) ($I_{\rm HCN}$ = 21.4 $\pm$ 1.0 K). Integrated intensity of HCN is 4.7 $\pm$ 0.8 and 4.2 $\pm$ 0.8 in the northern ridge and the southern ridge, respectively. They are about four times smaller than that of the central region.

Single dish spectra of ^{13}CO (grey) and ^{12}CO (dashed) are overlaid on the HCN spectrum in Figure 3.12. In the central region and the northern ridge, three spectra are similar in both line profile and velocity coverage. However, in the southern ridge, as CO lines show two components with a central velocity of $\sim$ 30 km s^{-1} and $\sim$ 90 km s^{-1}, only single

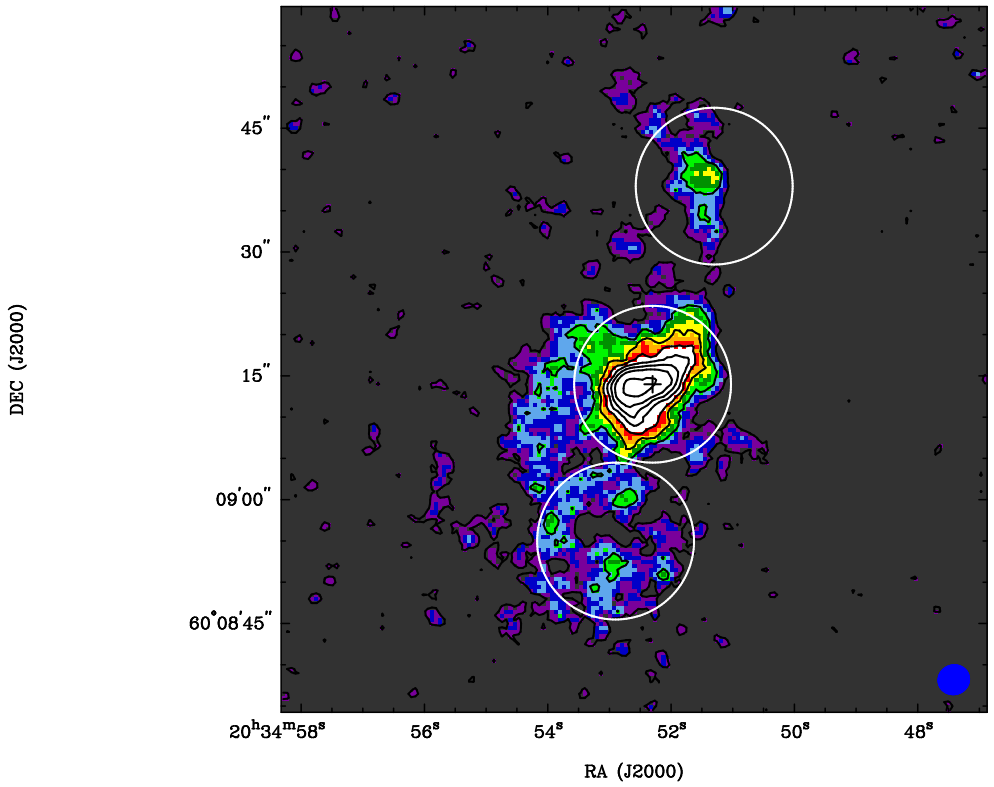

FIGURE 3.11: Positions of HCN observations. The color scale represents ^{13}CO integrated intensity map. Positions of HCN observations are indicated with white circles. Galactic center is marked with a black cross.

component is found in HCN around 90 km s^{-1}. Nonetheless, the spectrum of HCN is slightly broader than the individual spectra of CO lines at both velocities.

3.4.4 Observations and Data Reduction with Interferometer

Observations with CARMA (Combined Array for Research in Millimeter-wave Astronomy) was made in Feb – May 2009. CARMA is composed of six 10 m antennae from OVRO and nine 6 m antennae from BIMA. Seven-point hexagonal mosaic was used to map NGC 6946. ^{13}CO (1–0) and ^{12}CO (1–0) were observed simultaneously (The results of ^{12}CO (1–0) was published in Donovan Meyer et al. (2012)). Three bands were used, resulting in total bandwidth of ∼108 MHz. Channel width is 2.65 km s^{-1}. Total on source time is about 21 hours. Bandpass, gain, and flux calibrators are 1715+096, 2015+372, and MWC349, respectively.

Since ^{12}CO is much stronger than ^{13}CO, and the critical density of ^{12}CO is lower than ^{13}CO, i.e., ^{13}CO must be detected only at where ^{12}CO was found, we took the calibrated visibilities from Donovan Meyer et al. (2012) to generate a MASK for CLEANing the ^{13}CO dirty map. First of all, we use `invert` of `MIRIAD` to perform Fourier transformation from ^{12}CO visibility to brightness distribution, i.e., dirty image. The dirty image

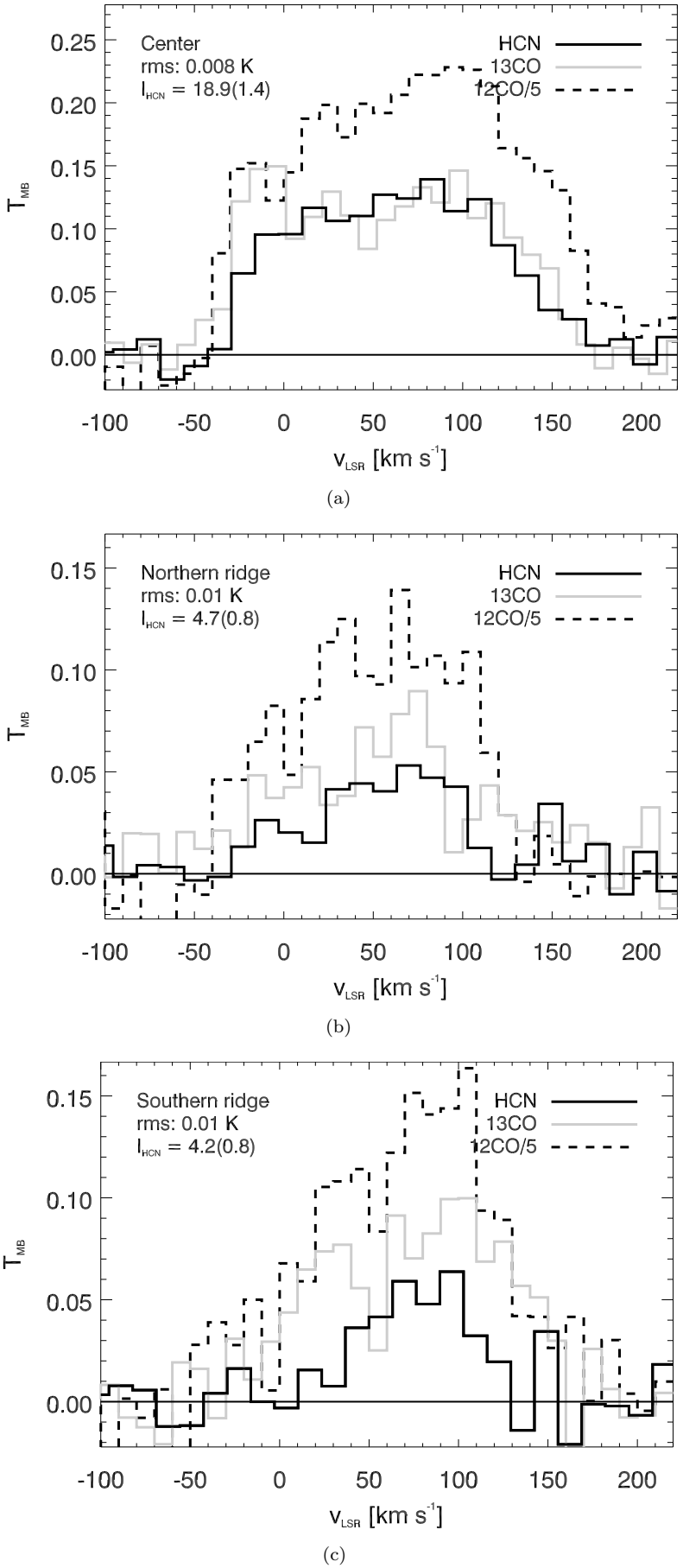

FIGURE 3.12: Single dish spectra of HCN (solid black) ^{13}CO (grey), and ^{12}CO (dashed). The intensity of ^{12}CO has been divided by a factor of five. The velocity resolutions of HCN and CO spectrum are 13 km s^{-1} and 10 km s^{-1}, respectively. All spectra correspond to a region of $\sim 20''$ in this figure. (a) Spectrum of the central region. (b) Spectra of the northern ridge. (c) Spectra of the southern ridge.

contains the convolution of the source with a dirty beam. Then `mossdi2` and `restor` are used for the deconvolution (CLEAN), generating residual maps and CLEANed map. (Task `mospsf` is used to combine dirty beams, then `imfit` is performed to estimate the size of the synthesized beam for `restor`.) Then we perform `invert`, `mossdi2` and `restor` to a cube of ^{13}CO.

The final cubes for ^{13}CO has a channel width of 10 km s^{-1} and the rms noise is 11 mJy beam^{-1}. The beam size is $3\farcs29 \times 3\farcs08$ (89 pc $\times$ 83 pc) with P.A = -71.81°.

3.4.5 Integrated Intensity Map of Interferometric Observations

The ^{13}CO integrated intensity map of CARMA observations is made with the final data cube. The map is displayed in Figure 3.13(a). There is a central component elongates with direction of NW – SE. Beyond the NW of the central component, a thin, extended emission shows up, sweeping to radius of $\sim 30''$. The extended structure is also seen in the single dish ^{13}CO map (Figure 3.10), but in the interferometric map, the emission shifts downstream, presumably due to better angular resolution.

At the southern part, only three peaks are significantly detected with interferometer. This result suggests that either ^{13}CO is sparse in this region or the emission is relatively diffuse since interferometers are not sensitive to diffuse components.

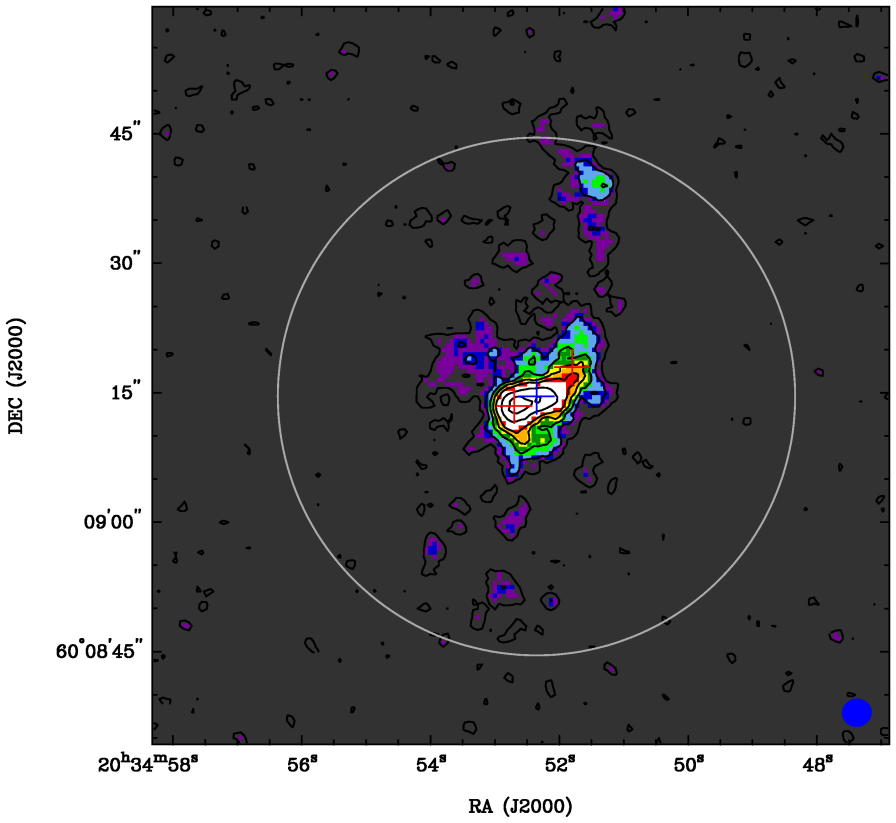

(a)

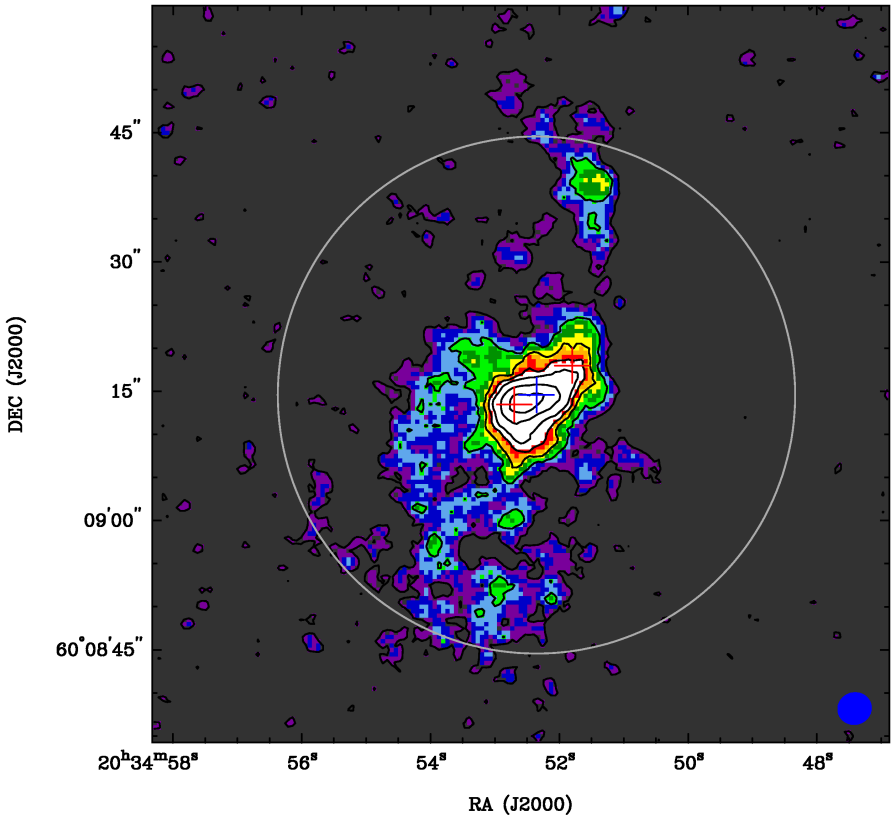

(b)

FIGURE 3.13: The moment maps of ^{13}CO. (a)Integrated intensity map made with CARMA data alone (color scale and contours). The beam is overlaid at the bottom right. The beam size is 3.″29 × 3.″08 and P.A = -71.81°. (b)Integrated intensity map made with CARMA+NRO45 data (color scale and contours). The contours are 10%, 20%, 30%, 40%, 50%, 70%, and 90% of the peak flux in each map. The beam size is 3.″84 × 3.″61 and P.A = -71.85°. The blue cross denotes the galactic center. The red crosses mark the bar ends of the minibar. The grey circle indicates the 1′ primary beam of CARMA.

3.4.6 Combination Procedure

In this section, I show the steps of combining single dish and interferometer data.

1. Enlarge single dish map to 486″ × 486″. Ideally, the mapping area of NRO45 should be larger than the mosaic area of CARMA, i.e., greater than 180″ × 180″ (Koda et al., 2011). However, due to the low intensity of ^{13}CO, it is difficult to map such a big area and obtain significant detection within reasonable time, so the actual mapping area is slightly smaller (160″ × 160″). It should not affect our results because the galactic features we concern are located in the central 1′, i.e.,, only the central pointing of the mosaic, which has been well protected by the adjoining six points. All of these seven points are inside our OTF area. We enlarged the map (with channel width of 2.65 km s^{-1}) with task `imframe` by nine times, centering at the original OTF map. The cube now has (81 pix × 6″) = 486″ at x and y direction.

2. Remove the noisy emission at the edge of the original OTF map. A Fermi-Dirac type function is adopted. Intensity of the function is 1.0 across most of the x range, and drops rapidly at the edge (Figure 3.14). Therefore, after the single dish cube is multiplied by the function, the real emission is conserved but the noise at the edge are significantly reduced. Two example channels of -22 and 92 km s^{-1} are shown in Figure 3.15. The red and blue contours show the emission before and after applying the function, respectively. The red contours are plotted below the blue ones. Therefore, the regions only showing in red are either removed or significantly reduced by the function.

3. Then we performed deconvolution to the single dish cube with the single dish beam. The cube was convolved with a beam of NRO 45-m telescope (20″) during the imaging process in NOSTAR. Therefore, deconvolution is required to revert to true emission distribution.

4. Apply a dummy beam. Then we multiplied a dummy beam to the cube to cheat the `MIRIAD` as if our single dish map was observed with interferometer with the same data structure as the CARMA observations. Since the CARMA observations consist of 19 point hexagonal mosaic, the deconvolved cube was divided into 19 areas with same pointing centers as CARMA. We multiplied a Gaussian primary beam with FWHM of 2′ to the 19 points of the deconvolved NRO cube.

5. Generate visibility data in $u - v$ space for single dish data. The visibilities have a Gaussian density profile. The size of Gaussian distribution of 10 kλ corresponds to the effective beam size of NRO 45-m telescope (20″).

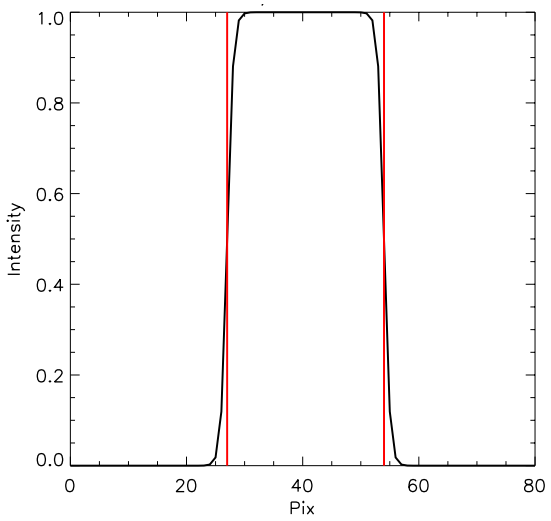

FIGURE 3.14: The Fermi-Dirac type function we used to reduce the noise at the edge of map. The red lines indicate the position where intensity drops to 0.5.

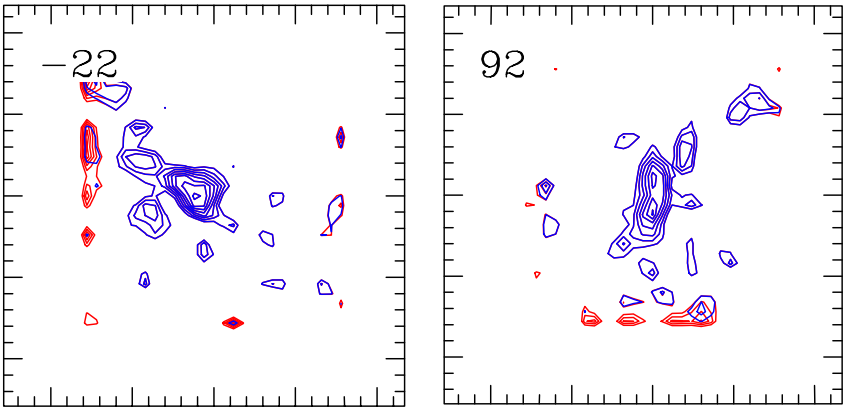

(a) (b)

FIGURE 3.15: Results of applying the Fermi-Dirac type function in the channels of NRO45. The red and blue contours show the emission before and after applying the function, respectively. The red contours are plotted below the blue ones, therefore, the regions only showing in red are either nearly removed or considerably reduced by the function.

6. Imaging. All visibility data (CARMA + NRO45) are used for `invert`. There are 4 types of baseline (antenna pairs), i.e., CARMA (10 m – 6 m), OVRO (10 m), BIMA (6 m), and NRO45, along with 19 pointings of mosaic ($u - v$ coverages), thus we have $4 \times 19 = 76$ types of dirty beam. The following imaging procedures are the same as in §3.4.4.

The final combined cube has a channel width of 10 km s^{-1} with noise level of 14 mJy beam^{-1}. The synthesized beam is $3\farcs84 \times 3\farcs61$ (104 pc × 97 pc) with P.A = -71.85°.

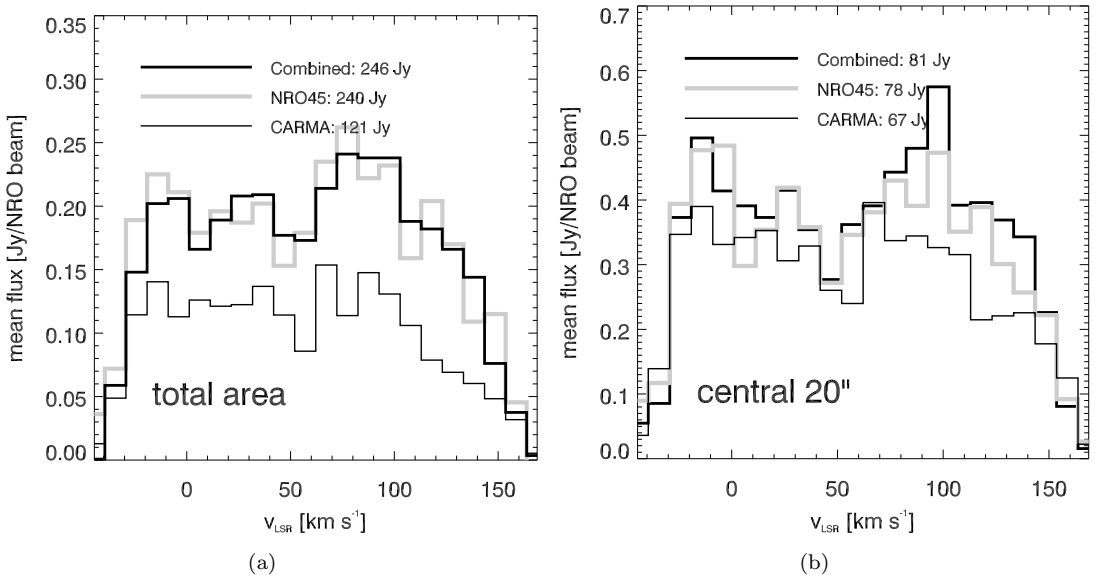

FIGURE 3.16: Averaged spectra of total area (a) and central region (b). The thick black line, gray line, and the thin black line represent the spectrum of the combined, single dish, and the interferometer map, respectively.

3.4.7 Missing Flux

To check the total flux and the spectral profile of the combined ^{13}CO map, the combined cube and CARMA cube are degraded to the resolution of NRO45, i.e., 20″. The mean spectra of the total area (central 30″ × 70″ along the bar) is displayed in the left panel of Figure 3.16. The spectrum of the combined and CARMA cube are plotted with thick and thin black histograms respectively. The NRO cube is overlaid with gray color. Total integrated flux of each data cube is shown in the legend of the figure.

The spectral shape of three data cubes is similar but the intensity of the CARMA spectra has only half height of the NRO45 and the combined cube. All the spectra show a two-peak shape centering at about 50 km s^{-1}. The total integrated flux of the NRO45 and the combined cube are in good agreement, about 240 Jy. The missing flux in the CARMA data is about 50% of the total flux, 120 Jy.

The mean spectra of the three data cubes at the central 20″ are presented in the right panel of Figure 3.16. The size of 20″ corresponds to an effective beamsize of NRO45. The style and the meaning of the lines are the same as above. At the most of the central region, even CARMA captures majority of the emission, about 83%, suggesting that most of gas at the central region are locked in compact structures, resulting in the small amount of missing flux. The integrated flux of combined, NRO45 and CARMA cube are consistent and ∼80 Jy.

3.5 Results

3.5.1 CO Morphology

3.5.1.1 Channel Maps

The channel map of ^{13}CO is displayed in Figure 3.17 with red contours. For comparison, the channel map of ^{12}CO is superposed with black contours. The galactic center is marked with a cross in each channel.

Distribution of ^{13}CO and ^{12}CO emissions are similar in all channels. Both transitions show a central peak around the galactic center. The central peak has a velocity width of about 180 km s^{-1} in ^{13}CO, ranging from -34 km s^{-1} to 149 km s^{-1}. Velocity width of the central peak is slightly larger in ^{12}CO from -45 km s^{-1} to 169 km s^{-1}, corresponding to $\sim$ 214 km s^{-1}. The central spectrum of ^{13}CO is shown in Figure 3.18. The spectrum show a two-peak profile with respect to a central velocity of $\sim$40 km s^{-1}, indicating a rotating structure. The ^{12}CO (combined) spectrum divided by eight is overlaid in Figure 3.18 for comparison. The profile and the velocity range of two CO lines are in excellent agreement.

Apart from the galactic center, two elongated structures emerging from the galactic center are seen, extending toward the north and the south, respectively. Emission of the northern ridge emerges from about -14 km s^{-1} in both CO lines, spreading a width of $\sim$ 112 km s^{-1} in ^{13}CO and $\sim$ 132 km s^{-1} in ^{12}CO. The southern emission starts from about -3.9 km s^{-1} in both lines. As in the northern ridge and the galactic center, ^{13}CO emission is narrower across the velocity axis ($\sim$122 km s^{-1}) than that of ^{12}CO ($\sim$142 km s^{-1}).

All ^{13}CO peaks are associated with counterparts in ^{12}CO. This is a natural result since ^{13}CO has larger critical density than ^{12}CO. To be more precise, when the gas becomes sufficiently dense to excite ^{13}CO emission, ^{12}CO must be excited already due to the large optical thickness.. On the contrary, ^{13}CO is absent at some ^{12}CO peak due to the lower density of the gas (e.g., at 6.3 km s^{-1} and 67.0 km s^{-1}). We will discuss this phenomenon from the integrated intensity maps.

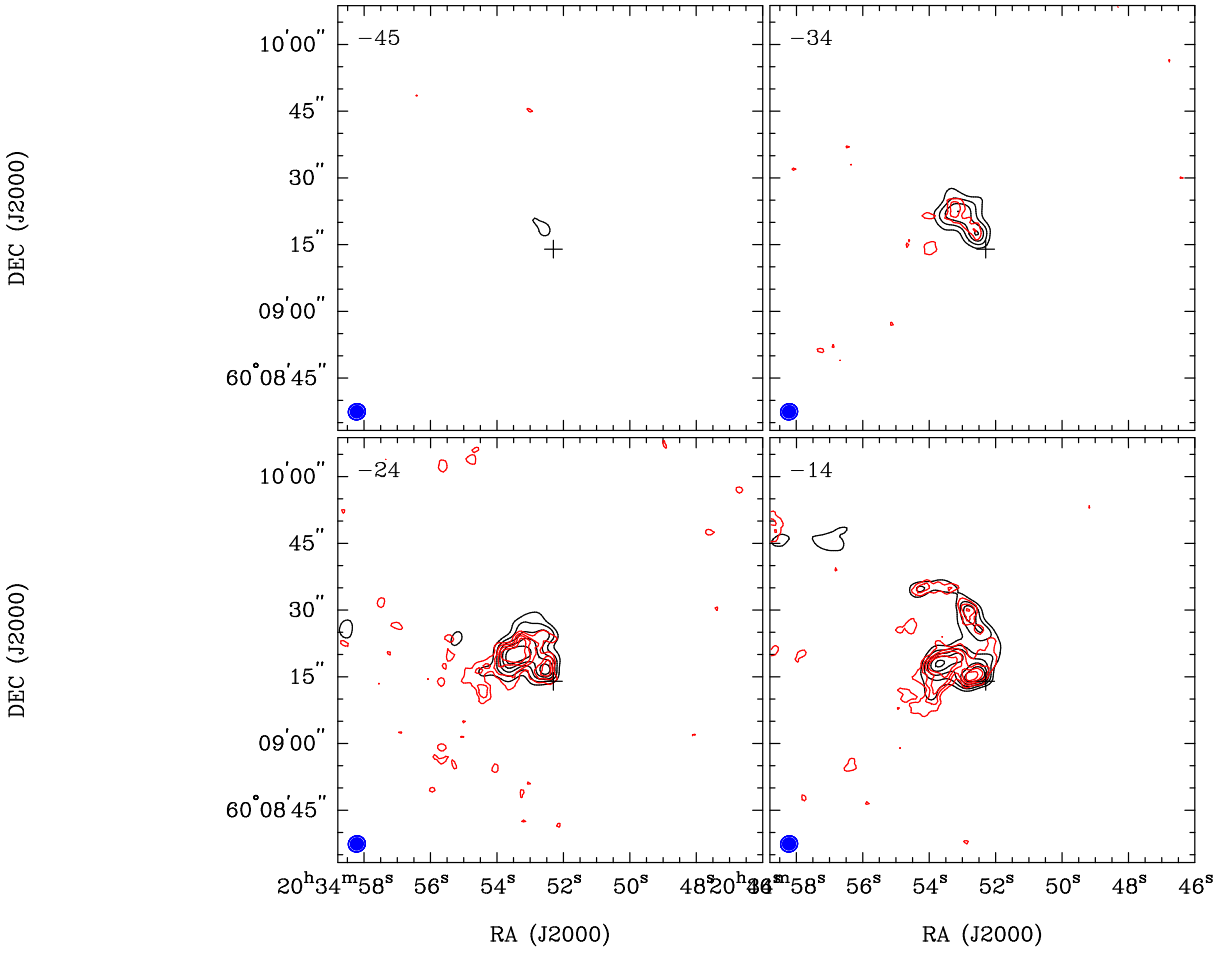

FIGURE 3.17: Channel maps of CO lines. ^{12}CO is shown in black contours and ^{13}CO in red. The beam size is overlaid in the bottom right of each channel. The outer circle is the beamsize of ^{13}CO and the inner circle is for ^{12}CO. The galactic center is marked with a cross in each panel. Velocity of each panel is indicated in upper left with a unit of km s^{-1}. ^{13}CO is plotted with a contour step of 25, 35, 45, 55, 75, and 90% of the maximum flux. Contours of ^{12}CO are 15, 25, 35, 45, 55, 75, and 90% of the maximum flux.

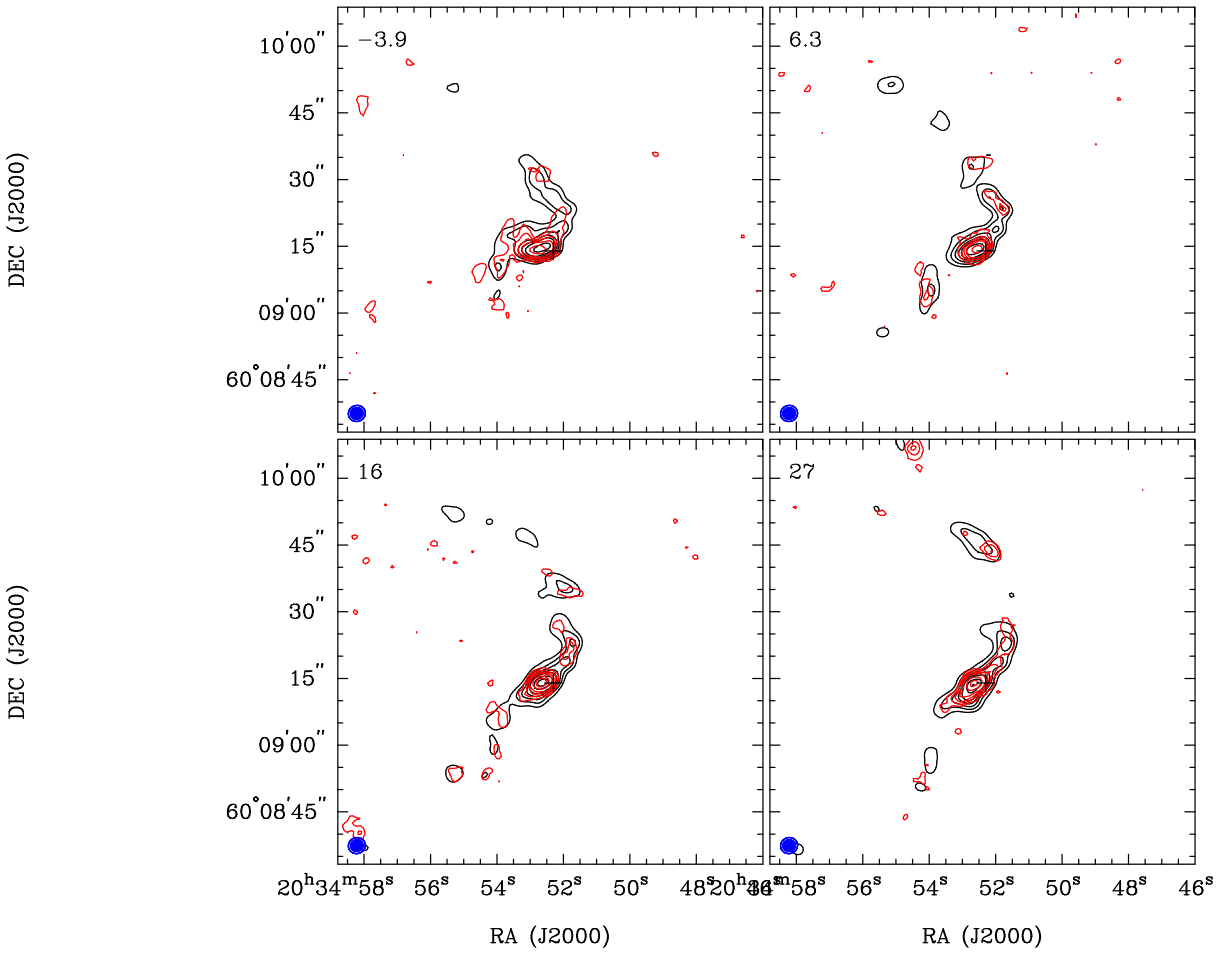

FIGURE 3.17: Continued.

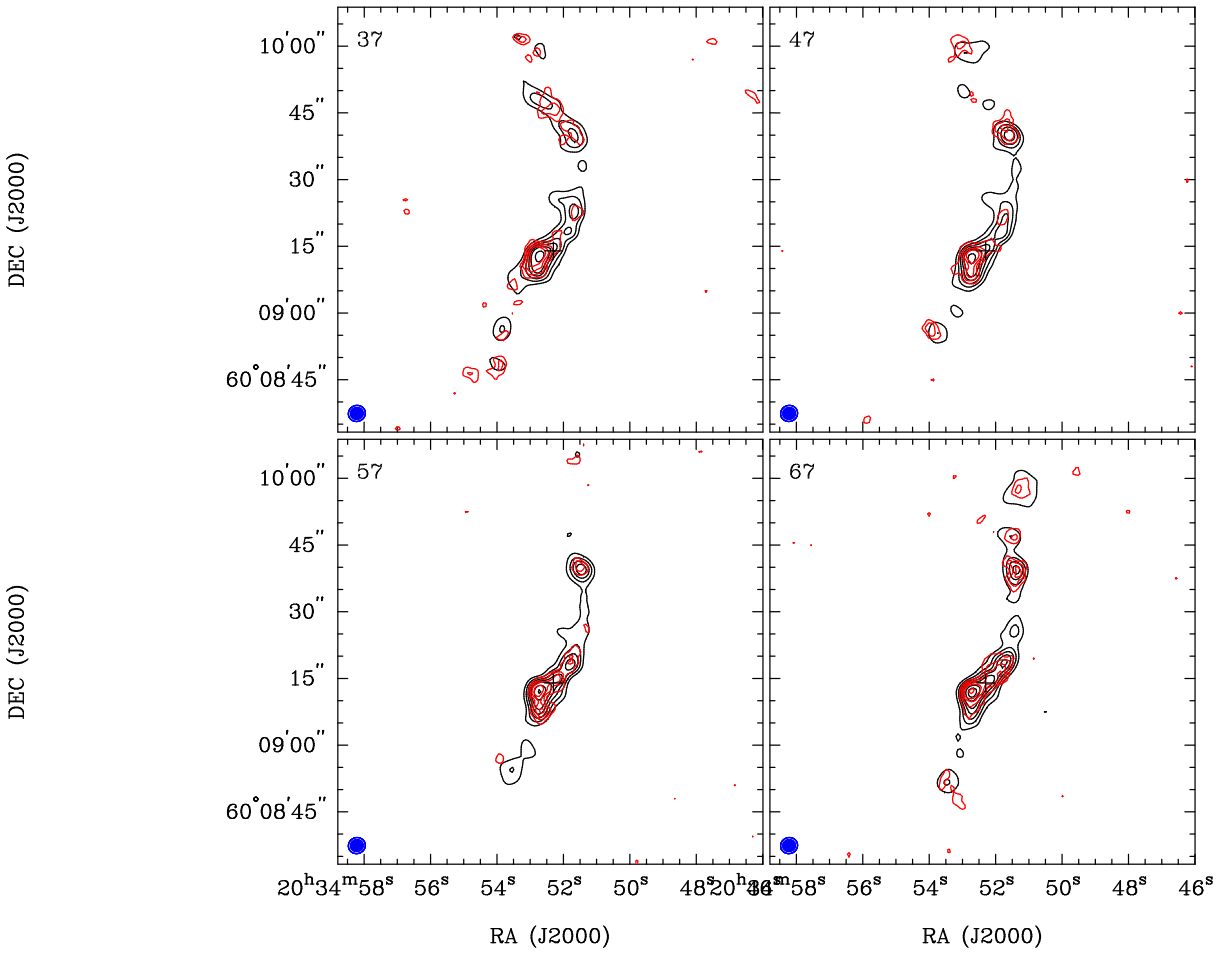

FIGURE 3.17: Continued.

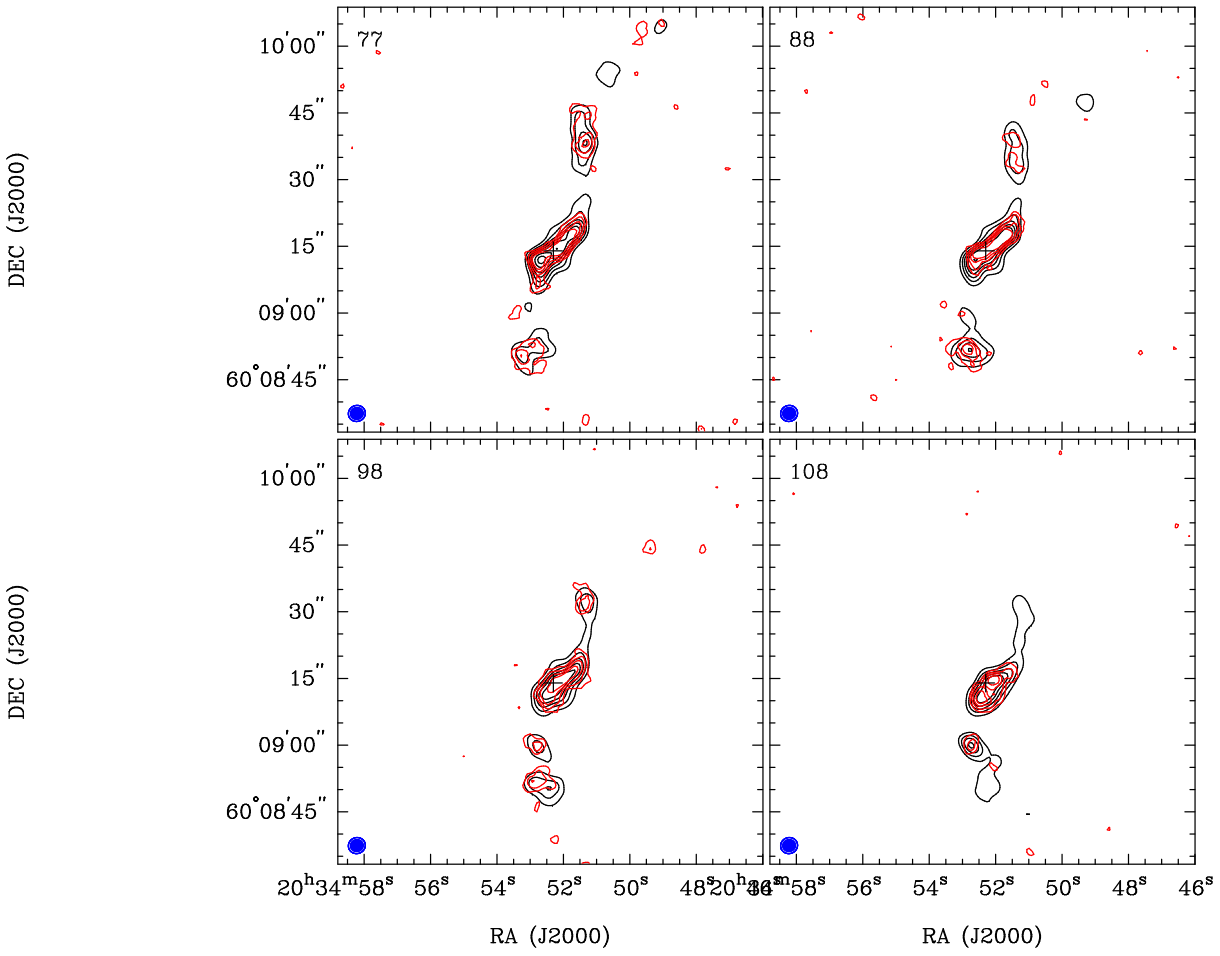

FIGURE 3.17: Continued.

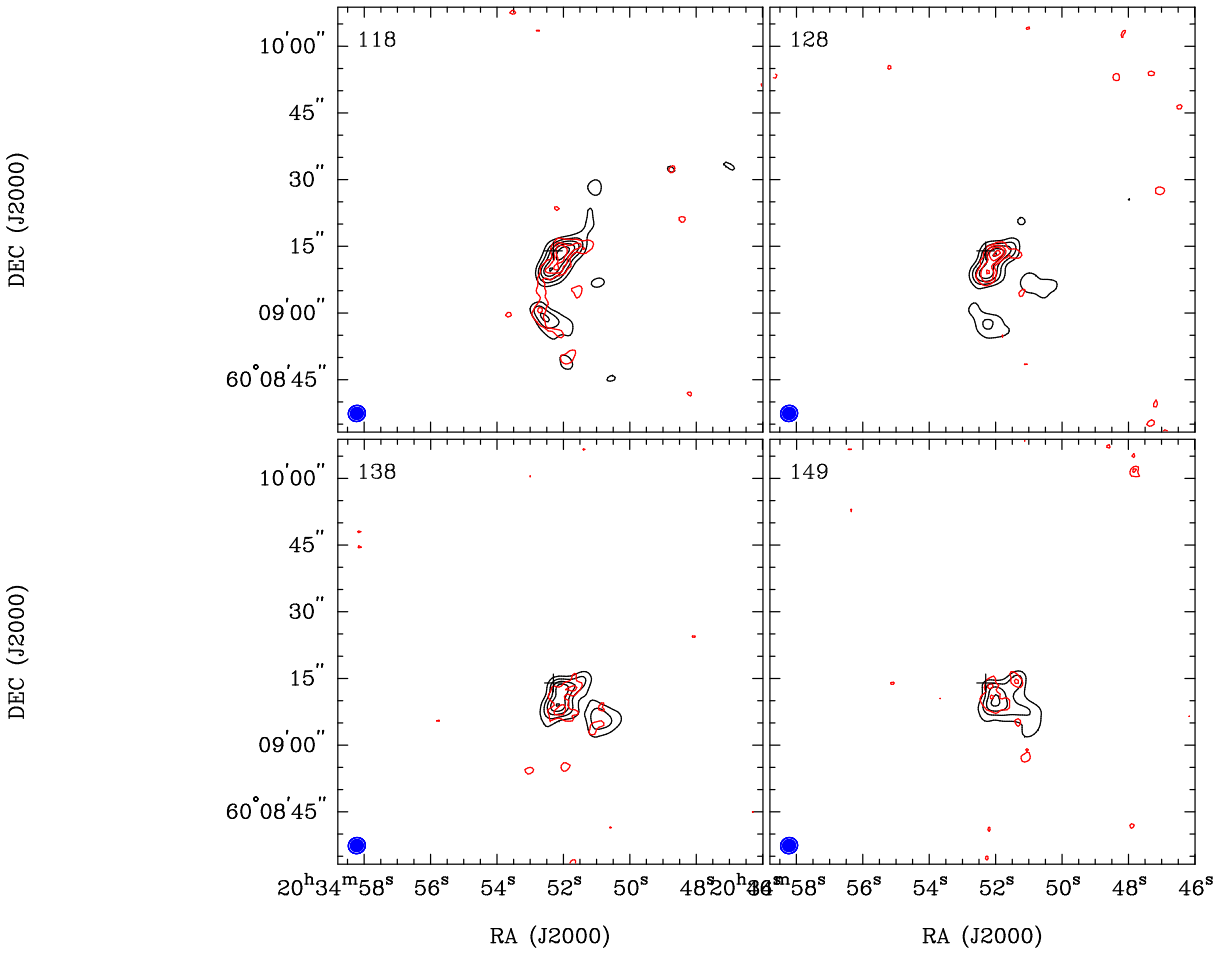

FIGURE 3.17: Continued.

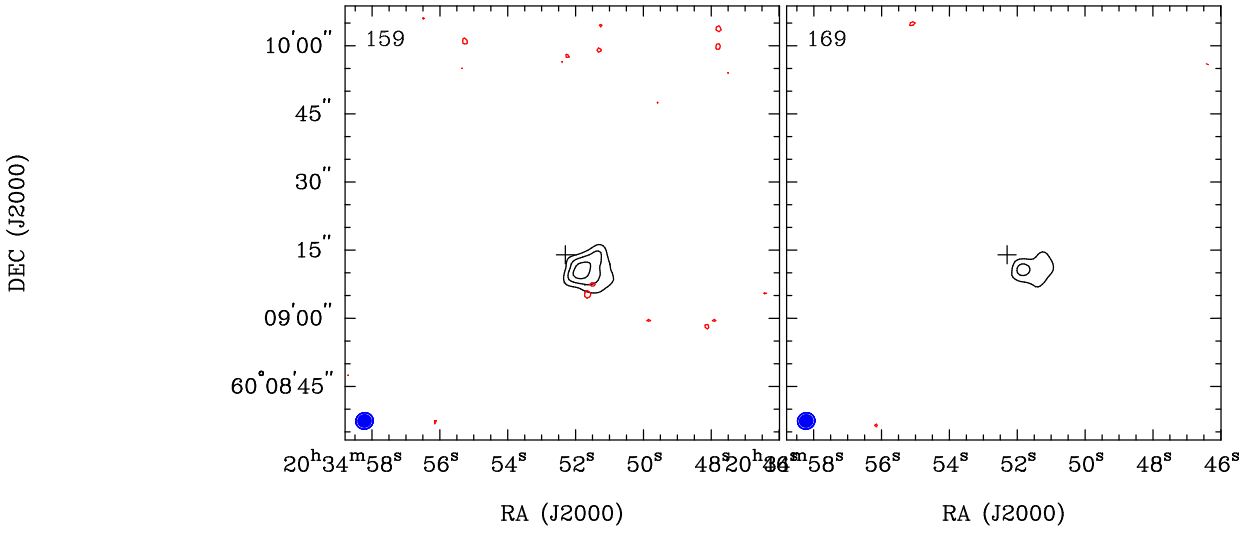

FIGURE 3.17: Continued.

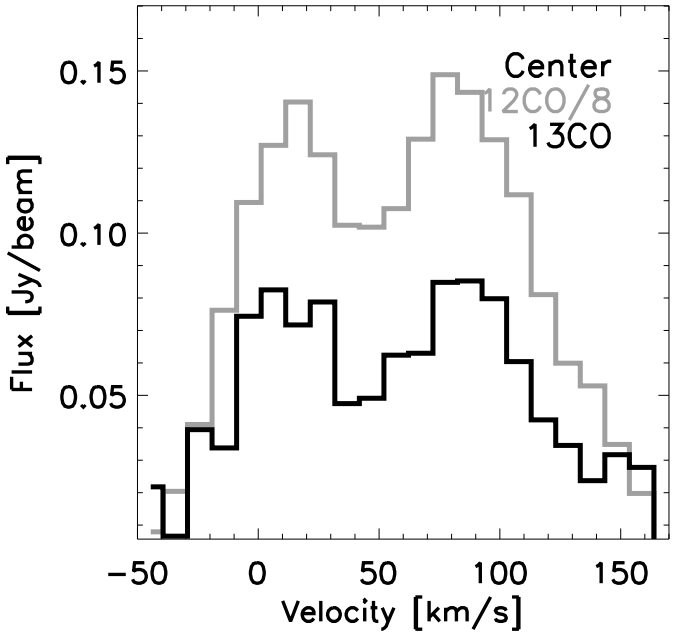

FIGURE 3.18: Spectra of the galactic center. Spectrum of ^{12}CO divided by eight is shown in grey color. ^{13}CO is displayed with black color.

3.5.1.2 Integrated Intensity Maps

Integrated intensity map of ^{13}CO made from the combined channel map (Figure 3.17) is shown in Figure 3.13(b). The *clip* parameter in `moment` is set to be 1.5σ of the channel map. The map peaks at a central concentration. The central concentration in this combined map is similar to that in the CARMA map, presumably due to the small amount of missing flux. The central peak has an oval shape with an orientation toward NW–SE direction. The radius of the oval is about 7.5″ ($\sim$ 200 pc), corresponding to a secondary bar suggested in Elmegreen et al. (1998) and Schinnerer et al. (2006), but not resolved in our map. Figure 3.19 is the minibar observed in^{12}CO (2–1) by Schinnerer et al. (2006). The minibar is composed of a central ring with a radius of 10 pc and two dust lanes. Molecular gas are traveling toward the ring through the lanes. Two clumps are seen in the ends of dust lanes. The two molecular clumps are indicated with red crosses in our moment maps in Figure 3.13.

At the north of the galactic center, a prolonged structure peaking at a radius of $\sim$30″ is seen. This is the northern primary bar of NGC 6946. Figure 3.20 shows a comparison of the ^{13}CO integrated intensity map (contour) and the optical image of *i*-band. It is obvious in the figure that the northern molecular bar coexists with a dust lane in the optical map.

The northern bar is also seen in the ^{12}CO integrated intensity map (Figure 3.21). The striking difference of the two maps is that ^{12}CO shows a continuous emission in the

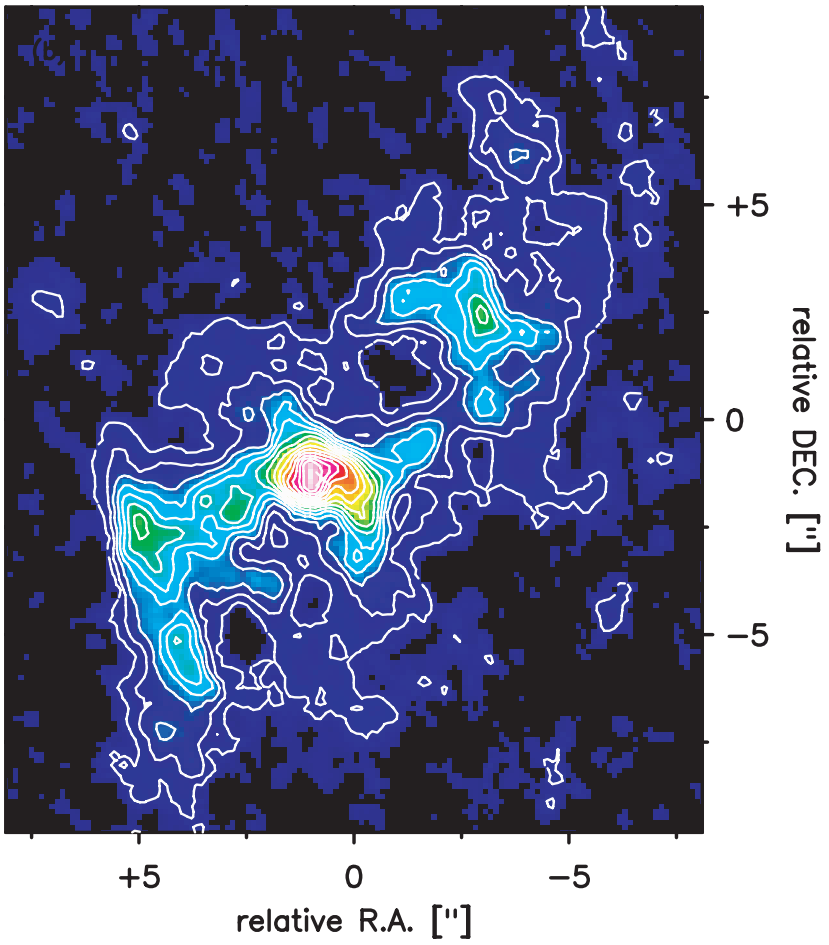

FIGURE 3.19: The central 7.5″ ($R < 200$ pc) from Schinnerer et al. (2006). Both contours and color scale represent the minibar in ^{12}CO (2 – 1). The white cross indicates the galactic center. The beam size is 0.″58 × 0.″48 (∼ 16 pc × 13 pc). The observation was made with IRAM Plateau de Bure interferometer (PdBI).

northern bar, however, there is a gap between the central concentration and the northern bar in ^{13}CO. The "missing bar" corresponds to the missing ^{13}CO emission in the ∼ 67 km s^{-1} of the channel map. Two possibilities of the missing ^{13}CO emission are considered here. In the first place, the "missing bar" in ^{13}CO map is simply due to the insufficient sensitivity. Secondly, it is lacking of ^{13}CO emission at the locus of the "missing bar". We can answer which is possible from the sensitivity of ^{13}CO map and the ^{12}CO/^{13}CO line ratio.

To estimate the line ratio, ^{12}CO map is convolved to the angular resolution of ^{13}CO map. The ^{12}CO flux at the missing bar is about 30 Jy beam $^{-1}$. Then a ^{13}CO flux of ∼ 1.8 Jy beam $^{-1}$ is expected assuming a line ratio of 15 (This is the mean line ratio of the northern bar; cf. §3.6.1), which corresponds to about 4 σ detection. Therefore, the missing ^{13}CO emission in this region is unlikely due to the sensitivity issue, instead, ^{12}CO/^{13}CO ratio is larger than the mean value.

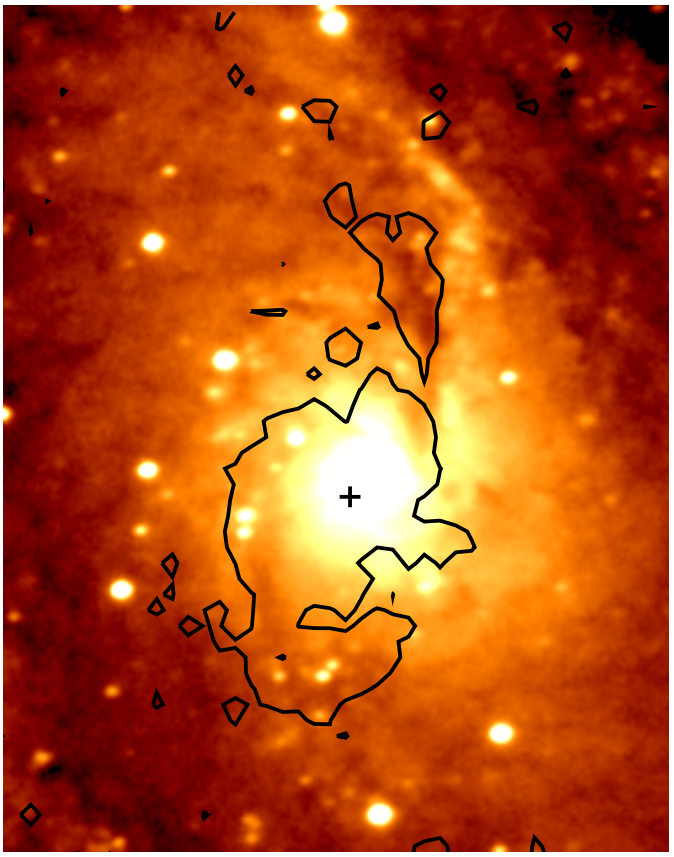

FIGURE 3.20: ^{13}CO integrated intensity map in contour overlaid on *i*-band image in color scale. The contour corresponds to 10% of the peak flux in ^{13}CO map. Galactic center is marked with a black cross.

At the south of the center, the galactic bar is not obvious in the integrated intensity maps. In the ^{12}CO map (Figure 3.21), there are two elongated structures emerging from the central concentration. Two brightest ^{12}CO emission at a radius of $\sim$ -18″[2] and $\sim$ -27″ are found. In the ^{13}CO map, the elongated structures are seen as well. There are three primary peaks (they are more clear in the interferometric map, see Figure 3.13(a)) located at the radius of $\sim$ -18″ and $\sim$ -27″, close to the loci of the ^{12}CO peaks. Since ^{13}CO is able to trace more compact emission than ^{12}CO, the peaks which we have seen in the ^{12}CO are broken into multiple small peaks in ^{13}CO. On the other hand, again, due to the higher critical density of ^{13}CO, the galactic features are more clear in the ^{13}CO map. The two elongated emission at the south of the center are also seen in ^{13}CO but the configuration is more complicated. We will define the name of each galactic feature in §3.5.2.

[2]Minus indicates the south.

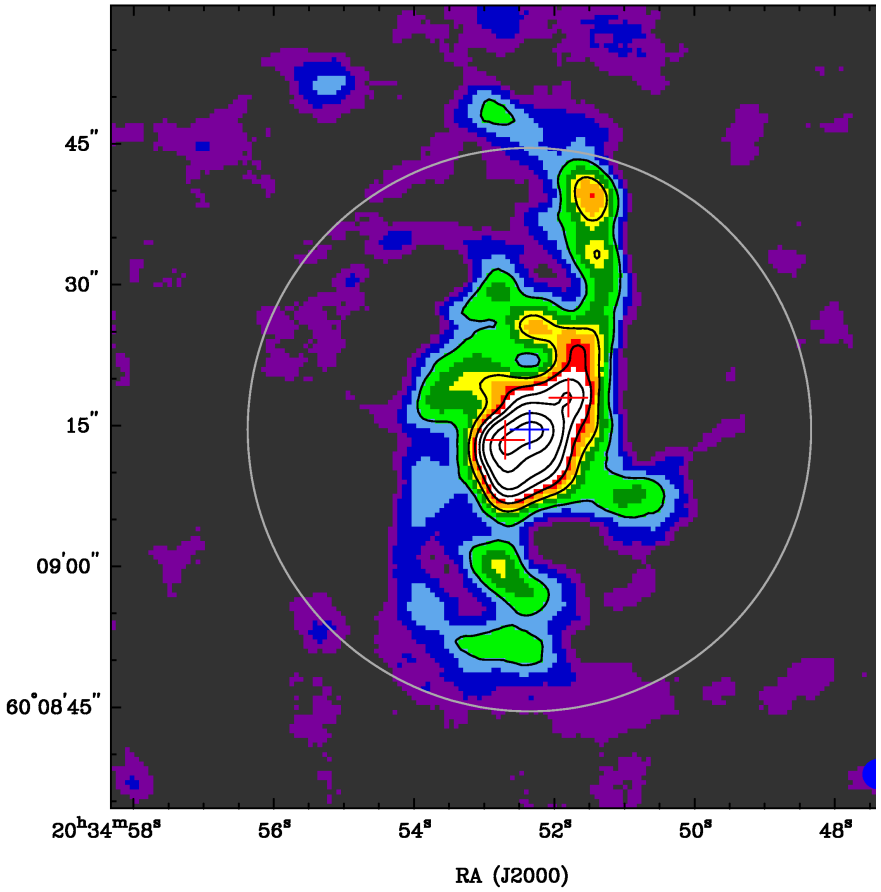

FIGURE 3.21: Integrated intensity map of ^{12}CO (color scale and contours). The contours are 10%, 20%, 30%, 40%, 50%, 70%, and 90% of the peak flux.The red crosses mark the bar ends of the minibar. The grey circle indicates the 1′ primary beam of CARMA. The beam size of 3.″26 × 3.″07 with P.A = -79.28° is superposed at the bottom right corner.

3.5.1.3 Velocity Fields

Velocity fields (first moment) of CO are shown in Figure 3.22. The velocity fields were made with task `moment`. Integrated intensity map is used as mask when making velocity fields. Major axis of velocity field is about 240° at the minibar and galactic center. It is obvious in both ^{13}CO and ^{12}CO maps. However, due to the insufficient sensitivity, velocity field at the ridges are not clear in the ^{13}CO map. The ^{12}CO map shows that the major axis of velocity gradients are about perpendicular to the ridges.

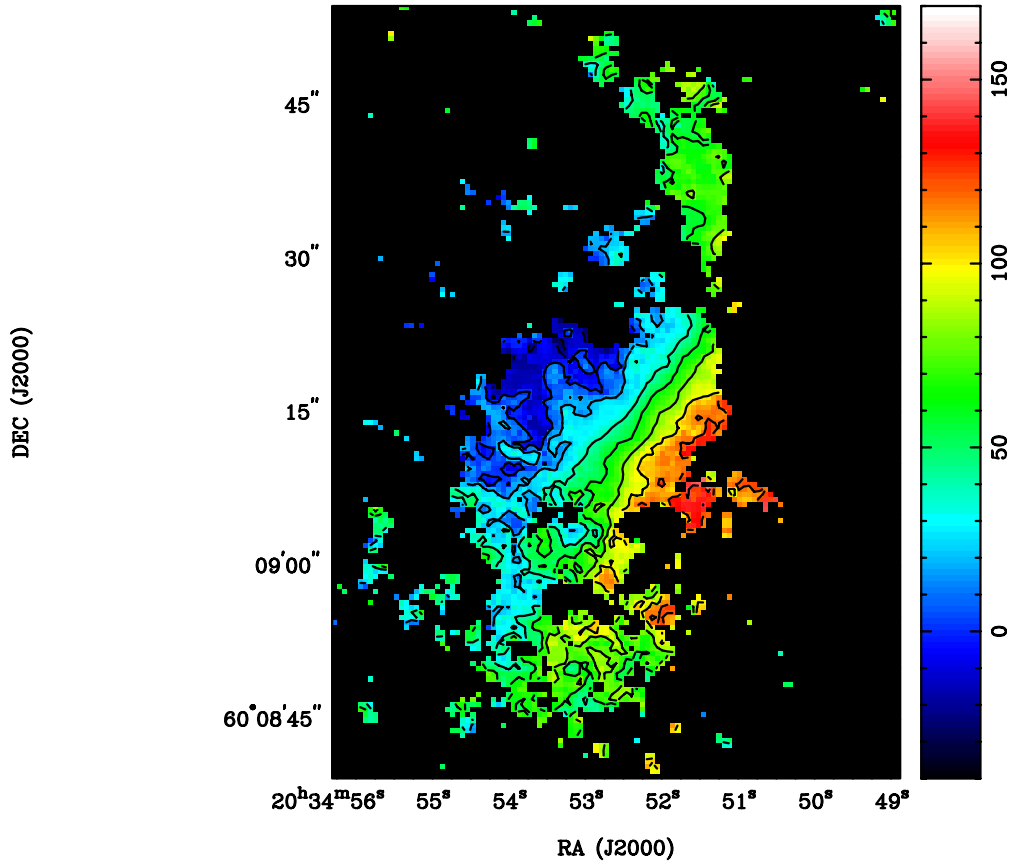

(a)

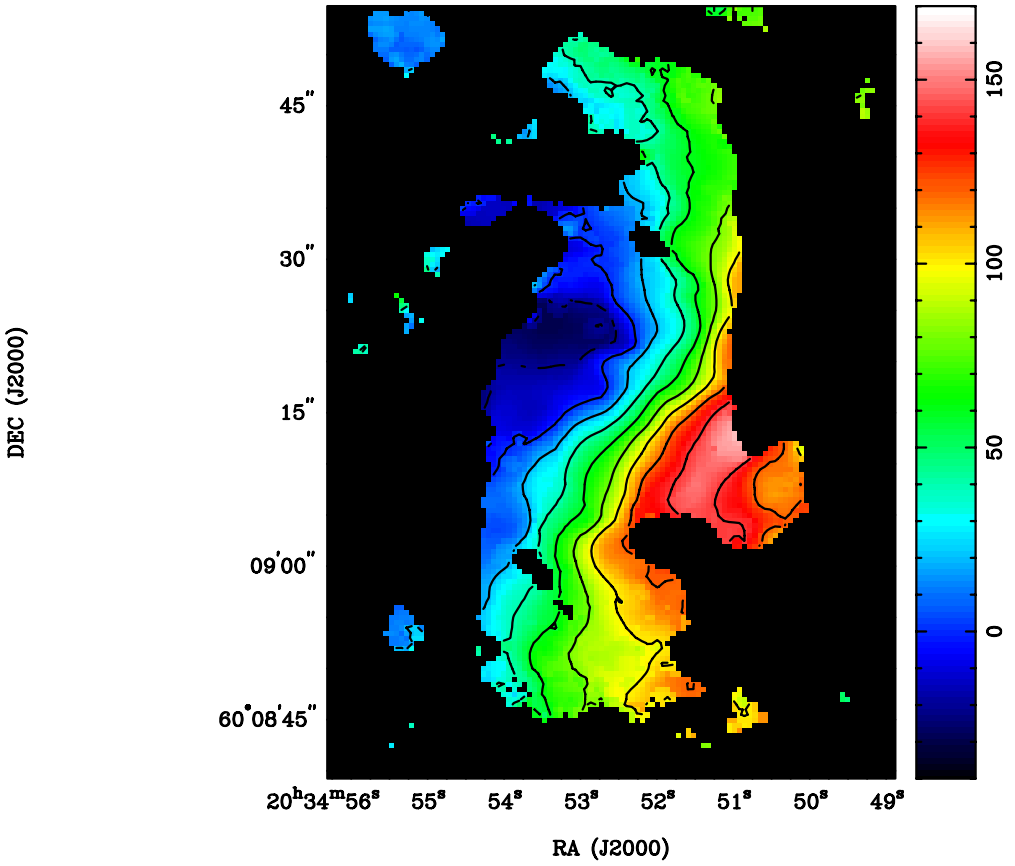

(b)

FIGURE 3.22: Velocity fields of ^{13}CO (a) and ^{12}CO (b). The corresponding velocities of colors are indicated in the wedge in the unit of km s^{-1}. The contours are plotted from -20 – 140 km s^{-1} with a step of 20 km s^{-1} in both maps.

3.5.2 Definition of the Galactic Features in NGC 6946

In the ^{12}CO map of the BIMA SONG[3] with resolution of 6″, the southern bar is more obvious and looks more symmetric relative to the northern bar (Figure 3.23(a)). However, with our resolution of ∼3″, the southern bar splits into two elongated structures (Figure 3.23(b)). It is more pronounced in the ^{13}CO map (Figure 3.13(b)) that one of elongated structures is emerging from the north of the central peak, showing as a very curved, arm-like structure. It merges with the southern bar at the south of the central region. Our angular resolution is not sufficient to resolve the actual configuration of these two galactic features yet. NGC 6946 is a weak bar galaxy, so the bar structure is not as clear as the strong bar galaxies.

Figure 3.24 shows the definition of each structure in this work. The secondary bar is named as the *minibar*, following the nomination in Schinnerer et al. (2006). For the northern bar, since we are not able to define its counterpart at the south, the northern bar is called the *northern ridge* in this work. The curved arm-like structure is referred to the *south spiral*. And the peak emission located at about -18″ is called the *southern blob*. Finally, if necessary, all emission at the south, i.e., the south spiral and the southern blob, will be mentioned as the *southern ridge*.

3.6 Physical Properties of Gas

3.6.1 Line Ratios

^{12}CO to ^{13}CO line ratio (R_{10}, i.e., $\int T_{\rm mb}(^{12}{\rm CO}){\rm d}v / \int T_{\rm mb}(^{13}{\rm CO}){\rm d}v$) can be used as a hint of the physical condition of the gas. The small ratio of $R_{10} < 10$ is seen in the normal disk GMCs of our Galaxy (e.g., Solomon et al., 1979). The intermediate ratio $10 \leq R_{10} \leq 20$ is an indication of starburst region and circumnuclear starburst (e.g., Aalto et al., 1995). The extreme value of $R_{10} > 20$ is found in galaxy mergers (e.g., Taniguchi & Ohyama, 1998). Various causes have been discussed for the observed R_{10}, such as the variation of intrinsic abundance ratio, kinetic temperature, velocity dispersion, density of gas, stellar feedback, and kinematics of galaxies (Aalto et al., 1995, Paglione et al., 2001, Sakamoto et al., 1997, Taniguchi & Ohyama, 1998).

R_{10} of NGC 6946 is shown in Figure 3.25. Pixels with S/N of ^{13}CO greater than 2.5σ were used. It is notable that R_{10} changes by more than three times within the central 1′ of NGC 6946. The galactic center has R_{10} of ∼17, which is consistent with the value for a nuclear starburst (Aalto et al., 1995). The minibar-ends also show a high R_{10} of

[3]The BIMA Survey of Nearby Galaxies

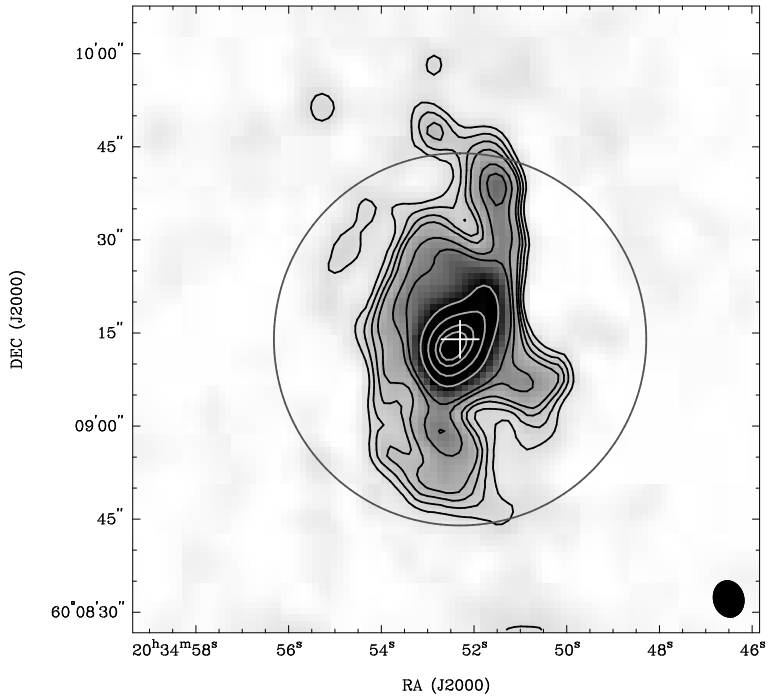

(a)

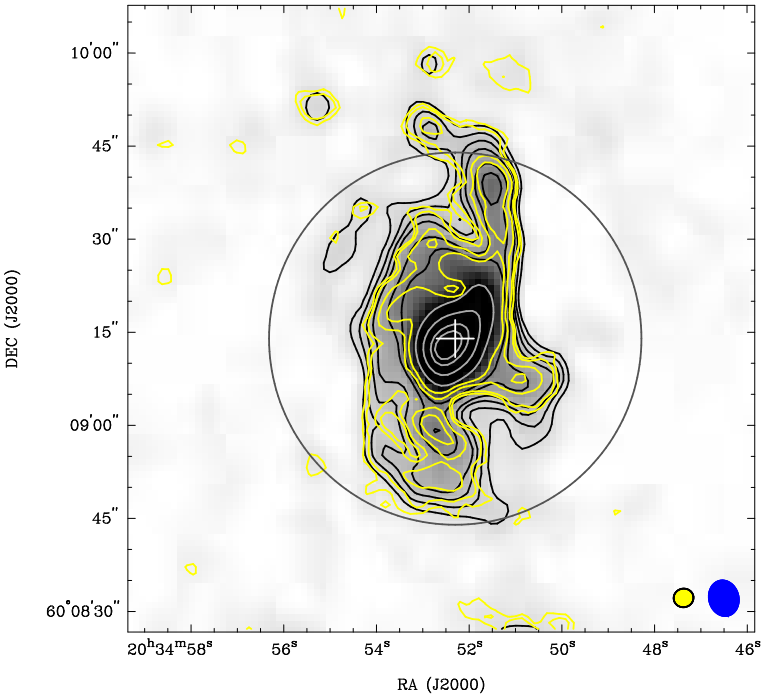

(b)

FIGURE 3.23: (a)The ^{12}CO (1–0) map from BIMA. The beam size of $5\farcs92 \times 4\farcs89$ with P.A = 14.19° is overlaid in the bottom right of the figure. The contours represent 5%, 7%, 9%, 11%, 16%, 20% ,40% ,60% ,80%, and 90% of the peak. The white cross indicates the galactic center. The circle shows the $1'$ primary beam of CARMA.(b) Same as panel (a) but the contours (yellow) of our higher resolution map are overplotted. The yellow contours are 6.5, 8.5, 15, and 22 Jy beam^{-1}.

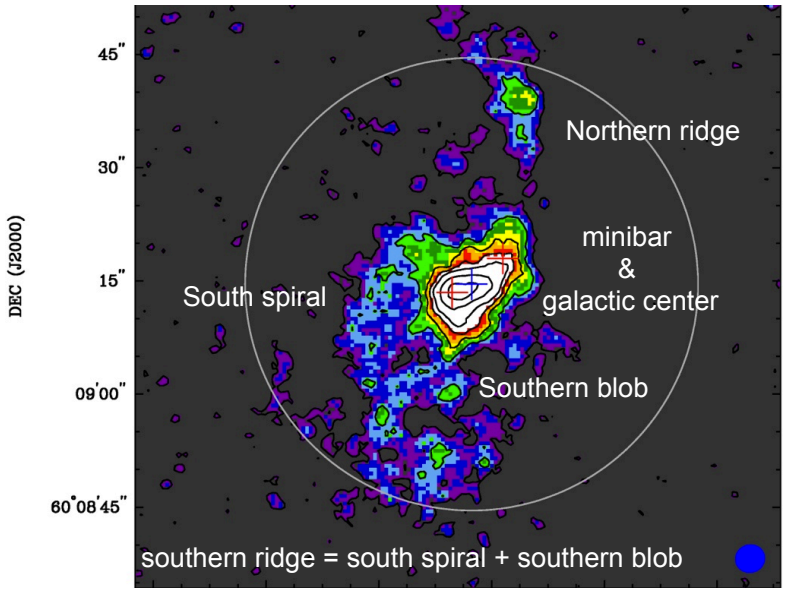

FIGURE 3.24: Definition of galactic features.

15 – 16. The northern ridge has R_{10} of ∼12 – 20, with a mean value of ∼ 15. In the south spiral, R_{10} is as high as ∼ 11 – 15 when it just emerges from the central region, then significantly decreases to 6 – 10 over the majority of the spiral. Then R_{10} increases again to ∼ 12 at the region where the spiral and the southern blob blend together. The southern blob also has a moderately high R_{10} with a mean value of ∼ 12 – 13. R_{10} of each galactic features are summarized in Table 3.3.

Previous works have suggested a moderately high R_{10} of $\geqslant$ 10 at galactic bars (Hirota et al., 2010, Hüttemeister et al., 2000, Watanabe et al., 2011). Thus the southern blob and the end of the south spiral may correspond to the southern bar.

We compare the derived R_{10} with the measurements carried out with other telescopes and other independent measurements of NRO45. The mean R_{10} in the central $1'$ of our map is 12.3 ± 0.4. The value is in good agreement with R_{10} measured by NRAO 12-m telescope (Sage & Isbell, 1991). They obtain a value of 11.1 ± 0.8 within a beamsize of $57''$. We also compare R_{10} with Young & Sanders (1986) and Paglione et al. (2001). Young & Sanders (1986) and Paglione et al. (2001) measure R_{10} with the FCRAO 14-m telescope. The 14-m dish results to a beamsize of ∼$45''$. R_{10} within the central $45''$ is 15.6 ± 0.3 in this work, 15.0 ± 1.4 in Young & Sanders (1986), and 17.0 ± 1.4 in Paglione et al. (2001). The values are comparable within the uncertainties again. Then we compare R_{10} with other independent observations of NRO45. Within the central $20''$ (one beam of NRO45), our R_{10} is 16.8 ± 0.3. With the measurements of NRO45 in ^{12}CO from Komugi et al. (2008) and ^{13}CO from Matsushita et al. (2010), R_{10} within $20''$ is 17.9 ± 1.2. Again, the derived R_{10} in this work are in good agreement with other independent measurements.

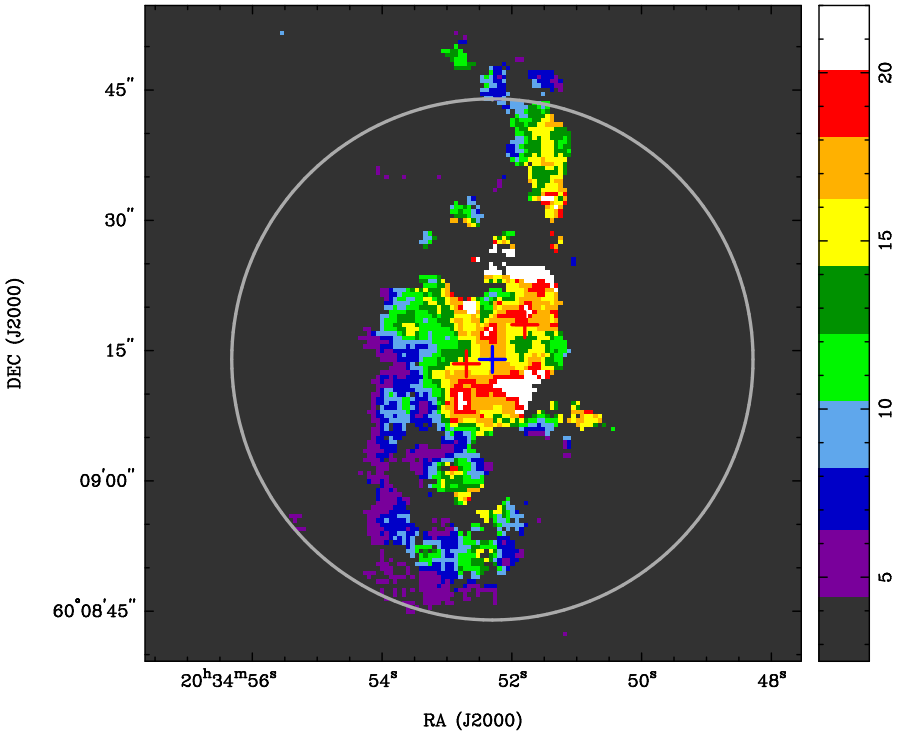

FIGURE 3.25: R_{10} ratio map ($R_{10} = \int T_{\rm mb}(^{12}{\rm CO}){\rm d}v / \int T_{\rm mb}(^{13}{\rm CO}){\rm d}v$). The blue and the red crosses denote the galactic center and the minibar ends, respectively. The gray circle shows the 1′ primary beam of CARMA. The corresponding color of R_{10} is indicated in the wedge.

TABLE 3.3: The R_{10} and R_{21} of each galactic feature. The R_{10} is derived based on a angular resolution 3.8″, and 20″ for R_{21}.

Component	R_{10}	R_{21}	($T_{\rm k}$,$n_{\rm H_2}$)
Center	17	∼1.0	($>$ 20 – 40 K, $\approx 10^{3.5}$ cm^{-3})
			($\approx$ 20 – 35 K, $> 10^{4.0-4.5}$ cm^{-3})
Minibar end	15– 16	∼1.0	($>$ 20 – 40 K, $\approx 10^{3.5}$ cm^{-3})
			($\approx$ 20 – 30 K, $> 10^{4.0-4.5}$ cm^{-3})
Northern ridge	12 – 20	∼0.8	($>$ 15–20 K, $\approx 10^{2-3}$ cm^{-3})
South spiral	6 – 15	$\leq$0.8	($<$ 30 K, $< 10^{3.0}$ cm^{-3})
			($>$ 3 K, $< 10^{3.0}$ cm^{-3})
Southern blob	12 – 13	$\leq$0.8	($>$ 3 K, $< 10^{3.0}$ cm^{-3})

3.6.2 Large Velocity Gradient Model (LVG)

We use single-component Large Velocity Gradient (LVG) models (Goldreich & Kwan, 1974, Scoville & Solomon, 1974) to estimate the physical properties of molecular gas. The physical conditions required to excite molecular lines are determined by line opacity (column density ($N_{\rm CO}$) per unit velocity change (dv)), kinetic temperature ($T_{\rm k}$), and volume density ($n_{\rm H_2}$) of the gas. Observed line ratio can be used to constrain the solutions of $T_{\rm k}$ and $n_{\rm H_2}$.

Low J transition of CO is excited by collisions with H_2. The CO-H_2 collisional cross sections are taken from Yang et al. (2010). Typical $\log(N_{\rm CO}/dv)$ of Galactic and M51 GMC is in the range of 16.6 – 17.3 (Koda et al., 2009, Schinnerer et al., 2010). For NGC 6946, typical $\log(N_{\rm CO}/dv)$ is about 17.0. The abundance of ^{12}CO relative to H_2 is set to be 8.0×10^{-5} (Schinnerer et al., 2010). The intrinsic abundance ratio of ^{12}CO-to-^{13}CO is set as 60, which is derived based on the Galactic GMCs (Frerking et al., 1982). Thus the ^{13}CO abundance is about 1.3×10^{-6}. The code of LVG calculations is the same as in Koda et al. (2012), which is written in `IDL`.

To get better constraints on two parameters, $T_{\rm k}$ and $n_{\rm H_2}$, at least two line ratios are required. In addition to R_{10}, one more transition is needed in this work. ^{12}CO (2–1) is reckoned as an ideal transition. Like R_{10}, ^{12}CO (2–1) to ^{12}CO (1–0) ratio (R_{21}) changes over galactic environments as well. First of all, R_{21} is ∼0.4–0.7 in the normal GMCs at the midplane of the Galactic disk up to about solar neighborhood and the inter-arm regions of spiral galaxies (Koda et al., 2012, Oka et al., 1998, Sakamoto et al., 1997). The warm and dense gas, presumably associated with star forming regions, have higher R_{21} of 0.7–0.9 in the Galactic disk and the spiral arm of external galaxies (Koda et al., 2012, Sakamoto et al., 1997). Around the galactic centers, R_{21} is about 1.0 (Koda et al., 2012, Sawada et al., 2001). Thus the most probable R_{21} is in a range of 0.4 – 1.0.

We do not have ^{12}CO (2–1) data with compatible resolution as our combined map, but single dish ^{12}CO (2–1) map is available from IRAM HERACLES (The HERA CO-Line Extragalactic Survey). ^{12}CO (2 – 1) map of NGC 6946 is displayed in Figure 3.26 with an angular resolution of 13.″4.

The map of ^{12}CO (2–1) is convolved to a resolution of 20″ to compare with the single dish ^{12}CO (1–0) data in this work. The R_{21} map of our interested region is shown in the left panel of Figure 3.27. Within the central 1′, R_{21} ranges between ∼0.65 and 1.0. There is an oval region with $R_{21} \approx 1$, the orientation of the oval is consistent with the minibar but far from resolved. Under this resolution, the southern ridge is not found. At the location of the southern ridge, R_{21} is about unity, but obviously it is a contribution from the minibar. For this reason, we will discuss the results of LVG calculations of the

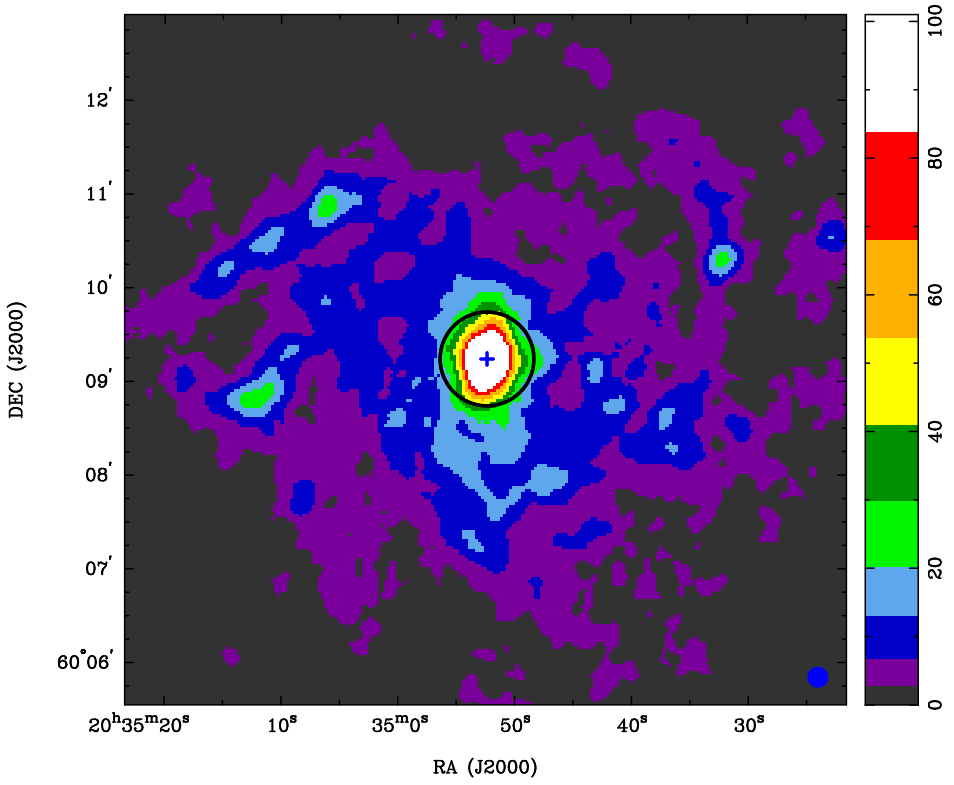

FIGURE 3.26: ^{12}CO (2 – 1) map of NGC 6946 from IRAM 30-m telescope. The beam size of 13.″4 is shown in the bottom right. Galactic center is marked with a cross. The circle indicates the 1′ primary beam of CARMA. The color bar is in the unit of K km s^{-1} in $T_{\rm mb}$.

southern ridge starting from $R_{21} \approx 1$ as an upper limit, and decrease R_{21} if necessary. The northern ridge shows $R_{21} \approx 0.8$. Beyond the central 1′, R_{21} decreases to 0.3 – 0.7. Specifically, R_{21} is about 0.5 – 0.8 in the spiral arms, and 0.3 – 0.5 in the inter-arm regions. The derived R_{21} is consistent with the ratio found in the spiral arms and the inter-arm regions of M 51 from Koda et al. (2012). Right panel of Figure 3.27 shows a comparison of R_{21} and star forming regions traced by Spitzer. The high R_{21} is associated with active star forming regions.

The results of LVG calculations are shown in Figure 3.28 for $R_{10} = 7$ and 10, and Figure 3.29 for $R_{10} = 12$ and 15. R_{21} of 0.4, 0.6, 0.8, and 1.0 are plotted in all panels of figures. Figure 3.28(a), 3.28(b), 3.29(a), and 3.29(b) represent the results of $R_{10} = 7$, 12, 15, and 17, respectively, assuming an isotopic abundance ratio of 60. The grey and black solid curves represent the corresponding line ratio of $\log(N_{\rm CO}/dv) = 16.6$ and 17.3, respectively. We find the possible solutions of $T_{\rm k}$ and $n_{\rm H_2}$ enclosed in the curves of R_{10} and R_{21}.

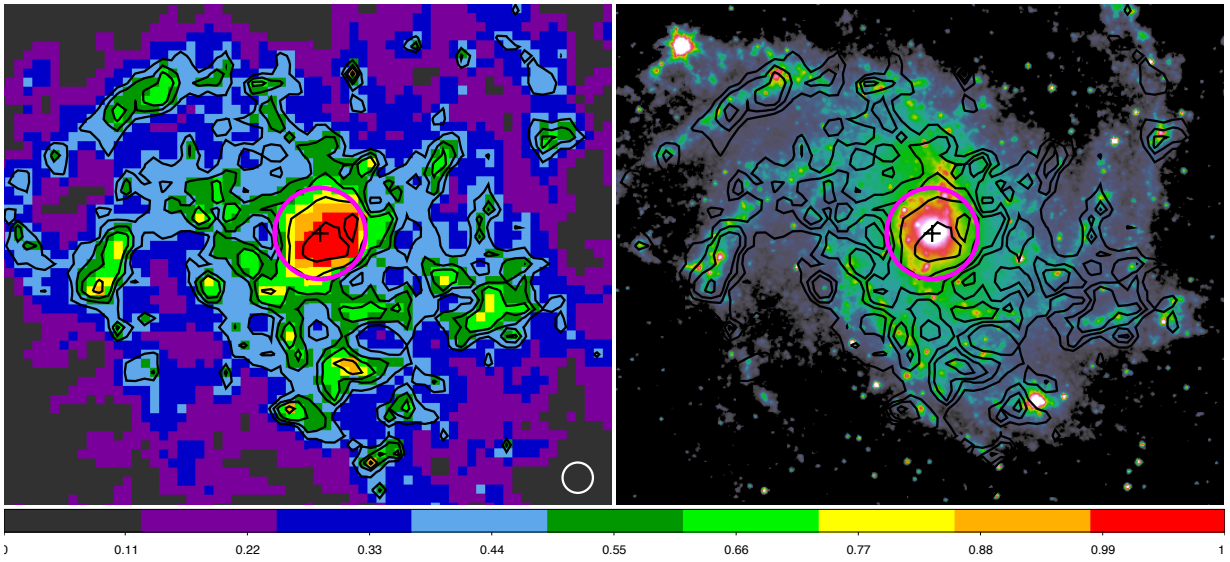

FIGURE 3.27: Left: R_{21} map. Both contours and color scale represent R_{21}. The contours are with steps of 0.4, 0.5, 0.6, 0.8, and 1.0. The color bar indicates R_{21}. The magenta circle indicates the central $1'$ in diameter. The black cross marks the galactic center. The beamsize of $20''$ is over-plotted at the lower right corner. Right: R_{21} map (contours) overlaid on Spitzer 8μm image (color scale). The steps of contour are the same as in the left panel. Coordinates of two panels are matched.

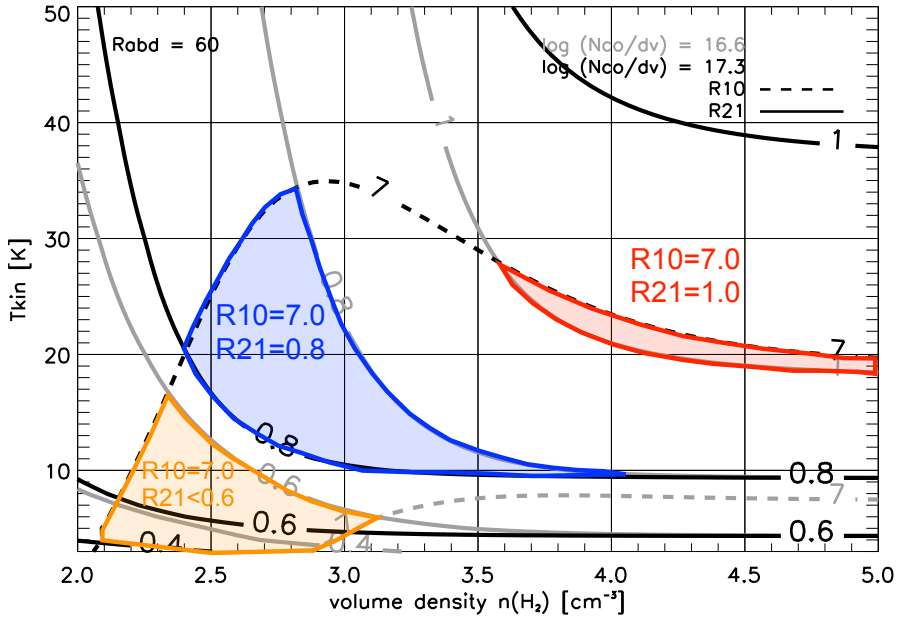

(a)

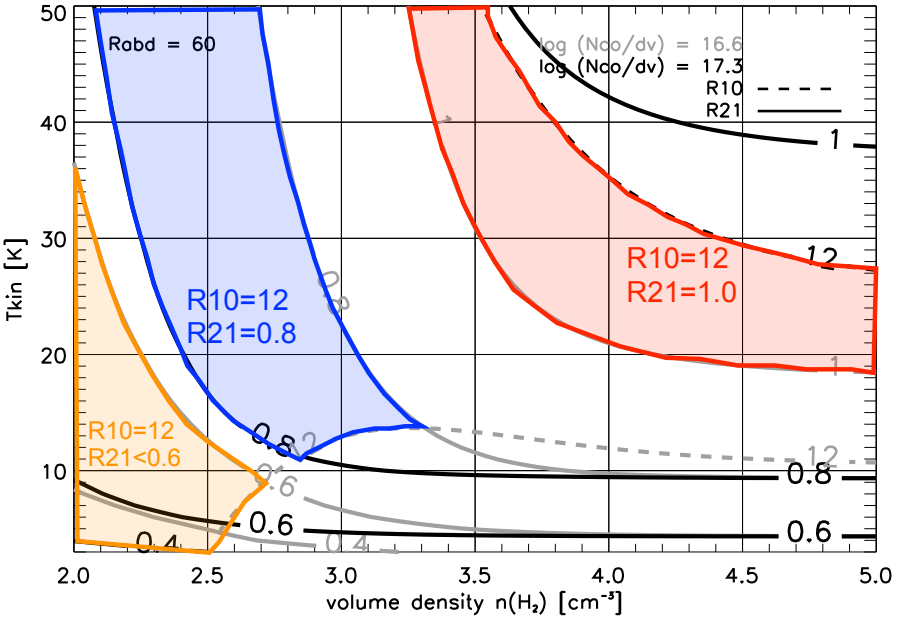

(b)

FIGURE 3.28: Large Velocity Gradient (LVG) calculations for $R_{10} = 7$ (a) and 12 (b). X- and Y-axis are temperature and volume density, respectively. The volume density is shown in log scale. The line ratio R_{10} is plotted with dashed lines, and R_{21} is in solid lines. The grey curves represent $\log(N_{\rm CO}/dv) = 16.8$ and the black curves are $\log(N_{\rm CO}/dv) = 17.3$. The isotopic abundance ratio is assumed to be 60 in all calculations. The red, blue and orange highlight the resultant solutions of the individual R_{10} of each panel along with $R_{21} = 1.0$, 0.8, and $\leqslant 0.6$, respectively.

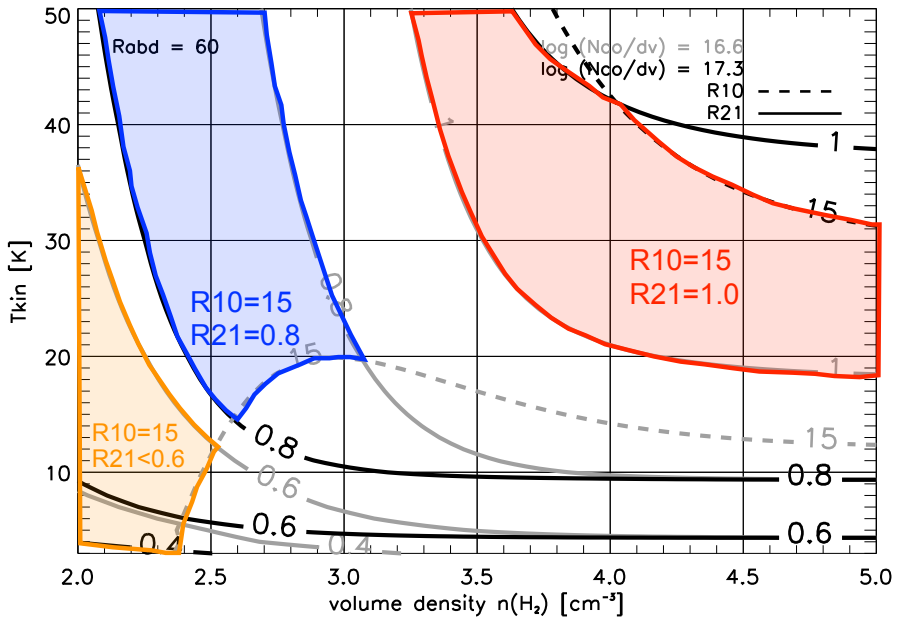

(a)

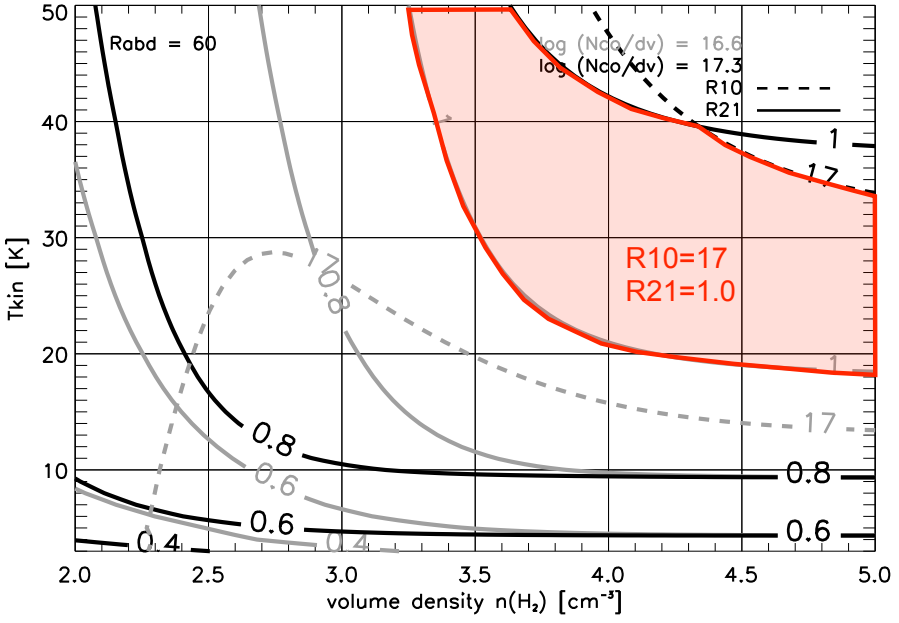

(b)

FIGURE 3.29: Large Velocity Gradient (LVG) calculations for $R_{10} = 15$ (a) and 17 (b). The line styles and color areas are the same as in Figure 3.29.

3.6.2.1 Gas Properties in the Ridges

At the northern ridge, R_{10} is ~ 15 and R_{21} is about 0.8. The solution of LVG calculations is displayed in Figure 3.29(a), and highlighted with a color of blue. The resultant $n_{\rm H_2}$ shows that the density is relatively low as 10^{2-3} cm^{-3}. A lower limit of $T_{\rm k}$ is derived as $> 15 - 20$ K. The results of LVG calculations are summarized in Table 3.3.

At the southern spiral R_{10} is $\sim$12 and R_{21} is ~ 1.0 in the low resolution R_{21} map. These ratios lead to $T_{\rm k} \approx 20 - 30$ K, $n_{\rm H_2} > 10^{3.5}$ cm^{-3} (Figure 3.28(a), red area).

At the south blob, the mean R_{10} is $\sim$12 and the R_{21} is ~ 1.0 in the low resolution R_{21} map. These ratios suggest two possible solutions (Figure 3.28(b), red area). One solution suggests a cold and dense gas with $T_{\rm k} = 20 - 30$ K and $n_{\rm H_2} > 10^{3.5}$ cm^{-3}. These conditions are suitable to initiate the future star formation. The second solution suggests a moderately warm and less dense gas with $T_{\rm k} > 30$ K and $n_{\rm H_2} \approx 10^{3.0} - 10^{3.5}$ cm^{-3}. This solution implies the existence of the gas associated with current star formation.

The solutions in the south spiral and the southern blob suggest that the gas in these regions are denser by more than two times than that in the northern ridge. However, it cloud be a result of a poor-constraint of R_{21}. If such a high density is true, we would see a significantly higher dense gas fraction in the southern ridge than that of the northern ridge. HCN (1–0) (§3.4.3) and $I_{\rm HCN}/I_{^{12}\rm CO}$ ($R_{\rm HCN/CO}$) can be used as an indication of the amount of dense gas and dense gas fraction, respectively.

Single dish $R_{\rm HCN/CO}$ at the northern and southern ridges are 0.068 and 0.053, respectively. The ratios do not support a larger dense gas fraction in the southern ridge. For comparison, the central region (galactic center and minibar) has a $R_{\rm HCN/CO}$ as high as 0.112, which is about two times higher than the ridges and consistent with $R_{\rm HCN/CO}$ of other starburst galaxies (see Figure 13 of Pan et al. (2013)). As the LVG calculations predict that higher R_{21} leads to denser gas (higher $R_{\rm HCN/CO}$), R_{21} of the southern ridge is unlikely greater than 0.8. It is because to produce $R_{21} > 0.8$, $n_{\rm H_2}$ should be larger than $\sim 10^3$ cm^{-3}, namely, denser than the northern ridge, which conflicts the observed $R_{\rm HCN/CO}$.

Provided that the the majority regions in the southern ridge have $R_{10} \approx 6 - 13$ and R_{21} is $\leqslant 0.8$, $n_{\rm H_2}$ would be at most $10^{3.0}$ cm^{-3} for $R_{10} = 7$ and 12 (Figure 3.28(a) and 3.28(b)). For low R_{10} (< 10), $T_{\rm k} < 30$ K, but at high R_{10} regime (> 10), $T_{\rm k} > 3$ K .

3.6.2.2 Gas Properties in the Minibar and the Center

R_{10} and R_{21} are about 15 and 1.0 at the minibar, respectively. The resultant solutions of LVG calculations is displayed in Figure 3.29(a). Two possible solutions are found, which are ($T_{\rm k} > 20 - 40$ K, $n_{\rm H_2} \approx 10^{3.5}$ cm^{-3}) and ($T_{\rm k} \approx 20 - 30$ K, $n_{\rm H_2} > 10^{4.0-4.5}$ cm^{-3}) (Figure 3.29(a), red area). Both solutions suggest that the molecular gas in the minibar are denser than the ridges.

The galactic center has R_{10} and $R_{21} \sim 17$ and ~ 1.0, respectively. The LVG model again predicts two gas components with ($T_{\rm k} > 20 - 40$ K, $n_{\rm H_2} \approx 10^{3.5}$ cm^{-3}) and ($T_{\rm k} \approx 20 - 35$ K, $n_{\rm H_2} > 10^{4.0-4.5}$ cm^{-3}) (Figure 3.29(b), red area). High density of $n_{\rm H_2} \geqslant 10^{3.5}$ is suggested in both the center and minibar with LVG calculations, which is consistent with predictions from the HCN observations and $R_{\rm HCN/CO}$ that minibar and center contain more dense gas and a higher dense gas fraction than the ridges. Moreover, it is possible that the gas is mostly dominated by the dense component in the central starburst regions. The fraction of dense gas can up to ~ 100 % (e.g., Kohno et al., 1999, Pan et al., 2013).

In the central region (galactic center and minibar), LVG calculations of CO lines suggest two solutions. One is cold (20 – 30 K) and extremely dense ($> 10^{4.0-4.5}$ cm^{-3}), another one is warm ($>$ 20 – 40 K) and moderalty dense ($\sim 10^{3.5}$ cm^{-3}). Both solutions are possible and may exist together. Mangum et al. (2013b) estimated the kinematic temperature of the central region of NGC 6946 with NH_3. They also found two components of temperature, 25 $\pm$ 3 K and 50 $\pm$ 10 K. Both are consistent with the LVG calculations in terms of the temperature. In terms of density, the detection of ^{13}CO and NH_3 implies the existence of gas $\geqslant 10^{3-4}$ cm^{-3}[4]. On the other hand, the detection of HCN (this work) and H_2CO Mangum et al. (2013a) suggests a gas with a density $\geqslant 10^5$ cm^{-3} . Hence, we are not able to rule out any population which suggested by the LVG results of CO lines in terms of density.

Henkel et al. (1998) suggest an isotopic abundance ratio of ~ 40 at the center of infrared bright galaxies. Our result of LVG calculations with the abundance ratio of 40 is displayed in Figure 3.30. The solutions are well consistent with the results with abundance of 60 because the solutions are controlled by the regime of in which $R_{21} = 1.0$ is reproduced, but R_{21} is irrelevant to constrain the isotopic abundance.

Physical properties of gas in the central 1′ of NGC 6946 is summarized below. The LVG calculations suggest that the galactic center is denser than the ridges by about an order magnitude. Density of the gas in the galactic center and minibar is on an order of $10^{3.5-4.5}$ cm^{-3}, and $< 10^3$ cm^{-3} in the ridges. HCN observations show that the dense

[4]The effective critical density NH_3 is $\sim 10^4$ cm^{-3} (Ho & Townes, 1983).

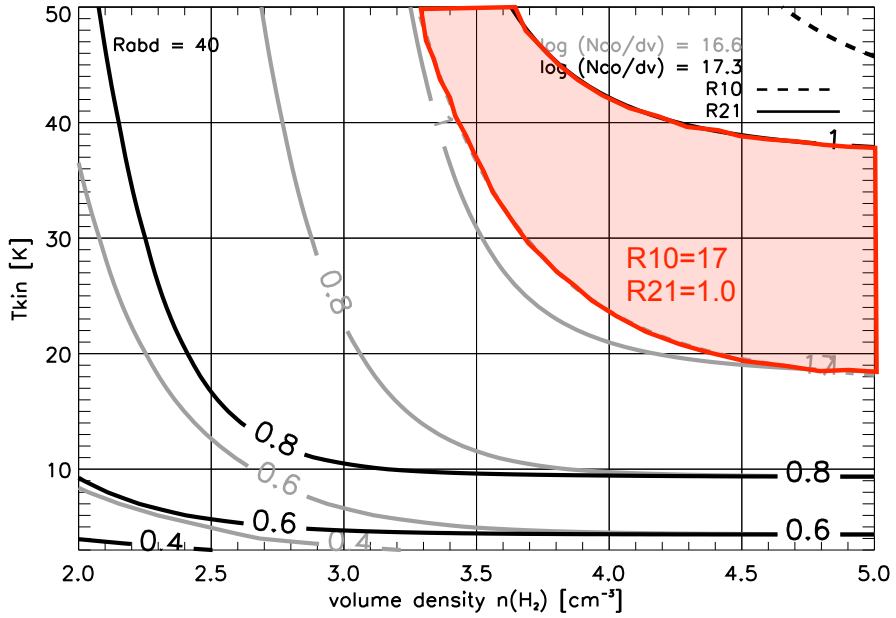

FIGURE 3.30: LVG results for the galactic center with $R_{10} = 17$ and isotopic ratio of 40. The line styles and color areas are the same as in Figure 3.29.

gas fraction in the central region (galactic center and minibar) is about two times larger than that of the ridges. On the other hand, dense gas fraction in the northern ridge is about 1.3 times larger than the southern ridge. Temperature is poorly constrained with the LVG calculations. Even so, there is a sign that the galactic center, minibar and the northern ridge are warmer, with a temperature of $\geqslant 15 - 40$ K, whereas the southern ridge is associated with colder gas with $T_{\rm k} < 30$ K.

3.6.3 Cause of the Variation of R_{10}

The ratio map shows that R_{10} has a broad range of $6 - 20$ within the central $1'$. LVG calculations and HCN observations indeed show some variations of gas temperature and density in this area. We consider more possibilities and details of the variation of R_{10} in this section.

Extreme starburst galaxies have been confirmed to have high dense gas fraction through HCN observations (e.g., Gao & Solomon, 2004a), and also very high R_{10} (> 20; Taniguchi & Ohyama, 1998). If R_{10} implies dense gas fraction, given that the effective critical density of ^{13}CO is larger than that of ^{12}CO, high R_{10} means the dense gas fraction is extremely low in these starburst objects, conflicting with the HCN observations (e.g., Gao & Solomon, 2004a). Thus dense gas fraction is not direct reason of the various R_{10}.

R_{10} could be changed due to the intrinsic variation of isotopic abundance ($[^{12}CO]/[^{13}CO]$). Stellar feedback, gas flow in galaxies, and chemical processes could alter isotopic abundance. In very early starburst, ^{12}C is produced quickly during helium burning of very massive star formation. ^{13}C is a secondary product which requires ^{12}C as seeds. It is produced during hydrogen-burning and is enriched in ISM by the ejections of stars (Henkel & Mauersberger, 1993). Moreover, ^{13}C can be produced during the third dredge-up of intermediate mass stars. In terms of the gas flow in galaxies, some works propose a possibility that when gas is transported toward the galactic center, fraction of ^{13}C around the central region is diluted by the less-processed gas (less ^{13}C) from the disk (e.g., Paglione et al., 2001, Taniguchi & Ohyama, 1998), resulting a depression of ^{13}CO and a large R_{10} in galactic centers. Chemical processes of photodissociation and fractionation are able to alter isotopic abundance as well, they have been discussed in §2.9.2.

Derivation of isotopic abundance relies on chemical study with chemical species, such as ^{12}CN, ^{13}CN. However, since these chemical species are generally weak, observations in external disk are impractical, hence it is difficult to constrain the variation of abundance ratio across the disk of an external galaxy. If NGC 6946 follows the gradient of $[^{12}CO]/[^{13}CO]$ of our Milky Way (although it is not necessary), variation of $[^{12}CO]/[^{13}CO]$ in the region of concern is < 10 (Milam et al., 2005). Such a small variation is comparable or even smaller than the uncertainty of $[^{12}CO]/[^{13}CO]$ measured in extragalactic studies (Henkel et al., 1998). Hence, variation of isotopic abundance is not preferred as well.

Because of the high opacity of ^{12}CO, R_{10} is much lower than the isotopic abundance ratio of ^{12}CO and^{13}CO. Thus R_{10} can reflect the variation of ^{12}CO opacity. Opacity (τ) is a function of physical properties of molecular gas:

$$\tau \propto \frac{N}{\Delta v \, {T_{\rm k}}^2}. \tag{3.2}$$

Equation 3.2 shows that increasing line width or velocity dispersion (Δv) is one of ways to make τ become smaller. In addition, τ strongly depends on kinetic temperature.

Figure 3.31 shows a plot of R_{10} versus Δv of ^{12}CO. Δv is derived by fitting a single Gaussian to the pixels with significant detection. Δv spreads over a wide range from about 10 – 50 km s^{-1}. A clear tendency is seen that Δv increases with R_{10}.

Some representative spectrum are shown in Figure 3.32. Spectrum of the northern ridge, southern ridge, and minibar are indicated with green (Position 1 – 4), blue (8 – 13), and magenta (6 and 7) boxes, respectively. The spectrum are presented with Jy versus km s^{-1}. Δv are shown in each panel. At the southern ridge, Δv is about 10 – 15 km s^{-1}. Δv in the northern ridge are 20 – 35 km s^{-1}, about two times broader than southern ridge.

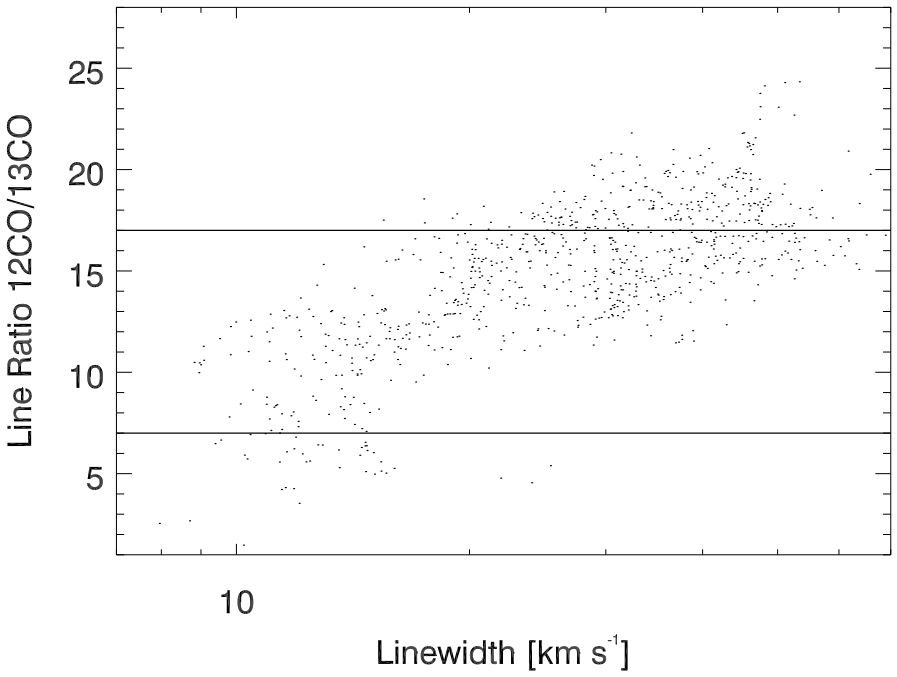

FIGURE 3.31: Line ratio of ^{12}CO-to-^{13}CO (R_{10}) versus linewidth (velocity dispersion). The linewidth is estimated by fitting with a single Gaussian.

However, the line profiles indicate that the broad Δv of the northern ridge is caused by the multiple gas component involving to a beam. Therefore we decomposed the spectrum in the northern ridge with two Gaussians. (Note that the number of fitting component is arbitrary.) The results are shown in Figure 3.33. After decomposition, individual spectrum lie within Δv of 9 – 26 km s^{-1}. Majority of the spectrum has width of 10 – 15 km s^{-1}, which is compatible with those in the southern ridge. We emphasize that the decomposed spectrum are accurate only when GMCs do not superpose along the line of sight. If there are multiple GMCs within a small beam of 100 pc, it is highly possible that the GMCs are overlapping with each other or they are not fully sampled with a beam. In such a case, the observed spectrum are affected by the geometry of GMCs. Our decomposition may be too simplified. Hence, we cannot rule out the possibility of the broadening effect that lower the τ of ^{12}CO.

Another factor which determines τ is $T_{\rm k}$. $T_{\rm k}$ of molecular gas can be raised by the surrounding UV photons. LVG calculations suggest a marginal trend that the gas with higher R_{10} is warmer, and vice versa. Since τ is a strong function of $T_{\rm k}$, it is worth examining the relation of R_{10} and $T_{\rm k}$ with other independent method.

Temperature of GMCs consist of gas and dust temperature. In the interior of GMCs where $n_{\rm H_2} > 10^4$ cm^{-3}, dust and gas start to couple thermally through the collisions. At this high density region, temperature of dust and gas equalize (Bergin & Tafalla, 2007, Galli et al., 2002, Goldsmith, 2001). However, at the low density regions, such as the

surface of GMCs, different dust and gas temperatures is seen. Due to the effective cooling of dust, dust normally cooler than gas. Temperature of dust is commonly derived from the spectral energy distribution (SED) at infrared regime. For the gas temperature, in addition to CO lines, NH_3 (ammonia) is an ideal thermometer tracing gas temperature in a broad range of environments from cool clouds ($\leqslant$ 10 K) to hot molecular core of high-mass star formation ($>$ 30 K) (e.g., Bergin et al., 2006, Longmore et al., 2007, Mangum et al., 2013b, Morgan et al., 2010, Pickett et al., 1998). Mangum et al. (2013b) derive kinetic temperature of nearby star forming galaxies with multiple transitions of NH_3. Two temperatures are found in the central region of NGC 6946, they are 25 $\pm$ 3 K and 50 $\pm$ 10 K.

To derive temperature for the interested regions, we choose to use dust temperature as a probe of gas temperature and assume that the dust temperature is proportional to gas temperature. We note that the difference of the two temperature depends on the strength of the external UV field. Hence, gas temperature ($T_{\rm g}$) may not linearly proportional to dust temperature ($T_{\rm d}$) but in general, high dust temperature regions are associated with high gas temperature (Mangum et al., 2013b). Eventually, we aim the gain the idea of the relative temperature between the central region, northern bar and the southern bar.

The spectrum energy distribution (SED) at 24 μm–500 μm of stellar components are often described with a two-component gray-body model, in which the intersection is at about 70 μm (Paladini et al., 2012). The component at $<$ 70 μm implies the presence of warm grains associated with HII and photodissociation regions, which have $T_{\rm d}$ of about 30 – 50 K. These warm gas leads the total SED peaks at $<$ 160 μm. On the other hand, the cold component at $>$ 70 μm is attributed to the grains $<$15 K, such as the gas around Young Stellar Objects (YSOs), which can shift the peak of total SED toward $>$ 160 μm. Therefore, the flux (S) ratio of 70 μm to 160 μm (S_{70}/S_{160}) can be used as a relative thermometer.

70 μm and 160 μm images are taken from the PACS on Herschel. Processed images are available from the website of KINGFISH project. The point spread function (PSF) of 70 μm and 160 μm maps are 5.″2 and 12″, respectively. The IDL program `conv image` and the convolution kernel from Gordon et al. (2008) are used to degrade the PSF of 70 μm map to match the 160 μm map. Our CO combined maps are convolved to a resolution of 12″ by the MIRIAD task `convol`, and then we derived R_{10} again. The plot of S_{70}/S_{160} versus the new R_{10} is displayed in Figure 3.34. We are not able to derive the exact value of temperature with this examination, but it is obvious from Figure 3.34 that R_{10} increases with increasing S_{70}/S_{160}, suggesting that higher R_{10} is associated

with warmer gas. The result is consistent with the trend indicated by LVG calculations of CO lines.

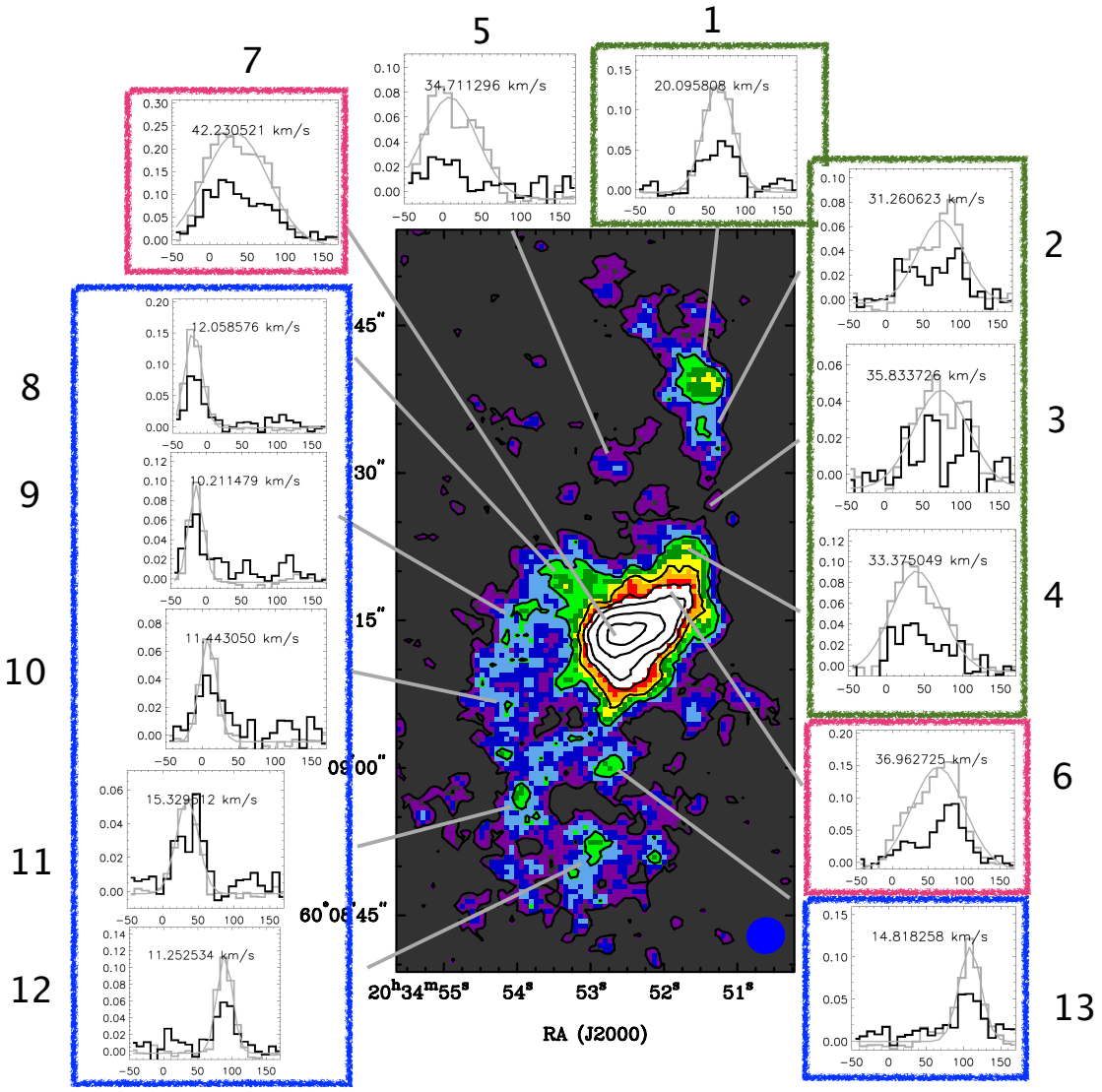

FIGURE 3.32: CO spectra at some positions. ^{12}CO/8 spectra are plotted in grey and ^{13}CO in black. All ^{12}CO/8 spectra are fitted with a single Gaussian, the results are overlaid with gray curves. Galactic features are indicated with color boxes. Green, magenta and blue boxes denote the northern ridge, minibar ends, and the southern ridge, respectively.

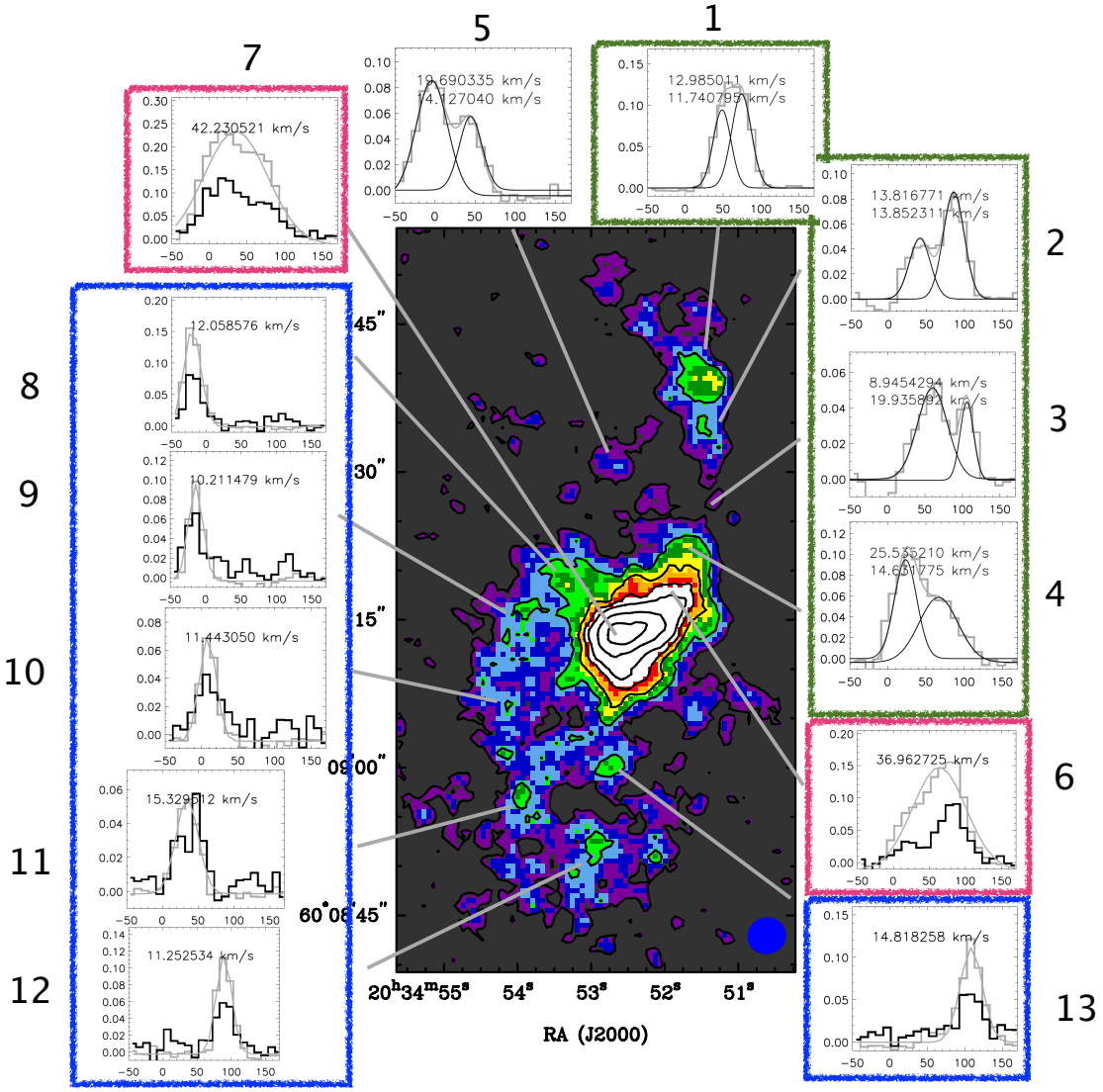

FIGURE 3.33: CO spectra at some positions. ^{12}CO/8 spectra are plotted in grey and ^{13}CO in black. The ^{12}CO/8 spectra of northern ridge are fitted with a two-component Gaussian, the results are overlaid with gray curves. Other spectra are fitted with single Gaussian. Galactic features are indicated with color boxes, same as in Figure 3.32.

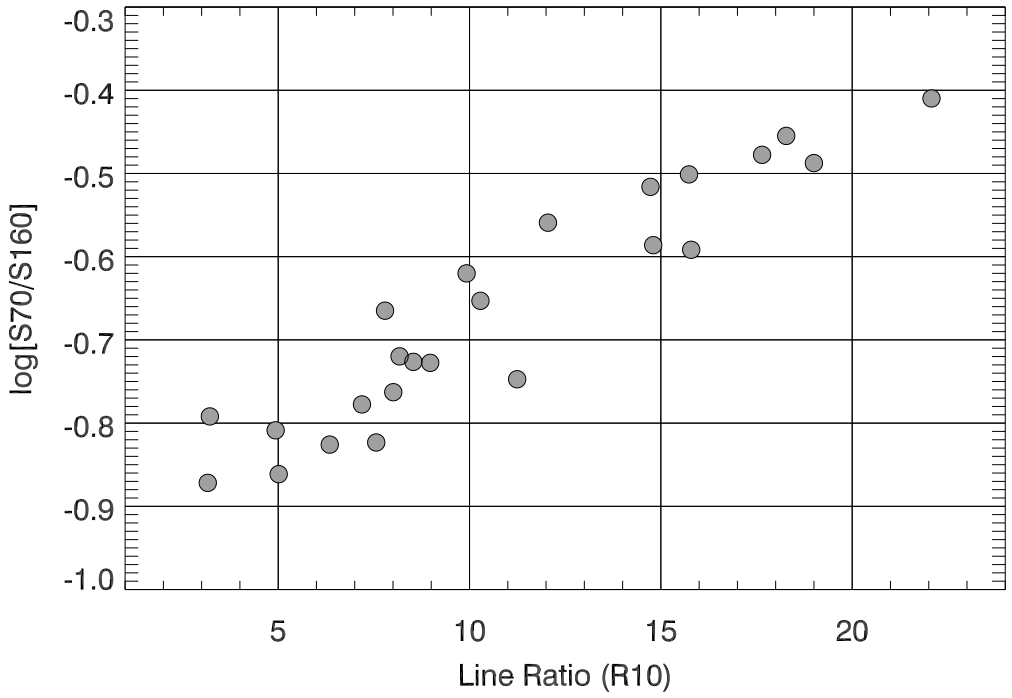

FIGURE 3.34: Line ratio of ^{12}CO-to-^{13}CO (R_{10}) versus infrared flux ratio of 70μm/160μm. The images of 70μm and 160μm are obtain from Herschel.

3.6.4 Mass of Molecular Gas

3.6.4.1 Mass of Molecular Gas Derived from CO Lines

Because of the small opacity (optically thin) of ^{13}CO, ^{13}CO is a better tracer of gas mass (Aalto et al., 2010). The mass of molecular gas ($M_{\rm H_2}$) can be estimated by the intensity of ^{13}CO assuming LTE (see Equation 2.11).

The optical depth is estimated by the mean of $1/R_{10}$ in each sub-regions (Paglione et al., 2001). We use ^{13}CO abundance of $8 \times 10^{-5}/60$ for the ridges and $8 \times 10^{-5}/40$ for the center and the minibar (Henkel et al., 1998). $T_{\rm k}$ derived from LVG calculations can be a hint of $T_{\rm ex}$ assuming that $T_{\rm ex} \approx T_{\rm k}$. We use $T_{\rm ex} = 40$ K for the center and minibar, which is about the mean temperature of the two gas components derived from our LVG calculations of CO lines and the NH_3 observations from Mangum et al. (2013b). $T_{\rm ex} = 20$ K is adopted for the northern ridge and the southern ridge (south spiral and the southern blob). The parameters used for deriving the mass from ^{13}CO flux are summarized in Table 3.4.

TABLE 3.4: Mass of Molecular Gas

Component	^{13}CO [Jy]	^{12}CO [Jy]	T [K]	R_{10} ...	$\frac{[^{12}CO]}{[^{13}CO]}$ ...	$M_{\rm H_2,13}$ $10^7 M_\odot$	$M_{\rm H_2,12}$ $10^7 M_\odot$	$I_{\rm HCN}$ [K km s^{-1}]	$L'_{\rm HCN}/L'_{\rm CO}$ $10^7 M_\odot$
center+minibar	67 ± 4	1420 ± 55	40	16	40	12.3	20.2	18.9 ± 1.4	0.092
Northern ridge	47 ± 2	622 ± 16	20	15	60	4.6	8.9	4.7 ± 0.8	0.055
South spiral	45 ± 2	365 ± 12	20	7	60	4.1	5.2	4.2 ± 0.8[a]	0.045[a]
southern blob	8 ± 1	101 ± 11	20	12	60	0.7	1.4	4.2 ± 0.8[a]	0.045[a]

[a] for the south spiral and southern blob together, could not be resolved in the observations

$M_{\rm H_2,13}$ in the central region (galactic center and minibar) is estimated to be 1.2×10^8 $M_\odot$ from ^{13}CO data. It is about 2.7 times larger than that of the northern ridge. The mass of molecular gas in the southern blob and the south spiral are 7×10^6 $M_\odot$ and 4.1×10^7 $M_\odot$, respectively.

The mass of molecular gas can be estimated from the flux of ^{12}CO as:

$$M_{\rm H_2,12}[M_\odot] = 519295 S_{\rm CO} D^2 X_{\rm CO}/\nu^2, \tag{3.3}$$

where D is the distance of the target in Mpc, and ν is observed frequency in Hz. We adopt $X_{\rm CO}$ =1.2×10^{20} cm^{-2} (K km s^{-1})$^{-1}$ (Donovan Meyer et al., 2012), which was derived based on the virial theorem and is about 2 – 3 times lower than the Galactic standard value.

However, they comment that $X_{\rm CO}$ of NGC 6946 can vary by factor of two due to the measurement uncertainties (Donovan Meyer et al., 2012). Uncertainty of $X_{\rm CO}$ will be discussed in §3.7.3.5.

The flux and the derived mass are listed in Table 3.4. The mass of molecular gas in the central region is 2.0 $\times$ 10^8 $M_\odot$. The mass of the northern ridge is 8.9 $\times$ 10^7 $M_\odot$. The south spiral and southern blob have a mass of 5.2 $\times$ 10^7 $M_\odot$ and 1.4 $\times$ 10^7 $M_\odot$, respectively.

We derive a mean $M_{H_2,13}/M_{H_2,12}$ of 0.6, where $M_{H_2,13}$ and $M_{H_2,12}$ are based on LTE assumption and X_{CO}, respectively. The mass ratio of two transitions is larger than the median ratio of Galactic GMCs derived from virial theorem, which is about 0.2 (Heyer et al., 2009). Heyer et al. (2009) show a trend that the ratio of $M_{H_2,13}/M_{H_2,12}$ decreases with increasing mass of GMCs. Since the mass of GMCs in NGC 6946 are about 10 times larger than that of Galactic GMCs (will show in §3.9 later), the larger $M_{H_2,13}/M_{H_2,12}$ found in this galaxy should be reasonable.

3.6.4.2 Dense Gas Fraction Derived from ^{12}CO and HCN

To compare the dense gas fraction with other galaxies, we will use L'_{HCN}/L'_{CO} as the indicator of dense gas fraction rather than the calculations of the exact number of mass. The advantage is that we can get rid of the uncertain ties in X_{CO} and X_{HCN}.

The sources of HCN emission, such as GMC cores, are much smaller than the beam size of a single dish telescope. In such a case, luminosity of HCN (L'_{HCN} in K km s^{-1} pc^2) is calculated by

$$L'_{HCN} = 4.1 \times 10^3 \, S_{HCN} \, \Delta v \, D_L^2 \, (1+z)^{-3} \tag{3.4}$$

where $S_{HCN}\Delta v$ is HCN line flux in Jy beam^{-1} km s^{-1}, D_L is the distance in Mpc, and z is redshift (Gao et al., 2007, Solomon et al., 1992, 1997). For NGC 6946, $(1+z)^{-3}$ is about unity since $z \approx 0.000133$. The derived L'_{HCN} are 1.1 $\times$ 10^6 K km s^{-1} pc^2, 1.0 $\times$ 10^6 K km s^{-1} pc^2 and 4.5 $\times$ 10^6 K km s^{-1} pc^2 at the northern ridge, southern ridge and the center, respectively.

L'_{CO} is calculated as

$$L'_{CO} = 3.25 \times 10^7 S_{CO} \Delta v \nu_{obs}^{-2} D_L^2 (1+z)^{-3}, \tag{3.5}$$

with ν_{obs} in GHz and D_L in Mpc (Solomon et al., 1997). We use single dish ^{12}CO map to compute L'_{CO} in K km s^{-1} pc^2. The derived L'_{CO} is 2.0 $\times$ 10^7 K km s^{-1} pc^2 for the northern ridge, 2.3 $\times$ 10^7 K km s^{-1} pc^2 for the southern ridge and 4.9 $\times$ 10^7 K km s^{-1} pc^2 at the center, resulting in L'_{HCN}/L'_{CO} = 0.055, 0.045, and 0.092, respectively. L'_{HCN}/L'_{CO} of the ridges are compatible with the values observed in normal galaxies. The mean L'_{HCN}/L'_{CO} of normal galaxies ($L_{IR} < 10^{11} L_\odot$) is 0.04 (Gao & Solomon, 2004b). On the other hand, L'_{HCN}/L'_{CO} in the center of NGC 6946 is between

the mean value of LIRGs (0.071) and ULIRGs (0.17), where the definition of LIRG is $10^{11}L_{\odot} < L_{\rm IR} \leq 0.8 \times 10^{12}L_{\odot}$, and $L_{\rm IR} \geq 10^{11.9}L_{\odot}$ for ULIRGs (Gao & Solomon, 2004b).

3.7 Star Formation in NGC 6946

3.7.1 Distribution of Star Forming Regions

3.7.1.1 Distribution of Star Forming Regions in Optical Image

The Hα image is obtained from the ancillary data of the Spitzer SINGS project. The observation was carried out using KPNO[5] 2.1-m telescope. The angular resolution of Hα image is $\sim 2''$ (54 pc). Hα traces ionized gas surrounding the most massive O- and B-stars. The ionizing flux is attributed to the stars with mass of > 17 M$_{\odot}$. Therefore, history of star formation traced by Hα is only a few Myr (Lee et al., 2009).

The Hα image shows three components at the innermost region (Figure 3.35(a)). Two of them are associated with the minibar and the galactic center, while the third one is about $2''$ away from the SE minibar end.

The northern ridge in our CO map has an counterpart to the Hα map. The Hα ridge is slightly shifted to the downstream of CO emission. Such offset has been seen in many galaxies (e.g., Egusa et al., 2009). Egusa et al. (2009) estimate the star formation timescale for the bar region of NGC 6946 by using the offset between ^{12}CO (from BIMA) and Hα. The derived star formation timescale is $\sim$1.1 Myr.

The south spiral appears to be weak in star forming activity, except for the place where the south spiral just emerging from the central region. Finally, there is a bright star forming region at the locus of the southern blob.

3.7.1.2 Distribution of Star Forming Regions in Infrared Image

24μm emission traces small grains heated by the UV photons from young stars with a timescale of $\sim$ 10 Myr (Calzetti et al., 2005).

The 24μm image is taken with the MIPS on Spizter. The data belongs to the SINGS project. The angular resolution is about $6''$ or $\sim$ 160 pc for MIPS at 24μm. The image is shown in Figure 3.35(b). For the bright source with high S/N, the complete extent

[5]Kitt Peak National Observatory

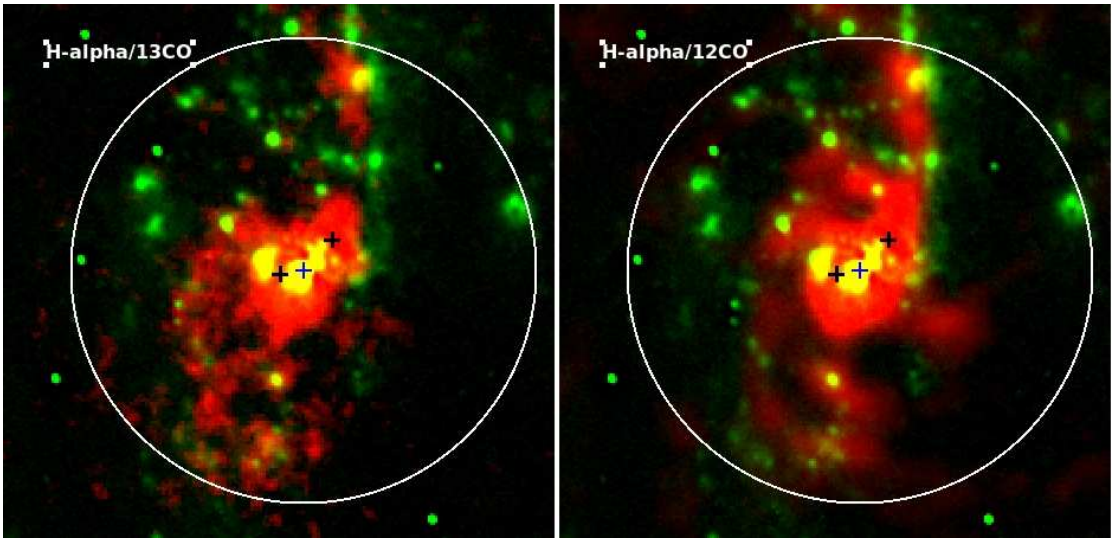

(a)

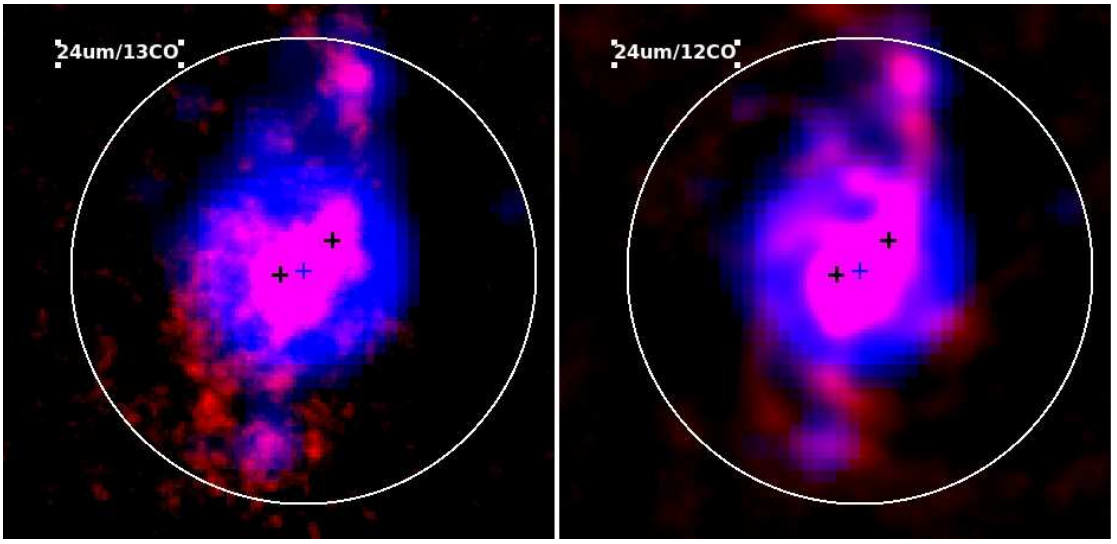

(b)

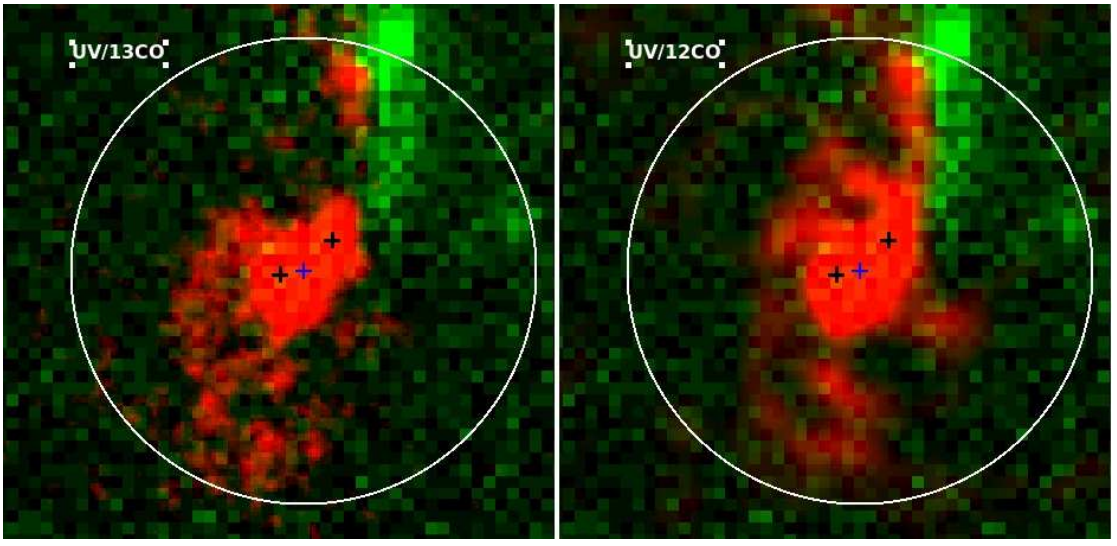

(c)

FIGURE 3.35: CO images overlaid on the star formation tracers. The left column displays the ^{13}CO map (red color scale) superposed on the star formation tracers, and the same plots with ^{12}CO map (red color scale) are shown in the right column. From the top to bottom, Panels (a) to (c), the star formation tracers are Hα (green), 24*um* (blue), and UV (green) respectively. The circle in each panel indicates $1'$ in diameter. The black and blue crosses mark the minibar ends and the center.

of the PSF of MIPS might be manifest. Such an effect is seen in the central region of NGC 6946. 24μm emission is found at the northern ridge and the position where the southern spiral and southern bar merge.

3.7.1.3 Distribution of Star Forming Regions in FUV image

UV emission origins from the photospheres of stars with mass > 3 M$_\odot$ (Lee et al., 2009). Hence, UV traces a longer history of star formation, say, < 100 Myr.

The FUV (1350 – 1750Å) image of NGC 6946 is taken from Galaxy Evolution Explorer (GALEX) Nearby Galaxies Survey (NGS). The angular resolution is $\sim$6″ ($\sim$ 160 pc). The background subtracted image is made by subtracting the sky background map from the intensity map. UV emission is only found at the northern ridge. Same as in the Hα map, FUV emission no longer coexists with molecular gas but shows at the downstream of the molecular bar.

3.7.2 Star Formation Rate

3.7.2.1 Total Star Formation Rate

The total infrared luminosity (8μm – 1000μm) of NGC 6946 is estimated to be $10^{10.22}$ $L_\odot$ from IRAS. SFR based on infrared luminosity can be derived by

$$\mathrm{SFR}(M_\odot\ \mathrm{yr}^{-1}) = L_{\mathrm{IR}}\ [L_\odot]/(5.8 \times 10^9) \times \cos i, \tag{3.6}$$

assuming a constant star formation during 10 – 100 Myr ago and a Salpeter IMF (Kennicutt, 1998). i in Equation 3.6 is inclination of the galaxy. The total SFR derived from the infrared luminosity is 2.4 M$_\odot$ yr^{-1}.

Global SFR can be also derived with 24μm alone by (Rieke et al., 2009):

$$\mathrm{SFR}(M_\odot\ \mathrm{yr}^{-1}) = 2.04 \times 10^{-43} L_{24}[\mathrm{erg\,s}^{-1}] \times 1.6 \times \cos i, \tag{3.7}$$

where the factor of 1.6 is a correction from Kroupa IMF to Salpeter IMF (Calzetti, 2012). (There are two SFR based on 24μm in this thesis. The difference of them is the scale of calibration. Equation 2.7 is calibrated for a local scale of $\sim$500 pc, whereas Equation 3.7 is calibrated for global SFR.). Global SFR based on Equation 3.7 is 1.6 M$_\odot$ yr^{-1}. The derived SFR (24μm) is lower than SFR (IRAS).

3.7.2.2 Regional Star Formation Rate

We estimate SFR with 24μm image from Spitzer. With Equation 2.7 (local SFR), we derived SFR of 0.05 $M_\odot$ yr^{-1} at the northern ridge and 0.02 $M_\odot$ yr^{-1} at the southern ridge. Galactic center has SFR an order of magnitude larger than the ridge, 0.21 $M_\odot$ yr^{-1}. The sum of SFR suggests that central $1'$ contribute about 10% of total SFR in this galaxy. Nonetheless, the optical disk of NGC 6946 is $10'$ in diameter. The central $1'$ then occupies only a percent of galaxy. It turns out that SFR surface density in the center is extremely high compared with the rest of disk.

3.7.3 Relation Between Gas and Stars in NGC 6946

To understand the relation of gas and stars, a pixel-by-pixel K–S law is the easiest way to study the spatially resolved K–S law. However, when the physical resolution is high, star forming region may shift from the sites of molecular gas. At the ridges of NGC 6946, Hα emission does not coexist with CO emissions. Specifically, the star forming region traced by Hα emission is located at the downstream of molecular gas. Such offset is commonly seen in galactic bars. For this reason, it is not fair to make pixel-base K-S law. To overcome the problem we make radius-base K-S law assuming the gas and stars are propagating at same radius. Since the northern ridge and the southern ridge contain different gas properties and star forming activity, we consider gas and stars in the northern and southern ridges separately. Physical properties of galactic center will be shown as well for comparison. Central $12''$ ($R < 12''$) is denoted as *center*, which includes the galactic center and the minibar.

3.7.3.1 Correction for Extinction

Hα is the only available map which has comparable resolution with CO maps. However, Hα emission could be affected by dust extinction due to its short wavelength, especially near the galactic center where gas and dust are found in abundant. Accordingly, correction is required to recover the embedded star formation in our interested area.

We use SFR(24μm) as the true SFR, then estimate the extinction of Hα ($A_{H\alpha}$) by the factor which is required to equalize SFR(24μm) and SFR(Hα). Similar method is used in Rebolledo et al. (2012) for the spiral arm of NGC 6946.

To equalize SFR(24μm) and SFR(Hα), $A_{H\alpha}$ of 1.8, 2.1 and 2.9 are required for the northern ridge, southern ridge and galactic center, respectively. $A_{H\alpha}$ derived for spiral arm by Rebolledo et al. (2012) is 1.0, implying that central $1'$ has higher extinction than

the spiral arm, which is not a surprising result (Leroy et al., 2008). High $A_{H\alpha}$ (> 2.0) is also found in the center of other nearby galaxies (e.g., James et al., 2005).

3.7.3.2 Azimuthal Distribution of Gas and Star Formation Rate/Efficiency

Figure 3.36(a) shows the radial distribution of Σ_{H_2} of the northern ridge in thick curves and the southern ridge in thin curves. Σ_{H_2} derived from ^{13}CO and ^{12}CO are plotted with a color of blue and black, respectively. Step of sampling is $3''$. Shadow area represents *galactic center* with $R < 12''$. Temperature and isotopic ratio which required for deriving ^{13}CO-base Σ_{H_2} are the same as in §3.6.4.1. For the galactic center, isotopic ratio is assumed to be 40 and the temperature is 40 K. For the northern and the southern ridges, the adopted parameters are (60, 20 K).

As seen in Figure 3.36(a), Σ_{H_2} from ^{13}CO ($\Sigma_{H_2,13}$) is lower than that from ^{12}CO ($\Sigma_{H_2,12}$) by a factor of 2 – 3 across all radii. To equalize the mass derived from two CO lines, either X_{CO} should be on the order of ^{19} cm^{-2} (K km s^{-1})$^{-1}$ for ^{12}CO or raise the temperature to 43 – 65 K for the galactic center and 35 – 50 K for ridges in ^{13}CO calculation. However, the masses derived from the two lines are not necessary to be equal as suggested by the virial masses of Galactic GMCs (Heyer et al., 2009).

$\Sigma_{H_2,13}$ shows a downward trend along radius. It is about 850 M$_\odot$ pc^{-2} at the center. At the northern ridge, $\Sigma_{H_2,13}$ sustains at $\sim$ 80 M$_\odot$ pc^{-2} till a radius of $+40''$. Similar trend is observed in the southern ridge that $\Sigma_{H_2,13}$ varies between 40 – 60 M$_\odot$ pc^{-2} till $-40''$[6], but the downhill trend is more obvious than the northern ridge. $\Sigma_{H_2,13}$ in the ridges of NGC 6946 is slightly larger than that of Galactic GMCs. Heyer et al. (2009) derive a median $\Sigma_{H_2,13}$ of Galactic GMCs, which is 42 M$_\odot$ pc^{-2}[7].

$\Sigma_{H_2,12}$ peaks at the galactic center, which is about 2500 M$_\odot$ pc^{-2} and about three times larger than $\Sigma_{H_2,13}$. In the majority of the ridges, $\Sigma_{H_2,12}$ is about 100 – 200 M$_\odot$ pc^{-2}, consistent with the surface density of Galactic GMCs (Heyer et al., 2009, Solomon et al., 1987). At a radius of $+40''$ and $-40''$, $\Sigma_{H_2,12}$ are about 150 M$_\odot$ pc^{-2} and 70 M$_\odot$ pc^{-2}, respectively.

Both transitions indicate a higher Σ_{H_2} in the northern ridge than the southern ridge, but the difference is not significant, only about 1.5 – 2 times.

[6] Minus represents south and vice versa.

[7] Heyer et al. (2009) only show a catalog of GMCs ^{13}CO mass based on LTE. But they have concluded that the virial mass determined by ^{13}CO is equal to that from LTE. Moreover, they also derive a virial parameter of unity to those GMCs, which again confirm that $M_{LTE,13} \approx M_{virial,13}$

SFR is estimated by Hα by

$$\mathrm{SFR}(M_\odot) = 5.3 \times 10^{-42} L_{\mathrm{H}\alpha} \times 10^{A_{\mathrm{H}\alpha}/2.5} \times \cos i, \tag{3.8}$$

where $L_{\mathrm{H}\alpha}$ is luminosity of Hα in erg s^{-1} (Calzetti et al., 2007). Equation 3.8 is calibrated for local SFR assuming a Kroupa IMF.

Figure 3.36(b) displays an radial plot of Σ_{SFR}. The line style and sampling size are the same as in Figure 3.36(a). In the central region, Σ_{SFR} is as high as ~3 M$_\odot$ yr^{-1} kpc^{-2}, then decreases toward both sides. Σ_{SFR} of the southern ridge decreases more rapidly than the northern ridge, reaching a small value of ~0.02 M$_\odot$ yr^{-1} kpc^{-2} at -40″. In contrast, Σ_{SFR} of the northern ridge sustains at a constant beyond a radius of +20″, fluctuating in the vicinity of 0.1 M$_\odot$ yr^{-1} kpc^{-2} out to +40″.

Azimuthal distribution of SFE (SFR/M$_{\mathrm{H_2}}$) is shown in Figure 3.36(c). Since $\Sigma_{\mathrm{H_2},13}$ is smaller than $\Sigma_{\mathrm{H_2},12}$, SFE derived from ^{13}CO (SFE$_{13}$) become larger than that from ^{12}CO (SFE$_{12}$).

SFE$_{13}$ and SFE$_{12}$ are about (1 – 4) × 10^{-9} yr^{-1} and (0.4 – 1.5) × 10^{-9} yr^{-1} in the galactic center, respectively. SFE$_{13}$ is about (4 – 10) × 10^{-10} yr^{-1} and (1 – 3) × 10^{-9} yr^{-1} in the southern and northern ridge, respectively. SFE$_{12}$ is about two to three times lower than SFE$_{13}$ in the ridges. SFE$_{12}$ of the northern ridge and the southern ridge are ~ 10^{-9} yr^{-1} and 3 × 10^{-10} yr^{-1}, respectively. The SFE$_{12}$ of the ridges is similar as the mean SFE (~ 4 × 10^{-10} yr^{-1}) derived from 30 nearby disk galaxies from Bigiel et al. (2011). This result is consistent with the similar dense gas fraction found among the ridges and normal galaxies (cf. 3.6.4.2).

3.7.3.3 Azimuthal Star Formation Law

Azimuthal K–S law is shown in Figure 3.36(d). The northern part and the southern part are plotted with diamonds and circles, respectively. Filled and open symbols represent the galactic center and ridges, respectively. A dotted line is overlaid to indicate a slope of unity with an arbitrary intersection for y-axis. In general, both transitions show positive correlation between $\Sigma_{\mathrm{H_2}}$ and Σ_{SFR}. However, for a given $\Sigma_{\mathrm{H_2}}$, Σ_{SFR} of the northern ridge seems to be enhanced.

The data points are fitted with K–S law. First of all, all points are used, resulting in a slope of 1.53 ± 0.09 for ^{13}CO ($N_{\mathrm{all},13}$) and 1.27 ± 0.10 for ^{12}CO ($N_{\mathrm{all},12}$). We note that the results of all data points may not faithfully represent the tendency because the northern ridge are obviously deviated from the trend. For this reason, we then fit K–S law without the northern ridge (N_{CS}), and obtain a slope of $N_{\mathrm{CS},13}$ = 1.66 ± 0.05 and

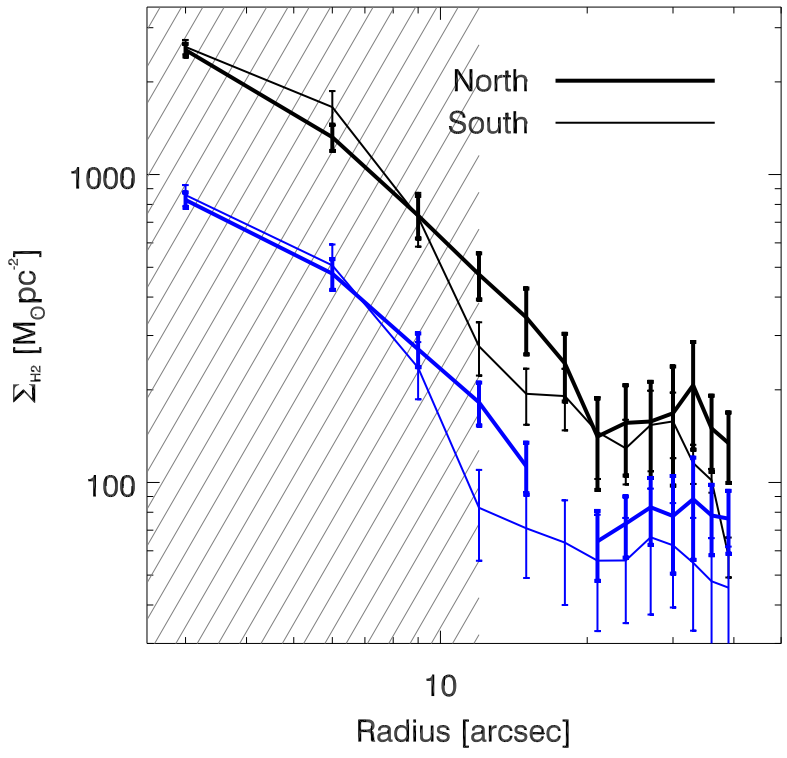

(a) Radial distribution of $\Sigma_{\rm Gas}$

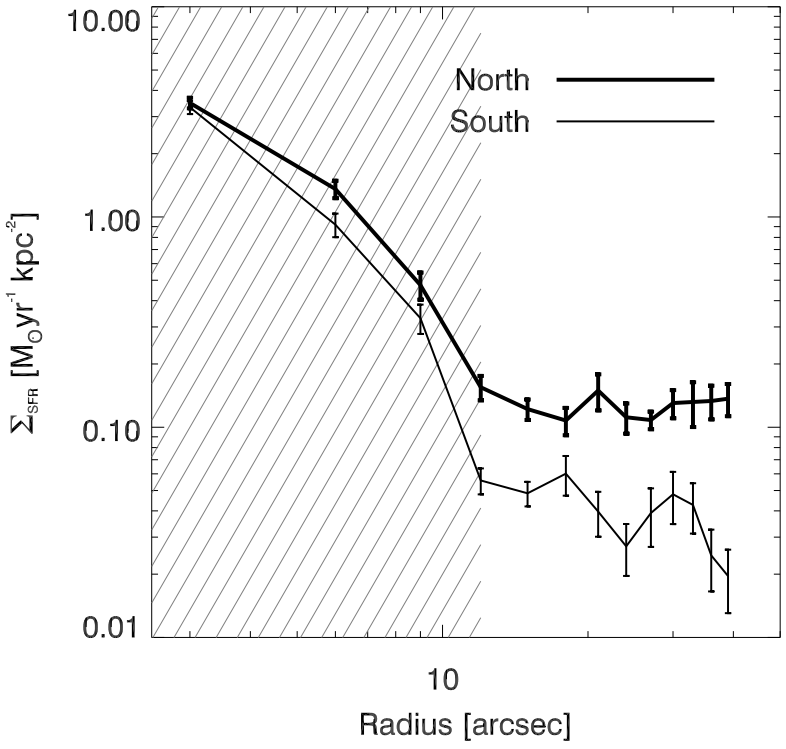

(b) Radial distribution of $\Sigma_{\rm SFR}$

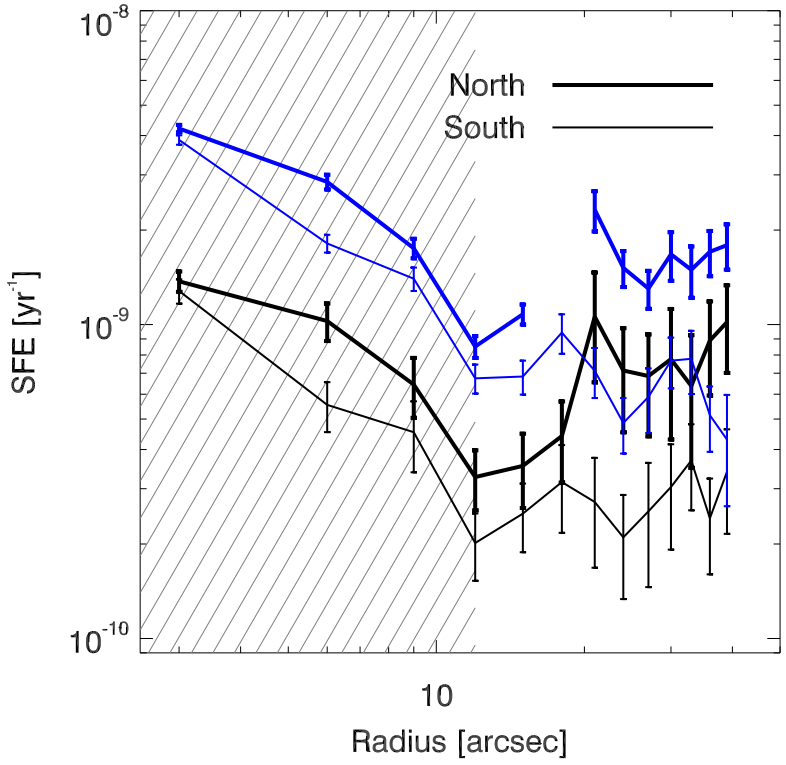

(c) Radial distribution of SFE

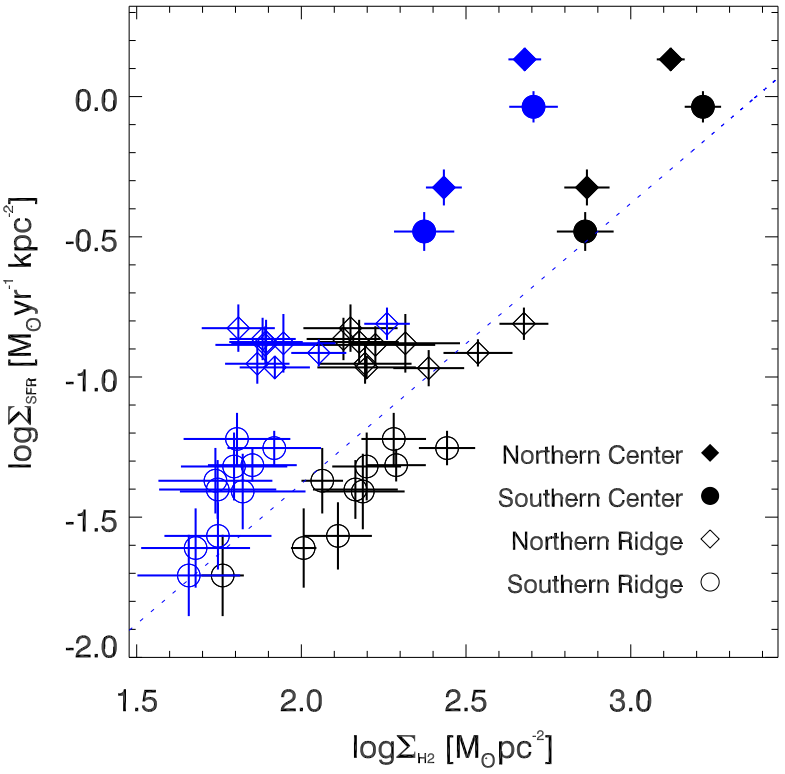

(d) Azimuthal K–S law

FIGURE 3.36: (a) Radial distribution of Σ_{H_2}. Blue and black curves denote Σ_{H_2} derived from ^{13}CO and ^{12}CO, respectively. Results of north is shown in thick line and south in thin line. Hatched area represents the central region. (b) Radial distribution of Σ_{SFR}. (c) Radial distribution of SFE. The colors and line styles are the same as in the panel (a). (d) Azimuthal K–S law. Results of ^{13}CO is colored blue, while ^{12}CO is in black. Data points of central region are shown as filled symbols. Open symbols represent the ridges. Diamonds and circles indicate the north and the south, respectively.

$N_{CS,12} = 1.44 \pm 0.07$. K–S law is also examined in individual galactic structures. Slopes of the galactic center (N_C) is larger than other slopes, $N_{C,13} = 1.77 \pm 0.16$ and $N_{C,12} = 1.65 \pm 0.14$. The slope of the southern ridge (N_S) is also derived to be $N_{S,13} = 1.69 \pm 0.18$ and $N_{S,12} = 0.77 \pm 0.17$. The large uncertainties are attributed to the small dynamic range at both axes.

In this study, we use the mean X_{CO} of NGC 6946, which is 1.2×10^{20} cm^{-2} (K km s^{-1})$^{-1}$. This X_{CO} is derived from virial mass of GMCs (Donovan Meyer et al., 2012). However, the slopes of K-S law from ^{12}CO could change if we use different X_{CO}. Donovan Meyer et al. (2013) shows that there is no specific trend of X_{CO} in the ridges. Both ridges harbor GMCs with X_{CO} greater or less than than 10^{20} cm^{-2} (K km s^{-1})$^{-1}$, suggesting that the true K-S law from ^{12}CO could be more disperse than we made.

Slopes of K-S law derived from ^{13}CO is consistent in both galactic center and the southern ridge while large difference is seen in the results of ^{12}CO. The superlinear correlations of ^{13}CO suggest that the gas traced by ^{13}CO does not directly trace the star forming core in which the SFR per mass of core is about constant. Nonetheless it could be a better probe of gas surrounding star forming region than ^{12}CO by reflecting a fix fraction of dense gas across a wider degree of environments, e.g., from the southern ridge to galactic center.

In this study, star formation law or K–S law appears to be a positive correlation between the two variables. However, this is not always the case for Galactic star formation law. Figure 3.37 plots the relation of the mass of local (< 500 pc) clouds and the number of YSO in them from Lada et al. (2010). The figure shows that the number of YSO per cloud mass (i.e., star formation efficiency) change by about 100 times in these clouds, suggesting that the total mass of clouds is a poor probe of SFR in some cases.

Heiderman et al. (2010) study K–S law with galactic YSOs and molecular clumps crossing two order magnitudes of Σ_{gas}, they found that there is a star formation threshold (Σ_{th}) at about 129 M$_\odot$ pc^{-2}. Below Σ_{th}, correlation of K–S law is about vertical ($N = 4.6$), while it becomes a slope of 1.1 above Σ_{th}. Lada et al. (2010) also suggest a Σ_{th} of 116 M$_\odot$ pc^{-2} based on the study of Galactic GMCs. Onishi et al. (1998) study the relation between the cores and YSO of Taurus. A Σ_{th} of 128 M$_\odot$ pc^{-2} is suggested. The above Galactic studies point to a Σ_{th} of $\sim$ 120 M$_\odot$ pc^{-2}. The explanation of the observed threshold can be magnetic field, photoionization-regulated star formation and the self-gravitational equilibrium of clouds. The theoretical critical Σ_{gas} of clouds above which magnetic field (B) cannot support the gas from collapse is about 50 – 110 M$_\odot$

pc^{-2} (Mouschovias & Spitzer, 1976), which is derived from

$$\sum_{\mathrm{crit}} > \left(\frac{80}{\mathrm{M}_{\odot}\,\mathrm{pc}^{-2}}\right)\left(\frac{B}{30\mu\mathrm{G}}\right), \tag{3.9}$$

where B is $\sim$ 20 – 40 μG. If star formation is controlled by ambipolar diffusion and the ionization levels in the cloud, the theoretical critical Σ_{gas} becomes 60 – 120 $\mathrm{M}_{\odot}$ pc^{-2} (McKee, 1989). On the other hand, Σ_{th} may reflect the amount of clouds that can become gravitationally bound. Heyer et al. (2001) suggest that the clouds greater than 10^4 $\mathrm{M}_{\odot}$ are bound, while less than 10^3 $\mathrm{M}_{\odot}$ are not based on their observations of Galactic GMCs. Krumholz et al. (2009) suggest a theoretical Σ_{th} of 85 $\mathrm{M}_{\odot}$. Below 85 $\mathrm{M}_{\odot}$, amount of stars that a GMC can form depends on the fraction of molecular gas in the GMC. In this regime, a superlinear correlation of K-S law is expected, consistent with the observing slope found in Heiderman et al. (2010). When GMCs reach a surface density of $\sim$ 100 $\mathrm{M}_{\odot}$, molecular clouds start to convert into stars with a roughly constant rate per free-fall time ($\sim$ 1%), thus surface density of gas and stars start to correlate with each other by a slope of unity. At very high surface density regime, density of GMCs should be regulated to maintain pressure balance with the large ambient pressure. While the density of GMCs increase rapidly, a superlinear K-S is expected again. The above literature suggested a Σ_{th} of about 60 – 130 $\mathrm{M}_{\odot}$ pc^{-2} to make gas and stars correlate with each other. Our observed $\Sigma_{\mathrm{H_2}}$ in the center and ridges of NGC 6946 are either comparable or larger than the threshold, hence, it is not a surprise that the relation of $\Sigma_{\mathrm{H_2}}$ and Σ_{SFR} is observed.

On the other hand, Lada et al. (2013) suggests that the scaling relation of star formation law only exist *within* GMCs but not between GMCs. While the Galactic GMCs have roughly constant Σ_{gas} as the Larson's relation implies and the GMC structure determines its SFR, there is no scaling relation between GMCs. Given that the GMCs in nearby galaxies also have a constant Σ_{gas} as that in the Milky Way, the scaling relation observed in the nearby galaxies is a result of sampling a continuous range of beam dilutions ($\sim$ 0.01 – 1.0) in unresolved observations. In other words, the scaling relation in nearby galaxies is a artificial result.

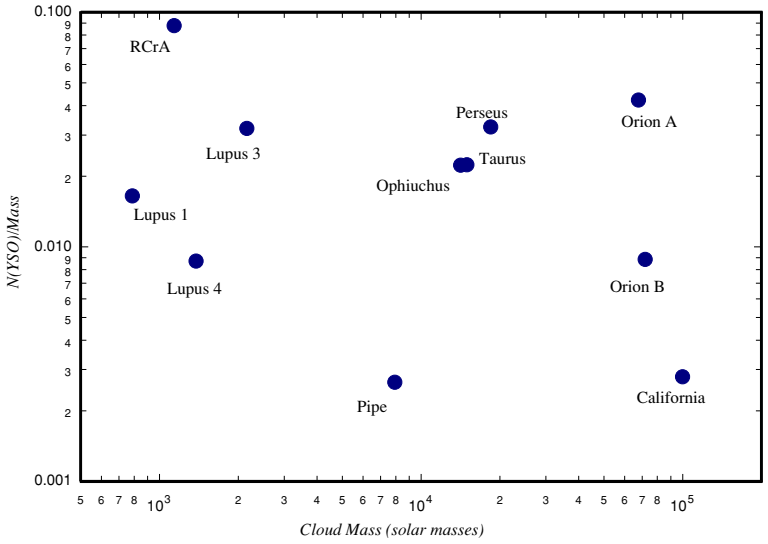

FIGURE 3.37: Number of YSO per cloud mass (star formation efficiency) versus cloud mass. The figure is taken from Lada et al. (2010).

3.7.3.4 More Interpretations on Line Ratio

Azimuthal distribution of R_{10} is shown in Figure 3.38(a). Generally R_{10} decreases with radius. R_{10} is divided into three ranges by different galactic features. In the central region, the radial R_{10} is 15 – 20. The northern ridge has a wide range of R_{10} from 10 – 20, and $<$ 10 in the southern ridge. R_{10} of the galactic center and northern ridge resemble the value found in starburst regions, while it is similar as the Galactic GMCs in the southern ridge. But we note that R_{10} varies more locally in the southern ridge than the northern ridge. Some regions in the southern ridge show higher R_{10}, such as the southern blob ($R_{10} \approx 12 - 13$). Such variation is smoothed out in the study based on radial distribution.

Figure 3.38(b) shows the correlation of R_{10} and $\Sigma_{\rm SFR}$. There is a clear trend that R_{10} increases with increasing $\Sigma_{\rm SFR}$. This is not a surprising result, because temperature is presumably higher in the high $\Sigma_{\rm SFR}$ regions. And we have seen that temperature is a dominant factor of changing opacity of ^{12}CO (§3.6.3) and R_{10} by the LVG calculations and the relation between R_{10} and the infrared flux ratio.

The best correlation between R_{10} and $\Sigma_{\rm SFR}$ appears at low R_{10} regime (< 10), where R_{10} rises with increasing $\Sigma_{\rm SFR}$. At the northern ridge, R_{10} ranges between 10 to 20 but $\Sigma_{\rm SFR}$ sustains at ~ 0.1 M$_\odot$ yr^{-1} kpc^{-2} across the width of R_{10}, suggesting that R_{10} does not simply reflect $\Sigma_{\rm SFR}$ or temperature. There must other factor which exists and controls the observed R_{10}. As will be shown later, the northern ridge are associated with large velocity jump across the ridge, broadening effect of line width is a factor of reducing the opacity of ^{12}CO and increasing R_{10} (Liszt, 2006).

In the galactic center (include minibar), a loose relation of R_{10} and $\Sigma_{\rm SFR}$ is seen. The correlation suggests that for a give $\Sigma_{\rm SFR}$, R_{10} does not increase as fast as the general trend expects. Such a correlation implies either overluminous ^{13}CO or underluminous ^{12}CO. Underluminous of ^{12}CO may be due to the superposition of GMCs along the line of sight in the innermost of galaxies, at the same time, optically thin ^{13}CO are faithfully detected, leading a resultant R_{10} lower than its $\Sigma_{\rm SFR}$ predicts. We note the true gas distribution and star formation enclosed in the defined galactic center is complicated, containing a minibar with compact gas distribution at its two ends, diffuse dust lanes, as well as a circumnuclear ring with a nuclear starburst in it. Our results at the central region is a convolution of all structures above, and may contain considerable uncertainties.

We also compare R_{10} with SFE in Figure 3.38(c). There is a better correlation between the SFE$_{13}$ and R_{10} that SFE$_{13}$ increases with increasing R_{10}. However, no significant relation of SFE$_{12}$ and R_{10} is seen.

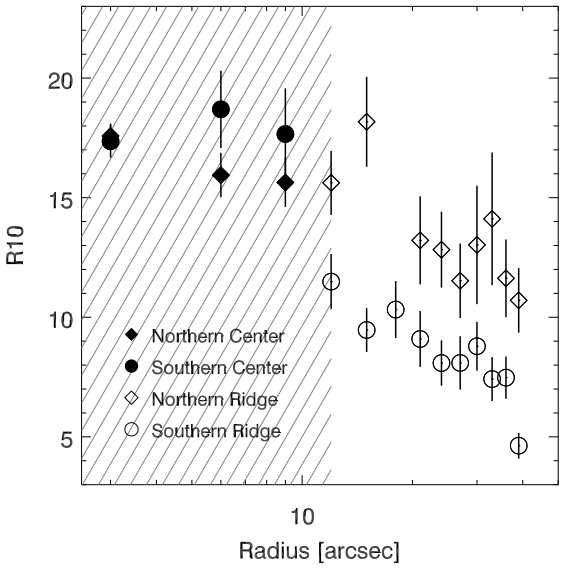

(a) Radial distribution of line ratio of R_{10}

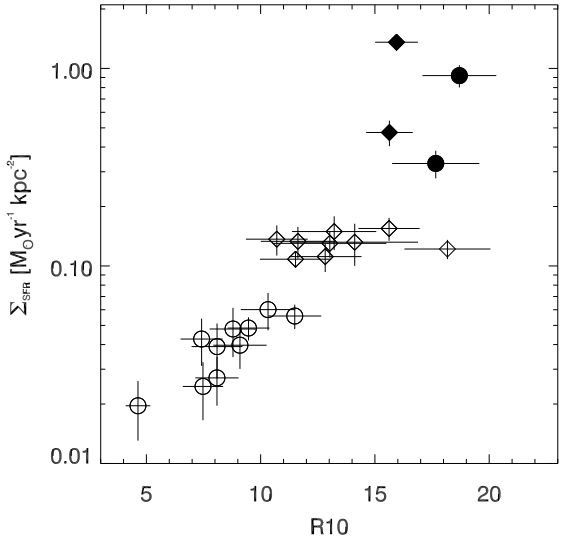

(b) R_{10} versus $\Sigma_{\rm SFR}$

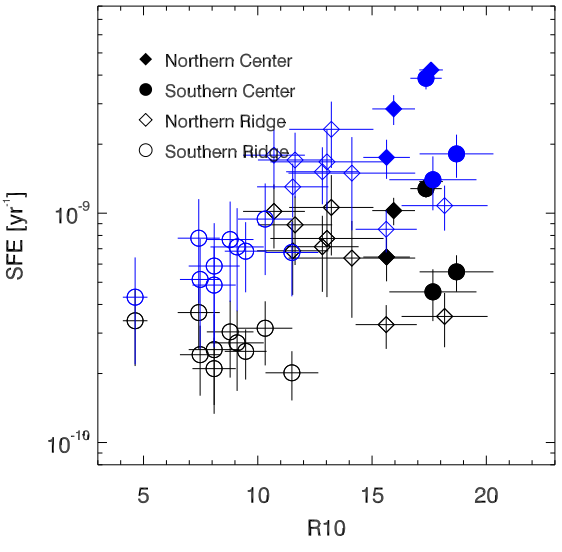

(c) R_{10} versus SFE

FIGURE 3.38: (a) R_{10} as a function of radius. Data within galactic center are presented with filled symbols, of which north is diamonds and south is circles. Hatched area represents the central region. (b) R_{10} versus $\Sigma_{\rm SFR}$. (c) R_{10} versus SFE. Blue symbols denote the SFE derived from ^{13}CO and black from ^{12}CO.

3.7.3.5 Uncertainty of SFE from Conversion Factor

In the above discussion, we assumed a constant $X_{\rm CO}$ to be 1.2 $\times$ 10^{20} (K km s^{-1})$^{-1}$ cm^{-2}. It is a mean value derived from Donovan Meyer et al. (2012). Any variation of $X_{\rm CO}$ can change SFE$_{12}$. Regan (2000) derive $X_{\rm CO}$ for the central 1′ of NGC 6946 by multi-color NIR extinction. However, $X_{\rm CO}$ derived with this method is an order magnitude smaller than Donovan Meyer et al. (2012) in the ridges, approximately 1 – 2 $\times$ 10^{19} (K km s^{-1})$^{-1}$ cm^{-2}. Moreover, Israel & Baas (2001) estimate mass of molecular gas within the central ∼1′ of NGC 6946 by measuring the gas-phase carbon abundance. They derive a corresponding $X_{\rm CO}$ to be $\sim$ 1 $\times$ 10^{19} cm^{-2} (K km s^{-1})$^{-1}$. Even the gas-phase carbon abundance is uncertain by a factor of 2 – 3 (Israel & Baas, 2001), the resultant $X_{\rm CO}$ is still significantly smaller than the Galactic standard value and the value derived by the virial theorem from Donovan Meyer et al. (2012), but consistent with Regan (2000). Thus, $X_{\rm CO}$ still has large uncertainty. The previous studies suggest values which could be different by 10 times.

3.8 Velocity Jump Across the Ridges

The relation of shocks and star formation is a long-standing question. The complication raised in galactic bars is that the loci of shocks corresponds to the sites where gas is accumulated. Shocks are playing completely opposite roles in the formation of GMCs and stars. Strong shocks and the turbulent gas can inhabit star formation by destroying GMCs (Reynaud & Downes, 1998, Tubbs, 1982, Zurita et al., 2004). The turbulent gas also prevents the formation of dense gas (e.g., Kohno et al., 1999), however, some studies show that proper shocks generated by cloud-cloud collisions can step up star formation in galaxies (Elmegreen, 2002, Koda & Sofue, 2006, Scoville et al., 1986, Tan, 2000, Tasker & Tan, 2009).

The different star forming properties in the northern and the southern ridges of NGC 6946 provide chance to study the dynamical influence on star formation. We use velocity gradient in Position-Velocity (P-V) diagrams as an indicator of the strength of shocks across the bar (e.g., Athanassoula, 1992, Koda & Sofue, 2006). P-V diagrams are cut perpendicular to the ridges. Results of the northern ridge are displayed in Figure 3.39 for ^{13}CO and 3.40 for ^{12}CO. For each transition, P-V diagrams are made at three radii of +15″, +24″, and +30″. The shape of the observing P-V diagrams are consistent with the simulation from Athanassoula (1992) (Figure 3.41). There are two components in all P-V diagrams. At the trailing side (position $<$ 0″), velocity gradients are nearly flat. At the leading side, there is a sudden velocity jump in all P-V diagrams, corresponding

to the gas meeting the shocks (Athanassoula, 1992). In the observed P-V diagrams, velocity changes by $\sim$ 100 km s^{-1} over $<$ 10 $''$ ($<$ 270 pc) in both transitions and all radii. There is a sign that the amplitude of velocity jump decreases toward large radius. To be precise, at the radii of 15$''$ and 24$''$, velocity jumps are approximately parallel to the axis of velocity, whereas they are slightly flattened at the radius of 30$''$.

P-V diagrams of the southern ridge are displayed in Figure 3.42. Because of the low sensitivity of ^{13}CO, only ^{12}CO-base P-V diagrams are shown. The typical P-V pattern across bar is obvious at the radius of -18$''$. However, such a pattern is not clear at a radius of -27$''$, where the south spiral merging with the southern bar. The velocity difference across $\sim$ 20$''$ is about 150 km s^{-1} and 130 km s^{-1} at -18$''$ and -27$''$, respectively.

It is apparent from Figure 3.39, 3.40 and 3.42 that velocity jumps are steeper in the northern ridge than the southern ridge. Provided that the velocity jump is proportional to the strength of the shocks generated by the gas orbits, stronger shocks are associated with higher SFR, and the enhanced SFE in the northern ridge, suggesting that the GMCs ongoing shocks should be survival.

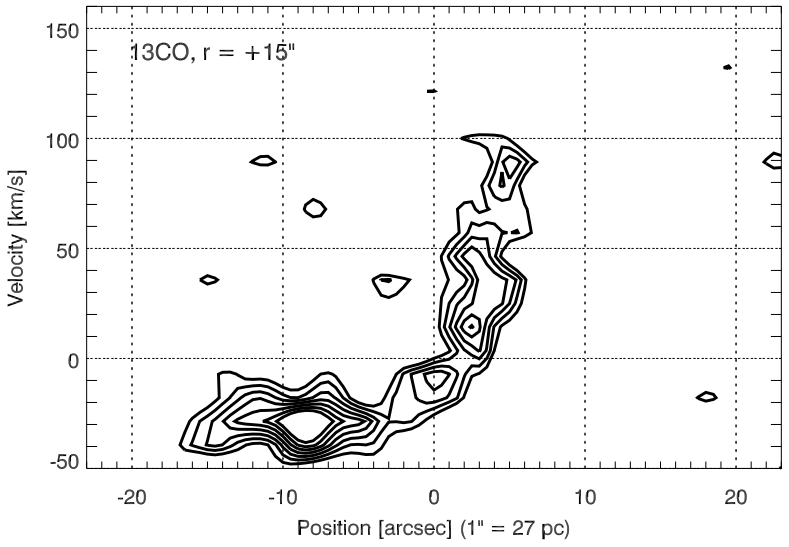

(a)

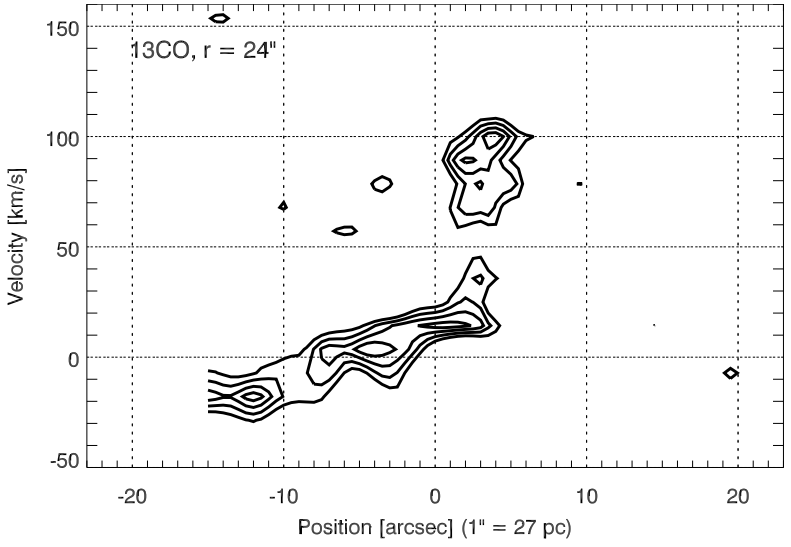

(b)

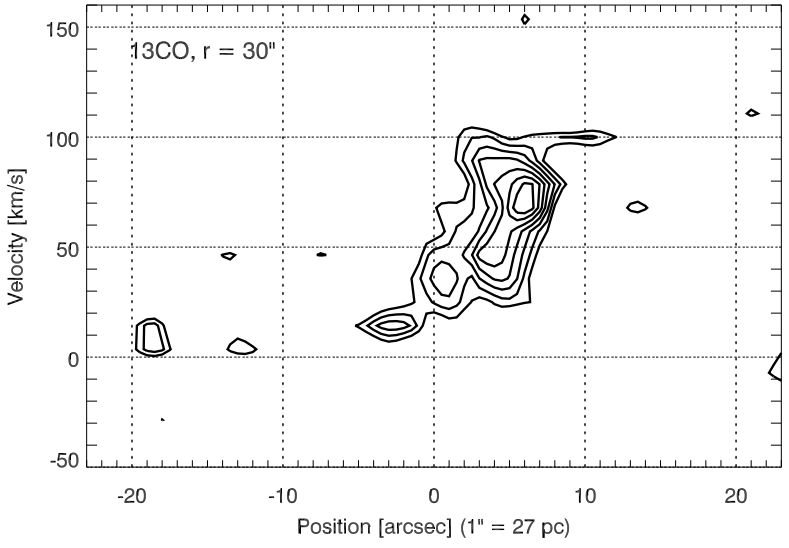

(c)

FIGURE 3.39: P-V diagrams of ^{13}CO cut perpendicular to the northern ridge. The radii are $+15''$, $24''$, and $30''$ in the panel (a) – (c), respectively

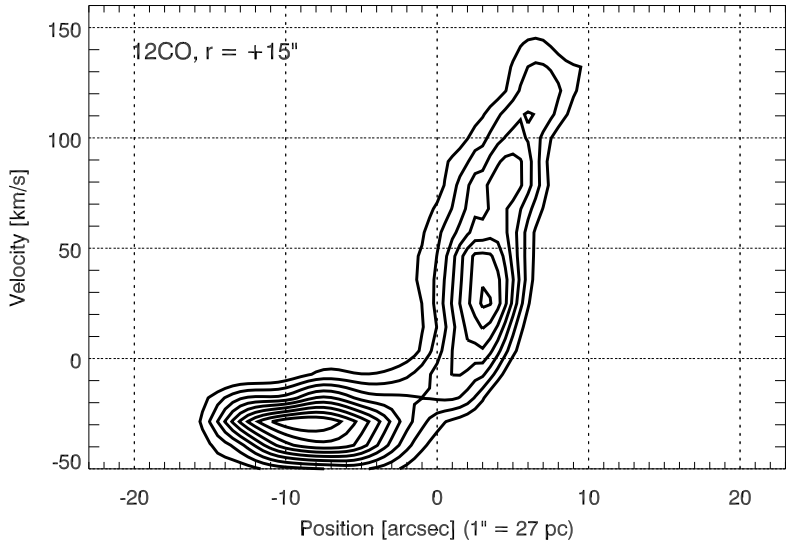

(a)

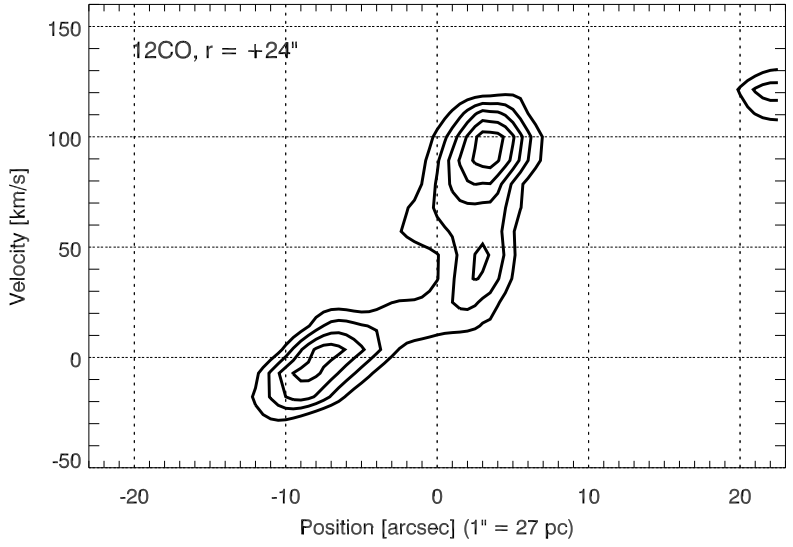

(b)

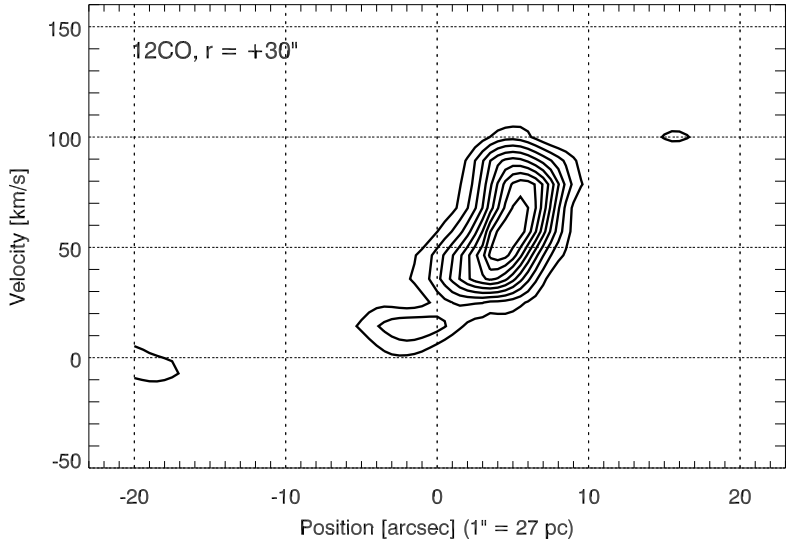

(c)

FIGURE 3.40: P-V diagrams of ^{12}CO cut perpendicular to the northern ridge. The radii are $+15''$, $24''$, and $30''$ in the panel (a) – (c), respectively.

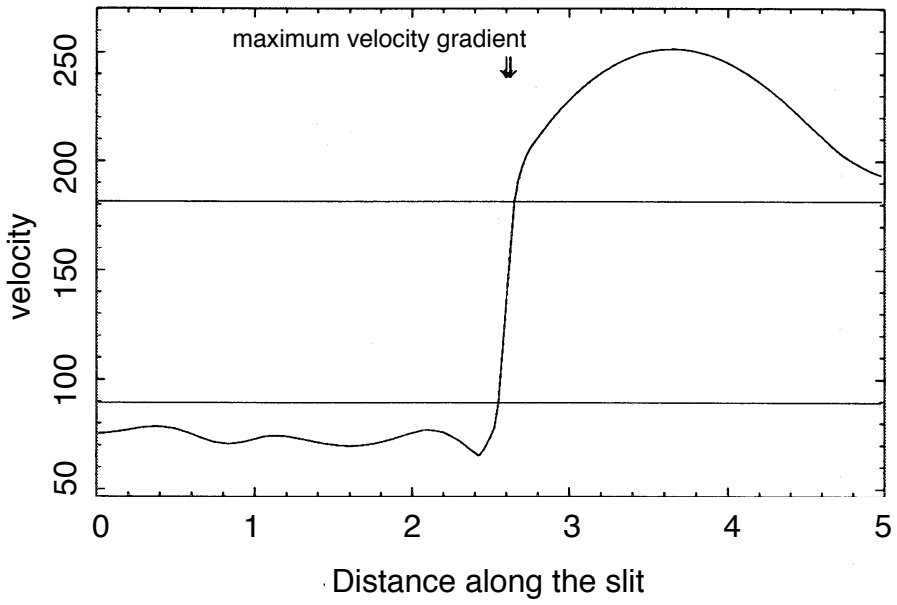

FIGURE 3.41: Simulation of P-V diagram cut perpendicular to a bar from Athanassoula (1992).

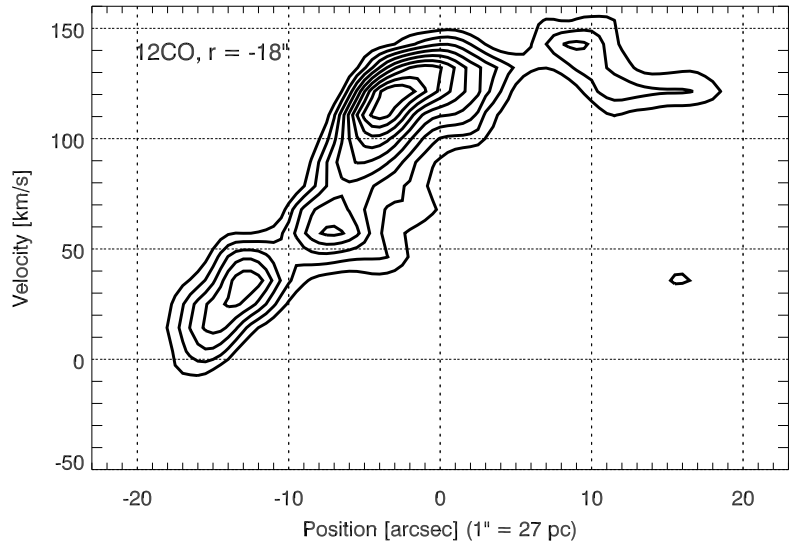

(a)

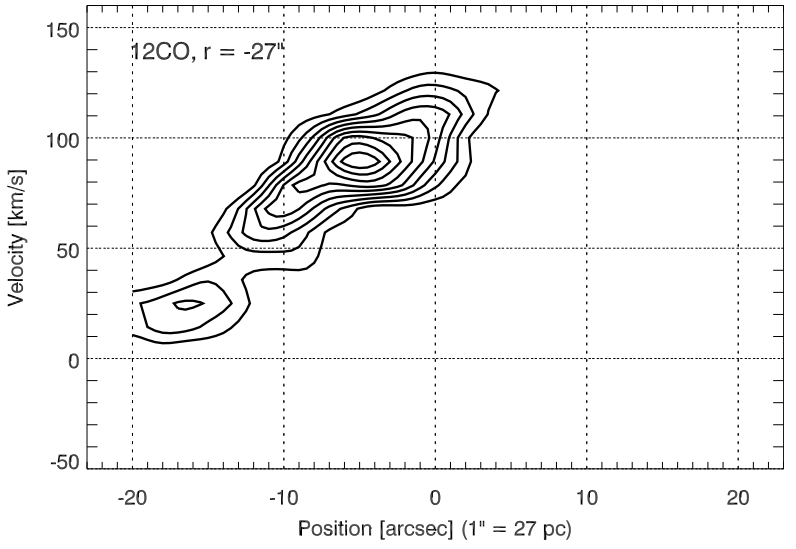

(b)

FIGURE 3.42: P-V diagrams of ^{12}CO cut perpendicular to the southern ridge. The radii are -18″ in the panel (a) and -27″ in the panel (b).

3.9 Resolved GMC Properties

In §3.7, we show that star formation is more active in the northern ridge than the southern ridge. In §3.8, we saw that velocity jumps are larger in the northern ridge than that in the southern ridge. In this section we check whether the resolved GMC properties are identical in the ridges along with a comparison with GMCs in the disk of NGC 6946.

We compare individual GMCs properties in this section. GMCs are obtained from Donovan Meyer et al. (2013) with the same ^{12}CO data with ours. The combination procedures are slightly different, by which they obtained a physical resolution of 60 pc. Donovan Meyer et al. (2013) define GMCs with the Clumpfind algorithm developed by Williams et al. (1994). 87 GMCs are defined. We only used the GMCs which are located in our ^{13}CO map. Moreover, we do not adopt the GMCs in the central region, namely, galactic center and minibar. The reason is that the actual structure of the central regions is far from resolved under a 60 pc resolution. On the other hand, only few GMCs are defined in this area (< 5). Such a small sample is less meaningful in terms of statistics. Comparison between the proprieties of GMCs of five nearby galactic centers (include NGC 6946) and our Galaxy has been discussed in Donovan Meyer et al. (2013). We refer the reader to the paper for detail discussion of central regions. Finally, we compile 49 GMCs, 12 in the northern ridge (GMC_N), 12 in the southern ridge (GMC_S), and rest of GMCs are classified as disk GMCs (GMC_D). Most of GMC_D are located in the spiral arms. Distribution of GMC is displayed in Figure 3.43, in which GMC_N, GMC_S, and GMC_D are marked with black, red, and cyan respectively.

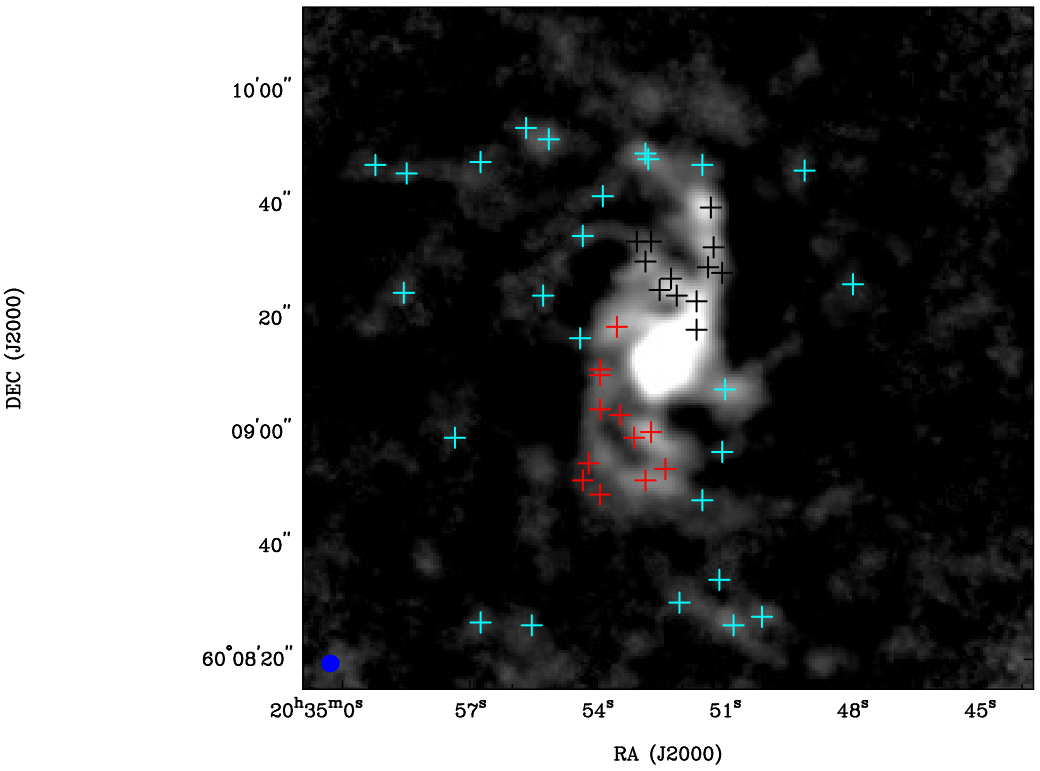

FIGURE 3.43: GMCs (crosses) overlaid on ^{12}CO integrated intensity map. The color black, red, and cyan represents the GMCs from the northern ridge (GMC_N), southern ridge (GMC_S), and rest of galactic disk (GMC_D), respectively. The GMCs are identified by Donovan Meyer et al. (2013).

3.9.1 Histograms of Individual Parameters

We plot various properties of GMC in Figure 3.44. GMC_D are shown as blue histograms, GMC_N and GMC_S are shown in black and red histograms, respectively. Median values of parameters are indicated with vertical lines with the same color as the population they represent and the values are presented in Table 3.5.

TABLE 3.5: Median properties of GMCs in the disk (GMC_D), southern ridge (GMC_S), and northern ridge (GMC_N).

	Δv [km s^{-1}]	Radius [pc]	Mass [10^5 M$_\odot$]	Σ_{gas} [M$_\odot$ pc^{-2}]	n_{H_2} [cm^{-3}]	τ_{ff} [yr]
GMC_D	5.2	88.9	17.6	101.0	18.6	8.9
GMC_S	6.8	97.9	41.3	148.7	28.3	7.9
GMC_N	9.3	98.1	78.9	370.6	70.4	4.7

The count distribution of velocity dispersion (Δv) is shown in Figure 3.44(a). Median Δv of GMC_D is about 5 km s^{-1}, consistent with that of the Galactic GMCs (Heyer et al., 2009). GMC_S have Δv of 5 – 15 km s^{-1}. The largest Δv of the southern ridge is contributed by the southern blob and the merging point of bar and spiral is $\sim$ 15 km s^{-1}. Median Δv of GMC_S is 7 km s^{-1}.

Δv of GMC_N has a wide range of 5 – 20 km s^{-1}. Median Δv of GMC_N is about 9 km s^{-1}. The larger Δv observed in GMC_N may be caused by rise of internal motions in GMCs due to the cloud-cloud collisions, large scale flow, such as spiral shocks (Bonnell et al., 2006, Dobbs et al., 2006, Klessen & Hennebelle, 2010, Koyama & Inutsuka, 2002), in this study, the galactic bar, and stellar feedback (Mac Low & Klessen, 2004).

Figure 3.44(b) shows a histogram of the radius of GMCs. Radius of GMCs typically lies within a range of 50 – 150 pc, slightly larger than Galactic GMCs (Heyer et al., 2009). From the histogram, there is no significant difference of radius among the three populations. Median masses of 90 – 100 pc are compatible among the galactic structures.

Mass distribution of GMCs is displayed in Figure 3.44(c). The median mass of GMC_D, GMC_S, and GMC_N are 1.7 × 10^6, 4.1 × 10^6, and 7.9 × 10^6 $M_\odot$, respectively. Ridge GMCs are more massive than GMC_D by about four times. Figure 3.44(d) is a zoom in view of Figure 3.44(c) towards the small count regime. Majority of GMC_N and GMC_S are located in a mass range of $< 1.5 \times 10^7$ $M_\odot$ while there are few GMC_N and GMC_S which have large mass of $(2 - 6) \times 10^7$ $M_\odot$.

Figure 3.44(e) displays the histogram of gas surface density derived from the above mass and radius, a zoom-in look is shown in 3.44(f). All of GMC_D are located below a Σ_{gas} of 250 $M_\odot$ pc^{-2}. Median Σ_{gas} of GMC_D is 101 $M_\odot$ pc^{-2}. Turing to the ridges, unlike the disk, distribution of Σ_{gas} in the ridges are rather disperse. About 50% of GMC_S have Σ_{gas} of $\sim$ 150 $M_\odot$ pc^{-2}. Other 50% spread at 300 – 500 $M_\odot$ pc^{-2}. The largest Σ_{gas} of GMC_S is 493 $M_\odot$ pc^{-2}. There is no specific peak of Σ_{gas} distribution among GMC_N. GMC_N equally spread a wide range of 100 – 1000 $M_\odot$ pc^{-2} with a median Σ_{gas} of 370 $M_\odot$ pc^{-2}.

Figure 3.45 shows the histogram of mean volume density of molecular clouds calculated from the mass and radius. Volume density of GMC_D and GMC_S are lower than that of GMC_N. Although LVG calculations cannot constrain density accurately, the mean density of GMCs derived from the virial mass is roughly consist with that from LVG calculations and the limit it suggests. Median n_{H_2} of GMC_N, GMC_S, and GMC_D are 70, 28, and 18 cm^{-3}, respectively. The median volume density of GMC_N is larger than elsewhere by 2 – 4 times.

Free-fall time (t_{ff}) is the time required for a GMC collapses to form stars. We estimate t_{ff} for individual GMC by

$$t_{ff} = \sqrt{\frac{3\pi}{32G\rho}}, \tag{3.10}$$

where ρ is the volume density of a GMC. Histogram of t_{ff} is shown in Figure 3.46. t_{ff} of GMC_N is shorter than that of GMC_S by about 1.6 times. The median t_{ff} of GMC_N

is about 5 Myr, while it is about 8 Myr for GMC_S, and 9 Myr for GMC_D. The shorter t_{ff} found in the northern ridge could be the cause of the higher Σ_{SFR} and SFE.

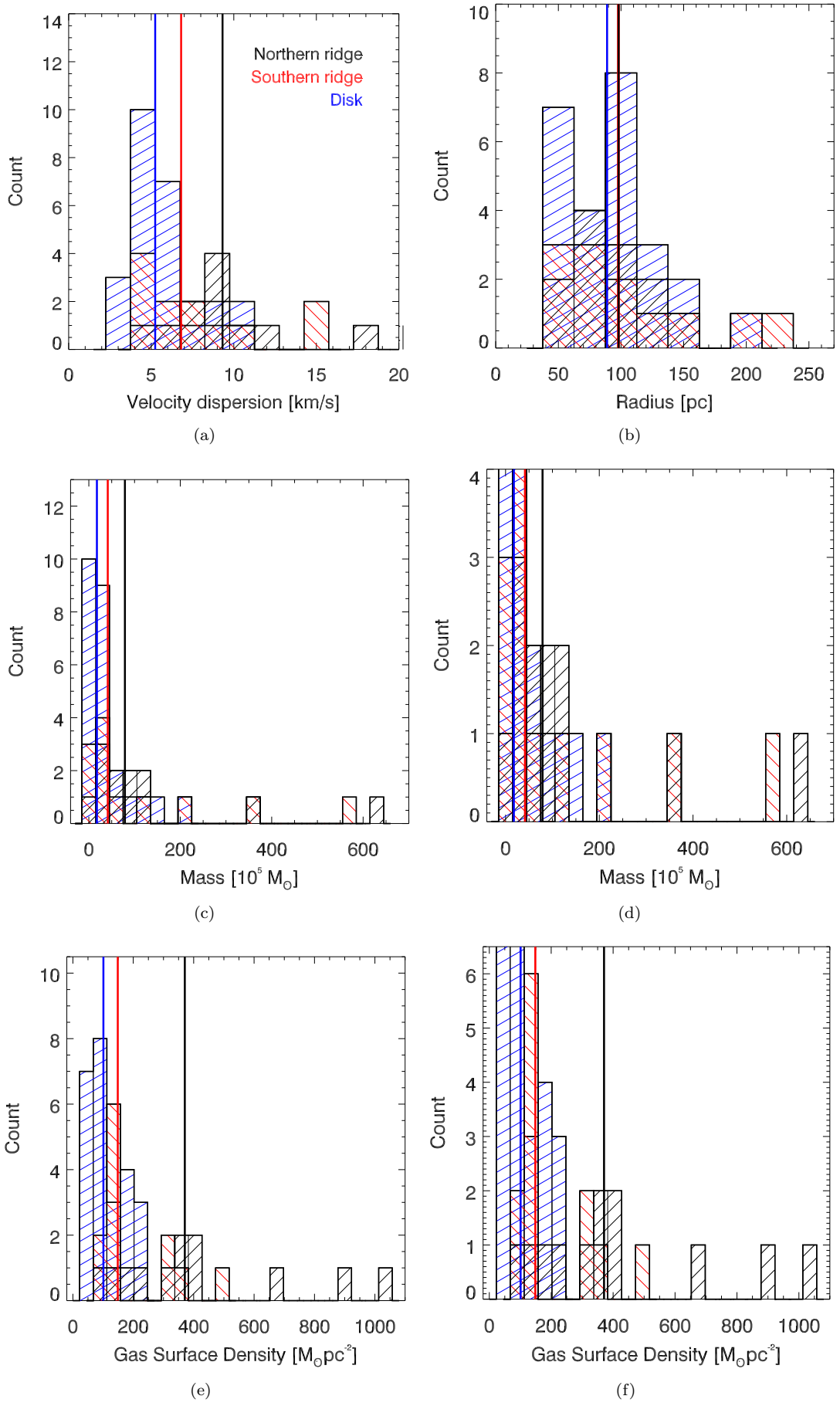

FIGURE 3.44: Histogram of GMC parameters. Black, red and blue histograms denote GMC_N, GMC_S and GMC_D, respectively. Vertical lines indicate median values of each parameters and GMC populations. (a) velocity dispersion. (b) radius, (c) mass, (d) zoom-in view of mass, (e) Σ_{gas}, and (f) zoom-in view of Σ_{gas}.

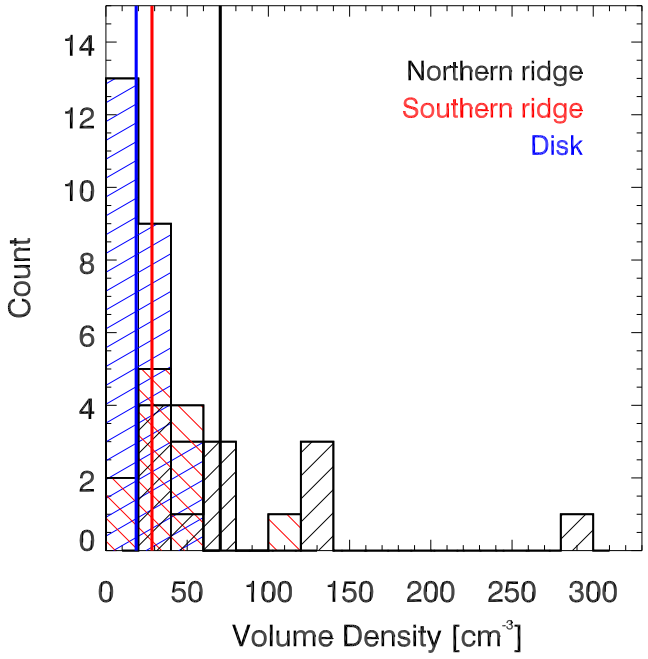

FIGURE 3.45: Histogram of volume density of molecular clouds. Black, red and blue histograms denote GMC_N, GMC_S and GMC_D, respectively. The median volume densities are indicated with vertical lines with the same color of each GMC population.

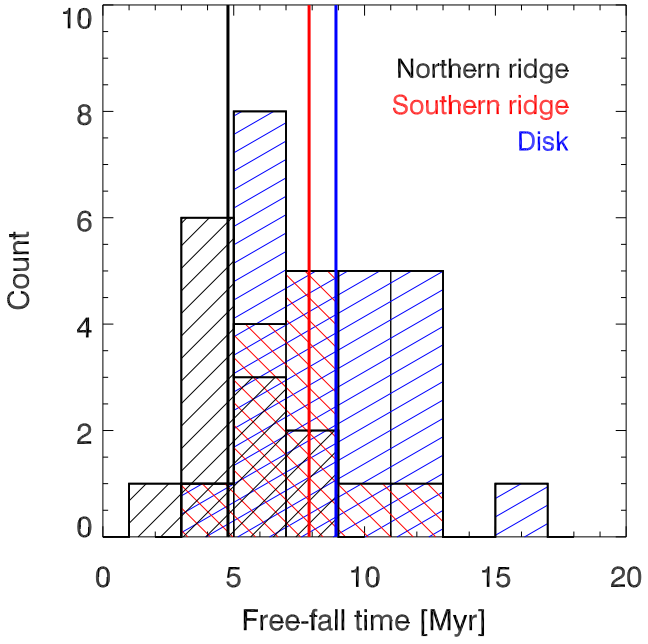

FIGURE 3.46: Histogram of free-fall time of molecular clouds. Black, red and blue histograms denote GMC_N, GMC_S and GMC_D, respectively. The median free-fall time are indicated with vertical lines with the same color of each population.

3.9.2 Scatter Plots of Parameters

Since Δv could arise due to shocks, thus, parameters are plotted as function of Δv in Figure 3.47. All panels are plotted in the same fashion, that is, GMC_N, GMC_S, and

GMC_D are colored black, red, and blue, respectively.

Firstly, the relationship of Δv and mass is shown in Figure 3.47. These two parameters show a tight correlation (cc[8] = 0.96). It is more obvious in the scatter plot than histogram that GMC_N have slightly larger Δv than $GMC_{S,D}$. The results are consistent with simulations that internal kinematics of GMCs could be attributed to cloud–cloud collisions or large-scale flow (e.g., shocks generated by spirals and bars, etc.) at the same time Δv arises. However, the masses of clouds are not significantly growing at the time (Dobbs et al., 2011a, Tasker & Tan, 2009).

Δv versus radius is shown in Figure 3.47. On the whole, there is a positive correlation between these two parameters. However, it is notable that the appearance of the correlation is produced by GMC_S and GMC_D. Correlation coefficient of Δv and radius are 0.81 and 0.70 for GMC_S and GMC_D, respectively, while it is only 0.54 for GMC_N. Radii of most of GMC_N are smaller than those suggested from the relation by a factor of two to three. Figure 3.47 suggests that the strong shocks in the northern ridge may promote the formation of GMCs with a normal mass but a smaller size (more compact). As a result, Σ_{gas} (Figure 3.47(c)) and the volume density (Figure 3.47(d)) of GMC_N are larger than those of GMC_S and GMC_D.

Figure 3.48 illustrates the relation of mass and radius of the molecular clouds. The mass–radius relation of GMC_D and GMC_S are similar, they are steeper than the relation of GMC_N. For GMCs with equivalent masses, GMC_N are smaller than $GMC_{S,D}$ by a factor of ~ 1.5. As a consequence, the volume density of GMC_N becomes three times larger.

Giant molecular clouds can form in the expanding front of supershells or the interface of two shells. The energy source of supershells can be stellar winds, supernovae, and HII regions. They have been found in our Milky Way and nearby (starburst) galaxies (Dawson et al., 2008, 2013, Fukui et al., 1999, García-Burillo et al., 2001, Matsunaga et al., 2001). Yamaguchi et al. (2001) observe supergiant shells in the LMC by NANTEN in the transition of ^{12}CO (1–0). They found that the clouds which are associated with the supergiant shells, such as being compressed, are smaller than the clouds which are not interacting with the shells. The more fragmented clouds associated with the expanding shells are found in our Galaxy as well (Sherman, 2012). The mass of GMCs in two groups of Yamaguchi et al. (2001) are similar. Moreover, the star formation is slightly more active in the GMCs which are interacting with the shell. All properties are consistent with what we found in the ridges of NGC 6946. Nevertheless, no significant difference of velocity dispersion is found between the two groups of LMC.

[8] correlation coefficient

Further, if suitable[9] velocity jumps in galactic bars can make compact (denser) molecular clouds and higher SFR/SFE, the shocks generated by supernova, HII regions (e.g., Ostriker & Shetty, 2011) and stellar winds may also have similar effect as shown by Yamaguchi et al. (2001). Accordingly, one can expect a larger slope of Kennicutt-Shimdt law (higher star formation efficiency) toward high surface density area, such as galactic centers where these energetic objects are frequently show and such effect can be dominant. The interaction of galaxy could also generate the similar influence on the molecular clouds by more violent compression. But note that the above-mentioned processes are not on the same scale. Galactic bars and the interaction of galaxies are large, galactic-scale process, while the influence from stellar populations is very local.

An anti-correlation between $t_{\rm ff}$ and Δv is shown in Figure 3.47(e). We estimated theoretical gas depletion time for each GMC based on the observed physical properties of them. Krumholz & McKee (2005) and Krumholz & Tan (2007) introduce a dimensionless SFR per $t_{\rm ff}$ ($\rm SFR_{ff}$). Physical meaning of $\rm SFR_{ff}$ is the fraction mass of a GMC converting to stars per $t_{\rm ff}$. Thus $\rm SFR_{ff}/t_{ff}$ is the inverse of the time required to convert all of gas into stars, namely, inverse of gas depletion time. $\rm SFR_{ff}$ is calculated with

$$\rm SFR_{ff} \approx 0.15 \epsilon_{core} \alpha_{vir}^{-0.68} \boldsymbol{M}^{-0.32}. \tag{3.11}$$

$\boldsymbol{M}$ is 1D Mach number of turbulence with $M = 20\alpha_{\rm vir}^{0.5}{\Sigma_{\rm cl}}'^{0.25}M_6^{-0.08}$, where ${\Sigma_{\rm cl}}' = \Sigma_{\rm cl}/85\,M_\odot\,{\rm pc}^{-2}$ and $\rm M_6$ is mass of the cloud in unit of 10^6 $\rm M_\odot$. $\alpha_{\rm vir}$ is virial parameter, which can be calculated by

$$\alpha_{\rm vir} = 5\pi^{-1/2}(M\Sigma_{\rm cl})^{-1/2}\Delta v^2/G \tag{3.12}$$

(Bertoldi & McKee, 1992). $\epsilon_{\rm core}$ is a fraction of the mass in a prestellar core that will be used for forming stars instead of being ejected by protostellar outflow. The fraction of mass that will be ejected by outflows is about 25% – 75% based on the theoretical calculation of Matzner & McKee (2000). Recently Alves et al. (2007) estimate $\epsilon_{\rm core}$ by the observations of the Galactic dense cores and stars. By comparing the mass function of dense cores and stars, they found that $\epsilon_{\rm core}$ is about 0.3. Thus we adopt the observational $\epsilon_{\rm core}$ of 0.3 in this work. Scatter plot of $(\rm SFR_{ff}/t_{ff})^{-1}$ (gas depletion time for a GMC) and Δv is shown in Figure 3.47(f). $(\rm SFR_{ff}/t_{ff})^{-1}$ of GMCs is in a range of 200 – 1000 Myr, or a SFE of (1 – 5) $\times$ 10^9 $\rm yr^{-1}$. $(\rm SFR_{ff}/t_{ff})^{-1}$ of $\rm GMC_N$ is about 300 – 1000 Myr ($\sim$ (1 – 3) $\times$ 10^9 $\rm yr^{-1}$), whereas it is 400 – 1000 Myr ($\sim$ (1.0– 2.5) $\times$ 10^9 $\rm yr^{-1}$) for most of $\rm GMC_S$ and $\rm GMC_D$.

[9] too large velocity jump may cause the disruption GMCs

For the sake of comparing the observed SFE to the $(\mathrm{SFR_{ff}}/t_{\mathrm{ff}})^{-1}$, we scale the observed SFE derived from ^{13}CO by a factor three to consider ϵ_{core}. The observed SFE become $\sim$4.5 $\times$ 10^{-9} and $\sim$ 1.2 $\times$ 10^{-9} yr^{-1} for the northern and the southern ridge, respectively. The values are consistent with the $(\mathrm{SFR_{ff}}/t_{\mathrm{ff}})^{-1}$ of individual $\mathrm{GMC_N}$ and $\mathrm{GMC_S}$. A caution arise from above comparison is that the current state of GMCs are not necessarily associated with the observed star formation, instead, they are in charge of future star formation. The consistence of SFE and $(\mathrm{SFR_{ff}}/t_{\mathrm{ff}})^{-1}$ suggests that current degree of star forming activity in the ridges will sustain till next star formation.

There is an interesting feature in the plot of $(\mathrm{SFR_{ff}}/t_{\mathrm{ff}})^{-1}$ and Δv. It shows a weak downhill relationship in $\mathrm{GMC_N}$ ($cc \approx$ -0.3), while $\mathrm{GMC_S}$ and $\mathrm{GMC_D}$ have opposite relation ($cc \approx 0.3$). Given that $\mathrm{SFR_{ff}}/t_{\mathrm{ff}}$ (star formation per free-fall time) is proportional to the degree of star formation, the results of $\mathrm{GMC_S}$ and $\mathrm{GMC_D}$ are consistent with the GMCs observed in the spiral arm of IC 342 and M83 that star forming GMCs tend to have smaller Δv. Yet $\mathrm{GMC_N}$ have larger Δv than other GMCs even the star formation is more active. This again suggests that the shocks generated by galactic bar may change GMC properties and their star forming ability.

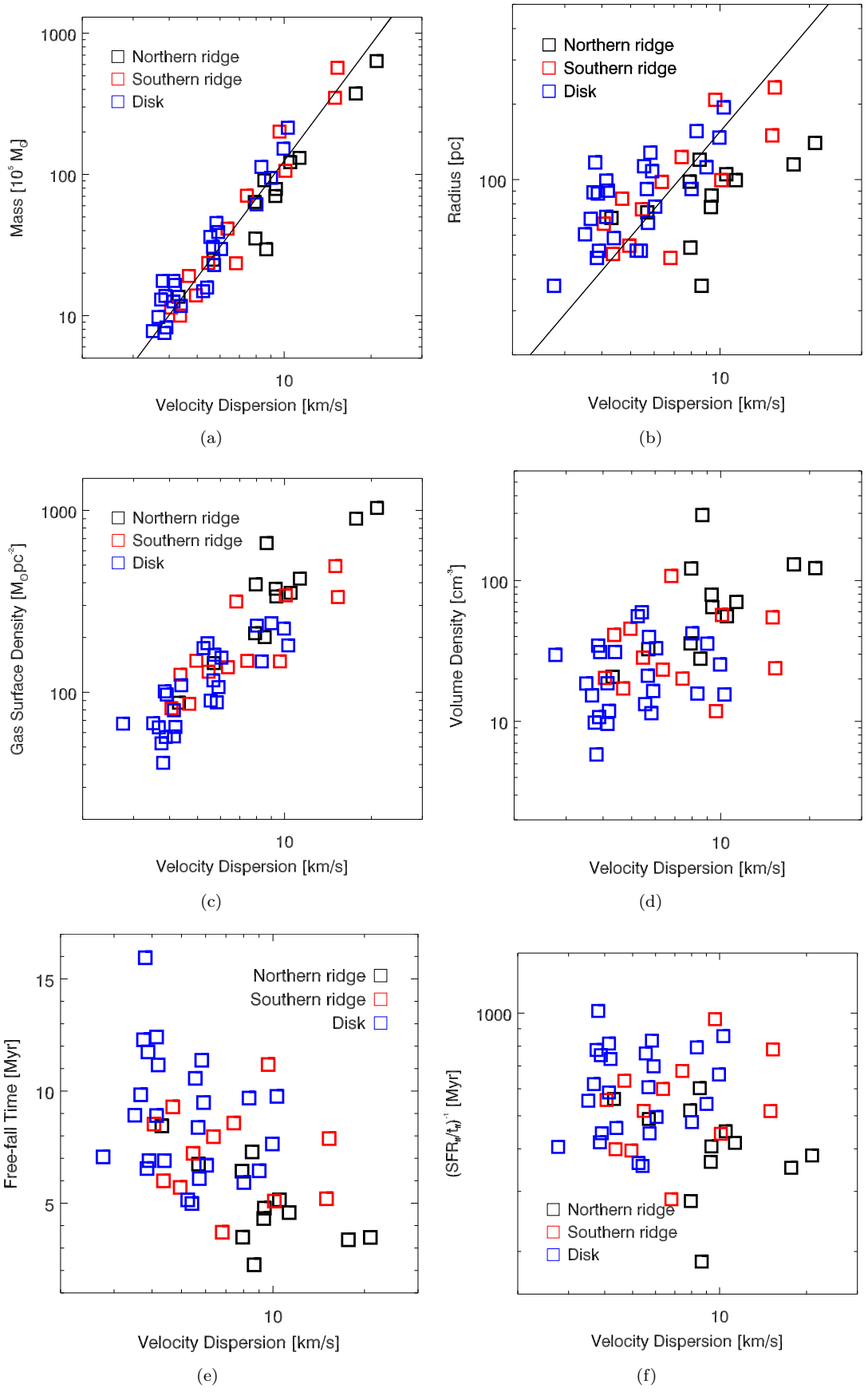

FIGURE 3.47: Scatter plots of parameters. All parameters are plotted as a function of velocity dispersion. Black, red and blue symbols denote GMC_N, GMC_S and GMC_D, respectively. (a) Mass versus velocity dispersion. (b) Radius versus velocity dispersion. (c) Surface density versus velocity dispersion. (d) Volume density versus velocity dispersion. (e) Free-fall time versus velocity dispersion. (f) The inverse of the time required to convert all of gas into stars versus velocity dispersion.

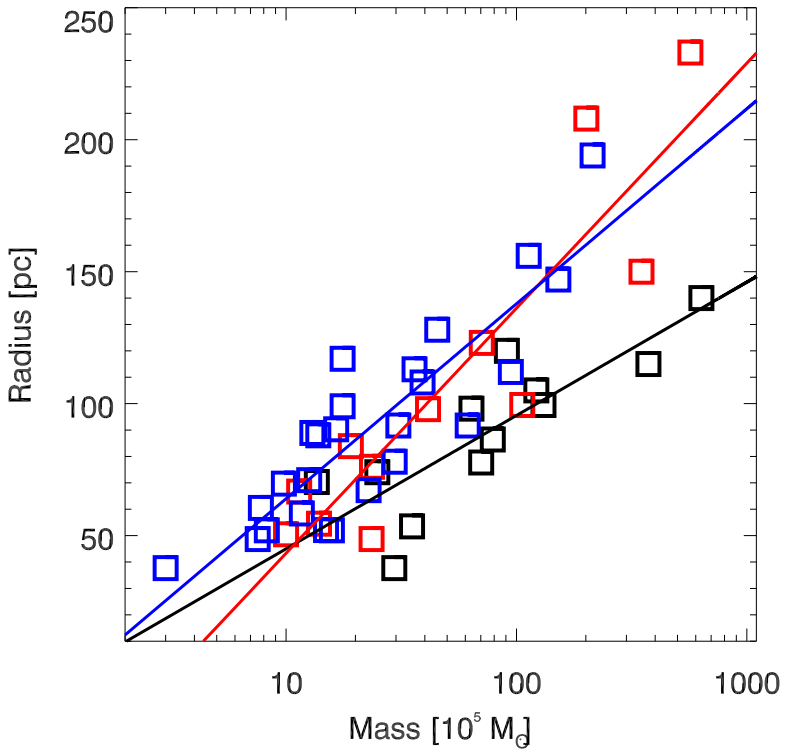

FIGURE 3.48: Mass versus radius of GMCs. Black, red and blue symbols denote GMC_N, GMC_S and GMC_D, respectively. Straight lines are the fits of data.

3.10 Comparison with Other Galaxies

3.10.1 Velocity Jumps in Galaxies

On the global scale, the inhibition of star formation is due to the strong shocks across the bar, which lead to the local destruction of clouds by strong cloud-cloud collisions when the clouds enter the shocks. Given that the pattern speed of NGC 6946 is $\sim$ 47 km s^{-1} kpc^{-1} with in the central 1$'$ (Fathi et al., 2007), and that the rotational velocity at 1 kpc is $\sim$ 90 km s^{-1} (Egusa et al., 2009, from CO observations), thus the clouds enter the shocks with a velocity of $\sim$43 km s^{-1}. A significantly larger velocity of $\sim$165 km s^{-1} is suggested in the non-star forming bar NGC 1530 (Reynaud & Downes, 1998). The difference suggests that the clouds likely survive from the shocks of NGC 6946. Hydrodynamic simulations also predict a threshold for clouds to be destroyed, and it is $>$ 20 – 60 km s^{-1} (Tubbs, 1982). Our observed value of NGC 6946 is just consist with threshold limit value suggested by the simulations. Future observations with high physical resolution of non-star forming bar such as NGC 1530 will be an interesting study to compare the GMC properties in different environments.

NGC 6946 is a weak bar galaxies, while the bar of NGC 1530 is strong. The strength of bar may be a reason of the different star forming properties. However, NGC 2903 which has a strong bar contains active star formation in the bar region. Hα shows that there is a string of HII regions along the bar. Dense gas traced by HCN (1–0) are found in the entire bar as well. The rotational velocity at the halfway ($\sim$ 1.2 kpc) and the end ($\sim$ 2.0 kpc) of the bar is about 150 and 190 km s^{-1}, respectively (Sofue, 1997, from CO observations). The pattern speed of NGC 2903 is $\sim$ 40 km s^{-1} kpc^{-1} (Hirota et al., 2009). The resultant velocity for clouds entering the shocks is $\sim$ 102 km s^{-1} at the halfway and 110 km s^{-1} at the end of the bar. The values exceed the threshold velocity for the clouds to survive suggested by the simulations of Tubbs (1982), although it is still considerably lower than that of NGC 1530. Accordingly, the strength of bar may not be the only cause of star formation in bars.

3.10.2 GMC Properties in Galaxies

Our results implies that large velocity gradients in bar can generate compact GMCs with a but a normal mass. As a result, the GMCs become denser along with a shorter free-fall time or faster star formation. Same situation is found in the GMCs formed at the front of a expanding shell. If the energy sources of the expanding shell (e.g., multiple supernovae in OB associations or HII regions) largely exist in the high-$\Sigma_{\rm gas}$ regions, such as galactic center, we could expect enhanced SFE toward the high-$\Sigma_{\rm gas}$

regions. In other words, the changing slope of K-S law can be attributed to a different star forming mechanism as we have examined in the disk and center of IC 342. On the other hand, it can be a result of changing GMC properties as seen in the case of NGC 6946.

We compare GMC properties in NGC 6946 and other galaxies, including Antennae galaxies, Galactic center (central 400 pc), Galactic disk (2 – 12 kpc), inner disk of spiral galaxies NGC 4826 and NGC 4736 (0.3 – 3 kpc). Outer disk of spiral galaxy M31 (11 kpc), and HI-dominant dwarf galaxies NGC 205, NGC 1569, NGC 2976, NGC 3077, NGC 4214, NGC 4449, NGC 4605, and IC 10. The data are compiled from literature. Observation parameters and references are summarized in Table 3.6. The most distant target is Antennae galaxies at 22 Mpc (Ueda et al., 2012). Spiral and dwarf galaxies are located within 7.5 Mpc. Resolutions of 30 – 150 pc of nearby galaxies are roughly compatible to the resolution that Donovan Meyer et al. (2013) use to define GMCs in NGC 6946 (∼60 pc). To minimize any artificial variation of GMCs properties due to the type of telescopes, we only adopt the extragalactic GMCs mapped with inteferometers. Antennae galaxies was mapped in ^{12}CO (3–2), while other galaxies are observed in ^{12}CO (1–0). The reason is to match the resolutions.

TABLE 3.6: Observation parameters of galaxies

Galaxies	Telescope	Resolution	Transitions	$r \propto M^{\mathrm{a}}$, a =	References
Antennae galaxies	SMA[a]	∼ 150 pc	^{12}CO (3–2)	0.20 ± 0.03	[b]
Galactic center[c]	NRO 45-m	1.4 pc	^{12}CO (1–0)	0.31 ± 0.02	[d]
Galactic disk[e]	FCRAO 14 m	. . .[f]	^{12}CO (1–0)	0.42 ± 0.01	[g]
NGC 4826/4736 (inner disks)[h]	CARMA/NRO	60–80 pc	^{12}CO (1–0)	0.27 ± 0.01	[i]
M31 (outer disk)[k]	BIMA	30 pc	^{12}CO (1–0)	0.40 ± 0.03	[l]
dwarf galaxies	BIMA/OVRO	∼20 – 120 pc	^{12}CO (1–0)	0.43 ± 0.02	[m]
NGC 6946 Northern ridge	CARMA/NRO	60 pc	^{12}CO (1–0)	0.25 ± 0.06	[i]
NGC 6946 Southern ridge	CARMA/NRO	60 pc	^{12}CO (1–0)	0.35 ± 0.04	[i]
NGC 6946 Disk	CARMA/NRO	60 pc	^{12}CO (1–0)	0.34 ± 0.04	[i]

[a] Submillimeter Array
[b] Ueda et al. (2012)
[c] Galactic center: < 400 pc
[d] Oka et al. (1998, 2001)
[e] Galactic disk: 2 – 12 kpc
[f] resolution of 0.2 pc at a distance of 1 kpc
[g] Solomon et al. (1987)
[h] inner disks: 0.3 – 3 kpc for NGC 4826, 0.6 – 1.5 kpc for NGC 4736
[i] Donovan Meyer et al. (2013)
[j] 2 kpc
[k] outer disks: 11 kpc
[l] Rosolowsky (2007)
[m] Bolatto et al. (2008) and reference therein

Figure 3.49 plots the virial mass versus radius of GMCs in each galaxy populations. For each population, data is fitted with a form of $r \propto M^{\mathrm{a}}$. Small a implies that the radii of GMCs are growing relatively slower when the mass is increasing. In other words,

variation of the volume density of GMCs is more pronounced and the fraction of dense GMCs relatively increases when a is small.

The index of a is summarized in Table 3.6. The smallest a occurs in Antennae galaxies, which is 0.20 $\pm$ 0.03. a of 0.31 $\pm$ 0.02 is shown in Galactic center. a of the northern ridge of NGC 6946 lies between the values of Antennae galaxies (Arp 244) and Galactic center. The inner disks ($<$ 3 kpc) of spiral galaxies also show a small a, which is 0.27 $\pm$ 0.02. Galactic disk, outer disk of M 31, nearby spiral galaxies, the southern ridge and the disk of NGC 6946 have comparable a about 0.35 – 0.40. The largest a of $\sim$0.43 occurs in the dwarf galaxies.

There is a modest trend between a and the degree of star forming activity. Antennae galaxies is an interacting system consisting of two galaxies NGC 4038 and NGC 4039. SFR and total molecular gas mass of Antennae is $\sim$22 $M_\odot$ yr^{-1} and 10^{10} $M_\odot$, respectively (Klaas et al., 2010, Ueda et al., 2012), resulting in a SFE of $\sim 2 \times 10^{-9}$ yr^{-1}. SFR of Galactic center within the central 400 pc is 0.14 $M_\odot$ yr^{-1} (Yusef-Zadeh et al., 2009). Mass of molecular hydrogen measured by Oka et al. (1998) is (2–7) $\times$ 10^7 $M_\odot$ within the 400 pc. The values suggest a SFE of (2–7) $\times$ 10^{-9} yr^{-1} at the Galactic center. The index a of radius-mass relation is 0.31 $\pm$ 0.02. SFE and a of the northern ridge of NGC 6946 ($\sim 2 \times 10^{-9}$ yr^{-1} and 0.25 $\pm$ 0.06) are comparable with that observed in the Antennae galaxies and the Galactic center. SFE of inner disks of NGC 4826 and NGC 4736 are $\sim \times 10^{-9}$ yr^{-1} (Leroy et al., 2008, Rosolowsky & Blitz, 2005).

For the galactic planes of normal disk galaxies, SFE is also about (5 – 10) $\times$ 10^{-10} yr^{-1} (Bigiel et al., 2008, Kennicutt, 1998, Leroy et al., 2008, Rahman et al., 2012, Tabatabaei & Berkhuijsen, 2010), while a is about $\sim$ 0.35 – 0.40. SFE of HI dwarf galaxies is similar to those found in the outer optical disks of spiral galaxies (Bigiel et al., 2008, Leroy et al., 2005, 2008, Yin et al., 2010), about 10^{-10} – 10^{-9} yr^{-1} in the centers and 10^{-11} – 10^{-10} yr^{-1} in their disks. a of dwarf galaxies (0.43 $\pm$ 0.02) is slightly smaller than that of molecule-rich galaxies.

3.10.3 Implications of the Non-universal Star Formation Law in Terms of External Pressure

The abovementioned properties suggest that galaxies with higher SFE tend to have smaller a or more dense GMCs. In our Milky Way, the internal pressures of GMCs far exceed the ambient ISM pressure, implying that GMCs are self-gravitating and hence decoupled from the environments. However, if ambient pressure increases, the internal pressures of GMCs (act outwards) must rise as well to be in pressure equilibrium with the surrounding diffuse interstellar gas. When the molecular clouds are compressed by

the external pressure, the gravitational force of GMCs also increase. Once the internal pressure of GMCs cannot support the external pressure and the gravitational force, GMCs will collapse and form stars. The origins of the external pressure cloud be ram pressure from inflow (Heitsch et al., 2009), weight of atomic gas (Harris & Pudritz, 1994, Heyer et al., 2001), hot gas (Keto et al., 2005, Oka et al., 1998), and other dynamical processes (Jog & Solomon, 1992, Keto et al., 2005, Wei et al., 2012). Physical properties of GMCs in the potential higher-pressure environments, such as spiral arm, dust lanes and inner disks of galaxies, may be consequently regulated by the ambient ISM. In the more extreme environments, such as interacting galaxies, the increase of external pressure may be the mechanism of the formation of super star clusters. Those clusters are very compact, which may be a result of their compact parent clouds (Bekki, 2004).

We can examine the relation of the internal pressures of GMCs and the external pressure of ISM in the concerned regions of NGC 6946. The internal pressure of a GMC is calculated by the observed GMC properties according to:

$$\frac{P_{\rm int}}{k}\ \left[{\rm cm^{-3}\ K}\right] = \rho\Delta v^2 = 212 \times \left(\frac{M}{M_\odot}\right) \times \left(\frac{r}{\rm pc}\right)^{-3} \times \left(\frac{\Delta v}{\rm km\ s^{-1}}\right)^2 \tag{3.13}$$

(Rosolowsky & Blitz, 2005). The median $\frac{P_{\rm int}}{k}$ of $\rm GMC_D$, $\rm GMC_S$, and $\rm GMC_N$ are 2.0×10^4, 4.4×10^4, and 2.8×10^5 cm $^{-3}$ K, respectively. The values lie in a normal range for the external GMCs (Hughes et al., 2013), which is 10^4 – 10^6 cm $^{-3}$ K. The median $\frac{P_{\rm int}}{k}$ of $\rm GMC_N$ is an order magnitude larger than $\rm GMC_D$, and ~ 6 times larger than $\rm GMC_S$.

External pressure at the boundary of a GMC is calculated using an expression for the midplane hydrostatic pressure (Blitz & Rosolowsky, 2004b, Elmegreen, 1989, Rosolowsky & Blitz, 2005), assuming a two-component disk, i.e., gas and stars:

$$\frac{P_{\rm ext}}{k}\ \left[{\rm cm^{-3}\ K}\right] = 272 \times \left(\frac{\Sigma_{\rm Gas}}{M_\odot\ {\rm pc^{-2}}}\right) \times \left(\frac{\Sigma_\star}{M_\odot\ {\rm pc^{-2}}}\right)^{0.5} \times \frac{v_{\rm g}}{\rm km\ s^{-1}} \times \left(\frac{h_\star}{\rm pc}\right)^{-0.5}, \tag{3.14}$$

where $\Sigma_{\rm Gas}$ is surface density of ISM, including molecular and atomic gas, $\Sigma_\star$ is surface density of stellar mass, $v_{\rm g}$ is velocity dispersion of the gas, and $h_\star$ is scale height of stellar disk. We define the diffuse $\Sigma_{\rm Gas}$ as $\Sigma_{\rm H_2,diff} + \Sigma_{\rm HI}$. The single dish ^{13}CO map is used to derive diffuse $\Sigma_{\rm H_2,diff}$ by assuming that diffuse gas occupies 50% of the gas. The amount of diffuse gas is hinted by the amount of missing flux and it is also a typical value observed in our Galaxy and nearby galaxies (e.g., Hirota et al., 2010, Rosolowsky & Blitz, 2005). $\Sigma_{\rm HI}$ of 6 $\rm M_\odot\ pc^{-2}$ is adopted, which is derived from Leroy et al. (2008) by using the THINGS map of VLA. $\Sigma_\star$ is estimated by using the 3.6 μm image observed by the IRAC of Spitzer. 3.6 μm traces the light from older stars. An empirical conversion

derived from Leroy et al. (2008) is used for $\Sigma_\star$:

$$\Sigma_\star = \Upsilon_{\star,K} \left(\frac{I_K}{I_{3.6}} \right) I_{3.6} \cos i = 280\, I_{3.6} \cos i. \tag{3.15}$$

$\Upsilon_{\star,K}$ is K-band mass-to-light ratio, $\Upsilon_{\star,K} = 0.5\ M_\odot / L_{\odot,K}$. $I_{3.6}$ and I_K show a tight correlation of $I_{3.6} = 0.55\ I_K$ (both in MJy ster^{-1}) derived from Leroy et al. (2008). The conversion assumes a Kroupa IMF, same as the equation we use for SFR. We find a $\Sigma_\star$ of 303, 534, and 826 M$_\odot$ pc^{-2} for GMC$_{\rm D}$, GMC$_{\rm S}$, and GMC$_{\rm N}$, respectively. Velocity dispersion of interstellar gas ($v_{\rm g}$) is assumed to be 7 km s^{-1} (Malhotra, 1994, Stark & Brand, 1989). Finally, a scale height of stellar disk of 350 pc is adopted, which is derived for the Milky Way and nearby galaxies (Narayan & Jog, 2002a,b). With the above parameters, $\frac{P_{\rm ext}}{k}$ is found to be 2.9 $\times$ 10^4, 5.2 $\times$ 10^4, and 1.5 $\times$ 10^5 cm^{-3} K for GMC$_{\rm D}$, GMC$_{\rm S}$, and GMC$_{\rm N}$, respectively.

Figure 3.50 plots $\frac{P_{\rm int}}{k}$ versus $\frac{P_{\rm ext}}{k}$ for the GMCs in NGC 6946. The solid line indicates the trend of $\frac{P_{\rm int}}{k} = \frac{P_{\rm ext}}{k}$. $\frac{P_{\rm int}}{k}$ and $\frac{P_{\rm ext}}{k}$ are nearly equivalent in all regions, implying the GMCs are likely in a pressure-bounded equilibrium. Moreover, the two variables show a clear positive correlation, suggesting that the larger surface density and volume density of GMC$_{\rm N}$ could be a result of higher external ISM pressure in this area. The external pressure might be arisen by the galactic bar and the stellar feedback.

The smaller and denser clouds observed in the northern ridges of NGC 6946, Antennae galaxies, Galactic center, and the inner disks of spiral galaxies cloud be a side effect on GMCs due to the high-pressure environments. For comparison, we estimate the median $\frac{P_{\rm int}}{k}$ of GMCs in the dwarfs and Antennae galaxies, they are 2.3 $\times$ 10^4 cm^{-3} K and 7.7 $\times$ 10^5 cm^{-3} K, respectively. $\frac{P_{\rm int}}{k}$ of dwarfs is comparable with that of the disk GMCs in NGC 6946, but smaller than the ridges. $\frac{P_{\rm ext}}{k}$ of dwarf galaxies derived from Leroy et al. (2008) are typically $<$10$^{4.3}$ ($\sim$ 2 $\times$ 10^4) cm^{-3} K, and often around 10$^{3.5}$ ($\sim$ 3 $\times$ 10^3) cm^{-3} K. The situation is more like our Milky Way that $\frac{P_{\rm int}}{k}$ is considerably larger than $\frac{P_{\rm ext}}{k}$. In such a case, the physical properties of GMCs are independent to the environments. GMC in the targets like NGC 6946 is a transition between dwarfs/Milky Way and starburst galaxies that the internal pressures of GMCs have to grow to reach the ambient pressure but not overpressure. For starburst galaxy (in this case, it is also interacting galaxies), $\frac{P_{\rm int}}{k}$ of Antennae galaxies is about five times larger than the high-pressure region of NGC 6946 (the northern ridge). It could be a result of the fact that the GMCs in Antennae galaxies are surrounding by the warm and high-pressure ISM due to the collision of galaxies (Jog & Solomon, 1992). However, Wilson et al. (2003) derive a $\frac{P_{\rm ext}}{k}$ of (4–8) $\times$ $\times$ 10^5 cm^{-3} K, which is consistent with the $\frac{P_{\rm int}}{k}$ estimated in this work. Wilson et al. (2003) also estimate $\frac{P_{\rm ext}}{k}$ of Antennae galaxies. They suggest a range of 6 $\times$ 10^5 – 6 $\times$ 10^6 cm^{-3} K, implying $\frac{P_{\rm ext}}{k} \geqslant \frac{P_{\rm int}}{k}$. Hence, GMCs in Antennae

galaxies may be either just in equilibrium or $\frac{P_{\rm ext}}{k} \geqslant \frac{P_{\rm int}}{k}$. In any case, they are different with the GMCs in the dwarfs and the Galaxy. We note that the GMCs in Ueda et al. (2012) (used in this work) and Wilson et al. (2003) may not be fully resolved due to the relatively low resolutions (150 pc in Ueda et al. (2012) and 380 pc in Wilson et al. (2003)). Future high resolution is required to make more reliable comparison.

There are some drawbacks of the comparison in this section that we would like to claim. First of all, observations of resolved extragalactic GMCs are still limited to very nearby galaxies, in which the galactic environments are relatively similar. Future observations by ALMA with high resolution and sensitivity can enlarge the galactic environments toward farther Universe, where extreme objects are found in abundance, such as ULIRGs. ULIRGs have SFR of ~ 100 $M_\odot$ (Sanders & Mirabel, 1996) along with a SFE as high as 10^{-8} – 10^{-7} yr^{-1} (e.g., Bothwell et al., 2010, Carilli & Walter, 2013), about 10 times higher than the disk galaxies and 100 times higher than the dwarfs. The difference of environments of GMC properties should be more pronounced than nearby galaxies (e.g., Boquien et al., 2011, Jog & Solomon, 1992). Thus, ULIRGs offer crucial laboratories to examine how environmental effects change GMCs properties in the future. On the other hand, galactic bars worth exploring more. They provide a site to understand the variation of GMC properties in disk galaxies. The variation of GMCs properties should be more obvious in strong bar galaxies. Comparison of GMCs in the strong bars with (e.g., NGC 5430, 2903) and without (e.g., NGC 1530) star formation is probably the most straight way to realize how environments shape GMCs. The study is able to be carried out with current powerful interferometers, such as CARMA.

Moreover, we emphasize that the GMCs of the Antennae galaxies we adopted in this work is defined by the transition of ^{12}CO (3–2). The high transition CO lines could trace denser gas than low-J lines. This effect may bring the bias into our comparison. Moreover, Antennae galaxies have a high SFR, but a modest SFE compared to other ULIRGs. By comparing the separation of interacting galaxies and their amount of molecular gas, Gao & Solomon (1999) and Gao et al. (2001) suggest that Antennae galaxies are ongoing an early stage of merging (large serration of two galaxies and large amount of molecular gas which has not been consumed to stars yet). The reservoir of molecular gas is sufficient to initiate a starburst with SFE more than ten times higher in the later stage of merging. Then it will place the SFE of the Antennae galaxies to a normal value of typical ULIRGs. Hence, it is reasonable that we found its SFE similar with our Galactic center but lower than other ULIRGs, as well as a index a not so different with the Galactic center.

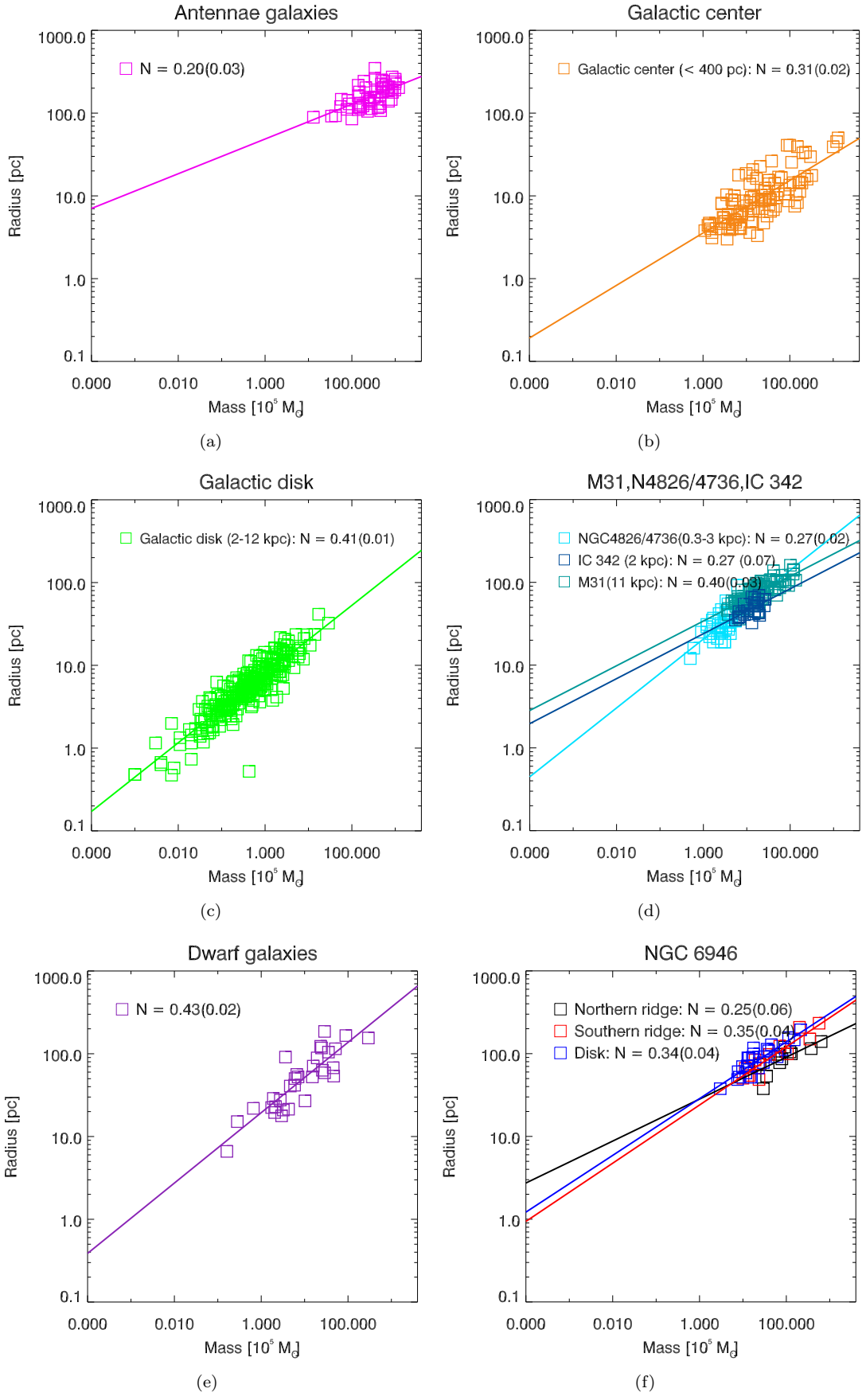

FIGURE 3.49: Relation of radius and mass of giant molecular clouds in galaxies. Name of galaxy is indicate in the top of each panel. Slope and uncertainty of the radius–mass relation is shown in upper left of panels. Results of NGC 6946 are displayed in panel (f), which is the same as in Figure 3.48. Observation parameters and references of the galaxies are summarized in Table 3.6.

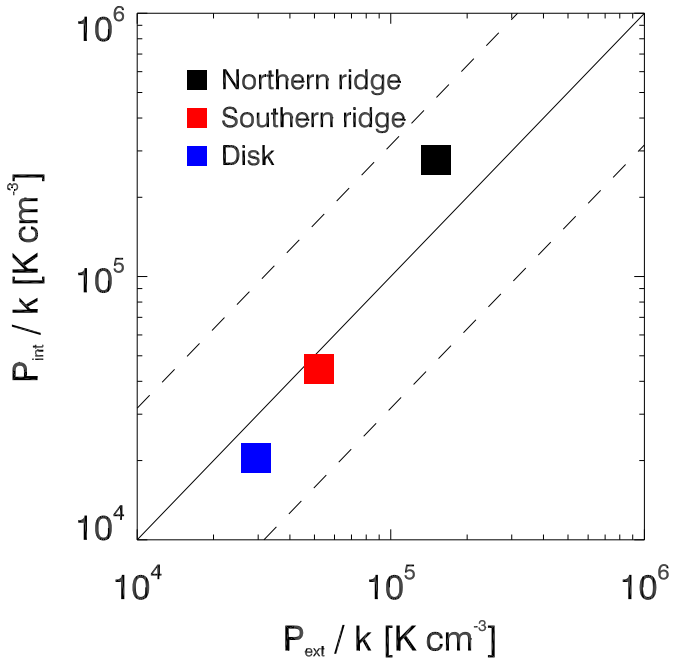

FIGURE 3.50: The median internal pressure ($\frac{P_{\rm int}}{k}$) of the GMC versus external pressure ($\frac{P_{\rm ext}}{k}$) of ambient ISM. The solid line indicates the equivalent of $\frac{P_{\rm int}}{k}$ and $\frac{P_{\rm ext}}{k}$, while the dashed line indicate $\frac{P_{\rm int}}{k} = 3\frac{P_{\rm ext}}{k}$ and $\frac{P_{\rm int}}{k} = (1/3)\frac{P_{\rm ext}}{k}$.

3.11 Summary of Chapter 3

We obtained optically thin ^{13}CO maps of NGC 6946 from single dish (Nobeyema 45-m telescope) and interferometer (CARMA). After combing the maps, the final resolution is 100 pc. From the map we found:

- There is an oval concentration around the central region, corresponding to the unresolved galactic center and a minibar.
- There is a northern bar (*northern ridge*) emerging around a barend of the minibar. The northern ridge shows a typical bar shape that molecular gas are concentrated at the leading side of the bar. Then star formation occurs at the downstream of the molecular ridge.
- Gas structures in the south is more complicated (*southern ridge*). There is a candidate of southern bar (*southern blob*) but it merges with a curved, spiral-like structure (*south spiral*).

We study physical properties of gas, including temperature, density and mass, by using our ^{13}CO map, the published ^{12}CO (1–0) map with comparable resolution (Donovan Meyer et al., 2012), the low resolution ^{12}CO (2–1) map from IRAM 30-m telescope, the

Herschel maps of 70μm and 160μm, and finally our HCN (1–0) data which was made by single-point observations. Results are summarized below:

- Within the central $\sim 1'$ of NGC 6946, ^{12}CO-to-^{13}CO intensity ratio (R_{10}) changes by a factor of three. R_{10} is as high as $\sim$ 17 in the galactic center. Minibar also has high R_{10}, approximately 15 – 16. Mean R_{10} of the northern ridge is 15. In the southern blob, R_{10} is about 12. R_{10}, and it is 7 – 10 at the majority of the south spiral.

- To better constrain the temperature and density with LVG calculations, ^{12}CO (2–1)-to-^{12}CO (1–0) (R_{21}) map was made by single dishes data (IRAM30 and NRO45). Central region (minibar and galactic center) has $R_{21} \approx 1$. R_{21} of northern ridge is about 0.8. Even though the single dish observations are not able to resolve the southern ridge from the central region, we constrain the possible R_{21} of the southern ridge by HCN observations. R_{21} of the southern ridge is < 0.8.

- LVG calculations of CO lines suggest that the galactic center and minibar contain two components of gas. One component is moderate warm (20 – 40 K) but dense ($> 10^{4.0}$ cm^{-3}). Another component is warm ($>$ 20 – 40 K) and moderate dense ($\sim 10^{3.5}$ cm^{-3}). Ridges are generally less dense ($< 10^{3.0-3.5}$ cm^{-3}). Northern ridge is warmer ($>$ 15 – 20 K) than the southern ridge ($<$ 30 K).

- HCN observations suggest that the dense gas fraction in the central region is larger than the ridges by a factor of two. Dense gas fraction in the northern ridge is larger than that of southern ridge by 1.3 times.

- The cause of the wide range of R_{10} is likely due to the change of gas temperature, instead of dense gas fraction and intrinsic abundance ratio of ^{12}CO and ^{13}CO. We are not able to conclude whether velocity dispersion (linewidth) is a cause of R_{10} just by the fits of observed spectrum.

- Images of star forming tracers (Hα, 24μm, and FUV) show that star formation is more active in the northern ridge than the southern ridge. This may be the reason of the higher R_{10} in the northern ridge, namely, higher temperature.

We compare azimuthal gas and star formation properties in NGC 6946. Hα image is used as the star forming tracer because of the high resolution of the map. To recover the embedding star formation, $A_{\mathrm{H}\alpha}$ is estimated by equalizing SFR(Hα) and SFR(24μm).

- The highest $\Sigma_{\mathrm{H_2}}$ occurs at the galactic center and minibar. $\Sigma_{\mathrm{H_2},13} \approx 850$ M$_\odot$ pc^{-2} is found from the transition of ^{13}CO. $\Sigma_{\mathrm{H_2},12} \approx 2500$ M$_\odot$ pc^{-2} is found from

^{12}CO. In the northern ridge, $\Sigma_{H_2,13}$ and $\Sigma_{H_2,12}$ are 80 and 100 – 200 $M_\odot$ pc^{-2}, respectively. The southern ridge has comparable Σ_{H_2} with the northern ridge, $\Sigma_{H_2,13}$ and $\Sigma_{H_2,12}$ are 40 – 60 and 100 – 200 $M_\odot$ pc^{-2}.

- Largest Σ_{SFR} is found at the galactic center and minibar, ~ 3 $M_\odot$ yr^{-1} kpc^{-2}. In the southern ridge, Σ_{SFR} decreases with radius, reaching a small value of 0.02 $M_\odot$ yr^{-1} kpc^{-2} at a radius of 40″. However, Σ_{SFR} sustains at a level of 0.1 – 0.2 $M_\odot$ yr^{-1} kpc^{-2} in the northern ridge.

- Generally, SFE derived from ^{13}CO is larger than that from ^{12}CO because $\Sigma_{H_2,13}$ is 2 – 3 times lower than $\Sigma_{H_2,12}$. SFE_{13} is (1 – 4) $\times$ 10^{-9} yr^{-1} at the center, comparable with the northern ridge, in which we found a SFE_{13} of (1 – 3) $\times$ 10^{-9} yr^{-1}. SFE_{13} is lower in the southern ridge as (4 – 10) $\times$ 10^{-10} yr^{-1}, respectively.

- The Kennicutt-Schmidt law shows that SFE in the northern ridge is enhanced, deviated from the general trend produced by the galactic center and the southern ridge.

- From the P-V diagrams cut perpendicular to the bar, we found that northern ridge is associated with steeper velocity jump (presumably stronger shocks). The large strong shock may help to shape the physical properties of GMCs in the northern ridge and subsequently cause the enhanced SFE.

We study the difference of GMC properties in the northern ridge (GMC_N), southern ridge (GMC_S) and galactic disk (GMC_D, mainly in spiral arms) by using the giant molecular clouds identified by Donovan Meyer et al. (2013).

- We found that the GMC_S resemble GMC_D. Their properties can be decried with Larson's relation. However, while GMC_N follow the same relation of velocity dispersion–mass as other GMCs, their radius are more compact than the correlation of velocity dispersion–radius predicts. Consequently, GMC_N have larger density and shorter free-fall time, suggesting a faster star formation.

- We compare the mass–radius relation of the GMCs in NGC 6946 (this work) and GMCs in literature, including Antennae galaxies (starburst/interacting galaxies), Galactic center, Galactic disk, inner disk of spiral galaxies, outer disk of spiral galaxy, and dwarf galaxies. The relations of the two variables follow the trend in NGC 6946. This may be an outcome for GMCs in high-pressure environments. Specifically, the density of GMCs in the high-pressure environments have to grow to keep the balance between their internal pressures and the external pressure of ambient ISM.

Chapter 4

Summary

In this thesis, I study whether/how environment affect the physical properties of giant molecular clouds (GMCs) and their ability of star formation in barred spiral galaxies.

The uniqueness of this study is the utilization of a transition ^{13}CO (1–0) (110.2 GHz), which was very difficult to be mapped in nearby disks with high resolution and sufficient sensitivity till very recent[1]. Small opacity (optically thin) is characteristic of ^{13}CO, leading to its effective critical density (a few 10^3 cm^{-3}) about 10 times larger than ^{12}CO. Furthermore, owing to its small opacity, ^{13}CO reflects the amount of gas more faithfully than ^{12}CO. Although due to the different optical depth they trace,^{13}CO and ^{12}CO may not trace the same volume of a molecular cloud.

The thesis is divided into two parts. The first part considers general and large scale view of the relation of molecular gas and star formation based on Kennicutt-Schmidt law. The second part is a local view of the influence of galactic dynamics on the physical properties of GMCs and their star forming activity, specifically, galactic bar. The procedures and the results of the two topics are summarized in §4.1 and §4.2, respectively. Figure 4.1 and 4.2 are the flow charts of the two projects. In §4.3 and Figure 4.3, we make a connection of the two projects and summarize the overall story of this thesis.

4.1 Star Formation Law

The role of surface density of molecular gas ($\Sigma_{\rm H_2}$) is evaluated in terms of star formation law, so-called Kennicutt-Schmidt law (K–S law), which is defined as $\log \Sigma_{\rm SFR} = N \log \Sigma_{\rm H_2} + A$. N is slope of K–S law. To overcome the uncertainties introduced from the evolutionary stages of GMCs and star forming regions, K–S law is investigated under

[1] ^{12}CO to ^{13}CO intensity ratio is 5 – 20 in nearby galaxies

sub-kpc resolution ($\sim$ 300 pc) in IC 342. All data mentioned in this project are archival data.

K–S law is created with ^{13}CO map. The abundance of ^{13}CO is assumed. The temperature of gas is estimated by the fit of spectral energy distribution (SED) from 24 μm to 500 μm. For comparison, K–S law is made with ^{12}CO with the same physical resolution. The latest calibration of *continuous* CO-to-H_2 factor ($X_{\rm CO,v}$) as a function of CO intensity and metallicity is adopted. It turns out that $X_{\rm CO,v}$ changes by about a factor of five in IC 342. Therefore, using the Galactic CO-to-H_2 factor in nearby galaxies (as most of works did) is not a proper method.

Figure 4.1 shows a flow chart of this project. The central region of IC 342 has $\Sigma_{\rm H_2}$ of $\geqslant$ 100 $M_\odot$ pc^{-2}, and $\leqslant$ 100 $M_\odot$ pc^{-2} in the spiral arms. These areas are referred to high- and low-$\Sigma_{\rm H_2}$ regions, respectively. The slope of K–S law derived from both transitions are about 2 at the high-$\Sigma_{\rm H_2}$ regions, while they are $\sim$ 1.4 at low-$\Sigma_{\rm H_2}$ regions. The Toomre Q parameter is used to examine the gravitational instability of IC 342. The unstable regions (Q $<$ 1) are well consistent with the peaks of 24μm, suggesting that the large scale star formation is triggered by gravitational instability. On the other hand, in the high-$\Sigma_{\rm H_2}$ regions where $\Sigma_{\rm H_2} \geqslant$ 100 $M_\odot$ pc^{-2}, a steeper slope of 2 is observed. The slope of $\sim$2 may reflect a star formation induced by cloud-cloud collisions. Indeed, previous works have shown the detection of shock tracers in the central regions of IC 342. The slope of 2 can be explained by the self-regulated star formation as well, in which star formation is regulated by stellar feedback. The abovementioned results of IC 342 are reproduced by similar analysis in 15 nearby galaxies.

Moreover, to observe how star formation law vary with $\Sigma_{\rm H_2}$, thresholds of $\Sigma_{\rm H_2}$ are set to control the scope of fitting (in IC 342 only), by which the mean $\Sigma_{\rm H_2}$ gradually increase. With this method, slope of star formation law continuously changes with increasing $\Sigma_{\rm H_2}$, suggesting that there is no universal star formation law within a galaxy. The non-universal star formation law also suggests that star formation efficiency depends on the surface density of molecular gas. Hence, SFR does not simply rely on the amount of gas. Instead, how the gas been accumulated, star formation mechanism and the physical properties of giant molecular clouds are more important in controlling SFR/SFE. We study this issue further in the next project.

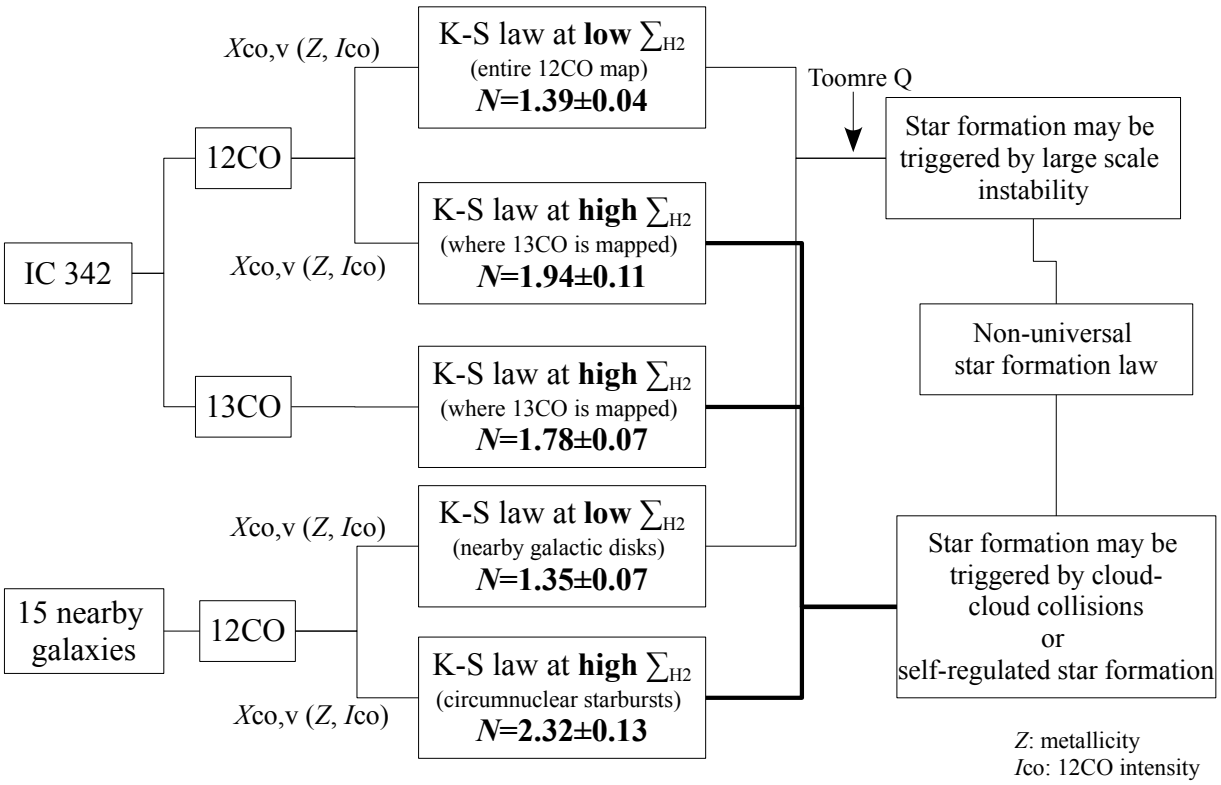

FIGURE 4.1: Flow chart of Chapter 2.

4.2 Influence of Galactic Bar in GMC Properties and Star Formation

One of the probable candidates which influence star formation efficiency is galactic dynamics. It plays an important role to redistribute gas in a galaxy.

Gas orbits in galactic bars generate large velocity jumps (shocks). The shocks can inhibit star formation by disrupting GMCs as simulations and some observations suggest. However, star formation is taking place in some galactic bars. The observed SFR in bars have a wide range of two order of magnitude. Hence, galactic bar is an ideal laboratory to study the environmental impact on GMC properties and their ability of star formation.

^{13}CO (1–0) observations are made toward the central $1'$ of NGC 6946, including the galactic center, bar and part of spiral arms. Both single dish (NRO 45-m telescope) and interferometer (CARMA) are used to preserve the total flux and resolution, respectively. The final physical resolution is 100 pc. The map shows that NGC 6946 contains an asymmetric bar, that is, the northern bar has a typical morphology of galactic bar, while the morphology of the southern bar is not clear. The northern and southern bar

are referred to strong bar and weak bar in this section[2]. Figure 4.2 shows a flow chart of this project.

Physical properties of molecular gas are derived with LVG calculations, our HCN observations, and infrared color map. The densest and warmest region is the central region, which consists of galactic center and a secondary bar (minibar). On the other hand, the strong bar is warmer and denser than the weak bar.

Σ_{H_2} of center/minibar is about 10 times larger than that of the strong and the weak bar. There is no significant difference of Σ_{H_2} among the bars. Σ_{SFR} is also $\sim$ 10 times larger in center/minibar than the strong bar; nevertheless, Σ_{SFR} of strong bar is 2 – 10 times larger than the weak bar. An uphill relation of Σ_{H_2} and Σ_{SFR} is seen in the center/minibar and the weak bar, but the slopes are different. Σ_{SFR} of the strong bar seems to be enhanced, deviated from the general trend of the K-S law.

Position-Velocity diagrams illustrate that the strong bar is associated with larger velocity jumps across the bar. The velocity jumps are expected to destroy GMCs and inhibit the subsequent star formation based on the theoretical works. However, in this study, large velocity jumps (shocks) are associated with the enhanced Σ_{SFR}.

The GMCs defined[3] by Donovan Meyer et al. (2013) are used to examine the difference (if there is) of GMC properties in the strong bar, weak bar, and galactic disk (mainly spiral arms). GMCs in the weak bar and galactic disk follow the Larsaon's relation of velocity dispersion–mass and velocity dispersion–radius. The former relation is valid for the GMCs in the strong bar, however, the later relation is unavailable. Specifically, GMCs in the strong bar are more compact than that predicted by the relation. In other words, with a given mass, GMCs in the stronger bar are smaller than those in the weak bar and the disk. As a result, they become denser, along with a shorter free-fall time. This can explain the enhanced SFE in the strong bar. Same phenomenon is found in the GMCs at the shock fronts of an expanding shell in the LMC. These results also provide some clues to understand the results of IC342. That is, the central source of the expanding shell can be supernova, HII regions, and stellar winds. These objects are found in abundance in the active star forming regions, such as galactic centers. Hence, in addition to the difference of star formation mechanism, the difference of GMC properties, namely, small clouds with larger Σ_{H_2} and shorter free-fall time, may contributes to the large slope of K–S law found in the center of IC 342.

We further compare GMCs properties in galaxies with different environments, including Antennae galaxies (starburst/interacting galaxies), Galactic center, Galactic disk, inner

[2]In the main text, I use different terms which are more specific.
[3]defined from ^{12}CO

disk of spiral galaxies, outer disk of spiral galaxy, and dwarf galaxies. The relatively small and dense GMCs are also found in those high-SFE environments, say, Antennae galaxies, Galactic center and the inner disk of spiral galaxies. Those GMCs seem to be an outcome for GMCs in high-pressure environments, in which the density of GMCs have to rise to maintain the balance between their internal pressures and the external pressure of ambient ISM.

FIGURE 4.2: Flow chart of Chapter 3.

4.3 Environmental Dependence of Star Formation

Summary of this thesis is illustrated in Figure 4.3. We first separate the story into two regimes, low-Σ_{H_2} and high-Σ_{H_2} regions.

At the low-Σ_{H_2} regions, such as the disk of normal spiral galaxies, star formation proceeds by gravitational instability. This star formation mechanism leads to an observed star formation law with a index of 1.5.

Galactic center, galactic bar and interacting galaxies have higher Σ_{H_2} than disks. Σ_{H_2} is often found to be $\geqslant 100$ $M_\odot$ pc^{-2}. Molecular clouds can be effectively collected into a region by large-scale galactic processes, such as galactic bars and the interaction of galaxies. Consequently, the clouds have more chance to collide with each other. The similar phenomenon is seen in the galactic center as well. If star formation is induced by the cloud-cloud collisions, one would expect a star formation law with a slope of 2. Indeed, we found this slope in the central region of IC 342 and other galaxies.

On the local scale, stellar populations, such as supernova explosions, heating of massive stars, and the expanding shells of HII regions, can raise the external pressure exerting on the surface of GMCs. As a result, GMCs become more compact and denser due to the increase in the external pressure on the surface of GMCs. If those compact and dense GMCs are formed in abundance, SFR and SFE become higher as well and more and more sources which can raise external pressure are generated. On the other hand, if the star formation rate is regulated by those stellar feedback, a slope of 2 of star formation law is expected again. This result is also consistent with the slope we found in the central starburst region of IC 342.

The external pressure could be risen by large-scale galactic process as well, for example, dust lane shocks and the interaction of galaxies. Indeed, in the bar of NGC 6946, we found that the compact GMCs are associated with larger dust lane shocks.

In summary, GMCs properties and star formation mechanisms respond to the galactic environments. The different star formation mechanism could be found in different regions of a galaxy. The physical properties of GMCs, for instance, size and density, could be affected by the galactic environments as well. In this work, we suggest that GMCs are more compact and dense in the high-pressure environments. The high pressure could be an outcome of large-scale galactic processes (e.g., galactic bar and interaction of galaxies) as well as the local stellar feedback (e.g., massive stars, HII regions, and supernova).

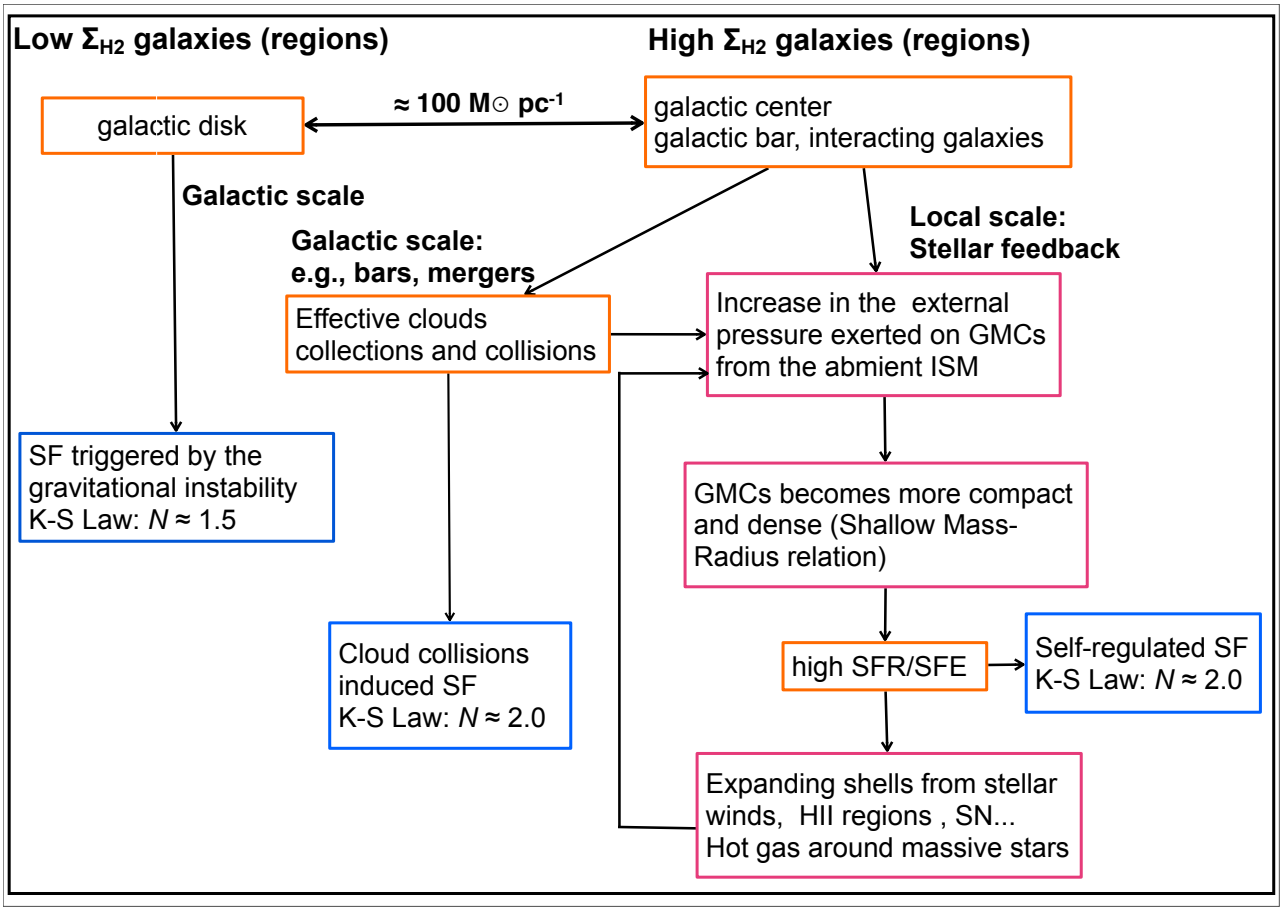

FIGURE 4.3: Summary of the thesis.

Chapter 5

Future Work

In Chapter 2, we suggest different star formation efficiency in the galaxy IC 342 with a study of relatively low physical resolution in molecular gas. We attribute the variation of star formation efficiency to different star formation mechanisms and speculate that the process of how molecular gas been accumulated is more important for determining star formation rate/efficiency. One of the efficient ways to collect molecular gas in a region is through the galactic dynamics. Indeed, we have seen that galactic dynamics (galactic bar) influence the GMCs properties in the study of NGC 6946 (Chapter 3). Future studies will focus on how galactic environments control the physical properties of GMCs and their star formation ability. A wide range of environmental properties is desired, e.g., disk galaxies to interacting galaxies/mergers.

This section is organized as follows. Firstly, I will show future work of GMCs properties in galactic bars in §5.1, and the GMCs and star formation within central < 1 kpc in §5.2. Implications of the relation of star formation and nuclear activity are introduced in §5.3. The possible relation between GMCs in disk galaxies and starburst/ineracting galaxies is in §5.4. Summary is of this section is shown in the chart of Figure 5.1.

5.1 Star Formation in Galactic Disks: Bars

To explore how galactic dynamics determine the properties of gas and star formation in bars, we need prior knowledge of: 1.) physical properties/conditions of GMCs, and 2.) kinematics of gas. Physical properties of GMCs require high-resolution observations. Physical conditions, such as temperature of gas can be inferred from radiation transfers based on multi-line observations in radio regime. Theoretical studies of gas motion in barred galaxy is rather robust. With these information, we can interpret the fate of

GMCs in bars, such as the direction of their motion, candidates of their counterpart of star forming regions. Moreover, galactic dynamics is a time dependent process in which bar strength is changing. Accordingly, analysis of GMC properties and kinematics across a wide range of bar strength is indispensable to constrain the full scenario.

In the future observations, optically thin ^{13}CO is still worth exploring more. Identify molecular clouds/clumps with ^{13}CO in nearby galaxies would be an interesting study. On the other hand, to fairly compare GMCs in external galaxies (external GMCs) and the Galactic GMCs, quality of data is essential. The most severe problem of observations of external GMCs is physical resolution. Hence, high frequency (transition) observations can solve the problems one step ahead. Moreover, although some molecular lines are still optically thick till high-transitions, high-transition lines typically trace higher density, i.e., closer to the site of star formation. Such high resolution and high transition observations rely on interferometers, such ALMA and SMA.

5.2 Star Formation within 1 kpc

Circumnuclear rings (CNRs) are nursery of super star clusters. Super star clusters are either be directly observed in CNRs (e.g., de Grijs et al., 2003, Díaz-Santos et al., 2007, Elmegreen et al., 2002, Galliano et al., 2005, Maoz et al., 2001) or indirectly suggested from the short star formation timescale and the top heavy (flatter) initial mass function of CNRs (Pan et al., 2013). Super star clusters are rarely observed in the disk of galaxies, but interacting galaxies and mergers. This suggests that the GMCs in CNRs should be different with that in the bars and disks but mimic GMCs in the more extreme objects. Hence, since we may not be able to study those distant, dramatically high SFR systems immanently with ALMA, CNRs offer a chance to study the physical properties of GMCs and their star forming ability in a similar environment.

Moreover, the large scale gas supply may tell the clues of star formation mode. Molecular gas in CNRs origins from their host galactic disks. The gas inflow rate ($\dot{M}_{\rm inflow}$) ranges incredibly large from 0.01 – 50 $M_\odot$ (Friedli & Benz, 1993, Haan et al., 2009). The latest works suggest that $\dot{M}_{\rm inflow}$ from large scale disk is playing a key role determining the properties of star formation in central kpc (e.g., Kruijssen et al., 2013, Seo & Kim, 2013). For example, if $\dot{M}_{\rm inflow}$ is so high that gas can always be gravitational unstable, one would expect a sustained star formation with $\dot{M}_{\rm inflow} \approx$ SFR in central kpc. On the other hand, if gas inflow is too small that gas need to accumulate to meet the threshold density for star formation, then $\dot{M}_{\rm inflow} >$ SFR, in such a case, episodic star formation is expected (Kruijssen et al., 2013). The relative intensity between $\dot{M}_{\rm inflow}$ and SFR along with the properties of molecular gas in CNRs then provide a clue of required physical

conditions (e.g., threshold density) to switch star formation on. Moreover, the observed distribution of diffuse/dense gas and stellar populations can be affected by $\dot{M}_{\rm inflow}$, the state of inflow gas (Seo & Kim, 2013) and the geometry of the gas orbits between dust lanes/bars and CNRs (Pan et al., 2013).

5.3 Star Formation within 1 kpc → Nuclear Activity

Gas supply from galactic disks to CNRs may have implications on central super massive black holes (SMBH)/active galactic nucleus (AGNs). There are some interesting observational results: 1.) A galactic scale fueling mechanism coupled with a central concentration is an efficient configuration to trigger nuclear activity (Hunt & Malkan, 1999); 2.) bar host AGNs show higher fraction of powerful AGN than those of non-bar hosts (Alonso et al., 2013). These results suggest that even though galactic disks are far from the central engines, they are playing a role of providing sufficient gas to central a kpc, but not all of gas fall into centers.

Growing SMBHs and AGNs requires gas at galactic disks be driven to $\approx$ 10 pc, where gas start to be controlled under the gravitational influence from BH. Mass required for central engines is on the order of 10^{6-7} $M_{\odot}$, which is only about 1 – 10% of gas mass within central 1 kpc of galaxies. The question is what physical process transport the 10% of gas from 1 kpc to 10 pc. It is complicated if we consider the dynamics of galaxy. The changing direction of torque is the formation mechanism of CNRs, yet it also stop the gas falling inward further. Hence, galactic dynamics itself may not be the direct driver of feeding central engine.

Star formation related processes seem to be the most convenient way to reduce angular momentum, such as shocks from supernova and cloud-cloud collisions (Fukuda et al., 2000, Jogee, 2006). Indeed, star formation has been attributed to these mechanisms in some CNRs (Ostriker & Shetty, 2011, Pan et al., 2013). The need of star formation related processes also explains the excess of young stellar populations in inner $\leq$ 1 kpc of active galaxies than non-active galaxies (e.g., Cid Fernandes et al., 2005, 2001, Kauffmann et al., 2003). Hence, physical properties of GMCs, and how star formation proceed in CNRs become crucial for understanding the fueling mechanism of central SMBHs/AGNs.

5.4 Relation of GMCs in Disks and Starbursts/Interacting Galaxies

We compare GMCs in disk galaxy and the GMCs in various environments in §3.10.2. We found a possible trend that when the ambient pressure of ISM increases, internal pressures of GMCs are forced to increase to keep the pressure balance. The ambient pressure of ISM rise from dwarfs → inner disk of disk galaxies → interacting galaxies. At the same, while the GMCs in disk galaxies are roughly in pressure equilibrium, GMCs in interacting galaxies are probably overpressure. Hence, GMCs in barred galaxies or disks galaxies may be just a snapshot of a sequential variation. Interacting galaxies are crucial because they can enlarge the galactic environments to a more extreme situation. GMCs properties in those galaxy cloud be just as simple as an exploration of that in the disk galaxies, but also possible that they are more complicated. Hence, comparison of GMCs in disk and interacting galaxies should offer a large picture of how environments determine the physical properties of GMCs.

As seen in the above sections, to constrain the large picture of how the physical properties of GMCs change over the galactic environments, comparative study is required. Different telescopes and transitions of observations cloud provide artificial variation of GMCs properties as noted by Sheth et al. (2008a). Hence, while interacting galaxies and starburst galaxies are found in abundance in the relatively far Universe, ALMA is the best to tool to carry out the most reliable comparative studies on this issue.

10 kpc
Galactic Star Formation: bars

The facts:
- Majority of SF★ takes place in disks of galaxies in the local Universe.
- Barred spiral galaxies are everywhere in the local Universe
- Bar can dynamically alter physical properties of gas and star formation efficiency in it (*Pan et al. 2014 in prep.*)
- Some bars have no SF, some have SF in bar ends, some have SF along bars, we found one with starburst in bar.
- We almost know nothing of the relation between gas and stars in bars.

The questions:
1. What cause the enhancement and inhibition of SF in bars even gas are plentiful? Bar strength?
2. What's the physical condition of gas that star formation favor in disks?
3. What's the implication of SF in bar for galaxy evolution?

↓

Some gas survive from SF in disks then enter CNRs. ★★
1. How much gas available?
2. What's the gas inflow rate?
3. What's the physical state of them?★★★ Ready or not ready for SF.

1 kpc
Local Star Formation: circumnuclear regions

The facts:
- Relation of gas and stars are different in galactic disks and centers (*Chapter 2*)
- Surface density of gas are extremely high in CNR (*Pan et al. 2013 ApJ*)
- Star Formation rate can be extremely high in CNR (*Pan et al. 2013 ApJ*), but not always high even dense gas fraction is high, e.g., Milky Way
- Nursery of super star cluster. Thus GMCs in CNRs should be more like that in mergers or high-z starburts

The questions:
1. Does the GMCs properties and the threshold density for star formation changing with environments?
2. How star formation proceed in 1 kpc?
3. What's the difference of the required condition for SF in CNR and disks ***(back to the box above)***

↓

We may not be able to observe gas supply in central engines immediately, but indirect constrain is possible.

10 pc
Nuclear Activity

The facts:
- There are black holes/AGNs in galactic centers. They need gas to grow up
- Amount of gas required is about 1 - 10% of the mass in CNR

The questions:
1. How gas reduce angular momentum and fall to 10 pc from < 1 kpc?
2. Star formation related processes are the convenient way, e.g, shocks from SN, clouds collisions. But how star formation star and proceed in few hundred parsec? ***(back to the box above)***

Interacting galaxies/mergers

The facts:
- They are often found to be starburst galaxies.
- Can produce super star clusters.

The questions:
1. Are GMCs in interacting galaxies different with that in disk galaxies?
2. GMCs in interacting galaxies is an exploration of disk GMCs towards a more extreme environment or they are totally different?

★ SF = Star Formation
★★ CNR = Circumnuclear Ring
★★★ It was believed that shocks in bars make gas diffuse and sparse star formation in terms of theory and simulations. But it conflicts with our observing results.

FIGURE 5.1: Summay of Future Plan.

Bibliography

Aalto, S., Beswick, R., & Jütte, E. 2010, A& A, 522, A59

Aalto, S., Booth, R. S., Black, J. H., & Johansson, L. E. B. 1995, A& A, 300, 369

Aalto, S., & Hüttemeister, S. 2000, A& A, 362, 42

Aalto, S., Radford, S. J. E., Scoville, N. Z., & Sargent, A. I. 1997, ApJL, 475, L107

Alonso, M. S., Coldwell, G., & Lambas, D. G. 2013, A& A, 549, A141

Alves, J., Lombardi, M., & Lada, C. J. 2007, A& A, 462, L17

Alves, J. F., Lada, C. J., & Lada, E. A. 2001, Nature, 409, 159

Aniano, G., Draine, B. T., Gordon, K. D., & Sandstrom, K. 2011, PASP, 123, 1218

Arimoto, N., Sofue, Y., & Tsujimoto, T. 1996, PASJ, 48, 275

Asayama, S., & Nakajima, T. 2013, PASP, 125, 213

Athanassoula, E. 1992, MNRAS, 259, 345

—. 2013, Bars and secular evolution in disk galaxies: Theoretical input, ed. J. Falcón-Barroso & J. H. Knapen, 305

Bachiller, R., & Cernicharo, J. 1986, A& A, 166, 283

Barnes, P. J., Yonekura, Y., Fukui, Y., et al. 2011, ApJS, 196, 12

Becklin, E. E., Gatley, I., Matthews, K., et al. 1980, ApJ, 236, 441

Bekki, K. 2004, PASA, 21, 167

Berentzen, I., Shlosman, I., Martinez-Valpuesta, I., & Heller, C. H. 2007, ApJ, 666, 189

Bergin, E. A., Maret, S., van der Tak, F. F. S., et al. 2006, ApJ, 645, 369

Bergin, E. A., Snell, R. L., & Goldsmith, P. F. 1996, ApJ, 460, 343

Bergin, E. A., & Tafalla, M. 2007, ARA& A, 45, 339

Bernard, J.-P., Paradis, D., Marshall, D. J., et al. 2010, A& A, 518, L88

Bertoldi, F., & McKee, C. F. 1992, ApJ, 395, 140

Bigiel, F., Leroy, A., Walter, F., et al. 2008, AJ, 136, 2846

Bigiel, F., Leroy, A. K., Walter, F., et al. 2011, ApJL, 730, L13

Blitz, L., & Rosolowsky, E. 2004a, ArXiv Astrophysics e-prints, astro-ph/0411520

—. 2004b, ApJL, 612, L29

Blitz, L., & Shu, F. H. 1980, ApJ, 238, 148

Boker, T., Forster-Schreiber, N. M., & Genzel, R. 1997, AJ, 114, 1883

Bolatto, A. D., Leroy, A. K., Rosolowsky, E., Walter, F., & Blitz, L. 2008, ApJ, 686, 948

Bolatto, A. D., Wolfire, M., & Leroy, A. K. 2013, ARA& A, 51, 207

Bonnell, I. A., Dobbs, C. L., Robitaille, T. P., & Pringle, J. E. 2006, MNRAS, 365, 37

Boomsma, R., Oosterloo, T. A., Fraternali, F., van der Hulst, J. M., & Sancisi, R. 2008, A& A, 490, 555

Boquien, M., Lisenfeld, U., Duc, P.-A., et al. 2011, A& A, 533, A19

Bothwell, M. S., Chapman, S. C., Tacconi, L., et al. 2010, MNRAS, 405, 219

Bournaud, F., & Combes, F. 2002, A& A, 392, 83

Bournaud, F., Combes, F., & Semelin, B. 2005, MNRAS, 364, L18

Burton, M. G., Braiding, C., Glueck, C., et al. 2013, PASA, 30, 44

Calzetti, D. 2012, ArXiv e-prints, arXiv:1208.2997

Calzetti, D., Kennicutt, Jr., R. C., Bianchi, L., et al. 2005, ApJ, 633, 871

Calzetti, D., Kennicutt, R. C., Engelbracht, C. W., et al. 2007, ApJ, 666, 870

Cambrésy, L. 1999, A& A, 345, 965

Carilli, C. L., & Walter, F. 2013, ARA& A, 51, 105

Caselli, P., Walmsley, C. M., Tafalla, M., Dore, L., & Myers, P. C. 1999, ApJL, 523, L165

Cedrés, B., Cepa, J., Bongiovanni, Á., et al. 2012, A& A, 545, A43

Cheung, E., Athanassoula, E., Masters, K. L., et al. 2013, ApJ, 779, 162

Chou, R. C. Y., Peck, A. B., Lim, J., et al. 2007, ApJ, 670, 116

Cid Fernandes, R., González Delgado, R. M., Storchi-Bergmann, T., Martins, L. P., & Schmitt, H. 2005, MNRAS, 356, 270

Cid Fernandes, R., Heckman, T., Schmitt, H., González Delgado, R. M., & Storchi-Bergmann, T. 2001, ApJ, 558, 81

Coelho, P., & Gadotti, D. A. 2011, ApJL, 743, L13

Cox, P. 1989, A& A, 225, L1

Crosthwaite, L. P., Turner, J. L., & Ho, P. T. P. 2000, AJ, 119, 1720

Crosthwaite, L. P., Turner, J. L., Hurt, R. L., et al. 2001, AJ, 122, 797

Dame, T. M., Elmegreen, B. G., Cohen, R. S., & Thaddeus, P. 1986, ApJ, 305, 892

Dame, T. M., Hartmann, D., & Thaddeus, P. 2001, ApJ, 547, 792

Dawson, J. R., Kawamura, A., Mizuno, N., Onishi, T., & Fukui, Y. 2008, PASJ, 60, 1297

Dawson, J. R., McClure-Griffiths, N. M., Wong, T., et al. 2013, ApJ, 763, 56

de Grijs, R., Anders, P., Bastian, N., et al. 2003, MNRAS, 343, 1285

Díaz-Santos, T., Alonso-Herrero, A., Colina, L., Ryder, S. D., & Knapen, J. H. 2007, ApJ, 661, 149

Dickman, R. L. 1978, AJ, 83, 363

Dickman, R. L., Snell, R. L., & Schloerb, F. P. 1986, ApJ, 309, 326

Dobashi, K. 2011, PASJ, 63, 1

Dobbs, C. L., Bonnell, I. A., & Pringle, J. E. 2006, MNRAS, 371, 1663

Dobbs, C. L., Burkert, A., & Pringle, J. E. 2011a, MNRAS, 417, 1318

—. 2011b, MNRAS, 413, 2935

Dobbs, C. L., & Pringle, J. E. 2009, MNRAS, 396, 1579

Dobbs, C. L., Pringle, J. E., & Naylor, T. 2013, MNRAS, arXiv:1309.6244

Donovan Meyer, J., Koda, J., Momose, R., et al. 2012, ApJ, 744, 42

—. 2013, ApJ, 772, 107

Downes, D., Radford, S. J. E., Guilloteau, S., et al. 1992, A& A, 262, 424

Downes, D., & Solomon, P. M. 1998, ApJ, 507, 615

Downes, D., Solomon, P. M., & Radford, S. J. E. 1993, ApJL, 414, L13

Egusa, F., Kohno, K., Sofue, Y., Nakanishi, H., & Komugi, S. 2009, ApJ, 697, 1870

Elmegreen, B. G. 1989, ApJ, 344, 306

—. 1993, ApJ, 411, 170

—. 1994, ApJL, 425, L73

—. 2002, ApJ, 577, 206

Elmegreen, B. G., & Elmegreen, D. M. 1983, MNRAS, 203, 31

Elmegreen, D. M., Chromey, F. R., McGrath, E. J., & Ostenson, J. M. 2002, AJ, 123, 1381

Elmegreen, D. M., Chromey, F. R., & Santos, M. 1998, AJ, 116, 1221

Encrenaz, P. J., Stark, A. A., Combes, F., & Wilson, R. W. 1979, A& A, 78, L1

Engargiola, G., Plambeck, R. L., Rosolowsky, E., & Blitz, L. 2003, ApJS, 149, 343

Engelbracht, C. W., Rieke, M. J., Rieke, G. H., & Latter, W. B. 1996, ApJ, 467, 227

Espada, D., Peck, A. B., Matsushita, S., et al. 2010, ApJ, 720, 666

Fathi, K., Toonen, S., Falcón-Barroso, J., et al. 2007, ApJL, 667, L137

Feldmann, R., Gnedin, N. Y., & Kravtsov, A. V. 2011, ApJ, 732, 115

Ferrière, K. M. 2001, Reviews of Modern Physics, 73, 1031

Field, G. B., & Saslaw, W. C. 1965, ApJ, 142, 568

Frerking, M. A., Langer, W. D., & Wilson, R. W. 1982, ApJ, 262, 590

Friedli, D., & Benz, W. 1993, A& A, 268, 65

Fukuda, H., Habe, A., & Wada, K. 2000, ApJ, 529, 109

Fukui, Y., Onishi, T., Abe, R., et al. 1999, PASJ, 51, 751

Gadotti, D. A. 2011, MNRAS, 415, 3308

Galametz, M., Kennicutt, R. C., Albrecht, M., et al. 2012, MNRAS, 425, 763

Galli, D., Walmsley, M., & Gonçalves, J. 2002, A& A, 394, 275

Galliano, E., Alloin, D., Pantin, E., Lagage, P. O., & Marco, O. 2005, A& A, 438, 803

Gao, Y., Carilli, C. L., Solomon, P. M., & Vanden Bout, P. A. 2007, ApJL, 660, L93

Gao, Y., Lo, K. Y., Lee, S.-W., & Lee, T.-H. 2001, ApJ, 548, 172

Gao, Y., & Solomon, P. M. 1999, ApJL, 512, L99

—. 2004a, ApJS, 152, 63

—. 2004b, ApJ, 606, 271

García-Burillo, S., Martín-Pintado, J., Fuente, A., & Neri, R. 2001, ApJL, 563, L27

Gardan, E., Braine, J., Schuster, K. F., Brouillet, N., & Sievers, A. 2007, A& A, 473, 91

Glenn, J., & Hunter, T. R. 2001, ApJS, 135, 177

Goldreich, P., & Kwan, J. 1974, ApJ, 189, 441

Goldsmith, P. F. 2001, ApJ, 557, 736

Goldsmith, P. F., Heyer, M., Narayanan, G., et al. 2008, ApJ, 680, 428

Gordon, K. D., Engelbracht, C. W., Rieke, G. H., et al. 2008, ApJ, 682, 336

Gratier, P., Braine, J., Rodriguez-Fernandez, N. J., et al. 2012, A& A, 542, A108

Haan, S., Schinnerer, E., Emsellem, E., et al. 2009, ApJ, 692, 1623

Harris, W. E., & Pudritz, R. E. 1994, ApJ, 429, 177

Harrison, A., Henkel, C., & Russell, A. 1999, MNRAS, 303, 157

Heiderman, A., Evans, II, N. J., Allen, L. E., Huard, T., & Heyer, M. 2010, ApJ, 723, 1019

Heitsch, F., Ballesteros-Paredes, J., & Hartmann, L. 2009, ApJ, 704, 1735

Helfer, T. T., & Blitz, L. 1995, ApJ, 450, 90

Henkel, C., Chin, Y.-N., Mauersberger, R., & Whiteoak, J. B. 1998, A& A, 329, 443

Henkel, C., & Mauersberger, R. 1993, A& A, 274, 730

Heyer, M., Krawczyk, C., Duval, J., & Jackson, J. M. 2009, ApJ, 699, 1092

Heyer, M. H., Brunt, C., Snell, R. L., et al. 1998, ApJS, 115, 241

Heyer, M. H., Carpenter, J. M., & Snell, R. L. 2001, ApJ, 551, 852

Heyer, M. H., & Ladd, E. F. 1995, ApJ, 439, 269

Hirota, A., Kuno, N., Sato, N., et al. 2009, PASJ, 61, 441

—. 2010, PASJ, 62, 1261

—. 2011, ApJ, 737, 40

Ho, P. T. P., Martin, R. N., & Ruf, K. 1982, A& A, 113, 155

Ho, P. T. P., & Townes, C. H. 1983, ARA& A, 21, 239

Hughes, A., Wong, T., Ott, J., et al. 2010, MNRAS, 406, 2065

Hughes, A., Meidt, S. E., Colombo, D., et al. 2013, ApJ, 779, 46

Hunt, L. K., & Malkan, M. A. 1999, ApJ, 516, 660

Hüttemeister, S., Aalto, S., Das, M., & Wall, W. F. 2000, A& A, 363, 93

Iono, D., Wilson, C. D., Takakuwa, S., et al. 2007, ApJ, 659, 283

Israel, F. P. 2009, A& A, 493, 525

Israel, F. P., & Baas, F. 2001, A& A, 371, 433

Jackson, J. M., Rathborne, J. M., Shah, R. Y., et al. 2006, ApJS, 163, 145

James, P. A., Bretherton, C. F., & Knapen, J. H. 2009, A& A, 501, 207

James, P. A., Shane, N. S., Knapen, J. H., Etherton, J., & Percival, S. M. 2005, A& A, 429, 851

Jog, C. J., & Solomon, P. M. 1992, ApJ, 387, 152

Jogee, S. 2006, in Lecture Notes in Physics, Berlin Springer Verlag, Vol. 693, Physics of Active Galactic Nuclei at all Scales, ed. D. Alloin, 143

Johnson, M. 2013, AJ, 145, 146

Kainulainen, J., Beuther, H., Henning, T., & Plume, R. 2009, A& A, 508, L35

Kato, S., Mizuno, N., Asayama, S.-i., et al. 1999, PASJ, 51, 883

Kauffmann, G., Heckman, T. M., Tremonti, C., et al. 2003, MNRAS, 346, 1055

Kauffmann, J., Pillai, T., & Zhang, Q. 2013, ApJL, 765, L35

Kawamura, A., Mizuno, Y., Minamidani, T., et al. 2009, ApJS, 184, 1

Keene, J., Schilke, P., Kooi, J., et al. 1998, ApJL, 494, L107

Kennicutt, R. C., & Evans, N. J. 2012, ARA& A, 50, 531

Kennicutt, R. C., Calzetti, D., Aniano, G., et al. 2011, PASP, 123, 1347

Kennicutt, Jr., R. C. 1998, ApJ, 498, 541

Kennicutt, Jr., R. C., Calzetti, D., Walter, F., et al. 2007, ApJ, 671, 333

Keto, E., Ho, L. C., & Lo, K.-Y. 2005, ApJ, 635, 1062

Kikumoto, T., Taniguchi, Y., Nakai, N., et al. 1998, PASJ, 50, 309

Kim, W.-T., Ostriker, E. C., & Stone, J. M. 2002, ApJ, 581, 1080

Klaas, U., Nielbock, M., Haas, M., Krause, O., & Schreiber, J. 2010, A& A, 518, L44

Klessen, R. S., & Hennebelle, P. 2010, A& A, 520, A17

Knapen, J. H., Stedman, S., Bramich, D. M., Folkes, S. L., & Bradley, T. R. 2004, A& A, 426, 1135

Koda, J., & Sofue, Y. 2006, PASJ, 58, 299

Koda, J., Scoville, N., Sawada, T., et al. 2009, ApJL, 700, L132

Koda, J., Sawada, T., Wright, M. C. H., et al. 2011, ApJS, 193, 19

Koda, J., Scoville, N., Hasegawa, T., et al. 2012, ApJ, 761, 41

Kohno, K., Kawabe, R., & Vila-Vilaró, B. 1999, ApJ, 511, 157

Komugi, S., Sofue, Y., & Egusa, F. 2006, PASJ, 58, 793

Komugi, S., Sofue, Y., Kohno, K., et al. 2008, ApJS, 178, 225

Kormendy, J. 1979, ApJ, 227, 714

Koyama, H., & Inutsuka, S.-I. 2000, ApJ, 532, 980

Koyama, H., & Inutsuka, S.-i. 2002, ApJL, 564, L97

Kravtsov, A. V. 2003, ApJL, 590, L1

Kruijssen, J. M. D., Longmore, S. N., Elmegreen, B. G., et al. 2013, ArXiv e-prints, arXiv:1303.6286

Krumholz, M. R., & McKee, C. F. 2005, ApJ, 630, 250

Krumholz, M. R., McKee, C. F., & Tumlinson, J. 2008, ApJ, 689, 865

—. 2009, ApJ, 699, 850

Krumholz, M. R., & Tan, J. C. 2007, ApJ, 654, 304

Kuno, N., Sato, N., Nakanishi, H., et al. 2007, PASJ, 59, 117

Kwan, J. 1979, ApJ, 229, 567

Lada, C. J., & Lada, E. A. 1991, in Astronomical Society of the Pacific Conference Series, Vol. 13, The Formation and Evolution of Star Clusters, ed. K. Janes, 3–22

Lada, C. J., Lada, E. A., Clemens, D. P., & Bally, J. 1994, ApJ, 429, 694

Lada, C. J., Lombardi, M., & Alves, J. F. 2010, ApJ, 724, 687

Lada, C. J., Lombardi, M., Roman-Zuniga, C., Forbrich, J., & Alves, J. F. 2013, ApJ, 778, 133

Lada, E. A., Bally, J., & Stark, A. A. 1991, ApJ, 368, 432

Langer, W. D., Wilson, R. W., Goldsmith, P. F., & Beichman, C. A. 1989, ApJ, 337, 355

Larson, R. B. 1981, MNRAS, 194, 809

Launhardt, R., Mezger, P. G., Haslam, C. G. T., et al. 1996, A& A, 312, 569

Lee, J. C., Gil de Paz, A., Tremonti, C., et al. 2009, ApJ, 706, 599

Leisawitz, D., Bash, F. N., & Thaddeus, P. 1989, ApJS, 70, 731

Leon, S., Jeyakumar, S., Pérez-Ramírez, D., et al. 2008, A& A, 491, 703

Leroy, A., Bolatto, A. D., Simon, J. D., & Blitz, L. 2005, ApJ, 625, 763

Leroy, A. K., Walter, F., Brinks, E., et al. 2008, AJ, 136, 2782

Li, A., & Draine, B. T. 2001, ApJ, 554, 778

Li, Y., Mac Low, M.-M., & Klessen, R. S. 2006, ApJ, 639, 879

Liszt, H. S. 2006, A& A, 447, 533

Lombardi, M., Alves, J., & Lada, C. J. 2006, A& A, 454, 781

Longmore, S. N., Burton, M. G., Barnes, P. J., et al. 2007, MNRAS, 379, 535

Mac Low, M.-M., & Klessen, R. S. 2004, Reviews of Modern Physics, 76, 125

Magnani, L., Blitz, L., & Mundy, L. 1985, ApJ, 295, 402

Malhotra, S. 1994, ApJ, 433, 687

Mangum, J. G., Darling, J., Henkel, C., & Menten, K. M. 2013a, ApJ, 766, 108

Mangum, J. G., Darling, J., Henkel, C., et al. 2013b, ApJ, 779, 33

Maoz, D., Barth, A. J., Ho, L. C., Sternberg, A., & Filippenko, A. V. 2001, AJ, 121, 3048

Markwardt, C. B. 2009, in Astronomical Society of the Pacific Conference Series, Vol. 411, Astronomical Data Analysis Software and Systems XVIII, ed. D. A. Bohlender, D. Durand, & P. Dowler, 251

Martel, H., Urban, A., & Evans, II, N. J. 2012, ApJ, 757, 59

Martin, P., & Friedli, D. 1997, A& A, 326, 449

—. 1999, A& A, 346, 769

Martin, P., & Roy, J.-R. 1994, ApJ, 424, 599

Martín, S., George, M. R., Wilner, D. J., & Espada, D. 2010, AJ, 139, 2241

Matsunaga, K., Mizuno, N., Moriguchi, Y., et al. 2001, PASJ, 53, 1003

Matsushita, S., Kawabe, R., Kohno, K., Tosaki, T., & Vila-Vilaró, B. 2010, PASJ, 62, 409

Matsushita, S., Kohno, K., Vila-Vilaro, B., Tosaki, T., & Kawabe, R. 1998, ApJ, 495, 267

Matzner, C. D., & McKee, C. F. 2000, ApJ, 545, 364

McCall, M. L., Rybski, P. M., & Shields, G. A. 1985, ApJS, 57, 1

McKee, C. F. 1989, ApJ, 345, 782

McKee, C. F. 1999, in NATO ASIC Proc. 540: The Origin of Stars and Planetary Systems, ed. C. J. Lada & N. D. Kylafis, 29

McKee, C. F., & Ostriker, E. C. 2007, ARA& A, 45, 565

McQuinn, K. B. W., Simon, R., Law, C. J., et al. 2002, ApJ, 576, 274

Meier, D. S., & Turner, J. L. 2001, ApJ, 551, 687

—. 2004, AJ, 127, 2069

—. 2005, ApJ, 618, 259

Meier, D. S., Turner, J. L., & Hurt, R. L. 2000, ApJ, 531, 200

—. 2008, ApJ, 675, 281

Milam, S. N., Savage, C., Brewster, M. A., Ziurys, L. M., & Wyckoff, S. 2005, ApJ, 634, 1126

Mizuno, N., Yamaguchi, R., Mizuno, A., et al. 2001, PASJ, 53, 971

Morgan, L. K., Figura, C. C., Urquhart, J. S., & Thompson, M. A. 2010, MNRAS, 408, 157

Mouschovias, T. C., Shu, F. H., & Woodward, P. R. 1974, A& A, 33, 73

Mouschovias, T. C., & Spitzer, Jr., L. 1976, ApJ, 210, 326

Moustakas, J., Kennicutt, Jr., R. C., Tremonti, C. A., et al. 2010, ApJS, 190, 233

Muraoka, K., Tosaki, T., Miura, R., et al. 2012, PASJ, 64, 3

Muraoka, K., Kohno, K., Tosaki, T., et al. 2009, ApJ, 706, 1213

Murray, N. 2011, ApJ, 729, 133

Myers, P. C., Fuller, G. A., Goodman, A. A., & Benson, P. J. 1991, ApJ, 376, 561

Nakai, N. 1992, PASJ, 44, L27

Nakai, N., & Kuno, N. 1995, PASJ, 47, 761

Nakai, N., Kuno, N., Handa, T., & Sofue, Y. 1991, in IAU Symposium, Vol. 146, Dynamics of Galaxies and Their Molecular Cloud Distributions, ed. F. Combes & F. Casoli, 63

Nakajima, T., Kimura, K., Nishimura, A., et al. 2013, PASP, 125, 252

Narayan, C. A., & Jog, C. J. 2002a, A& A, 390, L35

—. 2002b, A& A, 394, 89

Narayanan, D. 2013, ArXiv e-prints, arXiv:1304.6429

Narayanan, D., Krumholz, M., Ostriker, E. C., & Hernquist, L. 2011, MNRAS, 418, 664

Narayanan, D., Krumholz, M. R., Ostriker, E. C., & Hernquist, L. 2012, MNRAS, 421, 3127

Neininger, N., Guelin, M., Klein, U., Garcia-Burillo, S., & Wielebinski, R. 1998, A& A, 339, 737

Nozawa, S., Mizuno, A., Teshima, Y., Ogawa, H., & Fukui, Y. 1991, ApJS, 77, 647

Oka, T., Hasegawa, T., Hayashi, M., Handa, T., & Sakamoto, S. 1998, ApJ, 493, 730

Oka, T., Hasegawa, T., Sato, F., et al. 2001, ApJ, 562, 348

Onishi, T., Mizuno, A., Kawamura, A., Ogawa, H., & Fukui, Y. 1998, ApJ, 502, 296

Onodera, S., Kuno, N., Tosaki, T., et al. 2010, ApJL, 722, L127

Ostriker, E. C., McKee, C. F., & Leroy, A. K. 2010, ApJ, 721, 975

Ostriker, E. C., & Shetty, R. 2011, ApJ, 731, 41

Paglione, T. A. D., Yam, O., Tosaki, T., & Jackson, J. M. 2004, ApJ, 611, 835

Paglione, T. A. D., Wall, W. F., Young, J. S., et al. 2001, ApJS, 135, 183

Paladini, R., Umana, G., Veneziani, M., et al. 2012, ApJ, 760, 149

Pan, H.-A., Lim, J., Matsushita, S., Wong, T., & Ryder, S. 2013, ApJ, 768, 57

Papadopoulos, P. P., & Seaquist, E. R. 1999, ApJ, 516, 114

Papadopoulos, P. P., van der Werf, P. P., Xilouris, E. M., et al. 2012, MNRAS, 426, 2601

Parker, E. N. 1966, ApJ, 145, 811

Petitpas, G. R., & Wilson, C. D. 2003, ApJ, 587, 649

Pickett, H. M., Poynter, R. L., Cohen, E. A., et al. 1998, Journal of Quantitiative Spectroscopy and Radiative Trasfer, 60, 883

Pilyugin, L. S. 2000, A& A, 362, 325

—. 2001a, A& A, 369, 594

—. 2001b, A& A, 373, 56

Pilyugin, L. S., & Thuan, T. X. 2005, ApJ, 631, 231

Pilyugin, L. S., Vílchez, J. M., & Contini, T. 2004, A& A, 425, 849

Pineda, J. E., Caselli, P., & Goodman, A. A. 2008, ApJ, 679, 481

Pineda, J. L., Goldsmith, P. F., Chapman, N., et al. 2010, ApJ, 721, 686

Pirogov, L., Zinchenko, I., Caselli, P., Johansson, L. E. B., & Myers, P. C. 2003, A& A, 405, 639

Pisano, D. J., & Wilcots, E. M. 2000, MNRAS, 319, 821

Popescu, C. C., Tuffs, R. J., Völk, H. J., Pierini, D., & Madore, B. F. 2002, ApJ, 567, 221

Rahman, N., Bolatto, A. D., Xue, R., et al. 2012, ApJ, 745, 183

Rand, R. J., & Kulkarni, S. R. 1990, ApJL, 349, L43

Rebolledo, D., Wong, T., Leroy, A., Koda, J., & Donovan Meyer, J. 2012, ApJ, 757, 155

Regan, M. W. 2000, ApJ, 541, 142

Regan, M. W., Sheth, K., & Vogel, S. N. 1999, ApJ, 526, 97

Regan, M. W., Thornley, M. D., Vogel, S. N., et al. 2006, ApJ, 652, 1112

Reynaud, D., & Downes, D. 1998, A& A, 337, 671

—. 1999, A& A, 347, 37

Rieke, G. H., Alonso-Herrero, A., Weiner, B. J., et al. 2009, ApJ, 692, 556

Rieke, G. H., Young, E. T., Engelbracht, C. W., et al. 2004, ApJS, 154, 25

Robitaille, T. P., & Whitney, B. A. 2010, ApJL, 710, L11

Roman-Duval, J., Jackson, J. M., Heyer, M., Rathborne, J., & Simon, R. 2010, ApJ, 723, 492

Rosolowsky, E. 2007, ApJ, 654, 240

Rosolowsky, E., & Blitz, L. 2005, ApJ, 623, 826

Rosolowsky, E., Engargiola, G., Plambeck, R., & Blitz, L. 2003, ApJ, 599, 258

Sage, L. J., & Isbell, D. W. 1991, A& A, 247, 320

Saha, A., Claver, J., & Hoessel, J. G. 2002, AJ, 124, 839

Sakamoto, K., Ho, P. T. P., Mao, R.-Q., Matsushita, S., & Peck, A. B. 2007, ApJ, 654, 782

Sakamoto, K., Mao, R.-Q., Matsushita, S., et al. 2011, ApJ, 735, 19

Sakamoto, K., Ho, P. T. P., Iono, D., et al. 2006, ApJ, 636, 685

Sakamoto, S., Handa, T., Sofue, Y., Honma, M., & Sorai, K. 1997, ApJ, 475, 134

Sanders, D. B., Clemens, D. P., Scoville, N. Z., & Solomon, P. M. 1986, ApJS, 60, 1

Sanders, D. B., Mazzarella, J. M., Kim, D.-C., Surace, J. A., & Soifer, B. T. 2003, AJ, 126, 1607

Sanders, D. B., & Mirabel, I. F. 1996, ARA& A, 34, 749

Sanders, D. B., Solomon, P. M., & Scoville, N. Z. 1984, ApJ, 276, 182

Sault, R. J., Teuben, P. J., & Wright, M. C. H. 1995, in Astronomical Society of the Pacific Conference Series, Vol. 77, Astronomical Data Analysis Software and Systems IV, ed. R. A. Shaw, H. E. Payne, & J. J. E. Hayes, 433

Sawada, T., Hasegawa, T., Handa, T., et al. 2001, ApJS, 136, 189

Schinke, R., Engel, V., Buck, U., Meyer, H., & Diercksen, G. H. F. 1985, ApJ, 299, 939

Schinnerer, E., Böker, T., Emsellem, E., & Lisenfeld, U. 2006, ApJ, 649, 181

Schinnerer, E., Böker, T., & Meier, D. S. 2003, ApJL, 591, L115

Schinnerer, E., Weiß, A., Aalto, S., & Scoville, N. Z. 2010, ApJ, 719, 1588

Schlegel, D. J., Finkbeiner, D. P., & Davis, M. 1998, ApJ, 500, 525

Schmidt, M. 1959, ApJ, 129, 243

Schnee, S. L., Ridge, N. A., Goodman, A. A., & Li, J. G. 2005, ApJ, 634, 442

Schulz, A., Güsten, R., Köster, B., & Krause, D. 2001, A& A, 371, 25

Scoville, N. Z., & Hersh, K. 1979, ApJ, 229, 578

Scoville, N. Z., Sanders, D. B., & Clemens, D. P. 1986, ApJL, 310, L77

Scoville, N. Z., & Solomon, P. M. 1974, ApJL, 187, L67

—. 1975, ApJL, 199, L105

Seo, W.-Y., & Kim, W.-T. 2013, ApJ, 769, 100

Sherman, R. A. 2012, ApJ, 760, 58

Sheth, K., Vogel, S. N., Wilson, C. D., & Dame, T. M. 2008a, ApJ, 675, 330

Sheth, K., Elmegreen, D. M., Elmegreen, B. G., et al. 2008b, ApJ, 675, 1141

Shu, F. H., Adams, F. C., & Lizano, S. 1987, ARA& A, 25, 23

Shu, F. H., Allen, R. J., Lizano, S., & Galli, D. 2007, ApJL, 662, L75

Sofue, Y. 1997, PASJ, 49, 17

Solomon, P. M., Downes, D., & Radford, S. J. E. 1992, ApJL, 387, L55

Solomon, P. M., Downes, D., Radford, S. J. E., & Barrett, J. W. 1997, ApJ, 478, 144

Solomon, P. M., Rivolo, A. R., Barrett, J., & Yahil, A. 1987, ApJ, 319, 730

Solomon, P. M., Sanders, D. B., & Scoville, N. Z. 1979, in IAU Symposium, Vol. 84, The Large-Scale Characteristics of the Galaxy, ed. W. B. Burton, 35–52

Sonnentrucker, P., Welty, D. E., Thorburn, J. A., & York, D. G. 2007, ApJS, 168, 58

Stark, A. A., & Brand, J. 1989, ApJ, 339, 763

Stepnik, B., Abergel, A., Bernard, J.-P., et al. 2003, A& A, 398, 551

Stil, J. M., Taylor, A. R., Martin, P. G., et al. 2004, ApJ, 608, 297

Strong, A. W., Bloemen, J. B. G. M., Dame, T. M., et al. 1988, A& A, 207, 1

Tabatabaei, F. S., & Berkhuijsen, E. M. 2010, A& A, 517, A77

Tan, J. C. 2000, ApJ, 536, 173

Tan, Q.-H., Gao, Y., Zhang, Z.-Y., & Xia, X.-Y. 2011, Research in Astronomy and Astrophysics, 11, 787

Taniguchi, Y., & Ohyama, Y. 1998, ApJL, 507, L121

Tasker, E. J., & Tan, J. C. 2009, ApJ, 700, 358

Teyssier, D., Hennebelle, P., & Pérault, M. 2002, A& A, 382, 624

Tieftrunk, A. R., Megeath, S. T., Wilson, T. L., & Rayner, J. T. 1998, A& A, 336, 991

Tomisaka, K. 1984, PASJ, 36, 457

Toomre, A. 1964, ApJ, 139, 1217

Tosaki, T., Hasegawa, T., Shioya, Y., Kuno, N., & Matsushita, S. 2002, PASJ, 54, 209

Tubbs, A. D. 1982, ApJ, 255, 458

Turner, J. L., & Ho, P. T. P. 1983, ApJL, 268, L79

Turner, J. L., & Hurt, R. L. 1992, ApJ, 384, 72

Ueda, J., Iono, D., Petitpas, G., et al. 2012, ApJ, 745, 65

Wada, K., & Norman, C. A. 2007, ApJ, 660, 276

Walter, F., Brinks, E., de Blok, W. J. G., et al. 2008, AJ, 136, 2563

Watanabe, Y., Sorai, K., Kuno, N., & Habe, A. 2011, MNRAS, 411, 1409

Watson, W. D., Anicich, V. G., & Huntress, Jr., W. T. 1976, ApJL, 205, L165

Wei, L. H., Keto, E., & Ho, L. C. 2012, ApJ, 750, 136

Werk, J. K., Putman, M. E., Meurer, G. R., & Santiago-Figueroa, N. 2011, ApJ, 735, 71

Wilkins, S. M., Hopkins, A. M., Trentham, N., & Tojeiro, R. 2008, MNRAS, 391, 363

Williams, J. P., de Geus, E. J., & Blitz, L. 1994, ApJ, 428, 693

Wilson, C. D. 1995, ApJL, 448, L97

Wilson, C. D., Scoville, N., Madden, S. C., & Charmandaris, V. 2003, ApJ, 599, 1049

Wilson, C. D., & Walker, C. E. 1994, ApJ, 432, 148

Wilson, C. D., Walker, C. E., & Thornley, M. D. 1997, ApJ, 483, 210

Wilson, T. L., Rohlfs, K., & Hüttemeister, S. 2009, Tools of Radio Astronomy (Springer-Verlag), doi:10.1007/978-3-540-85122-6

Wolfire, M. G., Hollenbach, D., & McKee, C. F. 2010, ApJ, 716, 1191

Wong, T., Ladd, E. F., Brisbin, D., et al. 2008, MNRAS, 386, 1069

Wong, T., Hughes, A., Ott, J., et al. 2011, ApJS, 197, 16

Wu, J., Evans, II, N. J., Gao, Y., et al. 2005, ApJL, 635, L173

Yamaguchi, R., Mizuno, N., Onishi, T., Mizuno, A., & Fukui, Y. 2001, PASJ, 53, 959

Yang, B., Stancil, P. C., Balakrishnan, N., & Forrey, R. C. 2010, ApJ, 718, 1062

Yang, C.-C., Gruendl, R. A., Chu, Y.-H., Mac Low, M.-M., & Fukui, Y. 2007, ApJ, 671, 374

Yao, L., Bell, T. A., Viti, S., Yates, J. A., & Seaquist, E. R. 2006, ApJ, 636, 881

Yin, J., Magrini, L., Matteucci, F., et al. 2010, A& A, 520, A55

Yonekura, Y., Asayama, S., Kimura, K., et al. 2005, ApJ, 634, 476

Young, J. S., & Sanders, D. B. 1986, ApJ, 302, 680

Yusef-Zadeh, F., Hewitt, J. W., Arendt, R. G., et al. 2009, ApJ, 702, 178

Zhu, M., Seaquist, E. R., & Kuno, N. 2003, ApJ, 588, 243

Zurita, A., Relaño, M., Beckman, J. E., & Knapen, J. H. 2004, A& A, 413, 73